

Proceedings of the
**Magellan Workshop 2016 - Connecting
Neutrino Physics and Astronomy**

March 17-18, 2016
Hamburg, Germany

Editors: Stefan K. G. Dahmke, Mikko Meyer, Laura Vanhoefer

Verlag Deutsches Elektronen-Synchrotron

Impressum

Proceedings of the Magellan Workshop 2016 March 17-18, 2016, Hamburg, Germany

Conference homepage

<https://indico.desy.de/event/13130>

Slides at

<https://indico.desy.de/event/13130>

Online proceedings at

<http://www-library.desy.de/preparch/desy/proc/proc16-05.pdf>

The copyright is governed by the Creative Commons agreement, which allows for free use and distribution of the articles for non-commercial activity, as long as the title, the authors' names and the place of the original are referenced.

Photo credit:

ESO (back cover, p. 173)

NASA (front cover)

Photographic Archive of the Hamburg Observatory (p. 191)

Matthias Quad, Geographisch Handtbuch, Cologne, 1600

modified, taken from http://libweb5.princeton.edu/visual_materials/maps/websites/pacific/magellan-strait/magellan-strait-maps.html (p. v, p. 1)

Editors:

Stefan K. G. Dahmke, Mikko Meyer, Laura Vanhoefer

September 2016

DESY-PROC-2016-05

ISBN 978-3-945931-08-0

ISSN 1435-8077

Published by

Verlag Deutsches Elektronen-Synchrotron

Notkestraße 85

22607 Hamburg

Germany

Printed by

Kopierzentrale Deutsches Elektronen-Synchrotron

Organizing Committee

Benjamin Büttner
Institut für Experimentalphysik
Universität Hamburg
Luruper Chaussee 149
22761 Hamburg
benjamin.buettner@desy.de
Scientific and local organizing committee

Stefan Dahmke
Hamburger Sternwarte
Universität Hamburg
Gojenbergsweg 112
21029 Hamburg
sdahmke@hs.uni-hamburg.de
Scientific and local organizing committee

Mikko Meyer
Institut für Experimentalphysik
Universität Hamburg
Luruper Chaussee 149
22761 Hamburg
mikko.meyer@desy.de
Scientific and local organizing committee

Laura Vanhoefer
Max-Planck-Institut für Physik
(Werner-Heisenberg-Institut)
Föhringer Ring 6
80805 München
lvanhoef@mpp.mpg.de
Scientific organizing committee and workshop support team

Contact: magellan-workshop@desy.de

Workshop Support Team

Hennig Rebber (Universität Hamburg)
David Meyhöfer (Universität Hamburg)
Annika Vanhoefer (Universität Hamburg)
Laura Vanhoefer (Max-Planck-Institut für Physik)

Acknowledgments

We would like to thank Sylke Strien from the administration of the Hamburg University and our local support team for their wonderful help. Furthermore we would like to thank Martin Tluczykont for his advice during the preparation of the workshop. We also thank DESY for enabling us to hold the workshop at the auditorium and the DESY staff for their support.

Finally, we would also like to thank all speakers and participants for their interest and contributions.

Preface

The first Magellan Workshop took place on March 17th/18th 2016 in Hamburg. Several topics have been addressed during the workshop with the most time devoted to discussing stellar physics and supernova physics. These two key topics are especially interesting to two distinct fields, each with their own approach, method and extensive knowledge gained: astrophysics and neutrino physics. It is thus no surprise that the workshop specifically intended to bring these groups together was met with a certain enthusiasm. 46 scientists working in institutions across seven countries attended a total of 30 plenary talks during their two days in Hamburg. The workshop then concluded with a trip to the Hamburg Observatory, for a tour of the historic and current telescopes.

While supernovae of course were a primary topic, the presentations included many different, exciting projects. From relatively nearby objects in studies on geoneutrinos originating from inside the Earth via stellar physics in the refinement of solar models to high energy sources across multiple galaxies to the Cosmic Microwave Background.

One particular subject in the field of supernova physics for the past 29 years of course has been the supernova SN1987A, mostly owed to its fairly recent explosion enabling modern science to observe the event from Earth and space alike both in electromagnetic waves and particle fluxes. These measurements have greatly expanded our knowledge as many theories on both the internal mechanisms as well as the evolution of supernovae could consequently be tested. Not only does the Large Magellanic Cloud which hosts this famous supernova serve as a pictorial symbol for our workshop, it is also now commonly named after Ferdinand Magellan, who was not the first to discover this prominent feature in the southern night sky, but the one whose journey brought news of its marvellous sight to European astronomers back in the late 16th century. Furthermore this journey shall serve as a symbol of our own venture as Magellan led the expedition to circumnavigate the globe entirely, thus advancing the knowledge of his contemporaries with every mile travelled, but in doing so also became a connection between the Atlantic and Pacific oceans. Finding common ground for scientists of different fields to meet on thankfully is a much easier task than navigating the treacherous waters of the Magellan Strait, but nonetheless the Magellan Workshop hopefully opened a strait of sorts for future cooperations.

Benjamin Büttner
Stefan K. G. Dahmke
Mikko Meyer
Laura Vanhoefer



Ferdinand Magellan

- 1480** Born at Saborosa in Villa Real, Province of Traz os Montes in Portugal
- 1505** Magellan joins the expedition of Francisco d'Almeida to India
- 1512** During a posting to Morocco Magellan is badly wounded
- 1517** Magellan leaves Portugal and heads for Spain
- 1518** March: Magellan is promoted to the rank of Commander of the Order of Santiago and gets permission to search for the Spice Islands
- 1519** 10 August: Magellan leaves Seville with five ships
- 1519** 20 September: Magellan leaves Spain to start his voyage
- 1519** 6 December: Crew members spot South America
- 1520** Easter: While anchored off Patagonia waiting for favourable weather, a mutiny involving three out of the five ship captains breaks out
- 1520** October: After a series of delays, Magellan and his crew resume their voyage on the remaining ships
- 1520** 21 November: Enters the straits which would be named the Magellan Straits becoming the first Europeans ever to sail across the Pacific Ocean
- 1521** March 6: Magellan reaches the Pacific island of Guam
- 1521** 16 March: Discovers the Philippines
- 1521** April 27: Ferdinand Magellan is killed by natives on the island of Mactan. Only 110 of the original crew members remained so they abandoned one of the ships (Conception). On November 6th the remaining ships reached the Maluku Islands which was their original destination. Trinidad tried to return back to Spain the same way they had come but was forced to return to the Spice Islands where they were imprisoned by the Portuguese. The Victoria was the last remaining ship.
- 1522** September 6: The Victoria reaches Sanlucar de Barrameda in Spain with only 18 survivors led by the Spaniard Juan Sebastián Elcano who took over command after Magellan's death

Contents

Physics Opportunities with Supernova Neutrinos	3
Ninetta Saviano	
Neutrino-Nucleon Interactions in Core Collapse Supernovae	11
Andreas Lohs, Gabriel Martinez-Pinedo, Tobias Fischer	
Searches for point-like neutrino sources with the ANTARES neutrino telescope	19
Javier Barrios-Martí	
Solar models, neutrinos and composition	27
Aldo Serenelli, Nuria Vinyoles	
CNO neutrinos and metallicity of stars	35
Stefano Davini	
The GERDA Experiment: Search for the Neutrinoless Double Beta Decay	41
Michael Miloradovic	
The atmospheric muon charge ratio: a probe to constrain the atmospheric $\nu_\mu/\bar{\nu}_\mu$ ratio	47
Nicoletta Mauri	
A Search for Lorentz and CPT Violation Using the T2K Near Detectors	55
Gary Alexander Clifton	
Searching for neutrino oscillation parameters in long baseline experiments	65
Sampsa Vihonen	
Planck 2015 Cosmological Results	71
Daniela Paoletti	
The SNO+ experiment: current status and future prospects.	87
Valentina Lozza	
Measurement of solar neutrino fluxes with Borexino	95
Simone Marcocci <i>et al.</i>	
Monte Carlo simulations in neutrino physics: the example of the SOX experiment	105
Alessio Caminata <i>et al.</i>	
<i>Magellan Workshop 2016</i>	vii

Solar neutrino detection in a large volume double-phase liquid argon experiment	113
Davide Franco	
Neutrino Astrophysics with JUNO	121
Sebastian Lorenz	
Latest results from LUNA experiment	129
Francesca Cavanna	
Connecting neutrino Astrophysics to Multi-TeV to PeV gamma-ray astronomy with TAIGA	135
Martin Tluczykont <i>et al.</i>	
Simulation of imaging air shower Cherenkov telescopes as part of the TAIGA Project	143
Maike Kunnas <i>et al.</i>	
Recent Results from the MAGIC Telescopes	151
Dorit Eisenacher Glawion	
Neutrino Geoscience	157
Livia Ludhova	
SN 1987A - Exciting Physics	165
Bruno Leibundgut	
The SOX experiment: understanding the detector behavior using calibration sources	175
Alessio Caminata <i>et al.</i>	
Neutron Shielding Simulations and Muon-induced Neutrons	181
Laura Vanhoefer <i>et al.</i>	
On the history of the Hamburg Observatory	193
Stefan K. G. Dahmke	

Connecting Neutrino Physics and Astronomy

Plenary Talks



Physics Opportunities with Supernova Neutrinos

*Ninetta Saviano*¹

¹PRISMA Cluster of Excellence and Mainz Institute for Theoretical Physics, Johannes Gutenberg-Universität Mainz, 55099 Mainz, Germany

DOI: <http://dx.doi.org/10.3204/DESY-PROC-2016-05/16>

Core-collapse supernovae (SN) represent a unique laboratory to probe neutrino properties in the extreme conditions offered by a stellar gravitational collapse. The role of astrophysical messengers played by neutrinos during a stellar collapse is largely associated with the signatures imprinted on the observable SN neutrino burst by flavor conversions occurring deep inside the star. At this regard, the dense SN core represents a crucial environment to investigate neutrino flavor mixing in high-density conditions. Indeed, within a radius of a few hundred kilometers, the neutrino gas is so dense to become a “background to itself”, making the neutrino flavor evolution highly non-linear and leading in some situations to surprising and counterintuitive collective phenomena.

1 Introduction

Core-collapse supernovae (SNe) is one of the most energetic and spectacular phenomena in the Universe. They are powerful explosions which mark the violent death of massive stars ($M \gtrsim 8 M_{\odot}$) as they become unstable during the late phases of their evolution. The explosion is driven by a shock wave that eventually ejects the outer mantle of the collapsing star, liberating a gravitational binding energy $E_B \simeq 3 \times 10^{53}$ erg. Remarkably, 99% of this binding energy is carried away by neutrinos and antineutrinos of all the flavors, making a core-collapse SN one of the most powerful neutrino source. Therefore, neutrinos emitted during such a process are a promising tool to probe neutrino mass and mixing properties and to provide valuable information about SN mechanism itself. The neutrino fluxes and spectra are sensitive to many details of SN physics, notably the progenitor mass, the nuclear equation of state, and the occurrence of convection inside and outside the SN core. Originating deep inside the core and passing through the mantle of the star, the neutrino flavor conversions are affected by dense matter on their road through the stellar envelope. Moreover, in the deepest SN regions the neutrino density is so high that can dominate the flavor evolution, eventually producing a surprising collective behavior in the SN neutrino ensemble. As a consequence of these effects, the SN neutrino fluxes reaching the detectors would be deeply modified with respect to the initial ones, carrying fascinating signatures of oscillation effects occurring in the deepest SN regions. Thus detection of a high-statistics neutrino signal from the next nearby SN represents a new frontier in low-energy neutrino physics and astrophysics. For a more detailed treatment see the recent review [1].

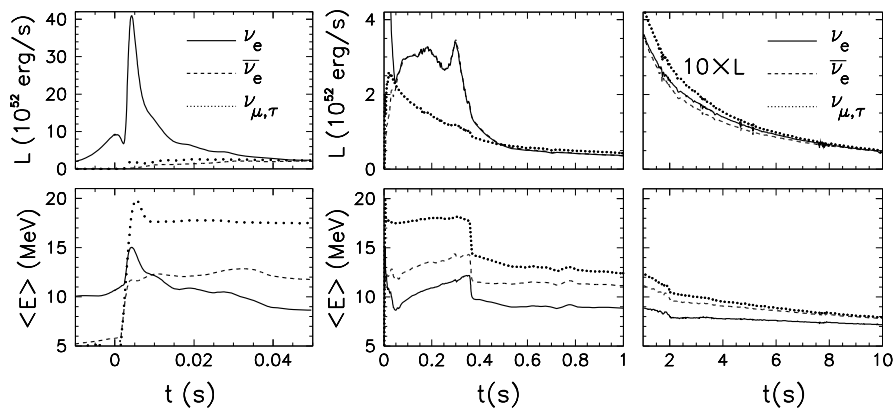


Figure 1: Neutrino signal of a core-collapse SN for a $10.8 M_{\odot}$ progenitor [2]. *Left*: Prompt neutrino burst. *Middle*: Accretion phase. *Right*: Cooling phase.

2 Neutrino emission

During and after the explosion, the star emits neutrinos in three main phases (Fig. 1).

1. *Prompt ν_e burst*: as the shock wave passes through the neutrino sphere, a ν_e burst, lasting $t \simeq 10$ ms, is released due to rapid electron capture on dissociated nuclei (deleptonization of the outer core layers) $e^- + p \rightarrow n + \nu_e$, leading to a sudden rise in the luminosity up to $L = 10^{53}$ erg s^{-1} . The fluxes of the other neutrino flavors are negligible compared to ν_e .
2. *Accretion phase*: the shock wave quickly loses its energy in dissociating nuclei and stagnates at a radius of 150-200 km. Material continues to fall onto the core (*accretion shock*) for the following few 100 ms and powers the emission of neutrinos and antineutrinos of all species, with a luminosity of $L = 10^{52}$ erg s^{-1} and characterized by a strong excess of the ν_e species over the others. Pronounced hierarchy of average energies $\langle E_{\nu_x} \rangle > \langle E_{\bar{\nu}_e} \rangle > \langle E_{\nu_e} \rangle$, where x stands for any of $\nu_{\mu,\tau}$ or $\bar{\nu}_{\mu,\tau}$.
3. *Kelvin-Helmholtz cooling phase*: after the successful explosion, the remaining proto-neutron star cools by neutrino emission over about 10 s. The luminosity is approximately equipartitioned between different species $L = 3 \times 10^{51}$ erg s^{-1} and the flavor hierarchy of average energies is probably mild.

A supernova can be roughly considered as a black-body that cools via neutrino emission. Indeed, supernova simulations typically provide neutrinos emitted with “quasi-thermal” spectra. The spectral characteristics evolve in time, are expected to vary for different supernova progenitors and depend on uncertain input physics such as the nuclear equation of state and the treatment of neutrino transport. Typically, one expects $\langle E_{\nu_e} \rangle \simeq 10$ –12 MeV, $\langle E_{\bar{\nu}_e} \rangle \simeq 12$ –15 MeV, and $\langle E_{\nu_x} \rangle \simeq 15$ –18 MeV.

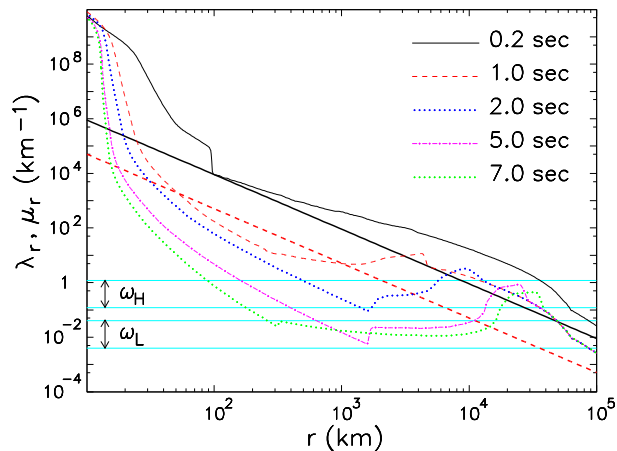


Figure 2: Snapshots of SN potentials for different post-bounce times. Continuous curves refer to the matter potential λ , dot-dashed to the neutrino potential μ (quoted in km^{-1}). Figure from [1].

3 Supernova potential profiles

Effects of flavor conversions on supernova neutrinos depend on the different densities encountered by neutrinos in their propagation in the stellar envelope. In Fig. 2 is represented a snapshot of the different interaction potentials associated with different supernova densities obtained from the Basel-Darmstadt simulations of a $10.8 M_{\odot}$ SN progenitor for different post-bounce times [2]. Self-induced neutrino oscillations, associated with the neutrino-neutrino interactions are related to the neutrino number densities through the neutrino-neutrino potential (Fig. 2)

$$\mu = \sqrt{2}G_F[n_{\nu_e} - n_{\bar{\nu}_e}] = \frac{1}{4\pi r^2} \left(\frac{L_{\nu_e}}{\langle E_{\nu_e} \rangle} - \frac{L_{\bar{\nu}_e}}{\langle E_{\bar{\nu}_e} \rangle} \right), \quad (1)$$

which decreases in time as the SN cools.

Matter effects on SN neutrinos depend on the potential

$$\lambda = \sqrt{2}G_F n_e, \quad (2)$$

where n_e is the net electron density n_e encountered by neutrinos in their propagation. The SN electron density profile is non-monotonic and time-dependent and presents an abrupt discontinuity, corresponding to the position of the shock-front. The two horizontal strips represent the regions associated with MSW resonant flavor conversions with the atmospheric oscillation frequency ω_H (violet band) and with the solar one ω_L (light blue) for an energy range $E \in [1 - 50]$ MeV.

From the comparison of the different densities we realize that in the deepest SN regions ($r < 10^3$ km) $n_{\nu} \gg n_e$, except during the accretion phase ($t < 0.5$ s). When the neutrino density dominates over the matter one (as during the cooling phase) self-induced flavor conversions would develop without any hindrance.

Conversely, at larger radii, the flavor conversions will be dominated by the ordinary matter effects.

4 SN neutrino flavor conversions

4.1 Three-neutrino oscillation framework

The evidence for flavor evolution comes from a series of experiments performed in about four decades of research with very different neutrino beams and detection techniques. Except for few controversial results from short-baseline neutrino experiments, that point towards the existence of extra sterile neutrino states (with $m \sim O(1)$ eV), all the data from the experiments are consistent with the simplest extension of the standard electroweak model needed to accommodate non-zero neutrino masses and mixings. Namely, three flavor eigenstates $\nu_{e,\mu,\tau}$ are mixed with the three mass eigenstates $\nu_{1,2,3}$ through a unitary matrix U , which in terms of one-particle neutrino states $|\nu\rangle$, is defined as $|\nu_\alpha\rangle = \sum_{i=1}^3 U_{\alpha i}^* |\nu_i\rangle$.

A common parametrization for the matrix U is [3]:

$$U = \begin{pmatrix} 1 & 0 & 0 \\ 0 & c_{23} & s_{23} \\ 0 & -s_{23} & c_{23} \end{pmatrix} \begin{pmatrix} c_{13} & 0 & s_{13}e^{-i\delta} \\ 0 & 1 & 0 \\ -s_{13}e^{i\delta} & 0 & c_{13} \end{pmatrix} \begin{pmatrix} c_{12} & s_{12} & 0 \\ -s_{12} & c_{12} & 0 \\ 0 & 0 & 1 \end{pmatrix} \quad (3)$$

with $c_{ij} = \cos\theta_{ij}$ and $s_{ij} = \sin\theta_{ij}$, θ_{ij} being the mixing angles and $\delta \in [0, 2\pi]$ being the CP-violating phase¹.

The three-neutrino mass spectrum $\{m_i\}_{i=1,2,3}$ is characterized by a “doublet” of relatively close states and by a third “lone” neutrino state, which may be either heavier than the doublet (“normal hierarchy,” NH) or lighter (“inverted hierarchy,” IH). Typically, the lightest (heaviest) neutrino in the doublet is called ν_1 (ν_2) and the corresponding mass squared difference is defined as

$$\delta m^2 = m_2^2 - m_1^2 > 0 \quad (4)$$

by convention. The δm^2 is traditionally named the *solar* mass squared difference. The lone state is then labeled as ν_3 , and the physical sign of $m_3^2 - m_{1,2}^2$ distinguishes NH from IH. The second independent squared mass difference Δm^2 , called also *atmospheric* mass squared difference, is

$$\Delta m^2 = \left| m_3^2 - \frac{m_1^2 + m_2^2}{2} \right|, \quad (5)$$

so that the two hierarchies (NH and IH) are simply related by the transformation $+\Delta m^2 \rightarrow -\Delta m^2$. Numerically, it results that $\delta m^2 \ll \Delta m^2$.

The latest solar, reactor and long-baseline neutrino oscillation analyses indicate the following $\pm 2\sigma$ ranges for each parameter (95% C.L.) taken from [4]

$$\begin{aligned} \Delta m^2 &= (2.43_{-0.13}^{+0.12}) \times 10^{-3} \text{ eV}^2, & \delta m^2 &= (7.54_{-0.39}^{+0.46}) \times 10^{-5} \text{ eV}^2, \\ \sin^2 \theta_{12} &= (3.08_{-0.34}^{+0.17}) \times 10^{-1}, & \sin^2 \theta_{23} &= (4.37_{-0.44}^{+1.15}) \times 10^{-1}, & \sin^2 \theta_{13} &= (2.34_{-0.39}^{+0.40}) \times 10^{-2}. \end{aligned} \quad (6)$$

Within the three-neutrino scenario, the most important unsolved problems require probing the CP-violating phase δ , the mass hierarchy, and the absolute neutrino masses. In this context, a high-statistics detection of Galactic SN neutrinos could give a unique help to solve some of these open issues.

¹We neglect here extra-phases possible if neutrinos are Majorana particles, since they are not relevant in oscillations.

4.2 Self-induced flavor evolution of SN neutrinos

Neutrinos free streaming beyond the neutrinosphere also interact among themselves (*neutrino self-interactions*). As pointed out in seminal papers [5, 6], in the deepest regions of a SN the neutrino gas is so dense that neutrinos themselves form a background medium triggering large *self-induced* flavor conversions in the deepest SN regions [7]. Under these circumstances, neutrinos emitted with different energies would be locked to oscillate in a collective fashion.

The neutrino-neutrino interactions make an additional contribution to the refractive energy shift in the neutrino propagation. This term is proportional to the neutrino density making the equations of motion non linear and so numerically challenging. The main complication in the ν - ν refractive term for SN neutrinos is the angular term coming from the current-current nature of the weak interactions. Consequently, for the non-isotropic neutrino emission from the SN core this velocity-dependent term would produce a net current that leads to a different refractive index for neutrinos that propagate on different trajectories. This is at the origin of the so-called “multi-angle effects” [7].

The multi-angle flavor evolution described by non-linear partial differential equations, has not been solved in its full complexity until now.

A few years ago multi-angle simulations were developed within the so-called “*bulb model*” where it is assumed that neutrinos are emitted uniformly and half-isotropically (i.e., with all the outward-going modes occupied, and all the backward going modes empty) from the surface of a spherical neutrinosphere, like in a blackbody. Moreover, it is assumed that there is azimuthal symmetry of the neutrino emission at the neutrinosphere and that all the physical conditions in the star only depend on the distance from the center of the star. Despite the numerous studies on the subject, at the moment a complete picture of the self-induced flavor conversions in SNe is still missing. Indeed, it has been recently questioned if removing some of the symmetries assumed in this model, this would trigger new instabilities in the flavor evolution. By means of a stability analysis of the linearized neutrino EoMs [8], it has been pointed out that removing the assumption of axial symmetry in the ν propagation, a new multi-azimuthal-angle (MAA) instability could emerge in the flavor evolution of the dense SN neutrino gas. The presence of MAA effects unavoidably implies the breaking of the spherical symmetry in the flavor evolution after the onset of the flavor conversions. This would lead to a challenging multi-dimensional problem involving partial differential equations. The MAA instability has shown as self-interacting neutrinos can *spontaneously break* the symmetries of the initial conditions. Such insight stimulated further investigations about the validity of the solution of the SN neutrino EoMs worked out within the bulb model. It has been recently realized that instabilities may grow once initial symmetries are relaxed, since self-interacting neutrinos can spontaneously break the translation symmetries in time [9, 10, 11] and space.

4.3 Suppression of collective oscillations

Predictions are more robust in the phases where collective effects are suppressed, i.e.:

- *Neutronization burst* ($t < 20$ ms), where the ν_e flux is strongly enhanced with respect to ν_x , while the $\bar{\nu}_e$ flux is strongly suppressed.
- *Accretion phase*, where $n_{e^-} - n_{e^+} \gg n_{\bar{\nu}_e} - n_{\bar{\nu}_x}$. The multi-angle matter effects could produce a large spread in the oscillation frequencies for neutrinos travelling on different trajectories, blocking the self-induced flavor conversions. Dedicated studies have been

performed in [12, 13, 14, 15, 16, 17] using inputs from recent hydrodynamic SN simulations. It has been found that the large matter term inhibits the development of collective oscillations at early times for iron-core SNe. The matter suppression of self-induced effects for iron-core SNe makes relatively easy the prediction of the oscillation effects during the accretion phase, since the neutrino fluxes will be processed by the only MSW matter effects. As a consequence, the detection of the SN neutrino signal at early times is particularly relevant for the mass hierarchy discrimination.

5 Observable signatures of SN neutrino flavor conversions

We present some of the possible observable signatures of flavor conversions in SNe and their sensitivity to the neutrino mass hierarchy. For definitiveness, we will refer to a Galactic SN at a distance $d = 10$ kpc from the Earth.

(a) Self-induced spectral splits. Observationally, the most important consequence of the self-induced flavor conversions is a swap of the ν_e and $\bar{\nu}_e$ spectrum with the non-electron species ν_x and $\bar{\nu}_x$ in certain energy intervals, and the resultant spectral splits at the edges of these swap intervals. Some of the spectral splits could occur sufficiently close to the peak energies to produce significant distortions in the SN neutrino signal, observable in the large underground detectors.

(b) Neutrinos from the SN neutronization burst. The ν_e neutronization burst is a particularly interesting probe of flavor conversions, since it can be considered almost as a “standard candle” being independent of the mass progenitor and nuclear EoS. Since self-induced effects are not operative on the SN ν_e neutronization burst, the ν_e flux would be only affected by MSW effects. At the very early post-bounce times relevant for the prompt burst, MSW flavor conversions would occur along the static progenitor matter density profile. We expect that the observable ν_e flux at Earth would be

$$F_{\nu_e} = F_{\nu_x}^0 \quad (\text{NH}) , \quad (7)$$

$$F_{\nu_e} = \sin^2 \theta_{12} F_{\nu_e}^0 + \cos^2 \theta_{12} F_{\nu_x}^0 \quad (\text{IH}) . \quad (8)$$

The observation of the neutronization peak would indicate the inverted mass hierarchy, while we do not expect its detection in NH. Concerning the possibility to detect the ν_e neutronization burst, while Mton class WC detectors measure predominantly the $\bar{\nu}_e$ flux using inverse beta decay, they are also sensitive to the subdominant ν_e channel via elastic scatterings on e^- (see Fig.). On the other hand, a large LAr TPC will make the cleanest identification of the prompt ν_e burst through its unique feature of measuring ν_e charged-current interactions, enabling to probe oscillation physics during the early stage of the SN explosion.

(c) Earth matter effect to discriminate the mass hierarchy. For the SN neutrinos reaching the detector from “below”, the Earth crossing would induce an energy-dependent modulation in the neutrino survival probability. The appearance of the Earth effect depends on the neutrino fluxes and on the mixing scenario. In particular, the Earth matter effect should be present for antineutrinos in NH and for neutrinos in IH, providing a potential tool to distinguish between these two cases. The accretion phase is particularly promising to detect Earth crossing signatures because the absolute SN ν flux is large and the flavor-dependent flux differences are also large.

(d) Rise time of the neutrino signal. The rise time of a Galactic iron-core SN $\bar{\nu}_e$ light curve, observable in large underground detectors, can provide a diagnostic tool for the

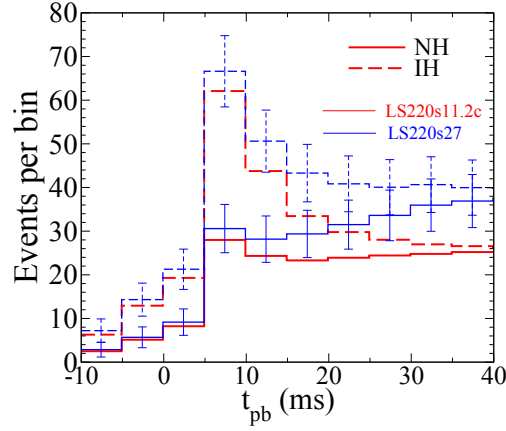


Figure 3: Neutronization events rate per time bin in a 560-kton WC detector for $27 M_{\odot}$ and $11 M_{\odot}$ SN progenitors at $d = 10$ kpc for both NH (continuous curve) and IH (dashed curve).

neutrino mass hierarchy. Due to the combination of matter suppression of collective effects at early post-bounce times and the presence of the ordinary MSW effect in the outer layers of the SN, one expects that the observable $\bar{\nu}_e$ flux at Earth would be given by

$$F_{\bar{\nu}_e} = \cos^2 \theta_{12} F_{\bar{\nu}_e}^0 + \sin^2 \theta_{12} F_{\bar{\nu}_x}^0 \quad (\text{NH}) , \quad (9)$$

$$F_{\bar{\nu}_e} = F_{\bar{\nu}_x}^0 \quad (\text{IH}) . \quad (10)$$

It is clear that the $F_{\bar{\nu}_e}$ flux at the Earth would basically reflect the original $F_{\bar{\nu}_x}^0$ flux if IH occurs, or closely match the $F_{\bar{\nu}_e}^0$ flux in NH. Figure 4 shows the expected *overall* signal rate $R(t)$ in the IceCube detector for a Galactic SN.

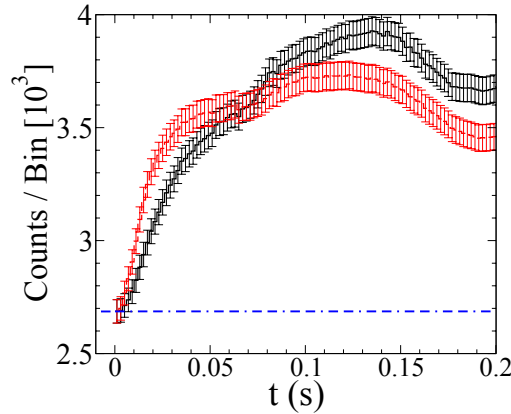


Figure 4: Supernova signal in IceCube assuming a distance of 10 kpc, based on a simulation for a $15 M_{\odot}$ SN progenitor from the Garching group. Figure from [1].

6 Acknowledgments

N.S. have received funding from the European Research Council (ERC) under the European Union's Horizon 2020 research and innovation programme (grant agreement No. 637506, “ ν Directions”).

References

- [1] A. Mirizzi, I. Tamborra, H. T. Janka, N. Saviano, K. Scholberg, R. Bollig, L. Hudepohl and S. Chakraborty, Riv. Nuovo Cim. **39** (2016) no.1-2, 1.
- [2] T. Fischer, S. C. Whitehouse, A. Mezzacappa, F.-K. Thielemann and M. Liebendorfer, Astron. Astrophys. **517** (2010) A80.
- [3] G. L. Fogli, E. Lisi, A. Marrone and A. Palazzo, Prog. Part. Nucl. Phys. **57**, 742 (2006).
- [4] F. Capozzi, G. L. Fogli, E. Lisi, A. Marrone, D. Montanino and A. Palazzo, Phys. Rev. D **89**, 093018 (2014).
- [5] J. T. Pantaleone, Phys. Rev. D **46** (1992) 510.
- [6] J. T. Pantaleone, Phys. Lett. B **342** (1995) 250.
- [7] H. Duan, G. M. Fuller, J. Carlson and Y. Z. Qian, Phys. Rev. Lett. **97**, 241101 (2006).
- [8] G. G. Raffelt, S. Sarikas and D. de Sousa Seixas, Phys. Rev. Lett. **111**, no. 9, 091101 (2013) [Erratum-ibid. **113**, no. 23, 239903 (2014)].
- [9] G. Mangano, A. Mirizzi and N. Saviano, Phys. Rev. D **89**, no. 7, 073017 (2014).
- [10] S. Abbar and H. Duan, Phys. Lett. B **751**, 43 (2015).
- [11] B. Dasgupta and A. Mirizzi, Phys. Rev. D **92**, no. 12, 125030 (2015).
- [12] S. Chakraborty, T. Fischer, A. Mirizzi, N. Saviano and R. Tomàs, Phys. Rev. Lett. **107**, 151101 (2011) [arXiv:1104.4031 [hep-ph]].
- [13] S. Chakraborty, T. Fischer, A. Mirizzi, N. Saviano and R. Tomàs, Phys. Rev. D **84**, 025002 (2011).
- [14] B. Dasgupta, E. P. O'Connor and C. D. Ott, Phys. Rev. D **85**, 065008 (2012).
- [15] S. Sarikas, G. G. Raffelt, L. Hudepohl and H. T. Janka, Phys. Rev. Lett. **108**, 061101 (2012)
- [16] N. Saviano, S. Chakraborty, T. Fischer and A. Mirizzi, Phys. Rev. D **85**, 113002 (2012).
- [17] S. Chakraborty, A. Mirizzi, N. Saviano and D. d. S. Seixas, Phys. Rev. D **89**, no. 9, 093001 (2014).

Neutrino-Nucleon Interactions in Core Collapse Supernovae

Andreas Lohs¹, Gabriel Martinez-Pinedo^{2,3}, Tobias Fischer⁴

¹Universität Basel, Departement Physik, Klingelbergstraße 82, 4056 Basel, Switzerland

²Technische Universität Darmstadt, Schlossgartenstraße 2, 64289 Darmstadt, Germany

³GSI Helmholtzzentrum für Schwerionenforschung, Planckstraße 1, 64291 Darmstadt, Germany

⁴Institute for Theoretical Physics, University of Wrocław, plac Maksa Borna 9, 50-204 Wrocław, Poland

DOI: <http://dx.doi.org/10.3204/DESY-PROC-2016-05/28>

Neutrino interactions in proto-neutron star matter are a major determinant for many key properties of core-collapse supernovae (CCSNe), such as the explosion mechanism or the nucleosynthesis of heavy elements. Recent works identify a need for increasingly precise interaction rates. This work presents an alternative way to compute the relativistic Hartree response for neutrino-nucleon interactions, improving upon previously derived expressions in several aspects. The result will then be compared to the so called elastic approximation which is widely used in supernova simulations, to assess the validity and limitations of the latter.

1 Introduction

The gravitational collapse of the inner core of a massive star at the end of its lifetime releases a huge amount of gravitational binding energy of the order of several 10^{53} erg. Eventually the collapsing core reaches supranuclear densities, where it is stopped by the strong repulsion of the nuclear interaction. At this point the binding energy is mostly converted into heat, leading to temperatures of several tens of MeV in the nascent protoneutron star (PNS). Neutrinos are emitted in large numbers both due to thermal production as well as the desire of the matter to reach weak chemical equilibrium via electron captures on protons. However for densities above 10^{11} g cm⁻³ the neutrino mean free path (MFP) becomes so short that neutrinos are trapped in the matter, forcing them into local thermal and chemical equilibrium. Nevertheless, due to the weak coupling of neutrinos to the matter compared to all other interactions in the supernova core, the diffusion and emission of neutrinos is by far the most efficient way to transport energy into the envelope of the massive star and beyond. Consequently, it was expected early on that the vast majority of the gravitational binding energy will be released in the form of neutrinos, a prediction that was confirmed by the observation of the neutrino signal from SN 1987A.

During the first ten seconds after core bounce, the most important region for the formation of the neutrino spectra is the so called neutrinosphere, where neutrinos decouple from the matter. The first neutrino signal is an initial deleptonization burst that is emitted after the supernova shock crosses this neutrinosphere. As the shock heats the matter, the heavy nuclei of the progenitor star are dissolved into free nucleons. Chemical equilibrium at these high

temperatures and densities favours then a significantly more neutron rich composition, causing rapid electron captures on free protons and subsequent emission of electron neutrinos on a timescale of only several milliseconds. After that, the neutrino spectra can be approximately understood as thermal emission from the neutrinosphere.

Once the neutrinos are outside of the neutrinosphere the probability of scattering or absorption in the envelope is rather small. However, since the neutrino luminosity is so large, on the order of a few $10^{52} \text{erg s}^{-1}$, the small fraction of neutrinos that do interact can have an enormous impact on the envelope above the PNS. The most important effect is probably the revival of the shock that leads to the eventual supernova explosion via the so called delayed neutrino heating mechanism (for a review on CCSNe simulations and possible explosion mechanisms see e.g. [1]). After the shock loses most of its energy by photodissociating heavy nuclei in the accretion flow, it quickly stalls. In the standard core-collapse scenario it is then expected that the region below the shock (outside the neutrinosphere) is heated faster by absorbing neutrinos from the PNS than it can cool by emitting neutrinos itself. This process transfers energy and momentum from the PNS to the shock, resulting in the eventual explosion. In this context multi-dimensional hydrodynamics have been identified as a most crucial ingredient, allowing for multi-D turbulences and convection which help to increase the heating efficiency. This proved necessary to achieve successful explosion in CCSN simulations. Yet, these advances in hydrodynamics have always been accompanied by essential improvements in the neutrino transport scheme and general relativity, as well as the microphysics of nuclear matter, nuclear interaction, and weak interaction between neutrinos and matter. Since the predicted explosions still differ significantly from observed explosion energies, this process of refinement is still ongoing.

Neutrinos also play a very important role in the nucleosynthesis of heavy or rare elements in CCSNe. One such scenario is the neutrino driven wind (NDW), matter that is ejected from the PNS surface after shock revival. The idea is again that absorptions of neutrinos transfer enough energy and momentum to this matter to drive a matter outflow. Once this wind expands and cools, nuclei are formed, with the possibility of reaching very large atomic numbers. Without going into the details of nucleosynthesis, the outcome of this scenario depends strongly on the initial conditions in the NDW, in particular the expansion timescale, the entropy per baryon and the chemical composition. All of these properties are strongly affected if not fully determined both by the absolute size of the neutrino flux as well as the specific spectral characteristics and even spectral differences of the distinct neutrino flavours.

Recent studies strongly hint towards the need to improve the precision of neutrino microphysics. With respect to the neutrino heating mechanism, it was found that reaching a successful explosion of a marginal supernova in 3D might depend on 10-20% changes to the rate for neutrino-nucleon scattering[2].

For the neutrino driven wind, it seems that core collapse supernova will not result in conditions that allow for a so called full r-process [3, 4], building the heaviest elements in the universe. However, a so called weak r-process is still very much possible [5] and might have contributed already to the early chemical evolution in the universe. Whether the neutrino driven wind will eventually allow for a weak r-process and to which extent depends on the detailed composition of the NDW, which depends in turn on a precise description of neutrino interactions at the level of 10%.

Eventually, it is predicted that the neutrino signal from a CCSN might undergo significant modifications due to neutrino oscillations [6]. Although this work will not look in detail on the topic of oscillations, referring instead to the various complementing contributions in this proceedings, the resulting neutrino spectra are obviously dependent on the initial spectral

differences between the neutrino flavours.

All these findings lead to the conclusion, that current research on core-collapse supernova and related nuclear astrophysics requires a sufficiently accurate description of neutrino interactions in hot at dense matter. The purpose of this contribution is to discuss several problems and uncertainties at this level of precision and to propose solutions for some of them. Section 2 presents an alternative formalism for the relativistic Hartree response of neutrino-nucleon interactions, an expression that yields very precise values for the neutrino MFP at various conditions in CCSNe. In Section 3 the relativistic Hartree response is used to assess the limitations of the so called elastic approximation[7], an analytic expression for the MFP that is widely used in supernova simulations. Finally, the work is concluded in Section 4.

2 Hartree Response for Neutrino-Nucleon Interaction

The general derivation of the Hartree response for neutrino-nucleon interactions is the same for charged and neutral-current reactions. This work studies reactions of the type

$$\nu_1 + N_2 \rightarrow l_3 + N_4.$$

The particle ν_1 can represent either a neutrino or an antineutrino, while the final state lepton l_3 will be a neutrino of the same type (neutral current) or the corresponding charged lepton (charged current). For charged leptons the finite mass is taken into account, so that the description is applicable to charged-current interactions of muon neutrinos. In free space and at the energies encountered in CCSNe, these weak interactions can be described by a current-current Lagrangian

$$\mathcal{L} = \frac{G}{\sqrt{2}} l_\mu j^\mu,$$

where $G = G_F V_{ud}$ for charged current and $G = G_F$ for neutral current, with G_F the Fermi coupling constant and V_{ud} the up-down element of the CKM-matrix. For reactions with a neutrino in the initial state the lepton current reads

$$l_\mu = \bar{\psi}_3 \gamma_\mu (1 - \gamma_5) \psi_1,$$

where the ψ_i are Dirac spinors. Note that for an antineutrino in the initial state, indices 1 and 3 have to be exchanged. The nucleon current is likewise given by

$$\psi_4 \left[c_V \gamma^\mu + \frac{iF_2}{2M_N} \sigma^{\mu\nu} q_\nu - c_A \gamma^\mu \gamma_5 \right] \psi_2$$

The value of the coupling constants c_V , c_A , and F_2 depends on the specific reaction (see e.g. [15]) For a noninteracting Fermi gas, the Lagrangian \mathcal{L} is equivalent to the matrix element. Hence, using Fermi's Golden Rule the mean free path λ , considering final state Pauli blocking, can be computed by

$$\frac{1}{\lambda(E_1)} = 2 \int \frac{d^3 \mathbf{p}_2}{(2\pi)^3} \int \frac{d^3 \mathbf{p}_3}{(2\pi)^3} \int \frac{d^3 \mathbf{p}_4}{(2\pi)^3} \frac{\langle |\mathcal{M}|^2 \rangle}{16E_1 E_2 E_3 E_4} \delta^4(P_1 + P_2 - P_3 - P_4) f_2 (1 - f_3) (1 - f_4),$$

with the particle four momenta P_i . The f_i are standard Fermi distributions.

When studying nucleonic matter at densities above $10^{12} \text{ g cm}^{-3}$ the assumption of noninteracting nucleons is not justified. Both the strong and the electromagnetic interaction affect the spectra of nucleons and/or the correlations between them. These effects have to be taken into account for neutrino interactions. One approach is to compute the nucleon response via the medium polarization tensor in the so called Hartree approximation [8, 9], which takes into account how the nucleon spectrum is altered by the mean effect of the interaction. Instead, this work computes the Hartree response by replacing the free space nucleon current with an effective nucleon current in medium, treating the nucleons as quasi free Fermions. However, the formalism of the medium polarization allows to go beyond the mean field by computing the nucleon response via the random phase approximation (RPA) [8, 10, 11, 12, 13]. The RPA includes correlations among the nucleons, stemming from the residual interaction. This is particularly relevant for the neutral-current response, where the correlations may be more important than the mean field, especially for subsaturation densities.

An advantage of the new formalism is that the relativistic Hartree response is analytically more closed, allowing for a simpler and faster numerical computation. Also, for the first time a finite lepton mass is taken into account to describe charged current reactions of ν_μ .

In astrophysical simulations the nucleonic matter is often described by a relativistic mean field (RMF) equation of state (EOS) [14], in particular by a $\sigma\omega\rho$ -model. Here, the free nucleon spectrum is replaced by a quasi-particle dispersion relation, given by

$$E_{n,p} = \sqrt{m_{n,p}^{*2} + \mathbf{p}^2} + U_{n,p},$$

where $m_{n,p}^*$ and $U_{n,p}$ are the nucleon effective masses and relativistic mean field potentials, respectively, of neutrons and protons. They are directly related to the mean meson fields.

To compute the Hartree response, one replaces the free nucleon spinors ψ_i in the nucleon current by effective nucleon spinors ψ_i^* ,

$$\psi_i^* = \frac{1}{\sqrt{E_i^{*2} + m_i^{*2}}} \begin{pmatrix} \chi_s \\ \boldsymbol{\sigma} \cdot \mathbf{p} \\ E_i^* + m_i^* \chi_s \end{pmatrix}.$$

Here χ_s are normalized Pauli spinors so that $\chi_s^\dagger \chi_{s'} = \delta_{ss'}$, $\boldsymbol{\sigma}$ is the vector of Pauli matrices, and E_i^* is given by

$$E_i^* = E_i - U_i = \sqrt{m_i^{*2} + \mathbf{p}_i^2}.$$

Note that ψ_i^* becomes the free nucleon spinor for vanishing meson fields. Plugging ψ_* in the nucleon current one can derive the squared matrix element in medium $\langle |\mathcal{M}_{HRT}|^2 \rangle$. To compute then the MFP one only needs to adjust the normalization of the phase space integrals to conserve Lorentz invariance,

$$\frac{1}{\lambda(E_1)} = 2 \int \frac{d^3 \mathbf{p}_2}{(2\pi)^3} \int \frac{d^3 \mathbf{p}_3}{(2\pi)^3} \int \frac{d^3 \mathbf{p}_4}{(2\pi)^3} \frac{\langle |\mathcal{M}_{HRT}|^2 \rangle}{16 E_1 E_2^* E_3 E_4^*} \delta^4(P_1 + P_2 - P_3 - P_4) f_2 (1 - f_3) (1 - f_4),$$

where the Fermi distributions for the nucleons describe the quasiparticle distributions,

$$f_{2,4}(E_{2,4}) = \left[1 + \exp \left(\left[\sqrt{m_{2,4}^{*2} + \mathbf{p}^2} + U_{2,4} - \mu_{2,4} \right] / T \right) \right]^{-1}.$$

The MFP cannot be computed fully analytically. However, it can be closed analytically up to a 2-dimensional numerical integral,

$$\frac{1}{\lambda} = \frac{G^2}{4\pi^3} \frac{1}{E_1^2} \int_{E_{2-}}^{\infty} dE_2 \int_{m_3}^{E_{3+}} dE_3 f_2 [1 - f_3] [1 - f_4] I_{tot}.$$

The integration limits E_{2-} and E_{3+} are constraints that arise from four-momentum conservation. The term I_{tot} is the fully analytical solution of the relation

$$I_{tot} = \frac{p_1 p_2 p_3 p_4}{4\pi^2} \int d\Omega_2 d\Omega_3 d\Omega_4 dE_4 \frac{\langle |\mathcal{M}_{HRT}|^2 \rangle}{16G^2} \delta^4(P_1 + P_2 - P_3 - P_4)$$

with $p_i = |\mathbf{p}_i|$. The detailed formalism and derivation will be presented in a future publication.

Previous solutions for the relativistic Hartree response were closed only up to three numerical integrals [12]. Yet, for neutral-current interactions the above approach can be applied only when the final state neutrino is either distributed isotropically or when final state neutrino blocking can be neglected. Otherwise the factor $(1 - f_3)$ cannot be factored out of the angular integrals. In that case the relativistic Hartree response as given in the literature cannot be further closed. The following section will therefore focus on charged-current interactions.

3 Comparison to Elastic Approximation

A simplification of the mean free path for neutrino-nucleon interactions that is often used in CCSN simulations is the so called *elastic approximation* [7]. Its advantage is that it delivers an analytic expression for λ . Starting from the noninteracting Fermi gas approach, the elastic approximation is inherently nonrelativistic. Expanding $\langle |\mathcal{M}|^2 \rangle$ in powers of (E_1/m_2) and dropping all terms of order 1 or higher, the squared matrix element simplifies to

$$\frac{\langle |\mathcal{M}|^2 \rangle}{16E_1 E_2 E_3 E_4} = c_A^2 (3 - x) + c_V^2 (1 + x),$$

where x is the angle cosine between initial and final lepton momenta \mathbf{p}_1 and \mathbf{p}_3 . Also, one assumes that the absolute momentum of the nucleons stays constant, $p_2 = p_4$. The final state lepton energy equals then the initial neutrino energy plus the mass difference between nucleons, and the mean free path can be derived analytically. It is straightforward to expand this approximation to consider the quasiparticle dispersion relation for nucleons in the mean field theory [3],

$$\frac{1}{\lambda_{elst}} = \frac{G^2}{\pi} (c_V^2 + 3c_A^2) E_3 p_3 (1 - f_3) \frac{n_2 - n_4}{1 - \exp[(\eta_4 - \eta_2)/T]} \Theta(E_3 - m_3),$$

with

$$E_3 = E_1 + m_2^* - m_4^* + U_2 - U_4 \quad \text{and} \quad \eta_i = m_i^* + U_i - \mu_i.$$

As an improvement over the elastic approximation, analytic correction factors for finite nucleon recoil and subleading order terms in the matrix element (often called *weak magnetism*

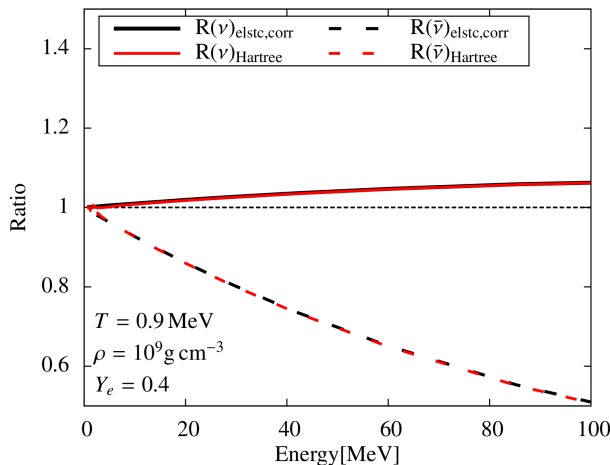


Figure 1: Ratio of mean free path from relativistic Hartree response to elastic approximation (bright/red) at low densities and temperatures, compared to nucleon recoil and weak magnetism correction factor (black). Solid and dashed lines correspond to neutrino and antineutrino absorption, respectively.

corrections) were suggested [15]. Essentially, these correction factors are the ratio of the exact free space cross section and its nonrelativistic approximation. Multiplying with this ratio shall correct the simplifications that were made in the matrix element and the final lepton phase space factor. This approach is nearly exact for nucleons at low densities and temperatures. However, it can not correct the approximations that were made in the Pauli blocking factors.

For charged-current reactions, the appropriate correction factor is

$$R(E_1) = \left\{ c_V^2 \left(1 + 4e + \frac{16}{3}e^2 \right) + 3c_A^2 \left(1 + \frac{4}{3}e \right)^2 \pm 4(c_V + F_2) c_A e \left(1 + \frac{4}{3}e \right) + \frac{8}{3}c_V F_2 e^2 + \frac{5}{3}e^2 \left(1 + \frac{2}{5}e \right) F_2^2 \right\} / \left[(c_V^2 + 3c_A^2) (1 + 2e)^3 \right].$$

Looking at the elastic approximation with nucleon recoil and weak magnetism corrections, one can compare it to the exact mean free path (bar correlations) from the Hartree response, in order to assess the precision of the former for various conditions in a CCSN. The situation at lower densities and temperatures, corresponding e.g. to the region in the neutrino driven wind, is investigated in Fig.1. Here the ratio between the Hartree response and the elastic approximation is shown along the analytic correction factor. Note that in both Fig.1 and Fig.2 the underlying composition and interaction of the nucleons is described by the Hempel-EOS [14] in the DD2-parametrization [16]. However, all findings presented here are practically independent of the chosen RMF-parametrization. For a temperature of $T = 0.9 \text{ MeV}$ and density $\rho = 10^9 \text{ g cm}^{-3}$ one can see a nearly perfect agreement between the two. This seems reasonable, as final state blocking is probably negligible under these conditions and the mean free path is almost proportional to the cross section. Also the thermal energy of the nucleons is not very large, justifying the assumption of an initial nucleon at rest. It seems safe to use the corrected elastic approximation e.g. to determine the equilibrium electron fraction in the

NDW when the neutrino spectrum from the proto-neutron star is known.

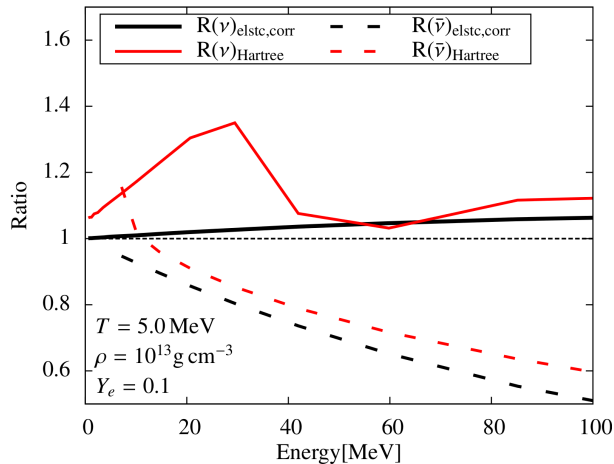


Figure 2: Ratio of mean free path from relativistic Hartree response to elastic approximation (bright/red) at low densities and temperatures, compared to nucleon recoil and weak magnetism correction factor (black). Solid and dashed lines correspond to neutrino and antineutrino absorption, respectively.

Higher densities and temperatures are studied in Fig.2. At a temperature of $T = 5$ MeV and a density of $\rho = 10^{13} \text{ g cm}^{-3}$ one finds that the corrected elastic approximation underestimates the mean free path for almost all energies, both for neutrinos and antineutrinos. The deviation is on the order of 10%, and it can reach more than 30% for neutrinos in the energy range around 20 MeV, which is particularly important for neutrino transport and emission in CCSN. Therefore it is likely that this might affect the neutrino spectrum in the early cooling and NDW phase, starting several hundred seconds post bounce. During the accretion and explosion phase, the electron type neutrinos decouple mostly from lower densities, where this deviation is smaller. However, one can find deviations on the order of 10% already above densities $\rho = 10^{12} \text{ g cm}^{-3}$. Also, for temperatures above 5 MeV an increase in the Hartree response compared to the corrected elastic approximation by several percent is observed, even for the lower densities, reaching $\sim 10\%$ for $T = 10$ MeV. Such temperatures can be realized at the neutrinospheres in the early postbounce phase, potentially affecting the accretion and explosion phase.

The general understanding behind the suppression of the elastic approximation compared to the Hartree response is that the restrictions on momentum and energy exchange force the final state particles into configurations with too large Pauli blocking. The correction factor cannot improve this situation since it does not address the statistical factors. Ultimately, further work has to be done to understand this observation in more detail. Yet one can conclude that the elastic approximation, despite adding nucleon recoil and weak magnetism corrections, does not reach a precision beyond the 10% level for charged current reactions of electron type neutrinos at high densities (relevant only later times) and/or high temperatures (relevant at early times postbounce). However, the approximation is well suited for conditions such as in the NDW, where it reproduces the Hartree response with great accuracy.

4 Conclusion

The relativistic Hartree response for weak neutrino-nucleon interactions was derived different from the standard formalism in the literature. For charged-current reactions, the resulting new expression is analytically more closed and allows to consider finite lepton masses like in charged-current ν_μ -absorption. The improvements can also be applied to neutral-current scatterings, if the neutrino distribution is isotropic or final state lepton blocking is negligible. The Hartree response was compared to the elastic approximation with nucleon recoil and weak magnetism corrections to assess the precision of the latter in CCSNe simulations. It was found that the accuracy will be less than 10% for temperature above 5 to 10 MeV and densities higher than $10^{12} \text{ g cm}^{-3}$. The likely reason is an artificially strong final state blocking enforced by the rigid kinematic constraints of the elastic approximation. Hence, it must be used with caution both during the early accretion and explosion phase as well as the initial cooling phase. Nevertheless it is well suited to describe neutrino-nucleon interactions in the neutrino driven wind, which takes place at lower densities and temperatures. Future studies should try to understand the limitations of the elastic approximation better. Also it would be interesting to compare both the Hartree response and the elastic approximation in the framework of a dynamical CCSN simulation to quantify the impact of different rates both on the explosion mechanics and the subsequent neutrino spectrum in the initial cooling phase.

Acknowledgements

The work of A. Lohs was partly supported by the ERC Advanced Grant ‘‘FISH’’.

T.F. acknowledges support from the Polish National Science Center (NCN) under grant number UMO-2013/11/D/ST2/02645.

G.M.P. was partly supported by the Deutsche Forschungsgemeinschaft through contract SFB 1245, and the Helmholtz Association through the Nuclear Astrophysics Virtual Institute (VH-VI-417).

References

- [1] H. T. Janka, *Ann. Rev. Nucl. Part. Sci.* **62** 407 (2012).
- [2] T. Melson, H. T. Janka, R. Bollig, F. Hanke, A. Marek and B. Müller, *Astrophys. J.* **808** no.2, L42 (2015).
- [3] G. Martinez-Pinedo, T. Fischer, A. Lohs and L. Huther, *Phys. Rev. Lett.* **109** 251104 (2012).
- [4] L. F. Roberts, S. Reddy and G. Shen, *Phys. Rev. C* **86** 065803 (2012).
- [5] G. Martinez-Pinedo, T. Fischer and L. Huther, *J. Phys. G* **41** 044008 (2014).
- [6] H. Duan, G. M. Fuller, Y. Z. Qian, *Ann. Rev. Nucl. Part. Sci.* **60** 569 (2010).
- [7] S. W. Bruenn, *Astrophys. J. Suppl.* **58** 771 (1985).
- [8] C. J. Horowitz and K. Wehrberger, *Phys. Lett. B* **266** 236 (1991).
- [9] S. Reddy, M. Prakash and J. M. Lattimer, *Phys. Rev. D* **58** 013009 (1998).
- [10] A. Burrows and R. F. Sawyer, *Phys. Rev. C* **58** 554 (1998).
- [11] A. Burrows and R. F. Sawyer, *Phys. Rev. C* **59** 510 (1999).
- [12] S. Reddy, M. Prakash, J. M. Lattimer and J. A. Pons, *Phys. Rev. C* **59** 2888 (1999).
- [13] C. J. Horowitz and M. A. Perez-Garcia, *Phys. Rev. C* **68** 025803 (2003).
- [14] M. Hempel and J. Schaffner-Bielich, *Nucl. Phys. A* **837** 210 (2010).
- [15] C. J. Horowitz, *Phys. Rev. D* **65** 043001 (2002).
- [16] S. Typel, G. Ropke, T. Klahn, D. Blaschke and H. H. Wolter, *Phys. Rev. C* **81** 015803 (2010).

Searches for point-like neutrino sources with the ANTARES neutrino telescope

J. Barrios-Martí¹ on behalf of the ANTARES collaboration

¹Instituto de Física Corpuscular (CSIC-Universitat de València) c/ Catedrático José Beltrán, 2 E-46980 Paterna, Valencia, Spain

DOI: <http://dx.doi.org/10.3204/DESY-PROC-2016-05/26>

ANTARES is the largest undersea neutrino telescope currently in operation. This telescope has been taking data continuously since 2007 with the aim to detect neutrinos from astrophysical sources. A review of the point-like neutrino sources with the ANTARES telescope is presented. The latest results of the all-flavour neutrino point-source analysis with data from 2007 to 2013 and the results of the first combined ANTARES and IceCube analysis are described.

1 The ANTARES neutrino telescope

ANTARES is the first undersea neutrino telescope [1]. It is in continuous operation since 2006, and completed since 2008. It is located in the depth of the Mediterranean Sea (2475 m deep) at coordinates (42° 48' N, 6° 10' E), 40 km South of Toulon (France). It consists of 12 lines of 350 m height with inter-line separations between 60 to 75 m, which house a total of 885 Optical Modules (OMs). An OM consists of a 10" photomultiplier tube (PMT) contained inside a 17" glass sphere. The OMs are facing downward at an angle of 45° in order to improve the detection of up-going muon-neutrinos. They are organized in triplets, so that there are 25 triplets (storeys) on each line, with a distance between consecutive storeys in the same line of 15m.

The detection principle is based on the indirect detection of high energy neutrinos which interact via charged current (CC) or neutral current (NC) interactions with a nucleus inside or nearby the detector volume. In case a muon neutrino interacts via CC, it produces a muon which can travel a long distance before decaying. Since this muon travels at relativistic speeds in water, Cherenkov radiation is emitted. This type of events are usually referred as *track-like*. A fraction of the photons emitted from this radiation are detected by the PMTs, which produces a signal or *hit*. With the collected charge and the time of arrival, a reconstruction of these events is performed. Tau neutrinos can also produce this type of events.

On the other hand, all neutrinos interacting via NC or electron neutrinos and sometimes tau neutrinos via CC can produce *cascade-like* events. In this case, a fraction of the original neutrino energy is deposited via a hadronic and/or an electromagnetic shower. The photons coming from these showers expand spherically from the interaction vertex. The reconstruction is performed with the detected photons coming from the shower.

2 ANTARES point-source search including cascades

For the first time, a search for point-like sources including cascades has been performed. The addition of cascades provides the ability to perform these searches with all flavours of neutrinos both via charged current and neutral current interactions.

2.1 cascade reconstruction

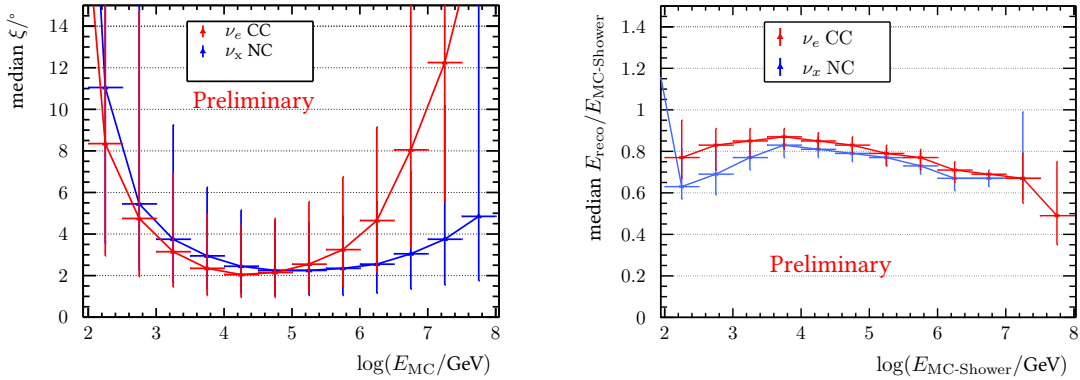


Figure 1: Left: Angular resolution for cascades coming from ν_e charged current interactions (red) and from NC interactions of neutrinos of all flavours (blue). Right: median energy resolution between the reconstructed energy and the deposited energy of the interaction. Both figures have been calculated for events with neutrino-interaction vertices of $|Z_{\text{vertex}}| < 200$ m, $\rho_{\text{vertex}} < 90$ m from the detector centre. The error-bars in the y axis denote the 1σ region.

A new reconstruction for cascade events [2] was developed to include these events in point-like source searches. This reconstruction is based on a two-step procedure.

The first step consists on the interaction vertex reconstruction, where an expanding spherically shell of photons from this point is assumed. This is done via a pre-fit with the information of all selected hits, in which we assume that they have been produced from the same interaction. That leads to a set of equations which are minimised via an M-estimator fit,

$$M_{Est} = \sum_i^N \left(q_i \sqrt{1 + t_{i-\text{res}}^2/2} \right) \quad (1)$$

where q_i and $t_{i-\text{res}}$ denote the charge and the time residual (difference between the expected and the actual arrival time) of the hit i .

The second step consists on the direction reconstruction. In this case, all hits coming from a triggered event in a time residual window of $-200 < t_{res} < 500$ ns are considered, where the t_{res} is the time residual with respect to the previously fitted vertex. The direction of the cascade is then obtained by performing a maximisation of a likelihood, defined as:

$$\begin{aligned}
 L = & \sum_{i=1}^{N_{\text{selected}}} \log [P_{q_i > 0}(q_i | E_\nu, d_i, \phi_i, \alpha_i) + P_{bg}(q_i)] \\
 & + \sum_i^{N_{\text{PMTs without hits}}} \log [P_{q=0}(E_\nu, d_i, \phi_i)]. \quad (2)
 \end{aligned}$$

In this equation, $P_{q_i > 0}$ denotes the probability for a PMT, i , to have measured a charge q_i , $P_{q=0}$ is the probability for an absence of a detection in a PMT, and P_{bg} is the probability for a hit to be originated via background. All of these probabilities depend on the charge of the hit, q_i . Also, $P_{q_i > 0}$ and $P_{q=0}$ depend on the neutrino energy, E_ν , the distance between the PMT i and the vertex of the interaction, d_i , the angle between the neutrino direction and the vector which connects the PMT i and the vertex of the interaction, ϕ_i , and the angle between the direction of the PMT with the same vector, α_i .

The performance of this reconstruction can be seen in figure 1. A median angular resolution between 2° and 4° degrees can be achieved for contained events (events within $|Z_{\text{vertex}}| < 200$ m, $\rho_{\text{vertex}} < 90$ m from the detector center according to our simulations) with neutrino energies of E_ν between 10^3 and 10^6 GeV for electron neutrino events interacting via CC. An estimate of the angular resolution of the cascade reconstruction can be obtained by using a data sample dominated by atmospheric muons. These events can be reconstructed both as track-like events and as cascades. Figure 2 shows the angular difference between the directions obtained from these two reconstructions for a loose cut dominated by atmospheric muons. The low difference between the reconstructed directions of both reconstructions shows the performance of the cascade reconstruction.

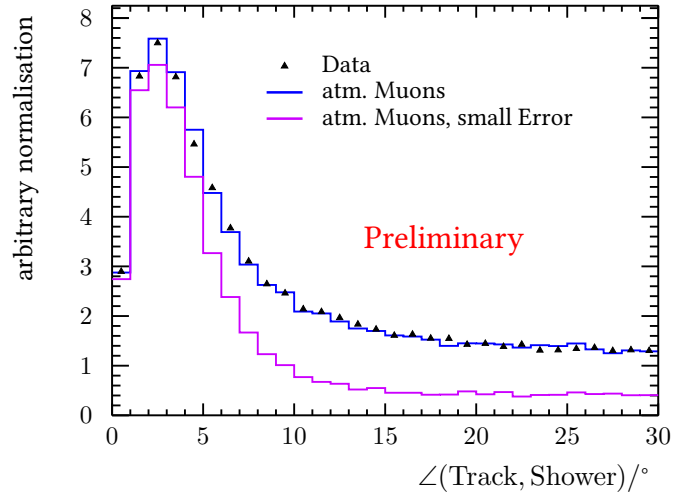


Figure 2: Angular difference between the reconstructed directions given by the track and cascade reconstructions. Black dots: Values obtained from data. Blue line: Values obtained from simulations. Magenta line: Values obtained for atmospheric muons from simulations with an angular resolution in the cascade channel lower than 5° .

2.2 Search method

The data sample contains data recorded from Jan 29, 2007 to Dec 31, 2013. The event selection for the track-like channel is identical to the last published point-source analysis [3], which consists on a cut on the reconstructed zenith angle, $\cos(\theta_{track}) < 0.1$, an angular error estimate of $0 < \beta_{track} < 1^\circ$, and a quality of the reconstructed track of $\Lambda_{track} > -5.2$. These parameters are obtained from the track reconstruction mechanism, which uses a maximum likelihood (ML) method [4, 5]. This reconstruction is based on a multi-step procedure to fit the direction of the muon by maximising the Λ_{track} parameter. The angular error estimate, σ , is calculated from the uncertainty on the zenith and azimuth angles extracted from the covariance matrix.

The event selection for the cascade channel is obtained via a set of multiple cuts. First of all, a veto of the events which have been selected in the track channel is performed. Secondly, only events reconstructed as up-going or with almost horizontal directions ($\cos(\theta_{sho}) < 0.1$), and with a reconstructed interaction vertex close or inside the detector volume ($\rho_{sho} < 300\text{m}$, $Z_{sho} < 250\text{m}$) are included. Additionally, a maximum angular error estimate of 10° degrees is allowed. A combined cut on the GridFit Ratio [6] parameter and the number of selected hits by the cascade reconstruction is performed. Finally, a cut on a muon/cascade likelihood discrimination parameter and a cut on the ratio between the collected charge before and after the expected expected time recorded by the OMs is applied.

Afer this criteria, a total number of 6490 track-like and 172 cascade-like neutrino candidates are obtained. Figure 3 shows the location of these events in equatorial coordinates.

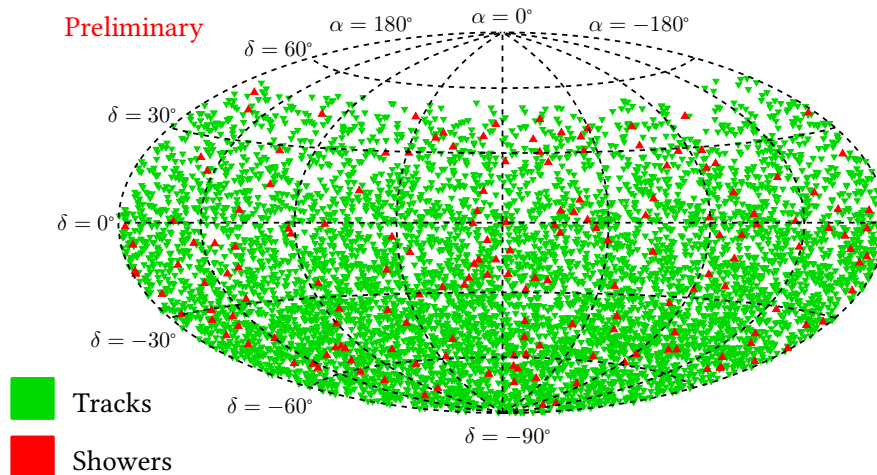


Figure 3: Skymap in equatorial coordinates of the reconstructed directions of the track-like (green) and cascade-like (red) events.

An unbinned likelihood maximisation with an extended likelihood definition is performed in order to search for excesses of events. This likelihood takes into account the directional information and the reconstructed number of hits, \mathcal{N} as information of each event. The likelihood, as a function of the total number of fitted signal events, μ_{sig} , can be expressed as:

$$\log L_{s+b} = \sum_S \sum_{i \in S} \log \left[\mu_{\text{sig}}^S \cdot \text{PSF}^S(\Delta\Psi_i) \cdot N_{\text{sig}}^S(\mathcal{N}_i) + B^S(\delta_i) \cdot N_{\text{bkg}}^S(\mathcal{N}_i) \right] - \mu_{\text{sig}}^S \quad (3)$$

$$+ P(\mu_{\text{sig}}^{\text{sh}} | \mu_{\text{sig}}^{\text{tr}} \cdot \mathcal{A}^{\text{sh}}(\delta_s) / \mathcal{A}^{\text{tr}}(\delta_s)).$$

where S denotes the track (tr) or cascade (sh) sample, $\text{PSF}(\Delta\Psi_i)$ is the point spread function value for a given event i at a distance $\Delta\Psi_i$ from the assumed source, $B(\delta)$ is the background rate of data events as a function of the declination δ , $N_{\text{sig}}^S(\mathcal{N})$ and $N_{\text{bkg}}^S(\mathcal{N})$ are the probability density functions which give the probability for an event to be signal or background given the number of hits \mathcal{N} , and $\mathcal{A}^S(\delta_s)$ is the acceptance (proportionality constant between a flux normalisation, Φ_0 and the number of expected events detected given an E^{-2} source spectrum at a declination δ_s). The poissonian term, $P(\mu_{\text{sig}}^{\text{sh}} | \mu_{\text{sig}}^{\text{tr}} \cdot \mathcal{A}^{\text{sh}}(\delta_s) / \mathcal{A}^{\text{tr}}(\delta_s))$ is included to take into account the expected ratio between the number of signal events between the track and cascade channels. Figure 4 shows the acceptance for the cascade and track channels.

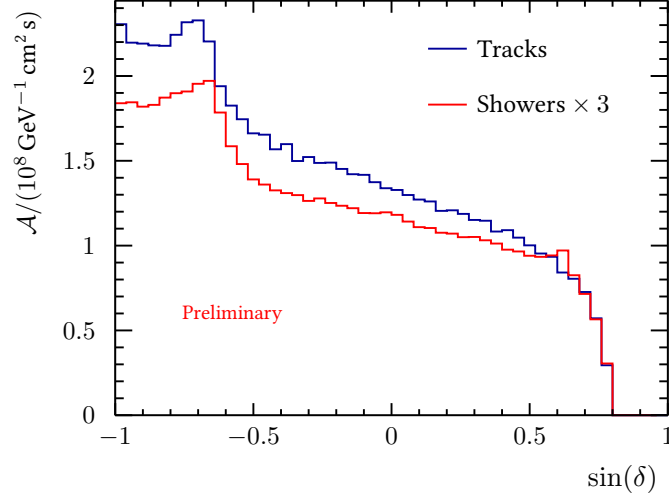


Figure 4: Acceptance for the track (blue) and cascade (red) channel assuming an E^{-2} spectrum. The cascade acceptance has been multiplied by 3 in this figure.

From this likelihood, a test statistic, TS , is defined so that $TS = \log L_{s+b} - \log L_b$, where L_{s+b} is the maximised likelihood, and L_b is the likelihood value for the background only case.

Different search strategies are followed in order to look for candidate clusters which could exceed the expected background. In the full sky search, the whole sky is scanned. Per each cluster, also the direction of the hypothetical source is fitted. In the candidate list search, the location of 52 known high-energy gamma-ray emitters are considered, where the coordinates of the source are fixed. A separate candidate list search for the location of the eight track-like events from the Southern Sky observed by the IceCube experiment in their 3 year High Energy neutrino sample [7] is considered, where the fitted location of the fitted source is set to twice the angular error estimate of the IceCube events. Finally, a scan over the region around the galactic center (half-axis radii of 30° in galactic longitude, and 15° degrees in latitude) is performed.

2.3 Results

No significant clusters of events are observed in this analysis. The most significant cluster in the full sky search is found at a location of $(\alpha, \delta) = (-46.8^\circ, -64.9^\circ)$ in equatorial coordinates with a post-trial significance of 4.2% (2.0σ in the two-sided convention). A total of 17(7) track-like events are observed within $3(1)^\circ$ degrees and 1 cascade event within 10° . The most significant cluster of the candidate list search corresponds to the one corresponding to the location of HESSJ0632+057, with a post-trial significance of 20% (1.27σ). A total of 6(1) track events are observed within $3(1)^\circ$, and a total of 3 cascades are observed within 15° . The most signal-like cluster corresponding with the location of an IC event corresponds to $(\alpha, \delta) = (130.7^\circ, 29.5^\circ)$, associated with IC track ID3. Finally, the most significant cluster of the search around the Galactic Centre is observed at $(\alpha, \delta) = (110.0^\circ, 50.8^\circ)$ with a post-trial significance of 74% (0.33σ).

Limits from the 52 candidate sources and the sensitivity at a 90% confidence level for a fixed-source search with an E^{-2} energy spectrum are reported in figure 5, which present the best sensitivities for a large fraction of the Southern sky. The comparison with the 4 year analysis of IceCube is also presented.

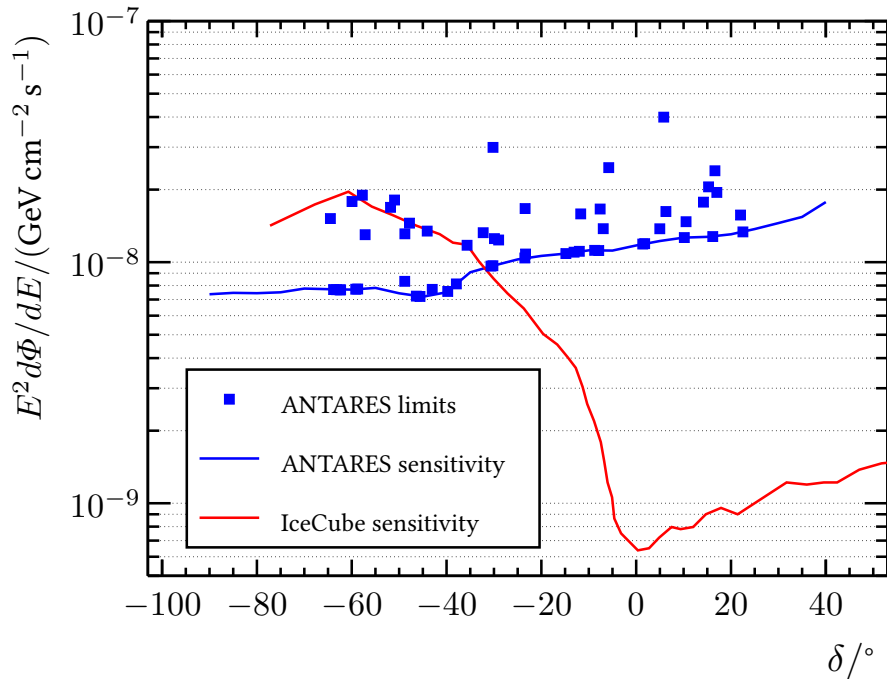


Figure 5: 90%CL limits and sensitivities following the Neyman approach [8]. The blue dots correspond to the limits of the 52 candidate sources. The blue line denotes the sensitivity for a point-source using a fixed-source analysis in this analysis. As a comparison, the sensitivity for the 4 year point-source analysis from IceCube is present.

3 Combined ANTARES-IceCube point-source analysis

The results of a search for point-like sources with data collected from the ANTARES and IceCube experiments were published recently[9]. Despite the significantly smaller volume of ANTARES compared with IceCube, its location provides a view of the Southern sky with significantly reduced background for neutrino energies below 100 TeV. The complementarity of both detectors with respect to sources coming from the Southern sky is due to the different geographical location, size and atmospheric muon background, allowing for a gain in sensitivity by combining data from both detectors.

The data sample corresponds to all events coming from the Southern Sky included in the three-year IceCube point-source analysis [10] and the 2007-2012 ANTARES one [3]. No cascade-like events were included in this analysis. The ANTARES sample contains data recorded from Jan 29, 2007 to Dec 31, 2012, whereas the IceCube one corresponds to data collected from Apr 5, 2008 to May 13, 2011 with the partially completed detector, and without the use of the Deep Core strings.

No significant clusters were found in this search. Figure 6 shows the sensitivities and limits obtained for the cases of an E^{-2} and a $E^{-2.5}$ energy source spectra. They are compared with the individual samples used in this analysis. The region of improvement due to the combination of the samples varies with the assumed energy spectrum of the source. An improvement factor of about 2 can be reached for an E^{-2} spectrum in regions close to the Galactic Centre. For steeper energy spectra the area of the sky with an improved sensitivity switches to declinations closer to the equator.

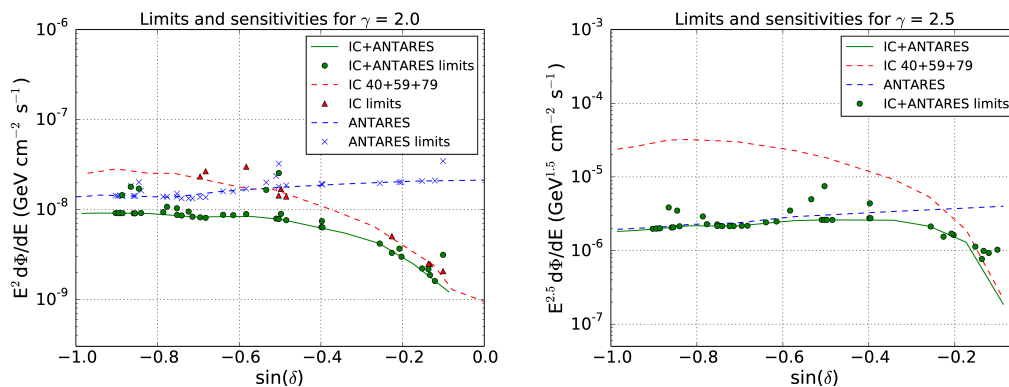


Figure 6: Point source sensitivities and limits for a 90% CL using the Neyman method [8] for energy spectra of E^{-2} (left) and $E^{-2.5}$ (right). The green line indicates the sensitivity for the combined search. Red and blue curves indicate the sensitivities for the individual IceCube and ANTARES analyses, respectively. As reference, the declination of the Galactic Center is approximately at $\sin(\delta = -29^\circ) \approx -0.48$.

4 Conclusions

A review of the latest results of point-like neutrino source searches with the ANTARES neutrino telescope has been shown. The first search for point-sources using both cascade and track events has been presented, with no statistically significant signal clusters found. A specific reconstruction for cascades had to be developed, leading to median angular resolutions between 2 and 4° for energies between 10^3 and 10^6 GeV. 90% CL limits and sensitivities for this search have been presented. A brief summary of the first combined analysis using data both from the ANTARES and IceCube experiments is also given, where an improvement up to a factor of 2 in sensitivity is achieved.

Acknowledgments

We gratefully acknowledge the financial support of Plan Estatal de Investigación (refs. FPA2015-65150-C3-1-P, -2-P and -3-P, (MINECO/FEDER)), Severo Ochoa Centre of Excellence and MultiDark Consolider (MINECO), Prometeo and Grisolia programs (Generalitat Valenciana), Spain., and Atracció de Talent of Universitat de València, Spain.

References

- [1] M. Agueron et al. (ANTARES Collaboration), Nucl. Instrum. Meth., **A656**, 11, (2011).
- [2] T. Michael, Light at the end of the Shower, PhD Thesis, NIKHEF, Amsterdam (2016).
- [3] S. Adrián-Martínez et al. (ANTARES Collaboration) ApJ, **786**, L5 (2014).
- [4] S. Adrian-Martinez et al. (ANTARES Collaboration) ApJ, **760**, 53 (2012).
- [5] S. Adrian-Martinez et al. (ANTARES Collaboration) JCAP, **1303**, 006 (2013).
- [6] E. L. Visser, Neutrinos from the Milky Way, PhD Thesis, NIKHEF, Amsterdam (2015).
- [7] M. G. Aartsen et al. (IceCube Collaboration), Phys. Rev. Lett. **113**, 101101 (2014).
- [8] Neyman J. Phil. Trans. Royal Soc. London A, **236**, 333 (1937).
- [9] Adrian-Martinez, S. et al. (ANTARES and IceCube Collaborations), ApJ. **823**, 65 (2016).
- [10] Aartsen M. G. et al. (IceCube Collaboration), ApJ, **779**, 132 (2013).

Solar models, neutrinos and composition

Aldo Serenelli¹, Nuria Vinyoles¹

¹Institute of Space Sciences (IEEC-CSIC), Carrer de Can Magrans S/N, 08193, Barcelona, Spain

DOI: <http://dx.doi.org/10.3204/DESY-PROC-2016-05/32>

In this presentation we review the current status of standard solar models (SSMs) and the solar abundance problem. We show that the most recent generation of SSMs (B16) yields neutrino fluxes that favors solar models with high metallicity interiors. This is in agreement with helioseismic probes of the solar interior, which also favor high-metallicity solar models. For the first time, both solar neutrino fluxes and helioseismology point towards the same preferred solution. However, because available neutrino data refers only to fluxes coming from the pp-chain, this preference is not towards a certain solar composition but rather towards a given internal temperature profile. At this point, the degeneracy between solar composition and radiative opacities cannot be broken. Future CNO solar neutrino experiments are the most promising way of elucidating the answer to this conundrum. In this presentation, we also show that for cases where the detailed solar composition is not a critical factor, SSMs are an excellent framework over which to test non-standard physics in solar (stellar) interiors and a laboratory for particle physics regardless of the solar abundance problem.

1 Introduction

About 15 years have passed since neutrino flavor oscillations were confirmed in solar neutrinos directly by the measurements of the ^8B solar neutrino flux, $\Phi(^8\text{B})$, by SNO [1, 2]. The discovery came after more than 30 years of controversy, following the initial results of the Homestake experiment [3], that have seen neutrino experiments, solar models and incomplete understanding of the physics of neutrinos being discussed as possible culprits of the *solar neutrino problem*. Kamiokande first [4], and the gallium experiments afterwards (SAGE [5, 6] and GALLEX [7]), confirmed the problem of the missing neutrinos. At the same time they established a pattern of fluxes with strong indications that an astrophysical solution, i.e. lowering the fluxes predicted by solar models, could not be reconciled with the experiments. Moreover, during the mid 90s, helioseismology was established as a reliable diagnostics tool of the structure of the solar interior, and the agreement between standard solar models (SSMs) and helioseismic inferences was astoundingly good [8, 9]. As a result, the second half of that decade saw a rapidly decreasing number of advocates favoring a solar model solution to the solar neutrino problem. Then, Super-Kamiokande discovered oscillations of atmospheric neutrinos [10]. And soon, SNO not only discovered solar neutrino oscillations but showed that SSM predictions for the $\Phi(^8\text{B})$ flux were spot on [11, 12]. These two experiments then firmly established the reality of neutrino flavor oscillations, showing at the same time the incompleteness of the standard model of particles and the soundness of SSMs as an accurate description of many properties of

the Sun [11, 13]. A recent historical account of the development of solar neutrino experiments and models can be found in [14].

Coincidentally with the discovery of neutrino oscillations, development of three dimensional models of the convective solar atmosphere [15, 16] and refinement of spectroscopic techniques and data (oscillator strengths of line transitions, line formation in non-local thermodynamic equilibrium) brought about a strong reduction in the spectroscopically determined metal abundances in the solar photosphere compared to older determinations [17, 18]. This is particularly important for the volatile and abundant carbon, nitrogen and oxygen, which added together amount to more than 2/3 of the solar metal content. This reduction, that amounts to up to 40% depending on the element and the authors [19], has a strong impact in solar modeling and puts into question the quality of SSMs as description of the solar interior properties as determined from helioseismic measurements. The apparent limitations of SSMs are evident in the predicted sound speed and density profiles, depth of the convective envelope, surface helium abundance, small frequency separation ratios (e.g. [13, 20]) among other diagnostics. Is the solar abundance problem in fact a *standard solar model problem* that shows the limitations of this framework? If so, then it is extensive to stellar modeling in general. Does the problem lay in the assumptions (simplifications) entering standard solar model calculations or in the microphysics (equation of state, radiative opacities, nuclear reaction rates) employed? Is it, on the contrary, a problem with solar abundances? If so, then it is extensive to almost all inferences of cosmic abundances, for most of which solar abundances are the yardstick against which they are determined. Or is the problem in our understanding of atomic physics, or of 3D solar model atmospheres? All these questions are of paramount importance not only for stellar astrophysics and astronomy, but for any field for which cosmic abundances are a quantity of interest.

In this presentation we briefly review the status of the solar abundance problem and present some results of an up-to-date generation of SSMs for both high (based on 1D model atmospheres, e.g. [17]) and low (based on 3D model atmospheres, [18]) solar metallicity. Theoretical predictions, based on updated SSMs, show for the first time since the solar abundance problem appeared, that helioseismic properties of the Sun and solar neutrino fluxes reflect the same stratification in the solar interior, consistent with that of high-metallicity SSMs. We argue, however, that this is not necessarily an indication of a high-metallicity but rather of a well determined temperature profile. Also, we discuss the limitations of the framework defined by SSMs and show that, by allowing variations of the microscopic inputs within the experimentally allowed space, SSMs continue to offer a good description of the solar interior. Therefore, and despite of the solar abundance problem, SSM predictions are still a benchmark against which to test more complex physical descriptions of the solar interior or even to test properties of hypothetical candidates to dark matter or non-standard properties of particles.

2 B16: a new generation of SSMs

In 2011, a round of SSMs was published [21] that included the nuclear cross sections recommended by the then recently published Solar Fusion II review article [22]. Since then, rates for some of the relevant nuclear reactions for solar models have been revised following both theoretical work or a reanalysis of existing experimental data. The changes in the rates are not dramatic, but $\Phi(^8\text{B})$ and $\Phi(^7\text{Be})$ solar fluxes are now measured to excellent precision [23, 12, 24] so even modest changes in the models translate into differences that are potentially

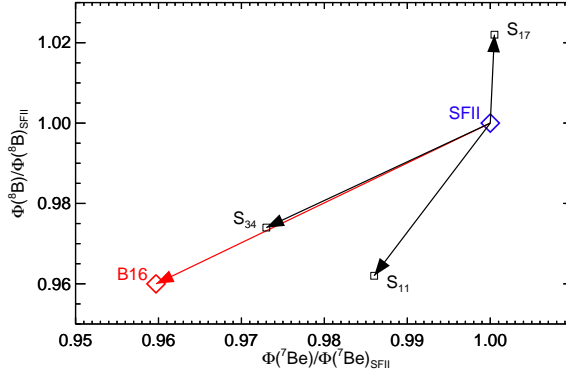


Figure 1: Fractional change of the SSM $\Phi(^7\text{Be})$ and $\Phi(^8\text{B})$ fluxes with respect to the previous generation of SSMs based on Solar Fusion II reaction rates.

measurable by current and future neutrino experiments.

The most important changes have occurred for $p + p$ [25], $^3\text{He} + ^4\text{He}$ [26] and $p + ^7\text{Be}$ [27]. While the latter only impacts the prediction of $\Phi(^8\text{B})$, the former two affect $\Phi(^7\text{Be})$ as well. It is worth mentioning changes in the astrophysical factor $S_{11}(E)$ stem not only from changes in $S(0)$ but also in $S'(0)$ and higher order derivatives. The relative variations introduced by each of these rates in the fluxes are shown in Fig. 1 in black arrows while the red arrow shows their cumulative effect, i.e. the overall change from the older generation of SSMs (SFII) to the new one (Barcelona 2016, B16 in short form). These changes are common to all SSMs regardless the detailed composition used to build them, so they are the same for GS98 and AGSS09 solar compositions. As shown in the figure, B16 predictions for $\Phi(^8\text{B})$ and $\Phi(^7\text{Be})$ are about 4% lower than for the SFII SSMs. Changes in other fluxes of the pp-chains are smaller, and well within the uncertainty from neutrino experiments.

Helioseismic probes are not sensitive to the changes in the nuclear rates from SFII to the newly adopted values to a measurable level. Only S_{11} could introduce some changes but these are too small to be of relevance. Fig. 2 shows results for the sound speed profile of SSMs corresponding to GS98 and AGSS09, the most widely used compositions. These are results of two sets of Monte Carlo simulations (Vinyoles et al. in prep.) consisting of 10000 SSMs each. In each panel, the red curve shows the results for the central SSM, green dotted lines show the $1\text{-}\sigma$ contours and the intensity of the color shade represents a histogram of the frequency of a given $\delta c/c$ occurring at a given depth r/R_{sun} . From the figures, it is clear that models based on AGSS09 do not describe helioseismic inferences properly, as it has been demonstrated often

	GS98	AGSS09	Helios.
α_{MLT}	2.18 ± 0.05	2.11	-
Y_{ini}	0.2717 ± 0.0056	0.2613	-
Z_{ini}	0.0187 ± 0.0013	0.0159	-
Y_{S}	0.2426 ± 0.0059	0.2316	0.2485 ± 0.0035
Z_{S}	0.0170 ± 0.0012	0.0134	-
Y_{C}	0.6320 ± 0.0053	0.6209	-
Z_{C}	0.0200 ± 0.0014	0.0159	-
R_{CZ}/R_{\odot}	0.7117 ± 0.0048	0.7224	0.713 ± 0.001
$\langle \delta c/c \rangle$	$0.0005^{+0.0006}_{-0.0002}$	0.0021	-

Table 1: Main SSM characteristics from the different sets of MC simulations. Also included are helioseismically inferred values.

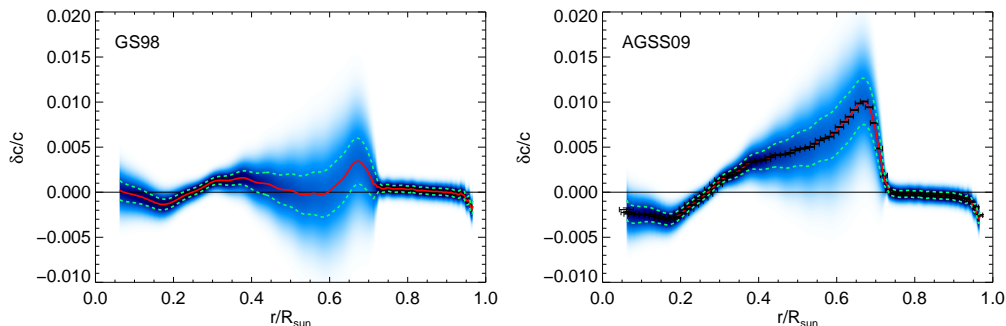


Figure 2: Histograms of sound speed profiles of SSMs where intensity indicates the frequency of $\delta c/c$ values at given r/R_{sun} in the MC simulations. Red lines correspond to central values and green dotted lines represent $1\text{-}\sigma$ contours of model uncertainties. Black crosses are the sound speed uncertainties propagated from uncertainties in p-mode frequencies.

in the past. Table 1 offers a summary of SSM properties and uncertainties derived from the MC simulations. For reasons of space, errors of the AGSS09 set have not been included in the table, but are quite similar to those of the GS98 MC set.

Results confirm earlier findings, with the B16 set of SSMs yielding very similar helioseismic results than the previous SFII generation of SSMs. Helioseismic probes of the solar interior clearly favor solar models based upon the GS98 composition, i.e. a high-metallicity solar composition, over the more modern and physically sound AGSS09 values. It is important to emphasize that the available set of helioseismic probes is not directly sensitive to the solar composition but to the actual temperature-density-pressure composition which, in turn, depends on the radiative opacity in the solar interior. The impact of metals in the solar structure is mostly through their importance as opacity sources. Therefore, helioseismic probes should be considered dependent on the opacity profile rather than on the abundance of metals. *The solar abundance problem still remains open.*

Detailed results for solar neutrino fluxes are given in Table 2. SSM results correspond to the MC sets and, again for reasons of space, fractional errors for the AGSS09 have been omitted (being very similar to those from GS98). Experimental results correspond to the results of the combined analysis of all available neutrino data [24] together with the luminosity constraint. Interestingly, the reduction in the predictions of $\Phi(^8\text{B})$ and $\Phi(^7\text{Be})$ in the B16 solar models brings the B16-GS98 results to a closer agreement with experimental results than its B16-AGSS09 counterpart for which now theoretical predictions are lower than experimental values. This is at odds with the previous SFII generation of models for which GS98 and

	GS98	AGSS09	Exper.
$\Phi(pp)$	$5.99(1 \pm 0.006)$	6.04	$5.971^{+0.037}_{-0.033}$
$\Phi(pep)$	$1.44(1 \pm 0.01)$	1.47	1.448 ± 0.013
$\Phi(hep)$	$8.00(1 \pm 0.30)$	8.27	$\leq 19^{+12}_{-9}$
$\Phi(^7\text{Be})$	$4.80(1 \pm 0.06)$	4.38	$4.80^{+0.24}_{-0.22}$
$\Phi(^8\text{B})$	$5.32(1 \pm 0.12)$	4.37	$5.16^{+0.013}_{-0.09}$
$\Phi(^{13}\text{N})$	$2.78(1 \pm 0.15)$	2.05	≤ 12.7
$\Phi(^{15}\text{O})$	$2.05(1 \pm 0.17)$	1.44	≤ 2.8
$\Phi(^{17}\text{F})$	$5.30(1 \pm 0.20)$	3.26	≤ 85

Table 2: Neutrino fluxes for the different B16 SSMs with the correspondent model errors and experimental results from a combined analysis of all neutrino experiments [24].

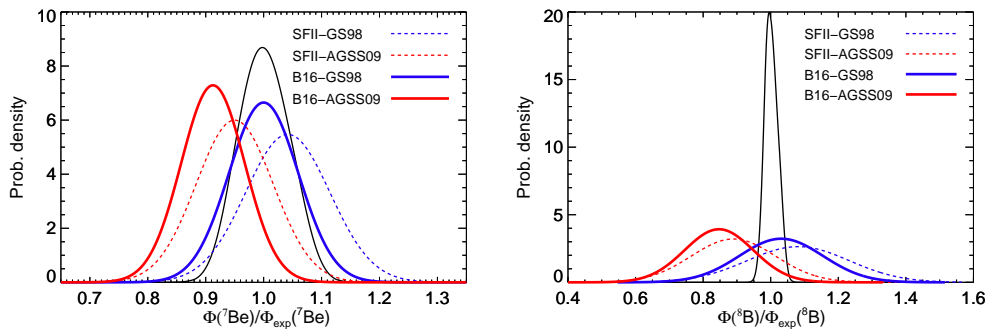


Figure 3: Comparison of solar neutrino fluxes determined from all available neutrino data (black lines [24]) and the previous (SFII - dotted lines) and current (B16 - thick solid lines) generations of SSMs.

AGSS09 compositions led to solar models that had $\Phi(^8\text{B})$ and $\Phi(^7\text{Be})$ fluxes in practically equal agreement with experimental data [21].

The new situation is more clearly illustrated in Fig 3 where model and experimental results are compared. Fluxes are normalized to experimental values [24]. Results from the older SFII SSMs are shown in dotted lines and, for GS98 and AGSS09 compositions, are almost symmetrically located to each side of the experimental result of the corresponding flux, $\Phi(^8\text{B})$ or $\Phi(^7\text{Be})$. With the B16 models, in solid lines, experimental results clearly show a preference for the GS98 SSM. A detailed quantification of the level of agreement of each of the B16 SSMs is ongoing work (Song et al. 2016 in prep.).

As stated above, helioseismic probes have a strong preference for GS98 based SSMs, although as also mentioned this cannot be interpreted as direct measurement of the solar composition but rather an indirect determination of the opacity profile in the solar interior [28, 29]. For the SFII models, it was not possible to claim that neutrino experiments had a preference of models of a given composition. Now, however, this situation has changed and for the B16 set of models solar neutrino fluxes also show the same results: GS98-based SSMs are to be preferred. *For the first time solar neutrinos and helioseismology favor the same solar interior properties, consistent with those inferred from high metallicity solar models.*

It is important to realize that neutrino fluxes originating in any of the pp-chain reactions are sensitive also to the temperature stratification in the solar core. This is to say, they are not directly sensitive to the composition but rather to the opacity profile. The situation is therefore very much the same as for the helioseismic probes: the sensitivity lies in the opacity profile, not the composition. For any of these probes, there is a degeneracy between opacity and metal abundances that needs independent constraints to be broken. At this moment, it is not possible to state whether AGSS09 metal abundances are too low or all atomic opacity calculations are intrinsically flawed and underestimate the actual radiative opacity in solar (and stellar) interiors.

Recently, the first ever experimental measurements of iron opacity under conditions quite close to those found at the base of the convective envelope of the Sun have become available [30]. These results seem to indicate that, in fact, opacity calculations [31, 32] underestimate the true iron opacity by large fractions that result in a final Rosseland mean opacity (the one actually relevant in solar interior calculations) that is underestimated by about 7% at the base of the

convective envelope. While clearly not enough to bring AGSS09 models into agreement with helioseismic data because an increase of the order of 15 to 20% is needed, these results are the first indication that in fact atomic opacity calculations might need a thorough revision. Some work in this direction has been carried out recently [33], showing that the treatment of line broadening alone may introduce an uncertainty level of several percents in opacity calculations.

3 Best-fit SSM

In the *standard* framework of SSM calculations the number of free parameters is kept to a minimum and phenomenological calibrations are avoided as much as possible (see e.g. [34] for more details). This strategy ensures that SSMs the *recipe* with which they are computed, being well defined, yields robust predictions. But, at the same time, it is clear that physical phenomena are modeled poorly in SSMs (e.g. near surface convection) or not modeled at all (e.g. rotation). It is also well known SSMs cannot account for some observations, e.g. the solar surface lithium abundance (more than 2 orders of magnitude lower than found in meteorites) among others.

A question that can be asked is: what are the limits of the SSM framework? Or, posed differently, what is the best possible description of solar interior properties the SSM framework can offer? The answer is important for several reasons. Among others: SSMs are used to set limits to exotic particles or non-standard properties of standard particles, SSM framework is the same entering most of stellar structure and evolution models, SSMs are the reference against which non-standard stellar physics is tested.

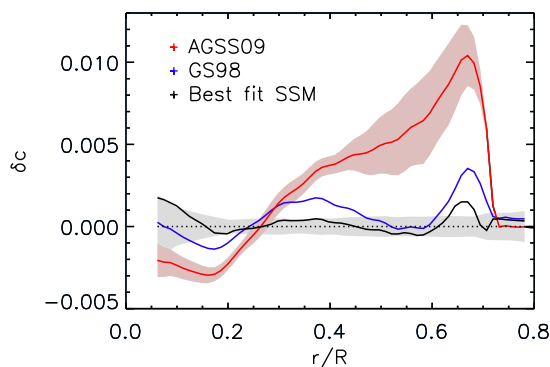


Figure 4: Sound speed profiles as in Fig. 2. The *best-fit SSM* (see text for details) is shown in black. The red and grey shaded area show the 1- σ model and sound speed inversion uncertainties respectively.

A way of answering this question is to allow input parameters (nuclear reaction rates, composition, opacity profile, etc.) in the SSMs as quantities that can be varied to provide the best possible fit to combined helioseismic and solar neutrino data. This exercise was carried out initially by [29], where a global χ^2 function was built using 32 helioseismic constraints (30 points of the sound speed profile, depth of convective envelope, surface helium abundance) and the $\Phi(^8\text{B})$ and $\Phi(^7\text{Be})$ neutrino fluxes. The response of each of these quantities to changes in the input parameters was built using power-law expansions and the input parameters were

allowed to vary around their measured values by introducing the concept of pulls with a penalty function in the global χ^2 . χ^2 is then minimized with respect to these pulls to offer a set of varied input parameters that allow the reconstruction of a *best-fit SSM*.

Later, the idea was extended to produce bounds for properties of exotic particles (axions and dark photons) [35]. In this approach, the solar composition is allowed to vary freely (no penalty). In the case of SSMs, the resulting sound speed profile of the *best-fit SSM* is shown in Fig. 4, where it is compared to those from GS98 and AGSS09 SSMs. As it can be seen in the figure, the performance of the GS98 model can be improved if input parameters in the SSM are varied (usually within $1\text{-}\sigma$) from the currently accepted values. Of course, the best-fit SSM reflects a solar composition close to that of GS98. The idea that SSMs can be used in studies of particle physics, regardless of the unsolved solar abundance problem, then relies on the fact that the interaction of these particles with standard matter (e.g. magnetic dipole of neutrinos), or the energy loss rates (in the case of weakly interacting particles), does not depend (or does so very weakly) on the detailed composition of the solar interior. This is very often the case, and under these conditions, the best-fit SSM offers a very stringent limit to the maximum impact non-standard physics can have in modifying solar interior properties. This has been exploited, for the first time, to improve existing constraints in axion-photon coupling and dark-photons kinetic coupling

4 Acknowledgments

AS thanks the organizing committee for the invitation to take part in the Magellan Workshop 2016: Connecting Neutrino Physics and Astronomy. AS and NV are partially supported by grants ESP2014-56003-R and ESP2015-66134-R (MINECO) and 2014-SGR-1458 (Generalitat de Catalunya).

References

- [1] Q. R. Ahmad et al. Measurement of the rate of $\nu_e + d \rightarrow p + p + e^-$ interactions produced by ^8B solar neutrinos at the Sudbury Neutrino Observatory. *Phys. Rev. Lett.*, 87:071301, 2001.
- [2] Q. R. Ahmad et al. Direct evidence for neutrino flavor transformation from neutral current interactions in the Sudbury Neutrino Observatory. *Phys. Rev. Lett.*, 89:011301, 2002.
- [3] Raymond Davis, Jr., Don S. Harmer, and Kenneth C. Hoffman. Search for neutrinos from the sun. *Phys. Rev. Lett.*, 20:1205–1209, 1968.
- [4] K. S. Hirata et al. Observation of B-8 Solar Neutrinos in the Kamiokande-II Detector. *Phys. Rev. Lett.*, 63:16, 1989.
- [5] A. I. Abazov et al. Search for neutrinos from sun using the reaction Ga-71 (electron-neutrino e-) Ge-71. *Phys. Rev. Lett.*, 67:3332–3335, 1991.
- [6] Dzh.N. Abdurashitov et al. Results from SAGE. *Phys. Lett.*, B328:234–248, 1994.
- [7] P. Anselmann et al. GALLEX results from the first 30 solar neutrino runs. *Phys. Lett.*, B327:377–385, 1994.
- [8] J. Christensen-Dalsgaard et al. The current state of solar modeling. *Science*, 272:1286–1292, 1996.
- [9] John N. Bahcall, Sarbani Basu, and M. H. Pinsonneault. How uncertain are solar neutrino predictions? *Phys. Lett.*, B433:1–8, 1998.
- [10] Y. Fukuda et al. Measurement of the flux and zenith angle distribution of upward through going muons by Super-Kamiokande. *Phys. Rev. Lett.*, 82:2644–2648, 1999.

- [11] John N. Bahcall, M. H. Pinsonneault, and Sarbani Basu. Solar models: Current epoch and time dependences, neutrinos, and helioseismological properties. *Astrophys. J.*, 555:990–1012, 2001.
- [12] B. Aharmim et al. Electron energy spectra, fluxes, and day-night asymmetries of B-8 solar neutrinos from measurements with NaCl dissolved in the heavy-water detector at the Sudbury Neutrino Observatory. *Phys. Rev.*, C72:055502, 2005.
- [13] John N. Bahcall, Aldo M. Serenelli, and Sarbani Basu. New solar opacities, abundances, helioseismology, and neutrino fluxes. *Astrophys. J.*, 621:L85–L88, 2005.
- [14] W. C. Haxton, R. G. Hamish Robertson, and Aldo M. Serenelli. Solar Neutrinos: Status and Prospects. *Ann. Rev. Astron. Astrophys.*, 51:21–61, 2013.
- [15] R. F. Stein and Å Nordlund. Simulations of Solar Granulation. I. General Properties. *Astrophys. J.*, 499:914–933, May 1998.
- [16] Carlos Allende Prieto, David L. Lambert, and Martin Asplund. The ‘Forbidden’ abundance of oxygen in the Sun. *Astrophys. J.*, 556:L63, 2001.
- [17] N. Grevesse and A. J. Sauval. Standard Solar Composition. *Space Sci. Rev.*, 85:161–174, 1998.
- [18] Martin Asplund, Nicolas Grevesse, A. Jacques Sauval, and Pat Scott. The chemical composition of the Sun. *Ann. Rev. Astron. Astrophys.*, 47:481–522, 2009.
- [19] Elisabetta Caffau, Hans-Gunter Ludwig, Matthias Steffen, Bernd Freytag, and Piercarlo Bonifacio. Solar Chemical Abundances Determined with a CO5BOLD 3D Model Atmosphere. *Solar Phys.*, 268:255, 2011.
- [20] William J. Chaplin, Aldo M. Serenelli, Sarbani Basu, Yvonne Elsworth, Roger New, and Graham A. Verner. Solar heavy element abundance: constraints from frequency separation ratios of low-degree p modes. *Astrophys. J.*, 670:872–884, 2007.
- [21] Aldo M. Serenelli, W. C. Haxton, and Carlos Pena-Garay. Solar models with accretion. I. Application to the solar abundance problem. *Astrophys. J.*, 743:24, 2011.
- [22] E. G. Adelberger et al. Solar fusion cross sections II: the pp chain and CNO cycles. *Rev. Mod. Phys.*, 83:195, 2011.
- [23] Gianpaolo Bellini. The impact of Borexino on the solar and neutrino physics. *Nucl. Phys.*, B908:178–198, 2016.
- [24] Johannes Bergstrom, M. C. Gonzalez-Garcia, Michele Maltoni, Carlos Pena-Garay, Aldo M. Serenelli, and Ningqiang Song. Updated determination of the solar neutrino fluxes from solar neutrino data. *JHEP*, 03:132, 2016.
- [25] L. E. Marcucci, R. Schiavilla, and M. Viviani. Proton-Proton Weak Capture in Chiral Effective Field Theory. *Phys. Rev. Lett.*, 110(19):192503, 2013.
- [26] R. J. deBoer, J. Gres, K. Smith, E. Uberseder, M. Wiescher, A. Kontos, G. Imbriani, A. Di Leva, and F. Strieder. Monte Carlo uncertainty of the ${}^3\text{He}(\alpha,\gamma){}^7\text{Be}$ reaction rate. *Phys. Rev.*, C90(3):035804, 2014.
- [27] Xilin Zhang, Kenneth M. Nollett, and D. R. Phillips. Halo effective field theory constrains the solar ${}^7\text{Be} + \text{p} \rightarrow {}^8\text{B} + \gamma$ rate. *Phys. Lett.*, B751:535–540, 2015.
- [28] Jorgen Christensen-Dalsgaard, Maria Pia Di Mauro, Gunter Houdek, and Frank Pijpers. On the opacity change required to compensate for the revised solar composition. *Astron. Astrophys.*, 494:205, 2009.
- [29] Francesco L. Villante, Aldo M. Serenelli, Franck Delahaye, and Marc H. Pinsonneault. The chemical composition of the Sun from helioseismic and solar neutrino data. *Astrophys. J.*, 787:13, 2014.
- [30] J. E. Bailey et al. A higher-than-predicted measurement of iron opacity at solar interior temperatures. *Nature*, 517:56–59, jan 2015.
- [31] Carlos A. Iglesias and Forrest J. Rogers. Updated Opal Opacities. *Astrophys. J.*, 464:943, 1996.
- [32] Nigel R. Badnell, M. A. Bautista, K. Butler, F. Delahaye, C. Mendoza, P. Palmeri, C. J. Zeippen, and M. J. Seaton. Up-dated opacities from the Opacity Project. *Mon. Not. Roy. Astron. Soc.*, 360:458–464, 2005.
- [33] M. Krief, A. Feigel, and D. Gazit. Line Broadening and the Solar Opacity Problem. *Astrophys. J.*, 824(1):98, 2016.
- [34] Aldo Serenelli. Alive and well: a short review about standard solar models. *Eur. Phys. J.*, A52(4):78, 2016.
- [35] Núria Vinyoles, Aldo Serenelli, Francesco L. Villante, Sarbani Basu, Javier Redondo, and Jordi Isern. New axion and hidden photon constraints from a solar data global fit. *JCAP*, 1510(10):015, 2015.

CNO neutrinos and metallicity of stars

Stefano Davini¹

¹Gran Sasso Science Institute, L'Aquila AQ 67100, Italy

DOI: <http://dx.doi.org/10.3204/DESY-PROC-2016-05/25>

The detection of neutrinos resulting from the CNO cycle would be the first direct evidence of the nuclear process that is believed to fuel massive stars. A precise measurement of the CNO solar neutrino fluxes would also help resolving the solar metallicity problem, as the predicted fluxes strongly depend on the inputs of the solar modelling. This articles, part of the Magellan 16 proceedings, reviews the connections between CNO neutrinos and solar metallicity, and the experimental attempts to detect them.

1 Introduction

CNO neutrinos are the neutrinos emitted in the CN and NO bi-cycle, one of the two set of fusion reactions in the Sun. The reactions in the CNO bi-cycle which involves the emission of neutrinos are the following:



where the energy in parenthesis is the kinetic energy available to the final states of the reactions. The relevance of the CNO bi-cycle to the total luminosity of the Sun is estimated to be of the order of $\sim 1\%$: the contribution to the energy budget of the CNO reactions is marginal in Sun-like stars and therefore the flux of the CNO neutrinos is low, in the ballpark of one hundredth of the pp solar neutrino flux, and hard to determine experimentally.

Nevertheless, a precision measurement of the CNO neutrino flux would be of paramount importance in astrophysics: the accuracy of the physical description of the Sun provided by Solar Standard Models (SSMs) has been challenged by developments in stellar spectroscopic techniques over the last decade. An experimental determination of CNO neutrino fluxes is likely the only probe to settle the challenge.

The accuracy of the description of the physics of the Sun is critical because of the fundamental role that Solar Standard Models play in our understanding of the Universe. The Solar Standard Model is the calibration input for stellar evolution and plays a fundamental role in cosmology. Examples of the role of the SSM as source of calibration in astrophysics and cosmology are the following: convection models in stars are calibrated forcing solar models to reproduce present day solar radius and temperature, the evolution of metals and helium in the Universe needs input from both Big Bang Nucleosynthesis and initial SSM composition, the SSM is used as a benchmark against additional physics processes in stars.

2 The Solar abundance problem

The agreement between solar models and helioseismology has been altered after new spectroscopic determinations of the photosphere composition [1]. The new determinations were obtained with an advanced three-dimensional hydrodynamic model instead of a one-dimensional model, better atomic and molecular data, and non local thermodynamic equilibrium (NLTE) calculations. Using the new input, the abundances of C, N, O in the Sun are lowered by 20-30%. The new abundances are challenging for the SSM, because the previous agreement with helioseismic data is lost.

Does this disagreement question the validity of the Solar Standard Models or stellar models in general? The answer is not easy. "It seems clear that the low metallicity solar abundances are here to stay", says Serenelli [2]. A good consequence of the Solar abundance problem is that it motivated further work on solar models, such as nuclear reaction rates, radiative opacities, and state equations.

Solar opacities and CNO neutrinos play a major role in the Solar abundance problem. A suitable change of solar opacity profile produces same effects on helioseismic observable and neutrino fluxes of a change of solar composition, *except for CNO neutrinos*. CNO neutrinos can thus break the degeneracy between solar abundances and radiative opacities.

3 Solar neutrinos and solar abundancies

This section is an informal review of the experimental determination of the solar neutrino fluxes and what the determinations can tell us about the Sun. Both the experimental determination and SSM predictions are subject to rapid changes over time, so the values reported here are truncated at the first significant digit or given as order of magnitude. Any reader interested in more digits can find them in the references.

The solar neutrino detectors which are operative at present day are Borexino [3], 300 ton (fiducial) liquid scintillator detector at Laboratori Nazionali del Gran Sasso (LNGS) in Italy, and Super-Kamiokande [4], 22.5 kton (fiducial) water Cherenkov detector at the Kamioka mine in Japan. Borexino is engaged in the spectroscopy of solar neutrinos, which is possible due to the low threshold (as low to detect pp neutrino recoils on electrons) and the ultra-pure detector conditions. Super-Kamiokande is exploiting its big mass and directionality capabilities to perform a precision measurement the flux solar neutrinos which recoils on electrons with kinetic energy above 3.5 MeV, which are essentially ${}^8\text{B}$ neutrinos (the flux of hep neutrinos is too low to allow for a detection at present time).

The neutrinos emitted in the pp and pep reactions are the ones whose fluxes are predicted with the highest accuracy by the SSM, because of the luminosity constraint. The uncertainty of the pp flux prediction in the SSMs is below the per-mille level, while the uncertainty of the pep flux is at the percent level. The neutrino fluxes from these reactions are not directly sensitive to the Solar abundances, but to the radiative opacities. The flux of pp and pep reactions is indeed mostly driven by the core temperature, therefore to the radiative gradient determined by the opacity. Neutrinos from pp and pep reactions are not good probes for the Solar abundances, but they may be excellent probes of the core temperature if their flux is measured with enough precision, and they provide a test of the solar luminosity.

The experimental accuracy is about 10% for pp neutrinos (Borexino, [5]) and about 25% for pep neutrinos (Borexino, [6]). The determination of the pp neutrino interaction rate in Borexino

is challenging because of the backgrounds due to ^{14}C . The determination of the *pep* neutrino interaction rate in Borexino is challenging because of the low statistics (few events per day in the region of interest and the fiducial volume) and the backgrounds due to the cosmogenic ^{11}C and the radiogenic ^{210}Bi .

^7Be and ^8B solar neutrinos are emitted in the proton-proton chain, therefore their fluxes are subject to the same degeneracy between the core temperature (then radiative opacity) and the Solar abundances described above. The experimental determination of the ^7Be and ^8B solar neutrino flux is more precise than their theoretical counterpart in the SSMs. The best measurement of the ^7Be solar neutrino flux is from Borexino [7], with an accuracy of about 5%. The uncertainty in the SSM is about 7%. The best measurement of the ^8B solar neutrino flux is from Super-Kamiokande [8], with an accuracy of about 3%. The uncertainty in the SSM is about 14%.

^8B solar neutrinos deserve a few more sentences of merit, even if a bit off-topic. The measurement of the ^8B solar neutrino interaction rate in the SNO experiment, exploiting both neutral current (sensitive to all neutrino flavors) and charged current reactions (sensitive to electron neutrino only) in D_2O , firmly established the flavor conversion of solar neutrinos. Art Mc. Donald, spokesperson of SNO, was awarded half of the Nobel prize in 2015, and the other half was awarded to Takashi Kajita of Super-Kamiokande for the discovery of the atmospheric neutrino oscillation in Super-Kamiokande.

Closing this off-topic paragraph on neutrino oscillation and history of physics, we return to CNO neutrinos. The temperature profile in the solar core is established by the proton-proton chain (and not by the CNO bi-cycle), therefore the experimental measurement of CNO neutrino flux may be used to probe the Solar abundances, being the flux linear in the abundance of carbon and nitrogen. The only experimental limit on the CNO neutrino flux is from Borexino [6]. The limit is about 40% higher than the high metallicity SSM predictions, therefore the Solar abundances of metals are basically unconstrained.

4 The challenges of CNO neutrino detection

It should be clear from the previous sections that CNO neutrinos are the perfect probe to determine the solar abundances. The goal should be clear: measure the CNO neutrino fluxes to get the abundances. Why this has not been done? Because an experimental determination of the CNO neutrino flux is extremely, extremely, challenging.

The reason why CNO neutrinos are the best probe is also one of the reason why they are so hard to detect. The solar luminosity and the temperature in the core are driven by the proton-proton reactions, with the CNO bi-cycle reactions being a marginal source of energy in the Sun. This means that the CNO neutrino flux can discriminate between the high metallicity and low metallicity SSM models, breaking the degeneracy with the radiative opacity. But this also means that the CNO neutrino fluxes from the Sun are low, $3-5 \cdot 10^8 \text{ cm}^{-2} \text{ s}^{-1}$, at the level of 1% of the *pp* neutrino flux. The low flux alone would be not so much of a problem: ^8B neutrinos are even lower in flux (a factor hundred less), but many of their recoils have high enough energy to be detectable even with water Cherenkov detectors, at energy above backgrounds from radiogenic and cosmogenic radioactivity. The Nature is not so kind with CNO neutrinos: the CNO energy spectrum falls below 2MeV, and this means being overwhelmed by natural radioactivity backgrounds.

Even if a large fraction of the CNO neutrino spectrum is above the Cherenkov emission

threshold in water, CNO neutrinos are well below the experimental threshold of the water Cherenkov detector Super-Kamiokande (about 3.5 MeV). The only detector type available today for detecting CNO neutrinos are ultra-pure organic liquid scintillators. Borexino at LNGS *is the most radio-pure detector* between 200 keV and 2 MeV, among the detectors operated at present time and in the past. Even Borexino could only provide limits to the CNO neutrino flux, because of the residual radioactive backgrounds and the correlation with *pep* neutrinos in determining the fluxes with fit to the energy spectrum.

The main radioactive backgrounds in Borexino, which any future organic liquid scintillator detector for CNO neutrinos will have to fight, are the radiogenic ^{210}Bi and the cosmogenic ^{11}C .

^{210}Bi is a β^- emitter with end point 1.16 MeV and five days half-life. The real problem is that the spectral shapes of ^{210}Bi and electron recoils from CNO neutrinos are *very similar* and do not show distinct features like peaks. ^{210}Bi is part of the ^{238}U chain, its predecessor is ^{210}Pb and its daughter is ^{210}Po . ^{210}Bi and ^{210}Po are found not to be in secular equilibrium, therefore constraining the activity of ^{210}Bi from the rate of ^{210}Po (which is easier to measure) is not trivial (but not impossible *in principle*, as shown in [9]). It is particularly challenging to remove ^{210}Bi by purification methods [10]; it is indeed the only radiogenic β^- emitter in the phase-II of Borexino whose activity is above 10 decays per day per 100 tons (^{14}C is excluded in this evaluation).

^{11}C is a cosmogenic radioactive isotope, generated in the inelastic scattering of muons on ^{12}C , $\mu + ^{11}\text{C} \rightarrow \mu + ^{12}\text{C} + \text{n}$. ^{11}C is a β^+ emitter with end point 1.98 MeV (including the energy from the annihilation of the electron-positron pair) and 20 minutes half-life. The background due to cosmogenic isotopes can be of course reduced by increasing the detector overburden. Another way to reduce the background is to track the muon and locate the neutron capture, then apply space-time cuts to exclude regions of the detector where it is more likely that ^{11}C was produced (and decays), like it was done in Borexino [11]. This method however sacrifices substantial fractions of the total exposure. Also, it is possible to constrain ^{11}C by exploiting the slightly different scintillation pulse shape for β^- and β^+ decay in liquid scintillators, mainly due to ortho-positronium formation [12].

5 The ideal CNO hunter

It should be clear to the reader that hunting CNO neutrinos is not an easy task. I will review here the features that a CNO neutrino *must* have in order to have some chances to perform a measurement.

The detector must be large. The ideal scale is kiloton. The CNO neutrino fluxes and cross sections are low, therefore the detector should be large enough to collect a relevant number of CNO interactions. Large detectors also allow for better fiducialization, which is important because the low energy tails of the external background (due mainly to ^{208}Tl and ^{214}Bi γ -rays) must be negligible around the CNO neutrino endpoint.

High energy resolution. It is of paramount importance to discriminate the CNO neutrino electron recoils from the radioactive background and the residual solar neutrinos. In particular, the energy spectrum of ^{210}Bi decay and CNO neutrino electron recoils are very similar, and the risk is not being able to resolve the two components if the resolution is not high enough. Also in absence of any radioactive background (a dream detector), the spectrum due to CNO neutrinos must be identified below the spectrum of ^7Be and *pep* neutrinos.

Ultra-pure detector. In particular, the levels of ^{222}Rn , ^{210}Pb , ^{210}Bi , and ^{210}Po must be ultra-low. ^{210}Bi should be below the CNO interaction rate, which in Borexino is predicted to be 5 (3) decays per day per 100 tons in the high (low) metallicity SSM. Consider that it is *sufficient* to remove the contamination of ^{210}Bi to place *limits* on the CNO neutrino flux, but it is *necessary* to estimate the residual ^{210}Bi activity in the detector to *convincingly measure* the CNO neutrino flux.

Deep detector. Cosmogenic backgrounds must not be an issue. It is true that most of cosmogenic decays can be removed by space-time cuts, but these cuts usually remove a substantial fraction of the detector exposure.

Stable detector. In order to measure CNO neutrinos, the residual radioactive backgrounds in the detector must be known. The radioactive backgrounds should be stable in space in order to be measured with enough accuracy. In particular, there must be no convection moving radioactive contaminants around the detector and changing their concentration over time. Experiments should consider thermal insulation to prevent or decrease convective motions due to temperature changes in the experimental halls.

Particle identification. Discriminating α backgrounds from β backgrounds allows to tag ^{210}Po , $^{212}\text{Bi-Po}$, and $^{214}\text{Bi-Po}$, making it possible to evaluate the activity of branches in the ^{238}U and ^{232}Th chains, and investigate if the secular equilibrium condition is met. Discrimination of β radioactivity from γ radioactivity may be helpful to reduce external background and β^+ decays.

Directionality. Measuring the direction of recoil electrons, which is correlated to the incoming direction of neutrinos, would be tremendously helpful and nihil the relevance of mostly all internal radiogenic backgrounds. Unfortunately, today there is no demonstrated directional detection technology for neutrino recoils at 1 MeV, scalable to kiloton masses.

6 Future CNO hunters

Among experiments under construction, or ready to be approved, or proposed, there are few that may be good CNO hunters. This list is not exhaustive by purpose (and the space in this proceeding has an upper bound), therefore nobody should feel offended if their favorite experiment is not in the list.

SNO+ at SNOLab is an organic liquid scintillator detector with the advantages of being large (1 kton) and deep (the ^{11}C production rate should be reduced of a factor hundred respect to Borexino at LNGS). SNO+ may start a solar neutrino campaign after the neutrino-less double beta decay (in ^{130}Te) phase.

The JINPING Neutrino Experiment is a proposed organic liquid scintillator detector with the advantages of being even larger (20 kton) and even deeper (China JinPing Laboratory-II, already under construction, is going to be the deepest underground laboratory) [13]. In the letter of intent, one can read "We predict a capacity to discover solar neutrinos from the carbon-nitrogen-oxygen (CNO) cycle with more than 5 sigma of statistical significance".

ARGO at LNGS is a 200 ton fiducial two-phase liquid argon time projection chamber (LAr TPC) for direct dark matter WIMP searches [14]. LAr TPCs have the advantages of having higher Z and better scintillation light yield and resolution of organic liquid scintillators. Simulations in [14] show that "such a detector could measure the CNO neutrino rate with $\sim 15\%$ precision".

Solar neutrinos are going to be a background for the next (or the next to next) generation

of direct dark matter WIMP experiment. The reader should not be surprised of a possible growing interest in solar neutrino detection over the next decade(s).

7 Conclusion and outlook

There *is* a solar abundance problem. And it is likely that the new solar abundances are here to stay. The experimental measurement of the flux of neutrinos from the CNO bi-cycle can settle the problem. However, the experimental detection of CNO neutrinos is challenging. Some future projects may be able to detect CNO solar neutrinos.

Acknowledgments

I gratefully acknowledge the Organizers of Magellan 16 for the invitation.

Appendix A: Multidisciplinary workshop

Multidisciplinary workshops, like Magellan, are indeed very useful to strengthen the bonds between astrophysicist and particle physicists. Recalling a famous quotation from Feynman, even if we (or academia) split the topics in different subjects, the Nature does not.

A problem with multidisciplinary is that sometimes the lack of a common background is huge. Question time is very useful construct bridges over this gap. In the question time, I was asked if it is possible to detect neutrinos from other stars besides the Sun. The answer is no, except SuperNovae neutrinos. To convince yourself, you can try to compute the number of neutrino interactions detected in one year in a Borexino-like detector (Borexino detects about 200 neutrinos per day per 100 tons) from a Sun-like star one light year from us.

References

- [1] M. Asplund *et al.*, Annual Review of Astronomy & Astrophysics, **47** 481 (2009).
- [2] A. Serenelli, Eur. Phys. J. **A 52** 78 (2016).
- [3] G. Alimonti *et al.*, Nucl. Instr. Meth. A **A600** 568-593 (2009).
- [4] Y. Fukuda *et al.*, Nucl. Instr. Meth. A **A501** 418-462 (2003).
- [5] G. Bellini *et al.*, Nature **512** 7515, 383-386 (2014).
- [6] G. Bellini *et al.*, Phys. Rev. Lett **108** 051302 (2012) .
- [7] G. Bellini *et al.*, Phys. Rev. Lett **107** 141302 (2011).
- [8] K. Abe *et al.*, arXiv:hep-ex/1606.07538 (2016).
- [9] F.L. Villante *et al.*, Phys. Lett. **B701** 336 (2011).
- [10] G. Alimonti *et al.*, Nucl. Instr. Meth. A **A609** 58-78 (2009).
- [11] G. Bellini *et al.*, Phys. Rev. **D89** 112007 (2014).
- [12] D. Franco *et al.*, Phys.Rev. **C83** 0105504 (2011).
- [13] J.F. Beacom *et al.*, arXiv:physics,ins-det/1602.01733 (2016).
- [14] D. Franco *et al.*, arXiv:physics,ins-det/:1510.04196 (2015).

The GERDA Experiment: Search for the Neutrinoless Double Beta Decay

Michael Miloradovic¹ on behalf of the GERDA Collaboration

¹Physik Institut der Universität Zürich, Zürich, Switzerland

DOI: <http://dx.doi.org/10.3204/DESY-PROC-2016-05/34>

The Germanium Detector Array (GERDA) experiment is searching for the neutrinoless double beta decay of ^{76}Ge . The observation of this Beyond the Standard Model process would prove the existence of a neutrino Majorana mass component and provide information on the neutrino mass hierarchy and absolute mass scale. GERDA operates enriched germanium diodes, acting simultaneously as the source and detector material, directly submerged in liquid argon. Phase I achieved the world's best lower limit of $T_{1/2}^{0\nu\beta\beta} > 2.1 \cdot 10^{25}$ yr (90% C.L.). With the recent completion of the upgrade to Phase II, an additional 20 kg of germanium detectors – for a total of 35 kg – and a liquid argon veto system have been implemented. The goal is an order of magnitude lower background with a projected sensitivity of $1.4 \cdot 10^{26}$ yr for $T_{1/2}^{0\nu\beta\beta}$.

1 Matter antimatter asymmetry

Today, our universe is completely matter dominated. All galaxies and stars consist of baryons. Antimatter exists only as a product of high-energy particle collisions. In the early universe, this was not the case. According to the Standard Model of Particle Physics, the Big Bang should have created a completely symmetrical universe with equal amount of matter and antimatter. If this thought is developed further, the quark and antiquark pairs would interact in pairs leading to the complete annihilation of this symmetrical universe. In reality, a slight asymmetry introduced in the early stages of the universe is responsible for the small excess of matter in comparison to antimatter that now makes up our universe. The origin of this asymmetry could lie in neutrino nature. Determining the nature of the neutrinos is thus of fundamental importance in modern physics [1].

2 Neutrinos

In 1937, Ettore Majorana suggested that the neutrino could be its own antiparticle [2]. The recent discovery of neutrino oscillations establish the non-zero mass of neutrinos [3, 4]. The matter antimatter asymmetry could be explained through an extension of the Standard Model, wherein the see-saw mechanism introduces right-handed neutrinos. CP violating decays of these particles then spontaneously generate leptons resulting in a lepton asymmetry in the early universe. Baryogenesis via leptogenesis could thus lead to the observed matter antimatter

asymmetry [5]. The prime avenue to directly probe this fundamental characteristic and simultaneously obtain information on the absolute neutrino masses is the neutrinoless double beta decay. This postulated decay channel could involve two Majorana neutrinos, which annihilate off-shell in a lepton number violating interaction with zero neutrinos in the final state.

3 The GERDA experiment

The Germanium Detector Array (GERDA) experiment is searching for the neutrinoless double beta decay of ^{76}Ge . It is located underground in Hall A of the Laboratori Nazionali del Gran Sasso (LNGS) with a 1400 m rock overburden. The isotopically enriched germanium diodes are directly submerged inside a 64 m^3 high purity liquid argon cryostat and act simultaneously as the source and detector material. Surrounding the cryostat, a 10 m diameter purified water tank shields the experiment and serves as a Cherenkov muon veto featuring 66 photomultiplier tubes (PMTs). These shielding and veto layers ensure a substantial reduction of the background and the highest possible sensitivity for the experiment [6].

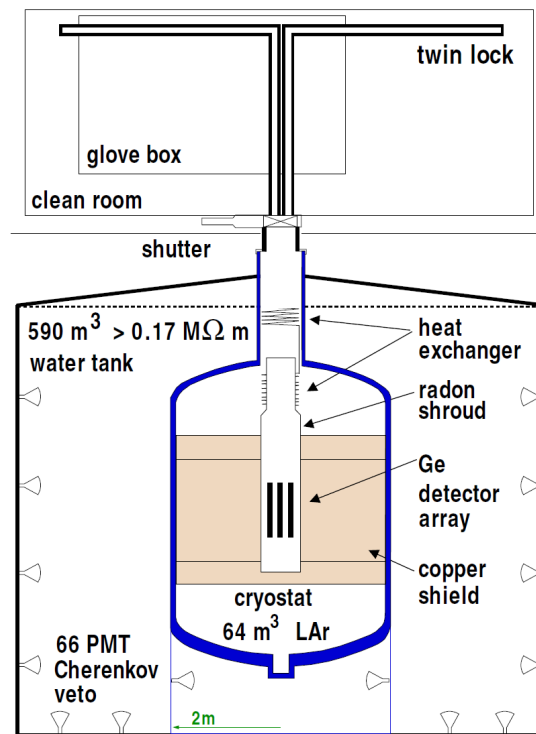


Figure 1: The GERDA experiment with its germanium detector array directly submerged in a liquid argon cryostat, surrounded by a water tank Cherenkov muon veto.

The germanium detectors offer an excellent energy resolution of $\sim 0.15\%$ FWHM at $Q_{\beta\beta}$. Another advantage is the possibility of Pulse Shape Discrimination (PSD), wherein the induced signal shapes are used to further reduce the background by identifying single site events (e.g.

$0\nu\beta\beta$), multi site events (e.g. Compton scattered γ), and surface events (e.g. α/β events).

Background reduction techniques are crucial as the sensitivity on the half-life of the neutrinoless double beta decay strongly depends on the background index (BI) as follows

$$T_{1/2}^{0\nu} \propto \sqrt{\frac{M \cdot t}{\Delta E \cdot BI}}. \quad (1)$$

Only in a zero background regime can a proportional scaling to the exposure ($M \cdot t$) be attained such that

$$T_{1/2}^{0\nu} \propto M \cdot t. \quad (2)$$

4 GERDA Phase I

In GERDA Phase I, running from November 2011 to May 2013, 15 kg of semi-coaxial and 3 kg of Broad Energy (BEGe) germanium detectors were used on four strings for a total exposure of 21.6 kg·yr. A tenfold lower background in comparison to previous experiments was obtained with a background index of around $1 \cdot 10^{-2}$ counts/(keV·kg·yr) at $Q_{\beta\beta}$, fulfilling the design goal. Figure 2 shows the best fit background model including the individual contributions, performed before unblinding a 40 keV window around $Q_{\beta\beta}$ [7].

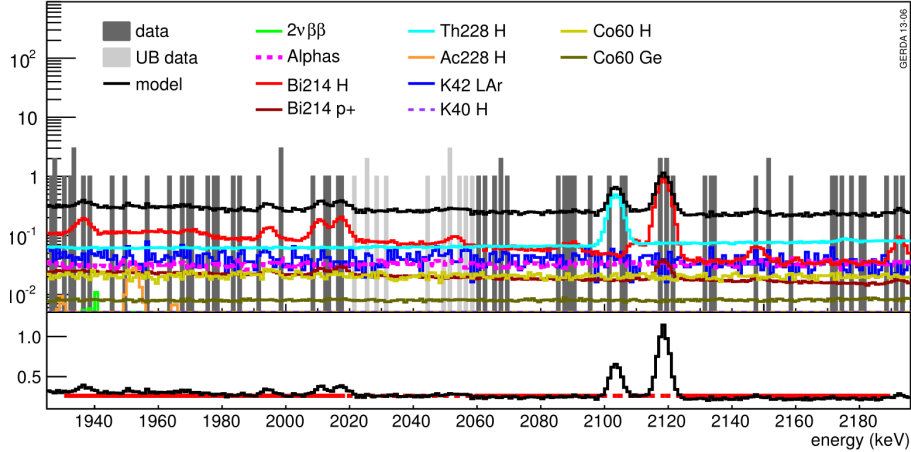


Figure 2: Phase I background best fit minimum model and individual contributions. The data inside the blinded window (UB, light grey) of size 40 keV is excluded from the fit. Figure from [7].

With this progress, it was possible to achieve the world's best lower limit of $T_{1/2}^{0\nu\beta\beta} > 2.1 \cdot 10^{25}$ yr (90% C.L.) for the half-life of the neutrinoless double beta decay of ^{76}Ge . Figure 3 depicts the region of interest, the relevance of the PSD, and the lower limit [8].

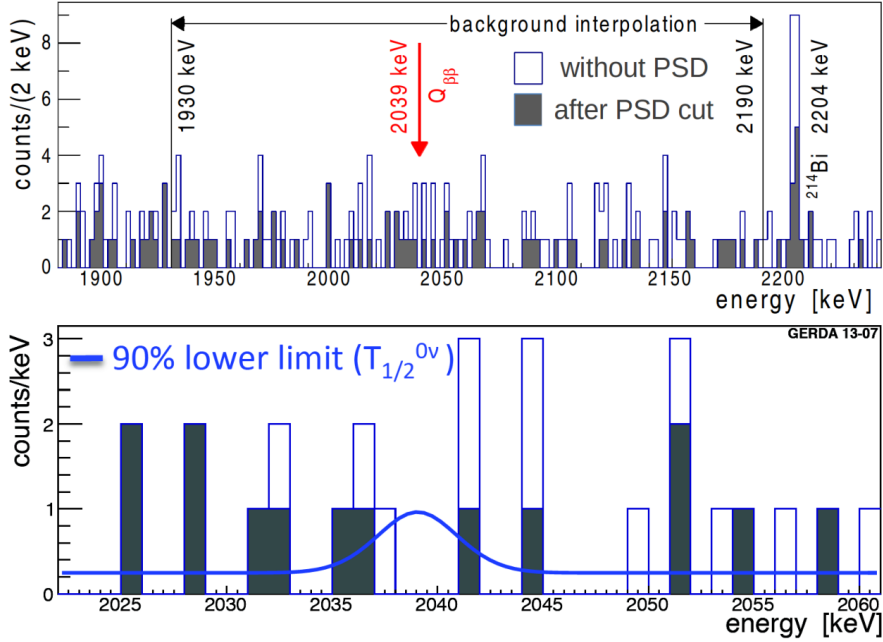


Figure 3: The results of GERDA Phase I in the region of interest (with and without PSD), leading to the lower limit of $T_{1/2}^{0\nu\beta\beta}$. Figure from [8].

5 GERDA Phase II

For Phase II of the experiment, the active mass of germanium diodes is increased by an additional 20 kg of BEGe detectors for a total of 40 detectors on 7 strings. The BEGe detectors offer superior PSD capabilities. A liquid argon hybrid veto system was introduced through the installation of PMTs and an optical fibre curtain coupled to silicon photomultipliers (SiPMs) inside the cryostat. The detection of liquid argon scintillation light is used to reject external background events. Combining all developments, the background can thus be efficiently reduced by an order of magnitude. The goal is to achieve a median sensitivity of $T_{1/2}^{0\nu\beta\beta} \sim 1.5 \cdot 10^{26}$ yr for a total exposure of 100 kg·yr. Table 1 summarises the Phase I and the aim of Phase II [9]. The upgrade to GERDA Phase II has been finished and the data taking has begun in December 2015.

Phase	Active Mass [kg]	BI [counts/(keV·kg·yr)]	$T_{1/2}^{0\nu}$ Sensitivity [yr]
I (finished)	15	10^{-2}	$2.1 \cdot 10^{25}$
II (expected)	35	10^{-3}	$1.4 \cdot 10^{26}$

Table 1: GERDA Phase I results and Phase II goals in terms of the active detector mass, background index and median sensitivity on the ^{76}Ge neutrinoless double beta decay half-life.

References

- [1] K. Nakamu and S. Petcov, Particle Data Group Review 2014, PDGRPP (2014).
- [2] E. Majorana, Teoria simmetrica dellelettrone e del positrone. *Il Nuovo Cimento* **14** 171 (1937).
- [3] Y. Fukuda *et al.*, *Phys. Rev. Lett.* **81** 1562 (1998).
- [4] Q. R. Ahmad *et al.*, *Phys. Rev. Lett.* **87** 071301 (2001).
- [5] M. Fukugita and T. Yanagida, *Phys. Lett.* **B174** 45 (1986).
- [6] The GERDA Collaboration, *Eur. Phys. J.* **C73** 2330 (2013).
- [7] The GERDA Collaboration, *Eur. Phys. J.* **C47** 2764 (2014).
- [8] The GERDA Collaboration, *Phys. Rev. Lett.* **111** 122503 (2013).
- [9] K. T. Knöpfle for the GERDA Collaboration, *PoS* **109** (TIPP2014).

The atmospheric muon charge ratio: a probe to constrain the atmospheric $\nu_\mu/\bar{\nu}_\mu$ ratio

Nicoletta Mauri

INFN - Sezione di Bologna, Viale Berti Pichat 6/2, 40127 Bologna, Italy

DOI: <http://dx.doi.org/10.3204/DESY-PROC-2016-05/11>

The atmospheric muon charge ratio, defined as the number of positive over negative charged muons, is an important observable to shed light on the physics of cosmic ray interactions in atmosphere. It allows studying the features of high-energy hadronic interactions in the forward region and the composition of primary cosmic rays. In particular, the TeV muon charge ratio provides sensitivity to the charge ratio of high energy kaons, the principal parents of atmospheric neutrinos. In this paper the results from the OPERA experiment in the TeV energy range are reviewed.

1 Introduction

The atmospheric muon charge ratio $R_\mu \equiv N_{\mu^+}/N_{\mu^-}$ is studied and measured since many decades over a wide muon energy range, from few GeV up to several TeV. It provides relevant information on both cosmic rays and particle physics through its dependence on several aspects: primary chemical composition and energy spectrum, hadronic interactions features and, at very high energy, production and prompt decays of charmed particles.

Atmospheric muons constitute the penetrating charged remnants of cosmic rays under the Earth's surface. They are produced when primary cosmic rays, typically protons, impinge on the Earth's atmosphere starting a particle cascade, in which secondary particles decay into muons (and muon neutrinos):

$$N + \text{air} \rightarrow \pi^\pm, K^\pm, (D^0, D^\pm, \Lambda_C \dots) \rightarrow \mu^\pm \begin{pmatrix} \nu \\ \bar{\nu} \end{pmatrix}_\mu$$

In the energy range up to ~ 100 GeV atmospheric muons come mostly from the decay of secondary pions. At higher energies, the kaon contribution to the muon flux increases, reaching the asymptotic value of $\sim 27\%$ at about 10 TeV [1]. The pion and kaon components constitute the *conventional* muon flux. At even higher energies, at $\mathcal{O}(100)$ TeV, also charmed hadron decays are expected to contribute (*prompt* muon component).

Atmospheric muon neutrinos share the mesonic origin with atmospheric muons, $\pi^\pm, K^\pm \rightarrow \mu^\pm \nu_\mu(\bar{\nu}_\mu)$, but the kaon and pion contributions are quite different due to the kinematics of their two-body decays. The muon carries most of the energy in pion decay ($m_\pi \gtrsim m_\mu$), so pions are the dominant parents for atmospheric muons (Fig. 1, left panel). Due to the different kaon decay phase space ($m_K \gg m_\mu$), kaons are more efficient than pions in producing neutrinos and their contribution is $\sim 80\%$ above $\mathcal{O}(1)$ TeV (Fig. 1, right panel).

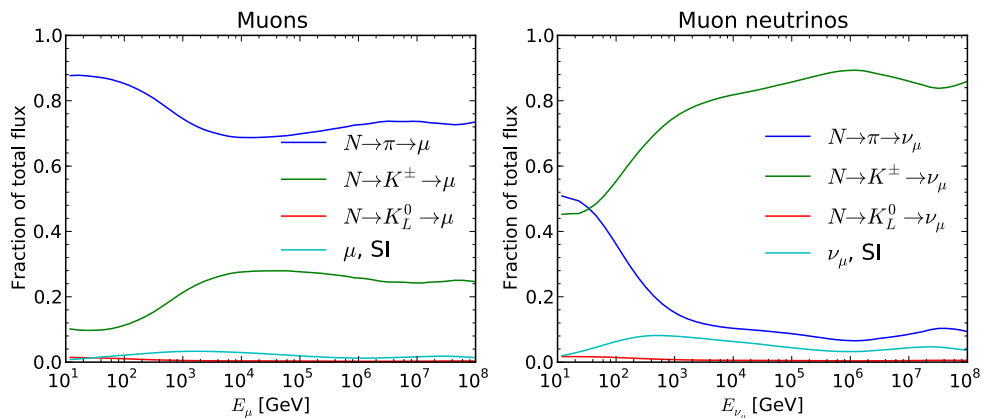


Figure 1: Conventional contributions to atmospheric muon and muon neutrino fluxes as a function of energy [2]. The steepness of the primary spectrum suppresses the contribution of secondary interactions (SI).

The results on the atmospheric muon spectrum and charge ratio are essential for a precise prediction of the atmospheric neutrino flux. This is needed both in the low energy range (from MeV to TeV) for detailed measurements of neutrino oscillations and mass hierarchy in atmospheric neutrino experiments and in the high energy range (from GeV to PeV) for background evaluation in the search for astrophysical neutrinos at neutrino telescopes. Moreover, the muon charge ratio in the TeV range allows to constrain the kaon production in a phase space inaccessible to collider and fixed target experiments, so it represents an important benchmark for neutrino flux calculations and the predicted $\nu_\mu/\bar{\nu}_\mu$ ratio.

In the following Secs. the key features of the atmospheric lepton flux parameterizations and charge ratio are recalled, then experimental results on the muon charge ratio in the TeV energy range are reviewed.

2 Inclusive production of atmospheric muons and neutrinos

The atmospheric leptons detected at the Earth's surface and underground are produced in the forward fragmentation region, with a large Feynman $x = E_{meson}/E_{nucleon} \approx E_{lepton}/E_{nucleon}$. Assuming scaling of particle production in the forward region, the inclusive fluxes of muons and muon neutrinos are well described by [1]

$$\Phi_l(E_l) = \frac{\Phi_N(E_l)}{1 - Z_{NN}} \sum_{i=1}^{N_{par}} \frac{a_{il} Z_{Ni}}{1 + b_{il} E_l \cos \theta^* / \varepsilon_i}$$

where $\Phi_N(E_l) \simeq \Phi_0 E_l^{-(\gamma+1)}$ is the spectrum of primary nucleons (evaluated at the lepton energy in the atmosphere E_l) with spectral index $\gamma + 1 \simeq 2.7$. The sum is over the contributions of lepton parents, i.e. charged pions, kaons, charmed particles, etc. The constants a_{il} and b_{il}

contain the kinematic factors for the i -th parent decay into lepton l . The critical energy $\varepsilon_i/\cos\theta^*$ is defined as the energy for meson i above which interaction processes dominate over decay, and θ^* is the zenith angle at the lepton production point.

The spectrum weighted moments for secondary particle production are defined as:

$$Z_{ij} = \frac{1}{\sigma_{ij}} \int_0^1 \frac{d\sigma_{ij}(x)}{dx} x^\gamma dx$$

where σ_{ij} is the inclusive cross-section for the production of a particle j from the collision of a particle i with a nucleus in the atmosphere and $x = E_j/E_i$ is the energy fraction carried by the secondary particle. In the scaling approximation the particle production depends only on x and not explicitly on the energy. The approximation is valid since it holds in the forward fragmentation region, which is enhanced by the x^γ weighting. Using the Z factors makes explicit that the particle production in cosmic ray cascades is concentrated in the forward fragmentation region at large x .

For each i -th contribution to the muon flux, at energies below the critical energy ε_i most mesons decay and the lepton flux follows the same power law of primary cosmic rays. For $E_\mu \gg \varepsilon_i(\theta)$, the meson interactions dominate, so the energy spectrum steepens by one power and the relative contribution is suppressed. Therefore each contribution to the muon charge ratio produced by different muon parents can be disentangled by studying the muon charge ratio as a function of the “vertical surface energy” $E_\mu \cos\theta^*$.

Considering only the conventional π and K parent mesons, the inclusive muon flux separated for μ^+ and μ^- is given by

$$\Phi_{\mu^\pm}(E_\mu) \propto \left(\frac{a_\pi Z_{N\pi^\pm}}{1 + b_{\pi\mu} E_\mu \cos\theta^*/\varepsilon_\pi} + \frac{a_K Z_{NK^\pm}}{1 + b_{K\mu} E_\mu \cos\theta^*/\varepsilon_K} \right)$$

The increasing kaon contribution to the muon flux in the range between 100 GeV and the TeV, $\varepsilon_\pi < E_\mu \cos\theta^* < \varepsilon_K$, is therefore explained by the two energy scales which determine the pion and kaon contributions, $\varepsilon_\pi \simeq 115$ GeV and $\varepsilon_K \simeq 850$ GeV.

These energies have to be compared with the corresponding value for charmed particles, $\varepsilon_X > 10^7$ GeV. The prompt muon component is therefore isotropically distributed since the corresponding $\cos\theta^*$ factor is suppressed, at least in the TeV region.

2.1 Parameterization of the muon charge ratio

The atmospheric muon charge ratio is larger than unity because the primary cosmic rays are mostly protons, favoring the production of π^+ and K^+ over π^- and K^- in the forward region. Each meson is likely to have an energy close to the one of the primary nucleon (high x_F) and comes from its fragmentation (valence quarks, majority of u), therefore the positive charge excess is preserved.

Considering the pion component, the isospin symmetry $Z_{p\pi^+} = Z_{n\pi^-}$ (i.e. the inclusive π^+ spectrum from protons is equal to the π^- spectrum from neutrons) allows expressing the pion contribution to the muon charge ratio in terms of the fraction of positive pions f_{π^+} , depending only on Z factors and the primary proton excess $\delta_0 = (p - n)/(p + n)$ [3]. Assuming Feynman scaling, the charge ratio does not depend on the energy E_μ nor E_π . The constant value of the muon charge ratio measured over the 10–100 GeV energy range, where almost only pion

contribute, is an experimental evidence of the validity of the Feynman scaling in the forward region, see Sec. 3.

The kaon component does not have the same isospin symmetry between positive and negative kaons. The associated production $N + \text{air} \rightarrow \Lambda K^+ (+ \text{anything})$, which has no analog for K^- , largely favors K^+ over K^- ($Z_{pK^+} \gg Z_{nK^-}$), therefore the K^+/K^- ratio is larger than the π^+/π^- ratio [1]. Hence the muon charge ratio increases with the increasing kaon contribution. An analytical description of the contributions in terms of δ_0 , f_{π^+} and kaon Z factors is given in Ref. [3], and used by the OPERA Collaboration to extract the Z_{pK^+} factor (see Sec. 3.1). The associated production process and Z_{pK^+} in particular cannot be constrained by accelerator experiments (high pseudo-rapidity regions), and the Monte Carlo predictions by various hadronic interaction generators differ up to several factors. This has a strong impact on the evaluation of the flux of TeV atmospheric neutrinos, which are dominated by kaon production.

Summarizing, in order to disentangle the different parent components to the muon flux (π , K , charm) the correct variable to describe the evolution of R_μ is the vertical surface energy $E_\mu \cos \theta^*$ [4], as seen in Sec. 2. This approach assumes a constant primary composition. If the energy dependence of the proton excess δ_0 in the primary cosmic rays is considered, the parameterization described in Ref. [3] should be used. Since δ_0 depends on the primary nucleon energy, which has an almost linear relation with the muon energy ($E_N \simeq 10 E_\mu$ for TeV muons [3]), the dependency on the surface muon energy E_μ and the zenith projection $\cos \theta$ should be considered separately, see Sec. 3.1.

3 Measurements of the atmospheric muon charge ratio

In the pion dominated energy region ($E_\mu \lesssim 100$ GeV), the muon charge ratio R_μ has been measured by several experiments on surface, by balloon-borne detectors and at shallow depths [5]. Its value is constant, $R_\mu \simeq 1.27$, as expected assuming the validity of Feynman scaling in the fragmentation region [1].

The increasing kaon contribution from a few hundred GeV to a few TeV causes a smooth transition to a higher value of the muon charge ratio, $R_\mu \simeq 1.38$. Recent results were presented by the CMS [6], MINOS [7, 8] and OPERA [9, 10] Collaborations in this energy range, around vertical surface energy $E_\mu \cos \theta^* \sim 1$ TeV. Underground experiments naturally select high energy down-going muons and the minimum energy threshold is fixed by the rock overburden surrounding the detector. The evaluation of the muon surface energy E_μ depends on the rock depth crossed by the muon coming from a particular direction and therefore the distribution of $E_\mu \cos \theta^*$ is related to the shape of the overburden.

Key elements for the accurate determination of the muon charge and momentum in the $\mathcal{O}(\text{TeV})$ energy range are magnetized detectors and large depth. MINOS and OPERA are long-baseline neutrino experiments located deep underground, while CMS is a collider experiment located at shallow depth but provided with an intense magnetic field. In the following Section the results from the OPERA experiment will be reviewed.

3.1 OPERA results

The OPERA experiment is a hybrid electronic detector/emulsion apparatus exposed to the CNGS neutrino beam from 2008 up to 2012. It is located in the underground Gran Sasso laboratory, at an average depth of 1400 m of rock corresponding to 3800 m.w.e. OPERA is

the deepest experiment able to measure charge-separated atmospheric muons. The minimum surface muon energy threshold is ~ 1 TeV (1.4 TeV averaged over all the directions and rock depths). The detector is composed of two identical parts, called supermodules, each consisting of a target section and a magnetic spectrometer. The target consists of scintillator strips interleaved with Emulsion Cloud Chambers, the spectrometer is a large dipole iron magnet instrumented with Resistive Plate Chambers. The magnetic field is almost uniform, with intensity 1.53 T, and directed along the vertical axis with opposite orientations in the two magnet arms. A muon crossing the spectrometer is deflected in the horizontal plane. The deflection is measured by six stations of vertical drift tubes, the Precision Trackers (PT), grouped in 3 pairs placed upstream of the first arm, in between the two arms and downstream of the second arm. The charge and momentum reconstruction is performed for tracks crossing at least one magnet arm using the angle $\Delta\phi$ in the bending plane, i.e. the difference between the track directions reconstructed by two PT stations before and after each magnet arm. For nearly horizontal muons up to four bending angles can be measured in the two dipole magnets.

Cosmic ray induced events in OPERA are reconstructed with a dedicated software procedure effective at identifying single and multiple muon tracks (*muon bundles*). Due to the charge-symmetry of the dipole magnet, the acceptance for μ^+ and μ^- is the same and, depending on the track topology, the maximum detectable momentum varies from a few hundred GeV/c up to 1 TeV/c [11, 10]. Data were collected with both magnetic field polarities in order to minimize systematic errors due to misalignment of PT stations.

OPERA reported a first measurement of the atmospheric muon charge ratio using the 2008 Run data [9] and the final results using the complete statistics from 2008 up to 2012 [10]. In the latter analysis the two data sets collected with opposite magnet polarities were combined reaching the most accurate measurement to date of R_μ in the TeV energy region. The muon charge ratio was computed separately for single muons, $R_\mu(n_\mu = 1) = 1.377 \pm 0.006$ (*stat.*) $^{+0.007}_{-0.001}$ (*syst.*), and for muon bundles, $R_\mu(n_\mu > 1) = 1.098 \pm 0.023$ (*stat.*) $^{+0.015}_{-0.013}$ (*syst.*). This is the first observation of a decrease in the charge ratio of high multiplicity events with respect to single muon events. The dilution effect in R_μ is expected since the multiple muon sample selects events generated by heavier primary cosmic rays and secondaries with a low value of Feynman- x_F , coming from the central region [11]. Recently also the MINOS Collaboration provided a measurement of the multiple-muon charge ratio, $R_\mu(n_\mu > 1) = 1.104 \pm 0.006$ (*stat.*) $^{+0.009}_{-0.010}$ (*syst.*) [12], in agreement with the OPERA result.

Thanks to the Gran Sasso orography, the amount of rock crossed by muons is not directly related to the zenith angle, and the high energy tail is not completely suppressed by the $\cos\theta$ factor. OPERA presented results on R_μ (for single muons) as a function of the vertical surface energy $E_\mu \cos\theta^*$, fitting data to the parameterized model described in Ref. [4]. The atmospheric muon charge ratio was measured in a large $E_\mu \cos\theta^*$ range, from 500 GeV up to ~ 10 TeV, and plotted in Fig. 2. With an average value $\langle E_\mu \cos\theta^* \rangle \simeq 2$ TeV, OPERA is the magnetized experiment measuring the charge ratio at the largest vertical surface energy. The fit of OPERA and L3+C data, shown in Fig. 2, yields the fractions of charged mesons decaying into positive muons $f_{\pi^+} = 0.5512 \pm 0.0014$ and $f_{K^+} = 0.705 \pm 0.014$. The prompt muon component does not significantly contribute to R_μ up to $E_\mu \cos\theta^* \lesssim 10$ TeV.

Taking into account the possible variation of the primary cosmic ray composition requires to disentangle the energy and zenith angle dependencies [3], as seen in Sec. 2.1. The fit in two dimensions ($E_\mu, \cos\theta^*$) yields the proton excess in primary cosmic rays $\delta_0 = (p - n)/(p + n) = 0.61 \pm 0.02$ at primary energy $\langle E_N \rangle \approx 20$ TeV/nucleon, and the spectrum weighted moment related to the associated kaon production, $Z_{pK^+} = 0.0086 \pm 0.0004$. The Z_{pK^+} factor, here

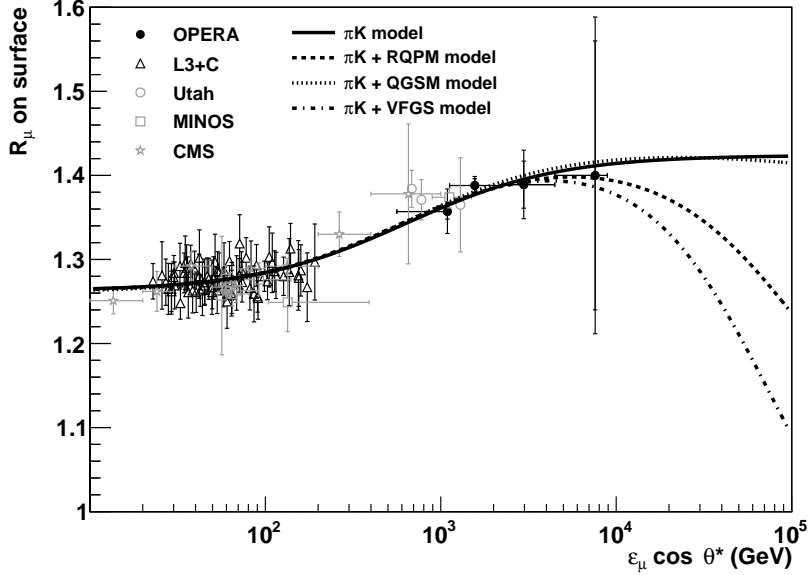


Figure 2: The atmospheric muon charge ratio measured by OPERA (*black points*) as a function of $E_\mu \cos \theta^*$. OPERA and L3+C data are fitted together and the fit result is shown by the continuous line [10]. Results from MINOS Near and Far Detectors [7, 8] and CMS [6] are also shown.

determined for the first time, allows to predict the atmospheric $\nu_\mu/\bar{\nu}_\mu$ ratio in the TeV range: the expected ratio for muon neutrinos increases from $\nu_\mu/\bar{\nu}_\mu \approx 1.5$ at low energy to ≈ 2.3 above a TeV [13].

4 Conclusions

The results on the atmospheric muon charge ratio from the OPERA, MINOS and CMS experiments show an increase of R_μ as a function of the vertical surface energy $E_\mu \cos \theta^*$ in the range between hundreds GeV and a few TeV. The measurements of OPERA in the TeV energy region are compatible with a simple parametric model where the rise is due to the increasing kaon contribution to the muon flux. No significant contribution from charm decay is observed up to energies ~ 10 TeV. A future experimental measurement of R_μ in the region $E_\mu \cos \theta^* > 10$ TeV, with a new detector at very large depths, could shed light on the prompt component even before the crossover between conventional and prompt muon fluxes.

The OPERA measurement of R_μ in the highest energy range to date allows to constrain the associated kaon production ΛK^+ in high energy primary interactions in the forward region. The result attains to a phase space inaccessible to accelerator experiments (high $x_F \leftrightarrow$ high pseudorapidity). It determined for the first time the spectrum weighted moment Z_{pK^+} , fundamental to accurately predict the atmospheric $\nu_\mu/\bar{\nu}_\mu$ ratio [13]. The Z_{pK^+} factor was extracted together with the primary proton excess δ_0 , which is consistent with direct measurements of the primary

composition [3]. The energy behaviour of R_μ measured by OPERA above a few TeV, compatible with the plateau corresponding to the asymptotic kaon contribution, supports the validity of Feynman scaling in the fragmentation region up to primary energies/nucleon around 200 TeV.

References

- [1] T.K. Gaisser, *Cosmic Rays and Particle Physics* (Cambridge University Press, Cambridge, 1990)
- [2] A. Fedynitch, LHC-CR Workshop: Results and prospects of forward physics at the LHC (2013)
- [3] T.K. Gaisser, *Astropart. Phys.* **35**, 801 (2012)
- [4] P.A. Schreiner, J. Reichenbacher, M.C. Goodman, *Astropart. Phys.* **32** (1), 61 (2009)
- [5] T. Hebbeker and C. Timmermans, *Astropart. Phys.* **18**, 107 (2002)
- [6] CMS Collaboration, *Phys. Lett. B* **692**, 83 (2010)
- [7] P. Adamson et al. (MINOS Collaboration), *Phys. Rev. D* **76**, 052003 (2007)
- [8] P. Adamson et al. (MINOS Collaboration), *Phys. Rev. D* **83**, 032011 (2011)
- [9] N. Agafonova et al. (OPERA Collaboration), *Eur. Phys. J. C* **67**, 25 (2010)
- [10] N. Agafonova et al. (OPERA Collaboration), *Eur. Phys. J. C* **74**, 2933 (2014)
- [11] N. Mauri, Ph.D. Thesis, Università di Bologna (2011)
http://inspirehep.net/record/1393857/files/phd_thesis-BO-2011_05_20-mauri.pdf
- [12] P. Adamson et al. (MINOS Collaboration), *Phys. Rev. D* **93**, 052017 (2016)
- [13] T.K. Gaisser, *EPJ Web of Conf.* **99**, 05002 (2015)

A Search for Lorentz and CPT Violation Using the T2K Near Detectors

Gary Alexander Clifton¹

¹Colorado State University, Fort Collins, Colorado USA

DOI: <http://dx.doi.org/10.3204/DESY-PROC-2016-05/36>

Lorentz symmetry violation (LV) arises when the behavior of a particle depends on its direction or boost velocity. The Standard Model Extension (SME) is a general theoretical framework that includes both General Relativity and the Standard Model while also allowing for the breaking of particle Lorentz symmetry through a set of controlling coefficients. A search for LV at the T2K near detectors with baselines of 280 m is described. The protons-on-target normalized neutrino event rate at the T2K near detectors is used to search for LV using a shape-only analysis via Fast Fourier Transform (FFT) analysis and a binned log-likelihood fit. No indication of LV is observed with either method in the T2K near detector data.

1 Conventional Neutrino Oscillations

For non-interacting neutrinos, the Hamiltonian eigenstates are the mass eigenstates and the mixing matrix is then equated to the Pontecorvo, Maki, Nakagawa, and Sakata (PMNS) matrix. The PMNS matrix may be parameterized with three mixing angles ($\theta_{12}, \theta_{23}, \theta_{13}$) and one complex phase factor (δ_{CP}). The probability of neutrino flavor oscillation in natural units is

$$P_{\nu_\alpha \rightarrow \nu_\beta}(L) = \delta_{\alpha\beta} - 4 \sum_{i>j} \text{Re}(U_{\alpha i}^* U_{\beta i} U_{\alpha j} U_{\beta j}^*) \sin^2\left(\frac{\Delta m_{ij}^2}{4E} L\right) + 2 \sum_{i>j} \text{Im}(U_{\alpha i}^* U_{\beta i} U_{\alpha j} U_{\beta j}^*) \sin\left(\frac{\Delta m_{ij}^2}{2E} L\right) \quad (1)$$

where

$$\Delta m_{ij}^2 = m_i^2 - m_j^2 \quad (2)$$

is the mass-squared splitting, $U_{\gamma k}$ are the elements of the PMNS matrix, L is the baseline of the neutrino experiment, and E is the neutrino energy. Thus, conventionally, neutrino oscillations are driven by a unique neutrino mass.

2 T2K Experiment

T2K utilizes a 2.5° off-axis neutrino beam for optimal detection of ν_e appearance at a peak neutrino energy of 0.6 GeV with a baseline of 295km at the Super Kamiokande far detector.

The experiment consists of a ν_μ beam produced at the JPARC facility in Tokai, Japan, near detector site, and a far detector site. An on-axis near detector, called the interactive neutrino grid (INGRID), monitors the beam stability and intensity while the off-axis near detector, called the near detector at 280m (ND280), is used to study neutrino interactions for different nuclear targets as well as study neutrino kinematics. Both near detectors are located at 280m from the graphite target used to create the T2K neutrino beam.

2.1 INGRID

INGRID was designed to measure the beam intensity and direction by utilizing neutrino interactions on iron [1] and lies on axis at 280m from the graphite target [2]. INGRID is arranged in a cross configuration with 14 identical modules [4] to detect neutrino interactions from the beam. In addition to these 14 modules, two shoulder modules exist to check the axial symmetry of the neutrino beam. Each module consists of alternating layers of scintillator and iron plates. In each module, there are 11 scintillator tracking planes that consist of 24 horizontal and 24 vertical scintillator bars glued together.

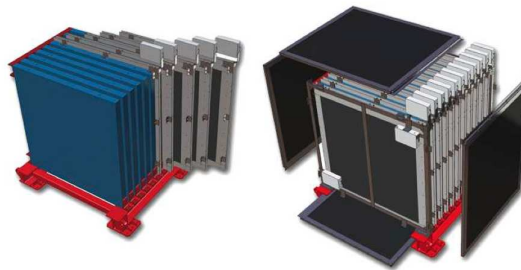


Figure 1: A diagram showing the layout of an INGRID module.

2.2 ND280

ND280 was designed to perform several measurements [2]:

1. Measure the neutrino flux and energy from the beam
2. Measure the inherent ν_e contamination of the beam
3. Measure neutrino event rates

It is a composite detector encased in the UA1 dipole magnet. The π^0 detector, or P0D, [7] was constructed to measure the following neutral current interaction on a water target:

$$\nu_\mu + N \rightarrow \nu_\mu + N + \pi^0 + X \quad (3)$$

Downstream of the P0D are three time projection chambers (TPCs). The TPCs measure the charge, momentum, and particle types of the different charged particles that are produced in neutrino interactions below a few GeV [2]. Each TPC consists of an inner and outer box [9]. The inner box contains an argon gas mixture for charged particles to ionize during their interactions.

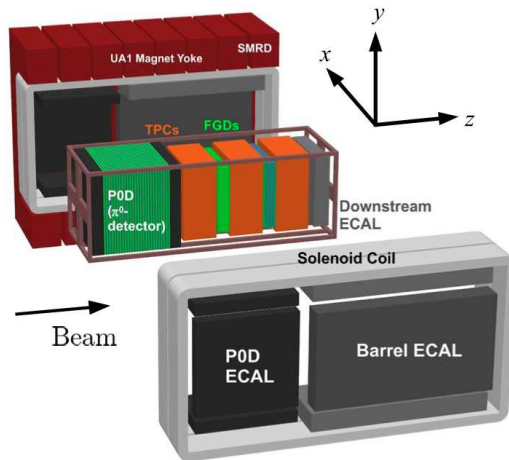


Figure 2: A blowout diagram of ND280 showing the different sub-detectors.

The outer box contains a CO_2 atmosphere which provides electrical insulation between the inner box and ground while also keeping atmospheric oxygen from entering the inner box. In addition to the P0D, two Fine Grained Detectors (FGD) were installed to provide a target for studying neutrino interactions as well as tracking of charged particles [8]. Each FGD consists of finely segmented scintillator bars arranged in X and Y planes. The electromagnetic calorimeters (ECals) of ND280 are sampling calorimeters located inside the magnet yokes and enclose the various subdetectors of ND280 (P0D, TPCs, FGDs). The ECals serve to measure the energy and direction of charged particles that exit the sides of the ND280 subdetectors in order to identify particle types [5]. Each ECAL module consists of alternating layers of scintillator bars and lead sheets. The Side Muon Range Detector (SMRD) system is located between the air gaps in each magnet yoke and uses scintillator planes to detect high angle muons that escape ND280 with respect to the beam line and measure their momentum [6].

3 The Standard Model Extension

The Standard Model Extension (SME) is a general theoretical framework conceived to facilitate experimental investigations of LV and CPT violation (CPTV) [3]. It is an effective field theory that contains General Relativity, the Standard Model, and all possible Lorentz violating operators. The SME allows for the breaking of Particle Lorentz symmetry which produces a tensor background field that permeates throughout the universe. Neutrinos couple to this background field with some given strength and the physics that the SME predicts becomes dependent, for example, on the absolute direction of neutrino propagation. This dependency can produce a number of effects, namely sidereal variations. LV is controlled by a set of coefficients which experiments may measure while working in the sun centered inertial frame. The probability of oscillation in the SME at short baselines is given by

$$P(\nu_\mu \rightarrow \nu_x) = L^2 |\mathcal{C}_{\mu x} + (\mathcal{A}_s)_{\mu x} \sin(\omega_\oplus T_\oplus) + (\mathcal{A}_c)_{\mu x} \cos(\omega_\oplus T_\oplus) + (\mathcal{B}_s)_{\mu x} \sin(2\omega_\oplus T_\oplus) + (\mathcal{B}_c)_{\mu x} \cos(2\omega_\oplus T_\oplus)|^2 \quad (4)$$

where ω_\oplus is the Earth's sidereal frequency and T_\oplus is the sidereal time of the neutrino event in the detector. The various amplitudes associated with each sidereal time harmonic consist of the SME coefficients $(a_L)_{\mu x}^\alpha$ and $(c_L)_{\mu x}^{\alpha\beta}$, the neutrino energy E , and geographical information about how the neutrino beam is setup on Earth. Thus, in the SME, neutrino oscillations vary with sidereal time producing a sidereal variation in the neutrino event rate at a given detector.

4 LV Analysis

To perform a LV search at the T2K near detectors, T2K data taken from 2010 to 2013 is used. This data was taken in various T2K data run periods throughout this time. For INGRID, all the data is combined into a single data sample, while for ND280 since the POD can be configured with or without water, two data samples are used corresponding to each configuration of the POD. The POT normalized neutrino event rate as a function of Local Sidereal Phase (LSP) for each data set is shown in Figures 3.

$$LSP = \text{mod}\left(\frac{T_\oplus}{23^h 56^m 4.0916^s}\right) \quad (5)$$

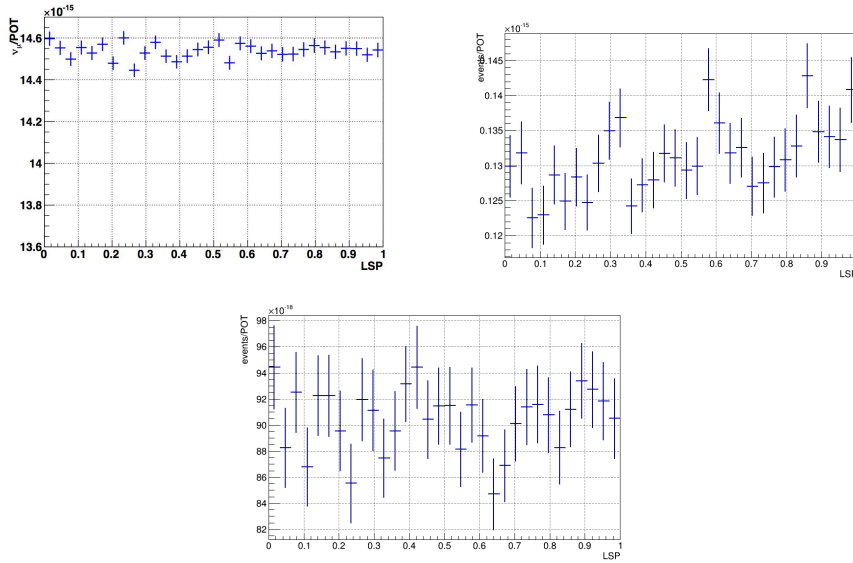


Figure 3: Corrected ν_μ event rate versus LSP in INGRID (top left), ND280 water-in (top right), and ND280 water-out (bottom).

Each data set consists of 32 LSP bins to avoid aliasing effects in the Fast Fourier Transform method (described below). Each data sample was analyzed for various sources of systematic

uncertainty that could mimic a LV signal. All sources of systematic error were found to be negligible compared to statistical uncertainty and corrections were calculated for each source and applied to the data.

The analysis is broken up into two parts: a Fast Fourier Transform (FFT) method and a binned likelihood fit method. The FFT method is applied to both INGRID and ND280 data while only the INGRID data is used to perform the binned likelihood fit as it is a significantly higher statistical sample.

4.1 Fast Fourier Transform Method

A set of 10,000 data-driven toy experiments is created for which any potential LV signal is removed by randomizing the various LSP bins for a given sample based off the total number of beam spills in that sample. An example is shown in Figure 4.

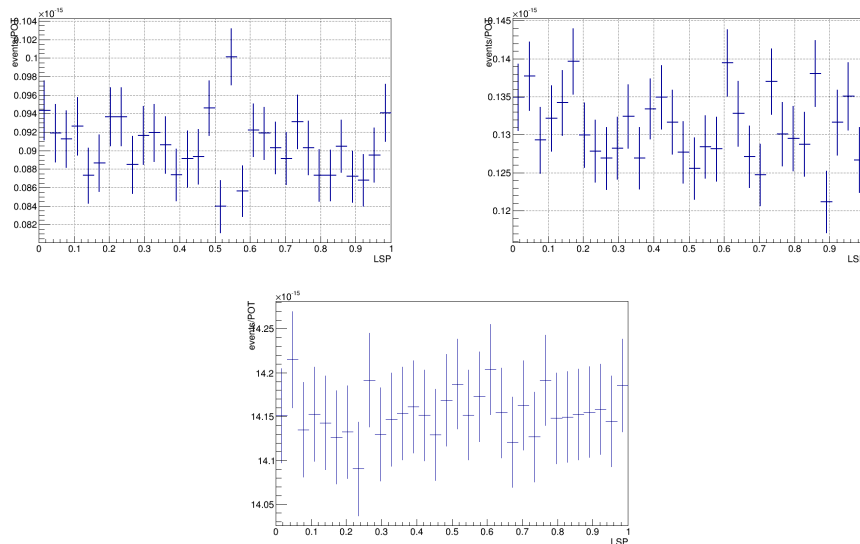


Figure 4: Examples of a ND280 flat toy MC for the water-in and water-out samples (left, middle) and an INGRID flat toy MC (right).

For a given detector, each toy is passed to a FFT tool which calculates the magnitude of the FFT. As such, a distribution of magnitude values for a given Fourier mode can be created for each detector. Such a distribution is shown in Figure 5. A 99.7% confidence level hypothesis test is performed to determine the significance of the FFT values in data. An overall detection threshold is calculated from the Fourier mode distributions of each Fourier mode as the largest detection threshold. A p-value is calculated utilizing the value observed in data, the Fourier mode distributions, and the total number of MC.

The corrected INGRID, ND280 water-in, an ND280 water-out ν_μ event rate as a function of LSP was analyzed with the method described above. The results of the FFT analysis can be

seen in Figure 6, Table 1, Table 2, and Table 3. The Fourier modes of interest to this analysis are below the 3σ detection threshold.

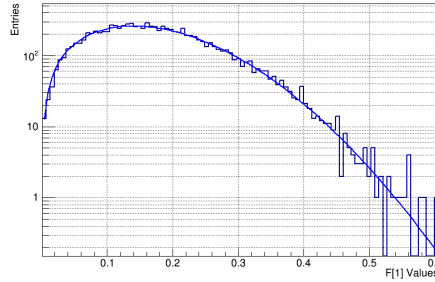


Figure 5: Distribution of the magnitude of the first Fourier mode for the 10,000 flat toy experiments of ND280 water-out. The distribution is fitted with a Rayleigh function.

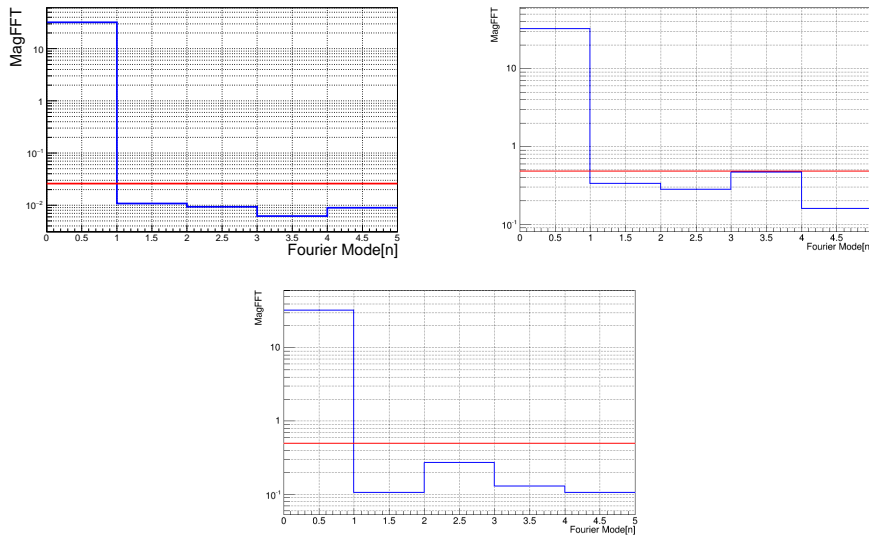


Figure 6: Magnitude of each Fourier mode in case of INGRID data (left), ND280 water-in (middle) data, and water-out (right) data after all corrections. The red horizontal line corresponds to the overall 3σ detection threshold.

A SEARCH FOR LORENTZ AND CPT VIOLATION USING THE T2K NEAR DETECTORS

Fourier Mode	Threshold	Magnitude	p-value
1	0.026	0.01076	0.35
2	0.026	0.00930	0.48
3	0.026	0.00620	0.69
4	0.026	0.00893	0.51

Table 1: FFT results for INGRID.

Fourier Mode	Threshold	Magnitude	p-value
1	0.4765	0.33537	0.055
2	0.4765	0.28221	0.126
3	0.4765	0.46355	0.004
4	0.4765	0.15999	0.511

Table 2: FFT results for ND280 water-in.

Fourier Mode	Threshold	Magnitude	p-value
1	0.4947	0.10501	0.765
2	0.4947	0.26948	0.162
3	0.4947	0.12856	0.659
4	0.4947	0.10649	0.751

Table 3: FFT results for ND280 water-out.

While the third Fourier mode p-value in the water-in sample is larger than the significance (0.003), it is still very close to it. If this were truly a LV effect in this data sample, this effect is expected to appear in the other samples. Since it does not, this affect is attributed to a statistical fluctuation. Thus, it is concluded that the INGRID, ND280 water-in, and ND280 water-out data are consistent with no sidereal variation in the relevant Fourier modes using the FFT analysis method. 99.7%C.L. upper limits on the SME coefficients may be extracted for the each sample utilizing the following procedure:

1. Set all but one SME coefficient to zero
2. Increase the size of the SME coefficient in a set of 10,000 signal toy Monte-Carlo until the nominal threshold has been crossed
3. Take the corresponding value of the coefficient as the upper limit

The 99.7%C.L. upper limits of the SME coefficients in each sample using this procedure are shown in Table 4.

Coefficient	ND280 Water-in	ND280 Water-out	INGRID
a_L^T	-	-	-
a_L^X	15.7 GeV	15.4 GeV	4.8 GeV
a_L^Y	16.3 GeV	17.4 GeV	4.8 GeV
a_L^Z	-	-	-
c_L^{TT}	-	-	-
c_L^{TX}	13.9	10.8	0.9
c_L^{TY}	13.9	13.0	0.9
c_L^{TZ}	-	-	-
c_L^{XX}	54.0	57.0	3.8
c_L^{XY}	25.0	25.0	1.6
c_L^{XZ}	-	-	3.1
c_L^{YY}	54.0	57.0	3.8
c_L^{YZ}	-	-	3.1
c_L^{ZZ}	-	-	-

Table 4: Standard Model Extension 3σ upper limits on SME coefficients related to $\nu_\mu \rightarrow \nu_e$ oscillation, for ND280 water-in and water-out, and INGRID (all values given in $\times 10^{-20}$).

4.2 Binned Likelihood Method

Due to the large degree of correlation, a five coefficient binned likelihood fit was developed instead of a full fourteen-coefficient to extract limits on the SME coefficients. The five coefficients are the amplitudes associated with each sidereal time harmonic in Equation 4. A binning of 32 bins in LSP was chosen for the likelihood fit, just as in the FFT method. For each LSP bin, the statistical errors are assumed to be Gaussian and the likelihood may be constructed as:

$$L = \prod_{i=1}^{32} e^{-\frac{(d_i - m_i)^2}{2\sigma_i^2}} \quad (6)$$

where, d_i and m_i are the POT normalized number of events in the i^{th} LSP bin for data and toy MC respectively, and

$$\sigma_i = \frac{N_{\nu_\mu}}{N_{\text{POT}}} \sqrt{\frac{\delta N_{\nu_\mu}^2}{N_{\nu_\mu}^2} + \frac{\delta N_{\text{POT}}^2}{N_{\text{POT}}^2}}, \quad (7)$$

with N_{ν_μ} and N_{POT} being, respectively, the number of neutrino events and the number of protons on target in LSP bin i , with δN_{ν_μ} and δN_{POT} the corresponding statistical errors. The fitter was run over the corrected INGRID data. Table 5 shows the best fit values for each coefficient.

	$(\mathcal{C})_{ab}$	$(\mathcal{A}_s)_{ab}$	$(\mathcal{A}_c)_{ab}$	$(\mathcal{B}_s)_{ab}$	$(\mathcal{B}_c)_{ab}$
Best fit (10^{-20} GeV)	$-0.61^{+2.63}_{-1.41}$	$0.38^{+1.83}_{-2.60}$	$-1.55^{+4.55}_{-1.44}$	$0.06^{+0.87}_{-1.00}$	$0.38^{+0.80}_{-1.57}$

Table 5: Best fit values with 1σ errors, and 2σ upper limit values on the different Standard Model Extension coefficients using the likelihood method.

All limits set by INGRID are consistent with zero (i.e. no LV) to 1σ .

5 Summary

The near detectors of T2K were used to search for indications of LV in the neutrino data. The two methods utilized (FFT method and binned likelihood fit) show that all data sets used are consistent with the null hypothesis, namely, no sidereal variations. Figure 7 compares the results using the FFT method of INGRID and ND280 with MiniBooNE and MINOS (left) and the results of the likelihood method for INGRID and MiniBooNE (right). For the likelihood, all limits set by INGRID are consistent with no LV to 1σ . $(\mathcal{B}_s)_{ab}$ and $(\mathcal{B}_c)_{ab}$ have now been constrained in INGRID as they previously were not.

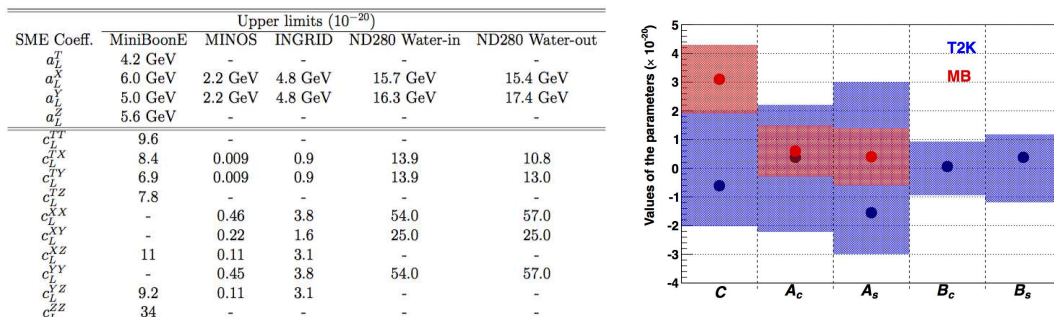


Figure 7: Comparison of SME Coefficients associated with ν_e appearance INGRID and ND280 with other experiments using the FFT method (left) and comparison between the T2K (blue) and MiniBooNE (red) best fit values and 1σ limits (right).

It should be stressed that this level of precision is still very valuable to theorists. T2K probes a different direction in the Sun-centered reference frame, and thus samples a different portion of the coefficient space. This information helps theorist improve their theories so that experimentalists may continue to test them.

6 Acknowledgements

I thank the J-PARC team for the superb accelerator performance and CERN NA61 colleagues for providing particle production data. I acknowledge the support of the US Department of Energy for my research. Finally, I want to thank the organizers of the Magellan Workshop for giving me the opportunity to present.

References

- [1] T. Le *et al.* Overview of the T2K long baseline neutrino oscillation experiment, Proceedings of the DPF-2009 Conference (2009).
- [2] K. Abe *et al.* Nuclear Instruments and Methods in Physics **69** 106 (2011).
- [3] D. Colladay, A. Kostelecky Phys. Rev. D. **58** 116002 (1998).
- [4] K. Abe *et al.* Nuclear Instruments and Methods in Physics. "Measurements of the T2K neutrino beam properties using the INGRID on-axis near detector" **A694** (2012).

- [5] D Allan *et al.* JINST. "The Electromagnetic Calorimeter for the T2K Near Detector ND280" **8** (2013).
- [6] S. Aoki *et al.* Nuclear Instruments and Methods in Physics. "The T2K Side Muon Range Detector" **A698** (2013).
- [7] S. Assylbekov *et al.* Nuclear Instruments and Methods in Physics. "The T2K ND280 Off-Axis Pi-Zero Detector" **A686** (2012).
- [8] P.-A. Amaudruz *et al.* Nuclear Instruments and Methods in Physics. "The T2K Fine-Grained Detectors" **A696** (2012).
- [9] N. Abgrall *et al.* Nuclear Instruments and Methods in Physics. "Time Projection Chambers for the T2K Near Detectors" **A637** (2011).

Searching for neutrino oscillation parameters in long baseline experiments

Sampsa Vihonen

University of Jyväskylä, Department of Physics, P.O. Box 35, FI-40014 University of Jyväskylä, Finland

DOI: <http://dx.doi.org/10.3204/DESY-PROC-2016-05/8>

Developing neutrino astronomy requires a good understanding of the neutrino oscillations mechanism. The European strategy for neutrino oscillation physics sets a high priority on future long baseline neutrino experiments with the aim to measure the intrinsic parameters that govern the neutrino oscillations. In this talk we take a look at the next generation of long baseline experiments and discuss their prospects in future research.

1 Introduction

The dream of using neutrino telescopes as messengers of the universe in the future is built on the idea that the neutrino oscillation mechanism is eventually resolved in the neutrino oscillation experiments. The prospects of these experiments include both determining the parameters of the standard three-neutrino paradigm and probing non-standard interactions (NSI) that may follow from potential Beyond Standard Model theories.

Neutrino oscillation experiments are typically categorized into solar, reactor, atmospheric and accelerator-based experiments. In this work we focus on long baseline neutrino experiments where an intense muon neutrino beam is directed to traverse long distances underground.

In the Standard Model of particle physics (SM) neutrino sector the relationship between the three neutrino mass states (ν_1, ν_2, ν_3) and the three flavour states (ν_e, ν_μ, ν_τ) is usually expressed as a 3×3 matrix known as the PMNS matrix after Bruno Pontecorvo, Ziro Maki, Masami Nakagawa and Shoichi Sakata. The mixing of neutrino states is the source to the phenomenon that is known as neutrino oscillations. The PMNS matrix can be written in terms of the three mixing angles and one phase in the form:

$$U = \begin{pmatrix} 1 & 0 & 0 \\ 0 & c_{23} & s_{23} \\ 0 & -s_{23} & c_{23} \end{pmatrix} \begin{pmatrix} c_{13} & 0 & s_{13}e^{-i\delta_{CP}} \\ 0 & 1 & 0 \\ -s_{13}e^{i\delta_{CP}} & 0 & c_{13} \end{pmatrix} \begin{pmatrix} c_{12} & s_{12} & 0 \\ -s_{12} & c_{12} & 0 \\ 0 & 0 & 1 \end{pmatrix} \times \text{diag}(e^{i\alpha_1/2}, e^{i\alpha_2/2}, 1) \quad (1)$$

where $s_{ij} = \sin \theta_{ij}$ and $c_{ij} = \cos \theta_{ij}$ for $i, j = 1, 2, 3$, $\theta_{ij} = [0, \pi/2]$ are the intrinsic mixing angles, $\delta_{CP} = [0, 2\pi]$ is the Dirac CP violation phase and α_1, α_2 are two Majorana CP violation phases.

The transition probability between two neutrino flavour states $\nu_l \rightarrow \nu_{l'}$ is calculated as:

$$P_{ll'} = \sum_{j,k} U_{lj}^* U_{l'j} U_{lk} U_{l'k}^* e^{-iL\Delta m_{jk}^2/2E}, \quad (2)$$

where L is the baseline length of the experiment and E is the energy of the neutrino produced. Here neutrino mass squared differences $\Delta m_{jk}^2 = m_j^2 - m_k^2$ for $j, k = 1, 2, 3$ are calculated from the neutrino masses m_1, m_2 and m_3 .

The expression in Equation (2) can be further simplified into

$$P_{ll'} = \delta_{ll'} - \sum_{j,k;j>k} \left[4 \sin^2 \Delta_{kj} \operatorname{Re} W_{ll'}^{jk} - 2 \sin 2\Delta_{kj} \operatorname{Im} W_{ll'}^{jk} \right], \quad (3)$$

where $W_{ll'}^{jk} = U_{lj}^* U_{l'j} U_{lk} U_{l'k}^*$ and $\Delta_{kj} = \Delta m_{kj}^2 L/4E$. It is seen from expression (3) that the oscillation probabilities can be tuned to desirable values by choosing L/E conveniently.

In this paper, we analyze the potential of the planned long baseline neutrino oscillation experiment LBNO at two tasks. On the one hand we study its performance for resolving the intrinsic θ_{23} octant degeneracy and on the other hand we study its ability to probe the matter NSI effects. That is, we derive numerically the values of θ_{23} for which the octant degeneracy can be resolved and also calculate the new upper bounds that LBNO could give to $|\varepsilon_{\alpha\beta}^m|$ where $\alpha, \beta = e, \mu, \tau$.

2 Oscillation parameters: A general outlook

The present values of the oscillation parameters are given in Table 1. The values of the reactor and solar mixing angles (θ_{13} and θ_{12} respectively) have been determined in previous neutrino experiments with good precision, but the value of the atmospheric mixing angle θ_{23} has yet to be determined accurately. The other unknown quantities are the sign of Δm_{31}^2 and the amount of CP violation δ_{CP} in the leptonic sector.

Parameter	Value
θ_{12}	31.8° ... 37.8°
θ_{13}	7.7° ... 9.9°
θ_{23}	38.8° ... 53.3°
Δm_{21}^2	$(7.11 \dots 8.18) \cdot 10^{-5} \text{eV}^2$
$ \Delta m_{31}^2 $	$(2.20 \dots 2.65) \cdot 10^{-3} \text{eV}^2$
δ_{CP}	0 ... 360°

Table 1: Standard neutrino oscillation parameters [1]. For the unknown δ_{CP} we have denoted the values considered in numerical calculations, and the extra phases $\alpha_{1,2}$ only come into play in double-beta decay experiments.

3 Simulation of long baseline neutrino experiments

In LBNO the aim is to send neutrino and antineutrino beams, produced at the CERN SPS accelerator, towards the Pyhäsalmi mine, located in central Finland at the distance 2288 km from CERN, where they will be measured using a two-phase Liquid Argon Time Projection Chamber (LArTPC) combined with a magnetized muon detector (MIND). In this experiment, the size of the LArTPC detector is planned to have 20 kton fiducial mass. In this phase a 0.75 MW conventional neutrino beam from the CERN SPS will be used. In this work we also study LBNO with other baseline lengths.

The analysis is done by using the GLOBES simulation software [2, 3]. GLOBES calculates the oscillation probabilities and the corresponding neutrino rates for any given set of oscillation parameter values. The standard set of the software simulates the neutrino propagation from source to detector and computes the standard matter interactions (SI) for the distance that neutrinos travel. A software extension then allows us to perform the same calculation but may also include all matter-induced NSI effects in the propagation. The software computes χ^2 distributions to compare different sets of oscillation parameter values, both with SI and NSI.

We will determine for both mass hierarchies the 1σ , 2σ and 3σ sensitivity limit of the angle θ_{23} that LBNO can achieve with 5+5 –years neutrino and antineutrino run, allowing the CP phase to vary in the range 180° to $+180^\circ$. We will also determine the new 90% confidence level upper bounds that LBNO could set to the absolute values of $\varepsilon_{\alpha\beta}^m$ parameters that describe the strength of non-standard interactions between neutrinos and the matter.

4 Determination of the θ_{23} octant

In long baseline experiments one is interested mainly in the oscillation channels $\nu_\mu \rightarrow \nu_\mu$ (disappearance channel) and $\nu_\mu \rightarrow \nu_e$ (appearance channel). In leading order, whereby omitting terms proportional to the small quantities $\Delta m_{21}^2/\Delta m_{31}^2$ and $\sin\theta_{13}$, the θ_{23} dependence of the oscillation probability $P_{\mu\mu}$ is of the form $\sin^2 2\theta_{23} \sin^2 \Delta$ where $\Delta = \Delta m_{31}^2 L/4E$. Since

$$P_{\mu\mu}(90^\circ - \theta_{23}) = P_{\mu\mu}(90^\circ), \quad (4)$$

the measurements of the channel $\nu_\mu \rightarrow \nu_\mu$ are not suitable for resolving the octant degeneracy. There are non-leading terms that are sensitive to the octant but they are typically too much suppressed to be useful.

In a future long baseline neutrino experiment this problem with θ_{23} octants is resolved by studying the electron appearance from $\nu_\mu \rightarrow \nu_e$ oscillations. The leading term of $P_{\mu e}$ has a dependence on θ_{23} that is not octant degenerate, and hence the $\nu_\mu \rightarrow \nu_e$ oscillations bring in the primary component to the determination of θ_{23} octant.

Using the GLOBES software, we simulated the hypothetical experiment that was described in the LBNO design study (see [4] for more details).

The results are presented in Figure 1. In both panels the white regions in the plots are the areas for which the values of θ_{23} , δ_{CP} can be established with a confidence level greater than 3σ . So for all θ_{23} , δ_{CP} data points in these areas, one can eliminate with a confidence level larger than 3 the possibility for these parameters to lie in the other octant. Conversely the coloured regions illustrate the cases where no such distinction is possible with the indicated confidence level.

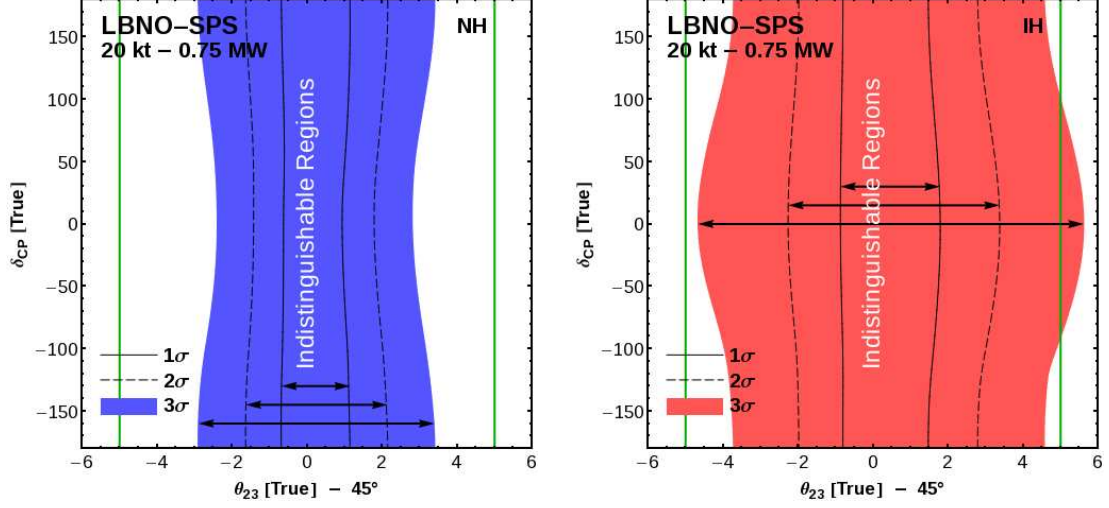


Figure 1: Determination ability of the θ_{23} octant in LBNO [4] in normal hierarchy mode.

In Figure 1 we have also marked the MINOS favoured θ_{23} values 40° and 50° by green lines. It is seen that for this particular setup the right θ_{23} octant can be asserted in NH with at least 3σ confidence level. As for IH this limit is reached for the lower octant, but for the higher octant it fails to be reached for δ_{CP} values between -100° and $+100^\circ$.

5 Constraining non-standard interaction parameters

In the low-energy regime, NSI can be parametrized in terms of effective charged current like (CC) and neutral current like (NC) Lagrangians, given respectively by

$$\begin{aligned}\mathcal{L}_{NSI}^{CC} &= -2\sqrt{2}G_F\varepsilon_{\alpha\beta}^{ff',C}(\bar{\nu}_\alpha\gamma^\mu P_L\ell_\beta)(\bar{f}\gamma^\mu P_C f'), \\ \mathcal{L}_{NSI}^{NC} &= -2\sqrt{2}G_F\varepsilon_{\alpha\beta}^{f,C}(\bar{\nu}_\alpha\gamma^\mu P_L\nu_\beta)(\bar{f}\gamma^\mu P_C f).\end{aligned}\quad (5)$$

Here f and f' label charged leptons or quarks ($\ell_i, u_i, d_i, i = 1, 2, 3$), $G_F = 1.166 \times 10^{-5}\text{GeV}^{-2}$ is the Fermi coupling constant, α, β refer to neutrino flavour (e, μ, τ), and $C = L, R$ refers to the chirality structure of the charged lepton interaction, P_L and P_R being the chiral projection operators. The NSI parameters $\varepsilon_{\alpha\beta}^{ff',C}$ and $\varepsilon_{\alpha\beta}^{f,C}$ are dimensionless numbers. It is assumed here that the effective non-standard interactions have V-A Lorentz structure, and for the charged fermions we allow both left-handed ($P_C = P_L$) and right-handed ($P_C = P_R$) couplings. The charged current Lagrangian \mathcal{L}_{NSI}^{CC} is relevant for the NSI effects in the source and detector, since both in the creation and detection processes involve charged fermions. The neutral current Lagrangian \mathcal{L}_{NSI}^{NC} in turn is relevant for the NSI matter effects. The effective low-energy Lagrangians (5) are assumed to follow from some unspecified beyond-the-standard-model theory after integrating out heavy degrees of freedom.

Concerning the propagation in matter, NSI could contribute to the coherent forward scattering of neutrinos in the Earth's crust. The effective Hamiltonian describing the time evolution of a neutrino state would take the form

$$H = \frac{1}{2E_\nu} \left[U \begin{pmatrix} 0 & 0 & 0 \\ 0 & \Delta m_{21}^2 & 0 \\ 0 & 0 & \Delta m_{31}^2 \end{pmatrix} U^\dagger + V \right] \quad (6)$$

where E_ν is the energy neutrino, U is the ordinary mixing matrix and V is the effective matter potential which includes both the SM and NSI matter effects:

$$V = A \begin{pmatrix} 1 + \varepsilon_{ee}^m & \varepsilon_{e\mu}^m & \varepsilon_{e\tau}^m \\ \varepsilon_{e\mu}^{m*} & \varepsilon_{\mu\mu}^m & \varepsilon_{\mu\tau}^m \\ \varepsilon_{e\tau}^{m*} & \varepsilon_{\mu\tau}^{m*} & \varepsilon_{\tau\tau}^m \end{pmatrix}. \quad (7)$$

We study numerically how the future neutrino oscillation experiments would constrain various NSI parameters. We will concentrate here on the future long baseline neutrino experiments, using the LBNO setup with a high-intensity beam, a baseline of 2300 km and 20 kt double-phase liquid argon detector as our benchmark. For each δ_{CP} value, we have calculated the 90% confidence level contour baseline range 100–5000 km and $\log_{10} |\varepsilon_{\alpha\beta}^m|$ range from 3.0 to 0.5. In every case, a 90% confidence level contour is found and the results merged in a contour band. The bands in $(L, \varepsilon_{\alpha\beta}^m)$ -plane are plotted in Figure 2.

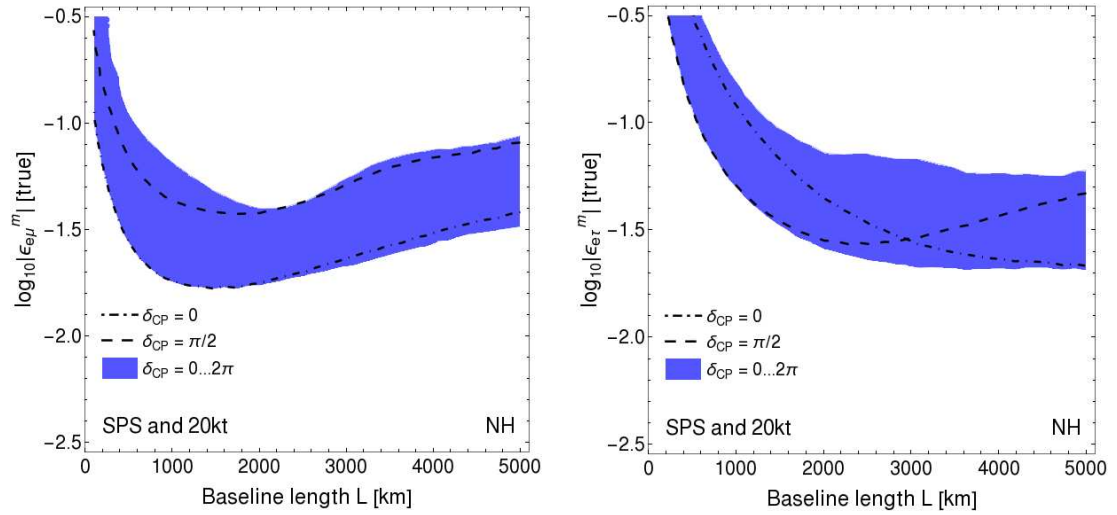


Figure 2: Constraining capability of LBNO for the absolute values of the non-standard interaction parameters $\varepsilon_{e\mu}^m$ and $\varepsilon_{e\tau}^m$. See Reference [5] for more details.

6 Summary

In this work we have presented the measurement potential of a potential future long baseline neutrino experiment in the determination of the θ_{23} octant and constraining the $|\varepsilon_{e\mu}^m|$ and $|\varepsilon_{e\tau}^m|$ parameter spaces for non-standard neutrino interactions that arise from the neutrino propagation in matter. In both cases we have demonstrated the interference both of these tasks suffer from the δ_{CP} parameter whose value is still unknown. We used the recent LBNO design study as our benchmark model and performed the numerical study with the GLoBES software.

References

- [1] D. V. Forero, M. Tortola, and J. W. F. Valle. Neutrino oscillations refitted. *Phys. Rev.*, D90(9):093006, 2014.
- [2] Patrick Huber, M. Lindner, and W. Winter. Simulation of long-baseline neutrino oscillation experiments with GLoBES (General Long Baseline Experiment Simulator). *Comput. Phys. Commun.*, 167:195, 2005.
- [3] Patrick Huber, Joachim Kopp, Manfred Lindner, Mark Rolinec, and Walter Winter. New features in the simulation of neutrino oscillation experiments with GLoBES 3.0: General Long Baseline Experiment Simulator). *Comput. Phys. Commun.*, 177:432–438, 2007.
- [4] C. R. Das, Jukka Maalampi, Joo Pulido, and Sampsa Vihonen. Determination of the 23 octant in LBNO. *JHEP*, 02:048, 2015.
- [5] Katri Huitu, Timo J. Karkkainen, Jukka Maalampi, and Sampsa Vihonen. Constraining the nonstandard interaction parameters in long baseline neutrino experiments. *Phys. Rev.*, D93(5):053016, 2016.

Planck 2015 Cosmological Results

Daniela Paoletti^{1,2}

on behalf of the *Planck* Collaboration

¹INAF/IASF-Bologna, via Gobetti 101, I-40129, Bologna, Italy

²INFN-Sezione di Bologna, viale Berti Pichat 6/2, 40127 Bologna, Italy

DOI: <http://dx.doi.org/10.3204/DESY-PROC-2016-05/19>

The *Planck* satellite has observed the full sky at nine frequencies between 30 GHz and 1 THz from 2009 to 2013. It represents the third generation of satellites dedicated to the observation of the Cosmic Microwave Background radiation (CMB). The CMB anisotropies represent the picture of primordial cosmological perturbations that originated the present structures of the Universe and *Planck* has performed their measurement with unprecedented accuracy in both temperature and polarization. In 2015 the *Planck* full mission data and results have been released to the public, here we will present some of the main cosmological results.

1 Introduction

The Cosmic Microwave Background (CMB) radiation is one of the most important source of information on the Universe origin, history, present and future status. It is the relic radiation from the Big Bang and it encodes the status of cosmological perturbations before stars and structures were formed. It was generated when the universe was cool enough to allow the recombination of neutral hydrogen (during the phase called *recombination*), increasing the mean free path of photons to lengths of the order of the Universe size. The CMB represents the first picture of the Universe just 400000 years after the Big Bang and its photons were emitted from an hypothetical surface called the *Last Scattering Surface* (LSS). The CMB is almost perfectly isotropic in the sky with a blackbody spectrum at a temperature of $T=2.72548 \pm 0.00057$ K [1], the small anisotropies of the order of $\Delta T/T \sim 10^{-5}$ are none other than the mirror of primordial cosmological perturbations. The CMB, thanks to the properties of the Compton scattering, is linearly polarized and polarization represents a crucial additional information for cosmology. The CMB polarization anisotropies are usually not analysed in terms of Q and U Stokes parameters but via their combination E and B [2]. Different cosmological models have different predictions for CMB anisotropies in temperature and polarization and therefore the CMB is crucial to investigate and constrain the standard cosmological model and its extensions. In this paper we will briefly review the main cosmological results by *Planck* 2015 [3, 4, 5, 6, 7, 8].

2 Planck 2015

The *Planck* mission¹ is the third generation of satellites dedicated to the observation of the sky in the microwaves. It is an ESA project and was launched on the 9th of May 2009 and has observed the sky continuously from the 12th of August 2009 to the 23rd of October 2013 in 9 bands between 30 GHz and 1 THz, it has angular resolutions between 5 and 30 arcmin and a sensitivity of $\Delta T/T_{CMB} \sim 2 \times 10^{-6}$ [9]. The satellite is composed by two instruments based on two different detector technologies: the Low Frequency Instrument (LFI), composed by radiometers at 30, 44, 70 GHz that operated for about 48 months, and the High Frequency Instrument (HFI), composed by spider-web bolometers at 100, 143, 217, 353, 545 and 857 GHz that operated for about 30 months. The first data, and associated scientific results, release took place in 2013 [10] with the delivery of the first 15 months of temperature data. In 2015 there has been the second data and result release [3] with the full mission data in temperature and, for the first time, also in polarization. With respect to the 2013 release some changes have been made to the data, in particular, there has been a strong improvement in the calibration, bringing the agreement between *Planck* and WMAP to less than few tenths of percent, the effect of the feature at $\ell \sim 1800$ in 2013 data has been removed, plus there have been some changes in the data analysis tools like the likelihood and the foreground modelling inside the likelihood.

2.1 Maps

Planck has produced full sky maps at all nine frequencies in temperature and polarization [11, 12]. But the microwave sky is not only the CMB signal but it is the composition of CMB and all the astrophysical signals like the contamination by our Galaxy and by unresolved point sources, which are called foregrounds. In order to separate the different components of the sky and extract the CMB in temperature and polarization *Planck* has used four different component separation methods all giving very consistent CMB maps [4]. In Fig.1 we show the results of one of the method (SMICA) in temperature and polarization².

2.2 Power Spectra

To perform a statistical analysis of the CMB anisotropies, they are expanded in spherical harmonics $\Delta T(\vec{x}, \hat{n}, \tau) = \sum_{l=1}^{\infty} \sum_{m=-l}^l a_{lm}(\vec{x}, \tau) Y_{m,l}(\hat{n})$. The angular power spectrum is then defined as $C_l = \frac{1}{(2l+1)} \Sigma_m \langle a_{lm}^* a_{lm} \rangle$. If the primordial fluctuations were Gaussian, the angular power spectrum would provide a complete description of the CMB anisotropies, whereas in case of non-Gaussianities, like are predicted in different cosmological models, higher statistical moments like the bispectrum and the trispectrum may be different from zero. In Fig.2 we show the *Planck* angular power spectra in temperature and polarization. The spectra shown are the temperature TT autocorrelation, the E-mode autocorrelation EE , the temperature-E-mode cross-correlation TE . We show also the B-mode polarization which has been derived

¹*Planck* (<http://www.esa.int/Planck>) is a project of the European Space Agency (ESA) with instruments provided by two scientific consortia funded by ESA member states and led by Principal Investigators from France and Italy, telescope reflectors provided through a collaboration between ESA and a scientific consortium led and funded by Denmark, and additional contributions from NASA (USA).

²Due to ongoing data analysis at the time of the release the lowest multipoles $\ell < 30$ of the polarization map have been filtered out, for a recent update on the low- ℓ polarization see [13]

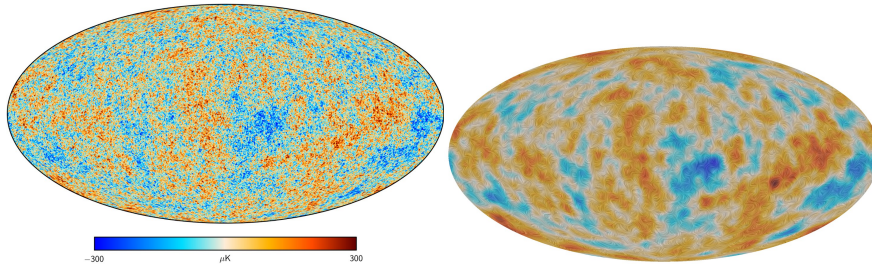


Figure 1: The component separated maps in temperature, left panel, and polarization, right panel.

with a joint analysis of the *Planck* and BICEP-2/Keck data [14]. The B-mode polarization is particularly important since it is not produced by the standard density perturbations, i.e. scalar perturbations, apart from a late time contribution on small angular scale by the CMB gravitational lensing. Therefore large scale B-modes in the standard cosmological model are representative of tensor primordial perturbations and are considered the smoking gun of inflation, in fact their amplitude would be directly connected to the energy scale of inflation ³.

2.3 Lensing

CMB photons travel almost unperturbed from the LSS, but during their crossing of the large scale structure they are subjected to the gravitational effects of the matter distribution in the Universe, the CMB lensing. The CMB lensing has distinctive signatures on the angular power spectra and it has a non-Gaussian contribution to the CMB anisotropies. The effect on the angular power spectra is a smoothing of the peaks in the temperature anisotropies, but most important, the lensing of the E-mode polarization generates a non-zero B-mode polarization with a peculiar shape which peaks on small angular scales. This signal is crucial since it represents one of the main contaminants for the detection of the primordial B-mode polarization from inflation. Using the non-Gaussian contribution of the lensing to the CMB anisotropies *Planck* detected the lensing with a significance of more than 40 sigma and was able to extract the information on the lensing potential with unprecedented precision at the level of 2.5% accuracy [15]. It was also possible to reconstruct a full-sky map of the projected mass distribution. In Fig.3 we show the results of both the analysis.

3 Cosmological Parameters

The *Planck* data are used to derive the constraints on the standard cosmological models and its extensions, exploring the cosmological parameter space using a Markov Chain Monte Carlo approach, e.g. with the public code *CosmoMC* [16]. To derive the constraints presented in the next sections we used the *Planck* 2015 likelihood, which is described in detail in [5]. The *Planck* likelihood uses a hybrid approach with the combination of one likelihood dedicated to low- ℓ and

³Although there are other possible sources of B-modes connected with exotic cosmological models, like the one which includes primordial magnetic fields.

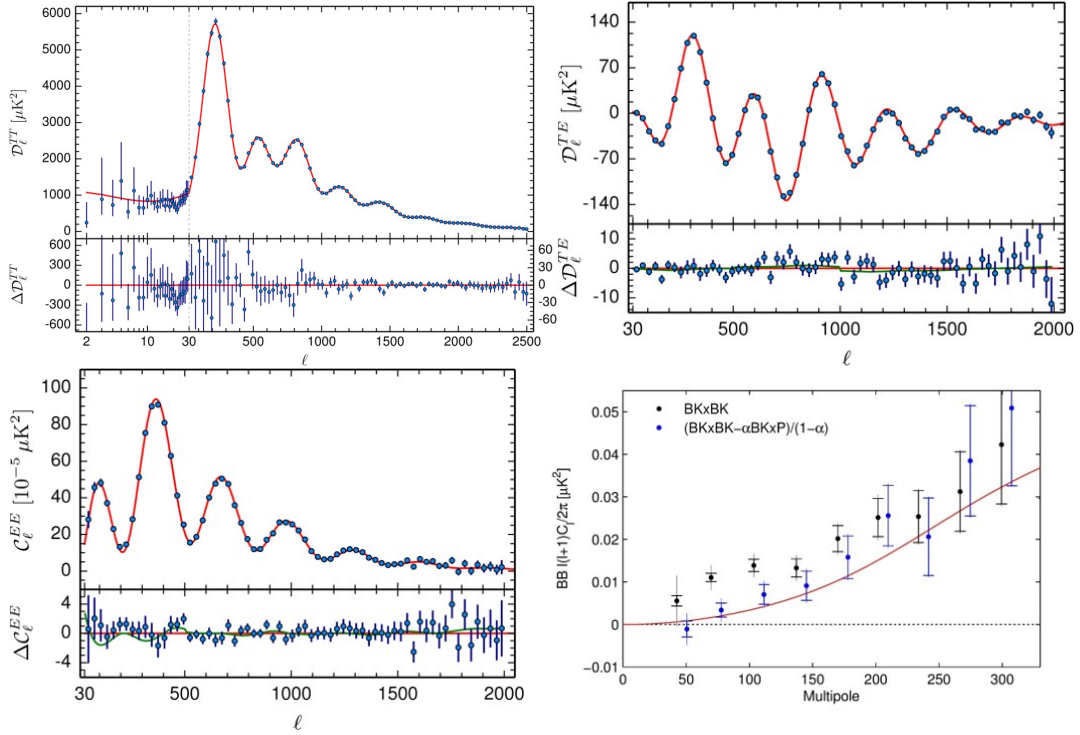


Figure 2: CMB anisotropy angular power spectra in temperature and polarization as measured by *Planck* 2015. The upper left panel is the temperature spectrum, the upper right is the temperature-E-mode cross-correlations, the lower left panel is the E-mode and the lower right panel is the joint analysis of Planck and BICEP2/Keck of B-mode polarization.

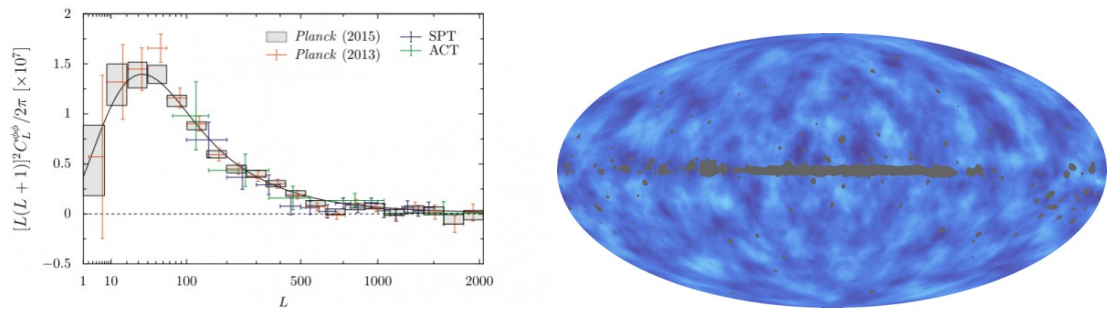


Figure 3: Planck 2015 lensing results, the lensing potential is on the left panel; the reconstructed matter distribution map on the right panel.

Parameter	TT+lowP	TT+lowP+lensing	TT,TE,EE+lowP	TT+lowP+lensing+ext
$\Omega_b h^2$	0.02222 ± 0.00023	0.02226 ± 0.00023	0.02225 ± 0.00016	0.02227 ± 0.00020
$\Omega_c h^2$	0.1197 ± 0.0022	0.1186 ± 0.0020	0.1198 ± 0.0015	0.01184 ± 0.0012
$100\theta_{MC}$	1.04085 ± 0.00047	1.04103 ± 0.00046	1.04077 ± 0.00032	1.04106 ± 0.00041
τ	0.078 ± 0.019	0.066 ± 0.016	0.079 ± 0.017	0.067 ± 0.013
$\ln(10^{10} A_s)$	3.089 ± 0.036	3.062 ± 0.029	3.094 ± 0.034	3.064 ± 0.024
n_s	0.9655 ± 0.0062	0.9677 ± 0.0060	0.9645 ± 0.0049	0.9681 ± 0.0044
H_0	67.31 ± 0.96	67.81 ± 0.92	67.27 ± 0.66	67.90 ± 0.55

Table 1: Parameter 68% confidence limits for the base Λ CDM model from *Planck* CMB power spectra, in combination with lensing reconstruction (“lensing”) and external data (“ext”, i.e. BAO+JLA+H0)[6].

another to high- ℓ . The *Planck* low- ℓ likelihood is a fully pixel-based likelihood with temperature and polarization with an ℓ -range $2 < \ell < 29$ in TT , TE , EE , and BB . The likelihood is based on the foreground-cleaned LFI maps at 70 GHz and the temperature map derived by the component separation method **Commander** [5]. This likelihood is denoted as *lowP* and is based entirely on *Planck* data for both temperature and polarization. The *Planck* high- ℓ likelihood is based on a Gaussian approximation and covers the ℓ -range $30 < \ell < 2500$. It uses the half-mission cross-power spectra of the 100 GHz, 143 GHz, and 217 GHz channels. The likelihood takes foregrounds and secondary anisotropies into account [5]. It is denoted as *Planck TT*, for temperature only, or *Planck TT, TE, EE*, for temperature plus polarization. In addition to the likelihood based on the CMB anisotropies, the *Planck* collaboration has also delivered a likelihood based on the lensing potential with a conservative range in ℓ of $40 < \ell < 400$ [15]. In addition to the CMB based likelihood *Planck* uses also a compilation of other non-CMB datasets denoted as *ext* which include: BAO acoustic oscillation from 6dFGS+SDSS+BOSS LOWZ; supernovae Ia “” Joint Light curve analysis from SNLS and SDSS, a prior on $H_0 = (73.9 \pm 3.3)$ Km/sec/Mpc, for details see [6].

3.1 Λ CDM

The standard cosmological model, the Λ CDM, is described by six cosmological parameters: the baryon density $\omega_b = \Omega_b h^2$, the cold dark matter density $\omega_c = \Omega_c h^2$, the reionization optical depth τ_{reion} , the ratio of the sound horizon to the angular diameter distance at decoupling θ , the scalar amplitude $\ln(A_s 10^{10})$, and the scalar slope n_s . The constraints derived with *Planck* 2015 likelihood are presented in Table 1. The Λ CDM is very well constrained and represents a very good fit to the *Planck* data.

3.2 Neutrinos

The baseline *Planck* model assumes a normal neutrino mass hierarchy with $\sum m_\nu = 0.06$ eV dominated by heaviest neutrino. The main effect of the mass of neutrinos is on large scale structure, the CMB is only slightly affected by neutrinos with masses below 1 eV. This is due to the fact that the effect of neutrino mass is caused by their transition from relativistic to non-relativistic, and becoming effectively an extra mass component for the CMB anisotropies, but this transition takes place well after recombination for masses below the eV. There is anyway

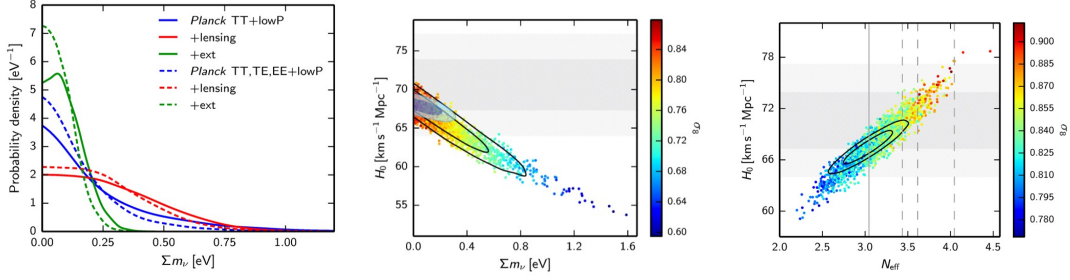


Figure 4: Constraints on neutrinos, on the first two panels we show the posterior distribution of the sum of the masses and then the 2D joint distribution of the mass and the Hubble constant. On the third panel we show the 2D joint posterior for the number of effective neutrinos and the Hubble parameter.

an effect at recombination which affects the early Integrated Sachs Wolfe effect, caused by the changes in the gravitational potential wells induced by the transition. If not much can be said with CMB anisotropies, the lensing is instead strongly affected by neutrino mass, in fact massive neutrinos suppress the clustering of structures on scales smaller than the horizon at the non-relativistic transition affecting the lensing potential. Therefore the lensing becomes a very powerful tool to constrain neutrino masses. In Fig.4 we show the results for the neutrino mass constraints. The 95% C.L. limits are $\sum m_\nu < 0.72$ eV for *Planck* TT+lowP; $\sum m_\nu < 0.21$ eV for *Planck* TT+lowP+BAO; $\sum m_\nu < 0.49$ eV for *Planck* TT,TE,EE+lowP; $\sum m_\nu < 0.17$ eV for *Planck* TT,TE,EE+lowP+BAO; $\sum m_\nu < 0.68$ eV for *Planck* TT+lowP+lensing; $\sum m_\nu < 0.59$ eV for *Planck* TT,TE,EE+lowP+lensing. The larger constraints with the addition of the lensing likelihood are due to the fact that the lensing likelihood based on the lensing potential reconstruction prefers lower values for the amplitude of the lensing signal with respect to the one derived with the CMB angular power spectra based likelihood and therefore the lensing likelihood allows for larger masses. Another possibility to investigate the neutrinos with CMB anisotropies are the constraints on the number of effective neutrinos. In fact, an increased number of effective neutrinos with respect to the standard prediction $N_{eff} = 3.046$ would lead to a faster expansion affecting both the Big Bang Nucleosynthesis predictions and the damping tail of the CMB anisotropies (it causes the recombination to happen earlier assuming the same size of the horizon as seen by Planck). The results are shown in the third panel of Fig.4. The *Planck* results are perfectly consistent with $N_{eff} = 3.046$ with single constraints given by (68% C.L.): $N_{eff} = 3.13 \pm 0.32$ *Planck* TT+LowP; $N_{eff} = 3.15 \pm 0.23$ *Planck* TT+LowP+BAO ; $N_{eff} = 2.99 \pm 0.20$ *Planck* TT,TE,EE+LowP; $N_{eff} = 3.04 \pm 0.18$ *Planck* TT,TE,EE+LowP+BAO. The constraints for the combination of variable mass and number of effective neutrinos confirms the results of the separate cases: $\sum m_\nu < 0.32$ eV and $N_{eff} = 3.2 \pm 0.5$ *Planck* TT+LowP+lensing+BAO. If we add a massive sterile neutrino in addition to the baseline three we have: $\sum m_\nu < 0.52$ eV and $N_{eff} < 3.7$ *Planck* TT+LowP+lensing+BAO and $\sum m_\nu < 0.38$ eV and $N_{eff} < 3.7$ *Planck* TT+LowP+lensing+BAO when restricting the prior on $m_{sterile}^{thermal} < 2$ eV instead of 10 eV of the first result.

3.3 Inflation

The inflation is a phase predicted in the standard cosmological model, in which the Universe underwent an exponential expansion [17]. Several models of inflation have been proposed through the years and each has its own predictions on the CMB anisotropies. Two of the main predictions of the most common inflationary models are a spectral index different from the scale invariance and the generation of tensor perturbations, therefore a tensor to scalar ratio r different from zero. In the left panel of Fig.5 we show the *Planck* 2015 and the combination of Planck+BICEP 2/KECK joint analysis results on the joint posterior distribution n_s and r compared with the predictions of some inflationary models. We note how *Planck* 2015, assuming a Λ CDM or Λ CDM+tensor model, excludes the scale invariance $n_s = 0.9655 \pm 0.0062$ (68% C.L.) with *Planck* TT+LowP, and gives strong upper limits on $r < 0.11$ *Planck* TT+LowP, reducing the allowed region of inflationary models [8].

3.4 Curvature, Dark Energy and Primordial Magnetic Fields

Two of the main extensions to the standard cosmological model consider models of dark energy which are not cosmological constants and the possibility to have non-zero curvature. In the first case *Planck* 2015 results are perfectly compatible with a dark energy in the form of a cosmological constant, this means that the parameter of the equation of state is $w = -1$. The *Planck* results on the dark energy are: $w = -1.54_{-0.50}^{+0.62}$ *Planck* TT+LowP; $w = -1.023_{-0.096}^{+0.091}$ *Planck* TT+LowP+ext; $w = -1.006_{-0.091}^{+0.085}$ *Planck* TT+LowP+lensing+ext; $w = -1.019_{-0.080}^{+0.075}$ *Planck* TT,TE,EE+LowP+lensing+ext. Also for the curvature *Planck* 2015 results are perfectly compatible with the standard cosmological model, namely with a flat geometry: $\Omega_k = -0.0512_{-0.055}^{+0.049}$ *Planck* TT+LowP; $\Omega_k = -0.040_{-0.041}^{+0.038}$ *Planck* TT,TE,EE+LowP; $\Omega_k = -0.005_{-0.017}^{+0.016}$ *Planck* TT+LowP+lensing; $\Omega_k = 0.0000 \pm 0.005$ *Planck* TT+LowP+lensing+BAO. The slight preference for negative values, closed universe, is due to a geometrical degeneracy and in fact note how adding the lensing and the BAO which break this degeneracy, brings the value in perfect compatibility with a flat geometry. The CMB allows to strongly constrain also more exotic cosmological models and in particular can give strong constrain to the one which considers the presence of primordial magnetic fields (PMF). PMF can naturally arise in the early Universe thanks to mechanisms related to inflation or phase transitions and may represent the progenitors of the fields we observe on large scale structures. PMF have several impact on CMB anisotropies [19, 18] and therefore CMB anisotropies can give strong constraints on PMF amplitude. *Planck* 2015 constraints are shown in the right panel Fig.5. The upper limits (95% C. L.) are: $B_{1Mpc} < 4.4$ nG *Planck* TT+lowP for generic spectral index; $B_{1Mpc}^{n_B=2} < 0.011$ nG; $B_{1Mpc}^{n_B=1} < 0.1$ nG; $B_{1Mpc}^{n_B=0} < 0.5$ nG; $B_{1Mpc}^{n_B=-1.5} < 4.8$ nG; $B_{1Mpc}^{n_B=-2.5} < 2.4$ nG; $B_{1Mpc}^{n_B=-2.9} < 2.0$ nG [7].

3.5 Conclusions

The *Planck* results represent a milestone in cosmology. The amount of data released is a legacy which will be exploited for years and years to come. *Planck* has confirmed that the Λ CDM model represents a very good fit to the CMB data, and has measured the cosmological parameters that describes it with unprecedented accuracy. But there are still a lot of challenges for the CMB future, the measurements of the B-mode polarization on large angular scales, the large scale anomalies etc. The final *Planck* release is expected for late 2016.

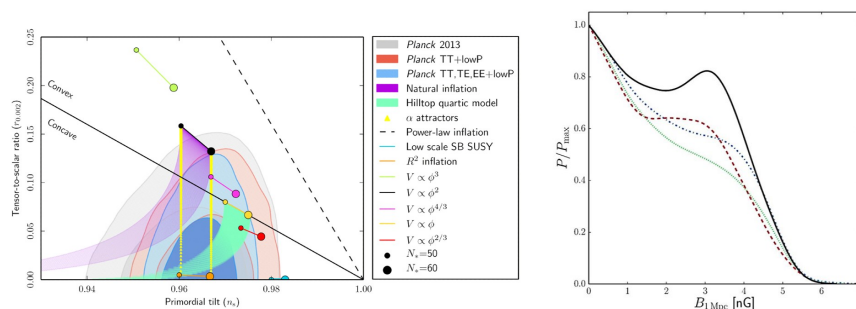


Figure 5: Constraints on inflation on the left and the constraints on primordial magnetic fields on the right: solid curve is Planck TT+lowP, compensated modes; the red dashed is Planck TT,TE,EE+lowP compensated; the green dotted line is Planck TT+lowP compensated+passive modes; the blue dot-dashed is the Planck TT,TE,EE+lowP compensated+passive modes. .

4 Acknowledgments

D.P. acknowledges the support by ASI/INAF Agreement 2014-024-R.0 for the *Planck* LFI Activity of Phase E2.

References

- [1] D. J. Fixsen, *The Astrophys. J.*, **707**, 916 (2009).
- [2] Hu W., White M., *NewA*, **2**, 323 (1997).
- [3] *Planck* Collaboration, arXiv:1502.01582 (2015).
- [4] *Planck* Collaboration, arXiv:1502.05956 (2015).
- [5] *Planck* Collaboration, arXiv:1507.02704 (2015).
- [6] *Planck* Collaboration, arXiv:1502.01589 (2015).
- [7] *Planck* Collaboration, et al., arXiv:1502.01594 (2015).
- [8] *Planck* Collaboration, et al., arXiv:1502.02114 (2015).
- [9] J.A. Tauber, N. Mandolesi, J.-L. Puget, et al. *A&A*, **520**, A1 (2010).
- [10] *Planck* Collaboration, *A&A*, **571**, A1 (2014).
- [11] *Planck* Collaboration, et al., arXiv:1502.01585 (2015).
- [12] *Planck* Collaboration, et al., arXiv:1502.01587 (2015).
- [13] *Planck* Collaboration, et al., arXiv:1605.02985 (2016).
- [14] BICEP2/Keck and Planck Collaborations, Ade, P. A. R., Aghanim, N., et al., *Physical Review Letters*, **114**, 101301,(2015).
- [15] *Planck* Collaboration, et al., arXiv:1502.01591 (2015).
- [16] Lewis A., Bridle S., ascl.soft, ascl:1106.025 (2011).
- [17] Liddle A. R., Lyth D. H., *cils.book*, 414 (2000).
- [18] Paoletti D., Finelli F., 2011, *PhRvD*, **83**, 123533
- [19] Paoletti D., Finelli F., Paci F., 2009, *MNRAS*, **396**, 523

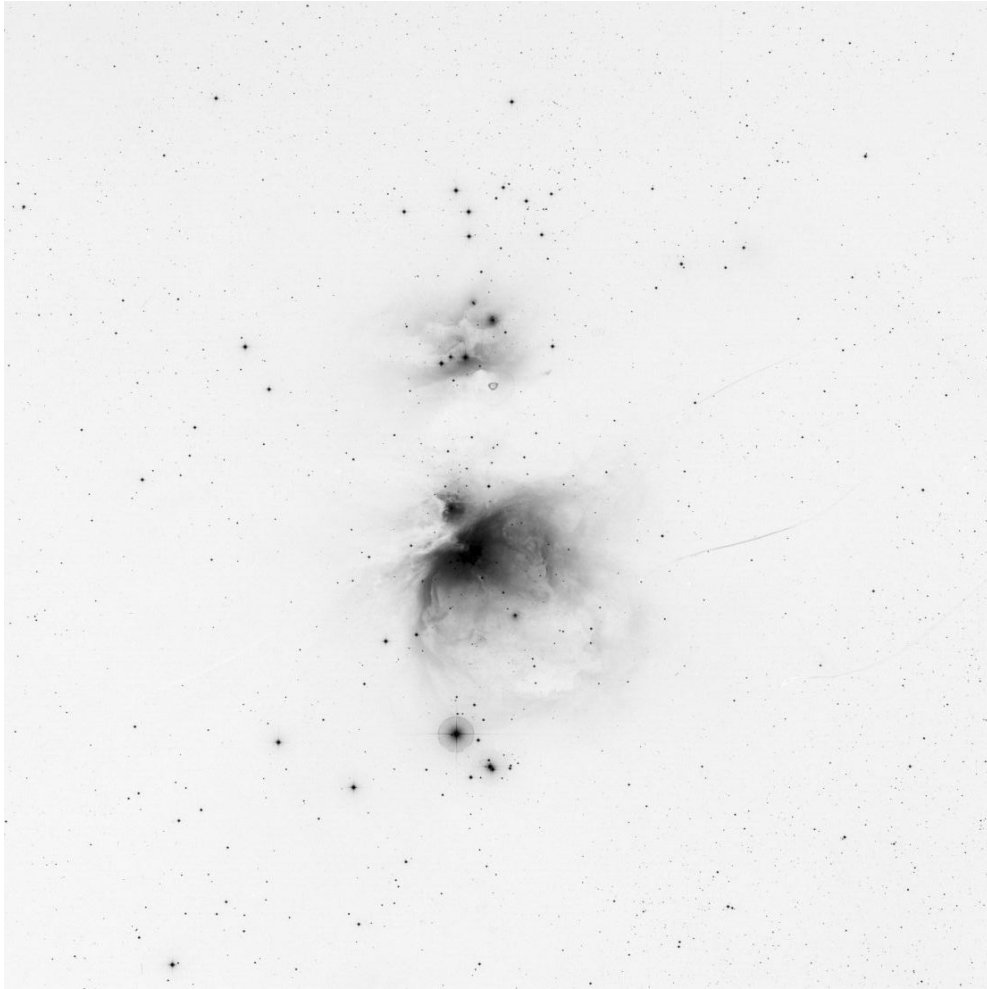


Figure 1: The Orion Nebula (M42) as photographed using Hamburg Observatory's Great Schmidt Mirror on 9th March 1959. Credit: Digital Plate Archives of Hamburger Sternwarte

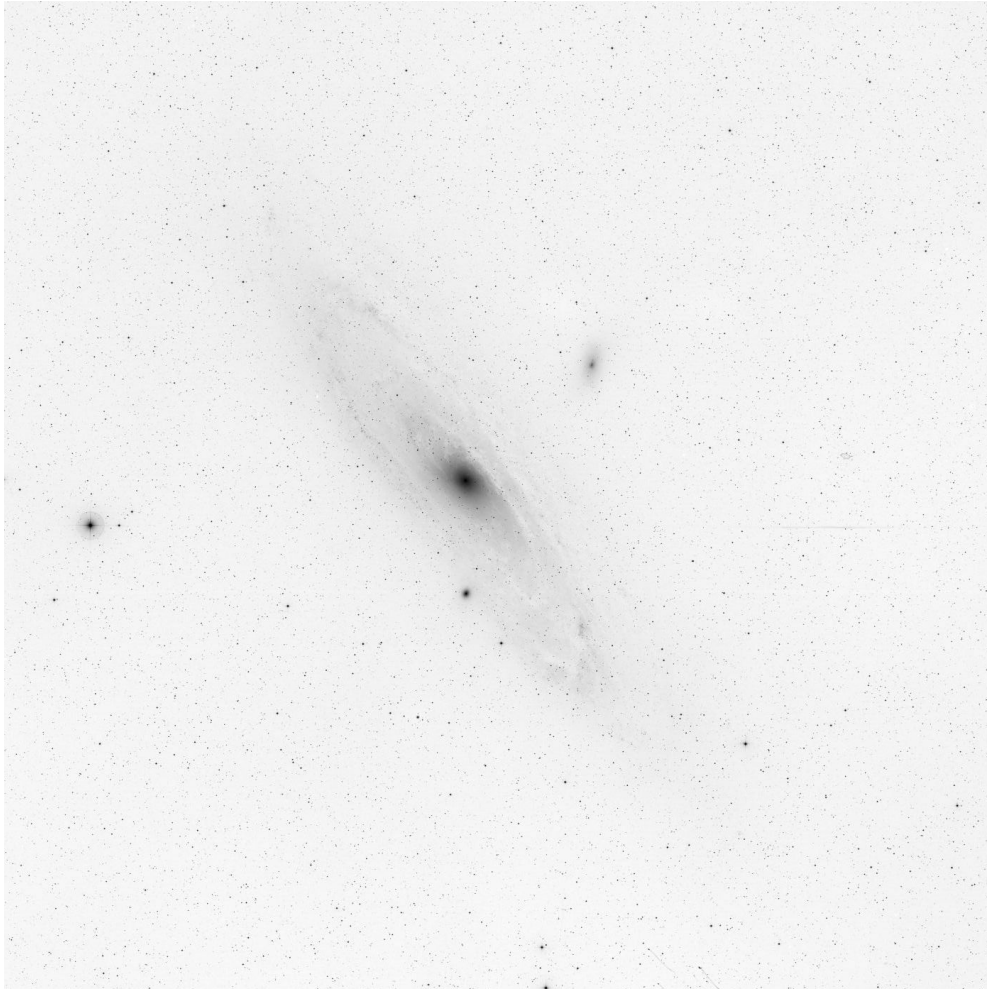


Figure 2: The nearby galaxy in Andromeda (M31) as photographed using Hamburg Observatory's Great Schmidt Mirror on 31st August 1959. Credit: Digital Plate Archives of Hamburger Sternwarte

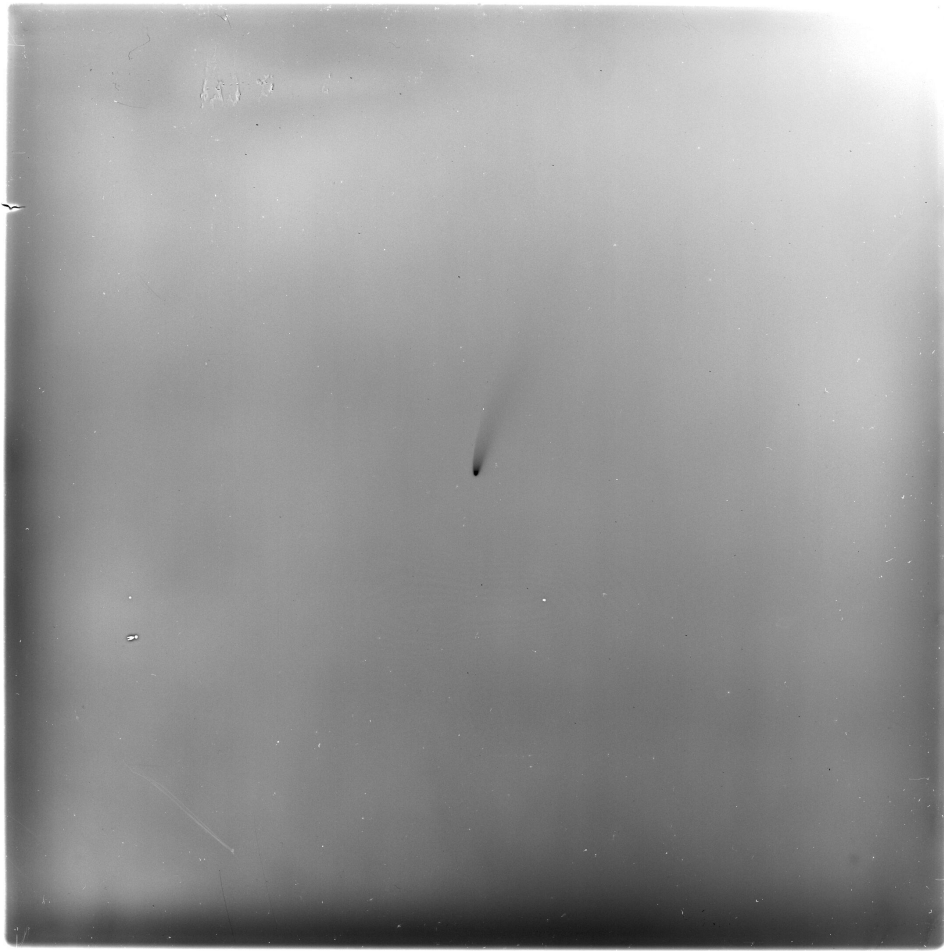


Figure 3: The Comet Mrkos, officially discovered by Czech astronomer Antonin Mrkos on 2nd August 1957. It probably had been seen by two others up to four days prior, but neither reported their sighting. Credit: Digital Plate Archives of Hamburger Sternwarte

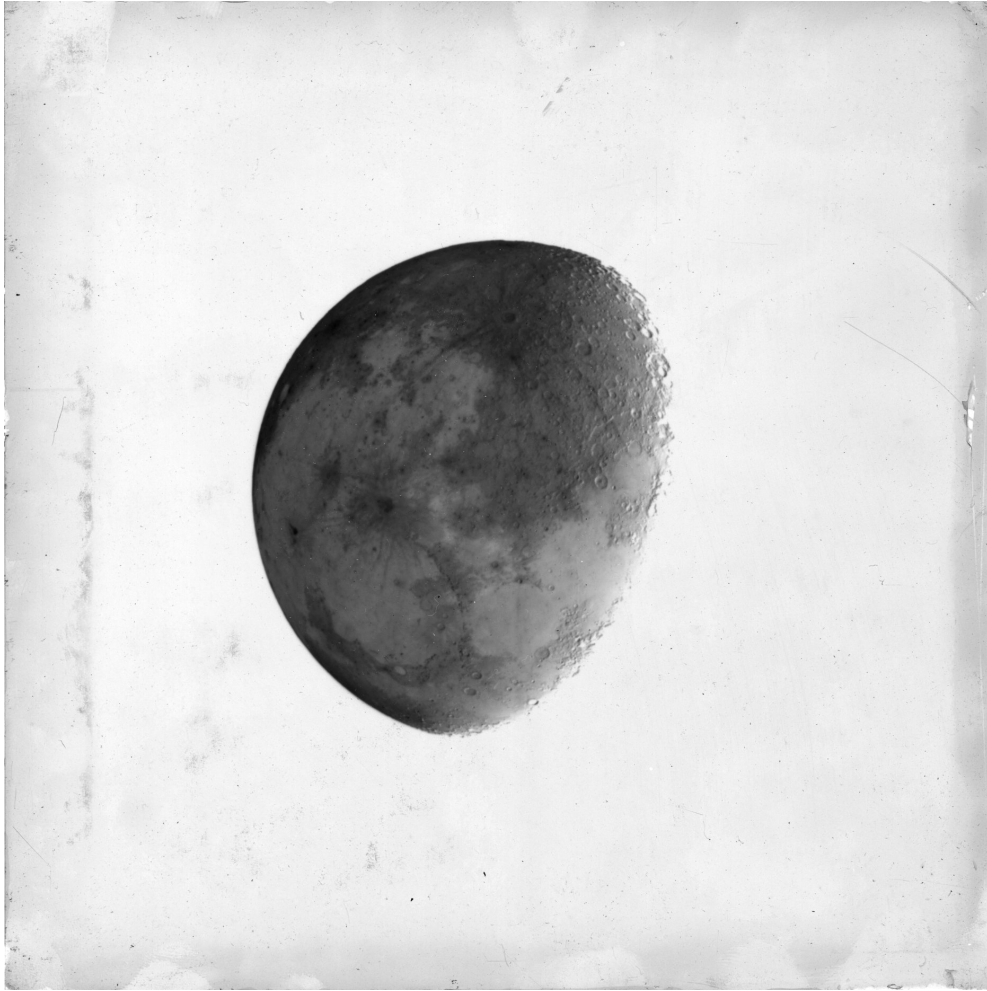


Figure 4: The Moon. Photograph taken with Hamburg Observatory's Great Refractor telescope in the night of 27th/28th February 1929. Credit: Digital Plate Archives of Hamburger Sternwarte



Figure 5: The Moon photographed using the Great Refractor on 17th March 1929. Credit: Digital Plate Archives of Hamburger Sternwarte



Figure 6: Hamburg astronomers gathered in the library to discuss results. Note Otto Heckmann and Richard Schorr in the center. Credit: Photographic Archive of the Hamburg Observatory



Figure 7: Hamburg astronomers preparing instruments for the observation of a solar eclipse in Russia. In the 1920s and 1930s multiple expeditions to various locations in South America and Asia were conducted to study eclipses or objects not visible from the northern hemisphere. Credit: Photographic Archive of the Hamburg Observatory

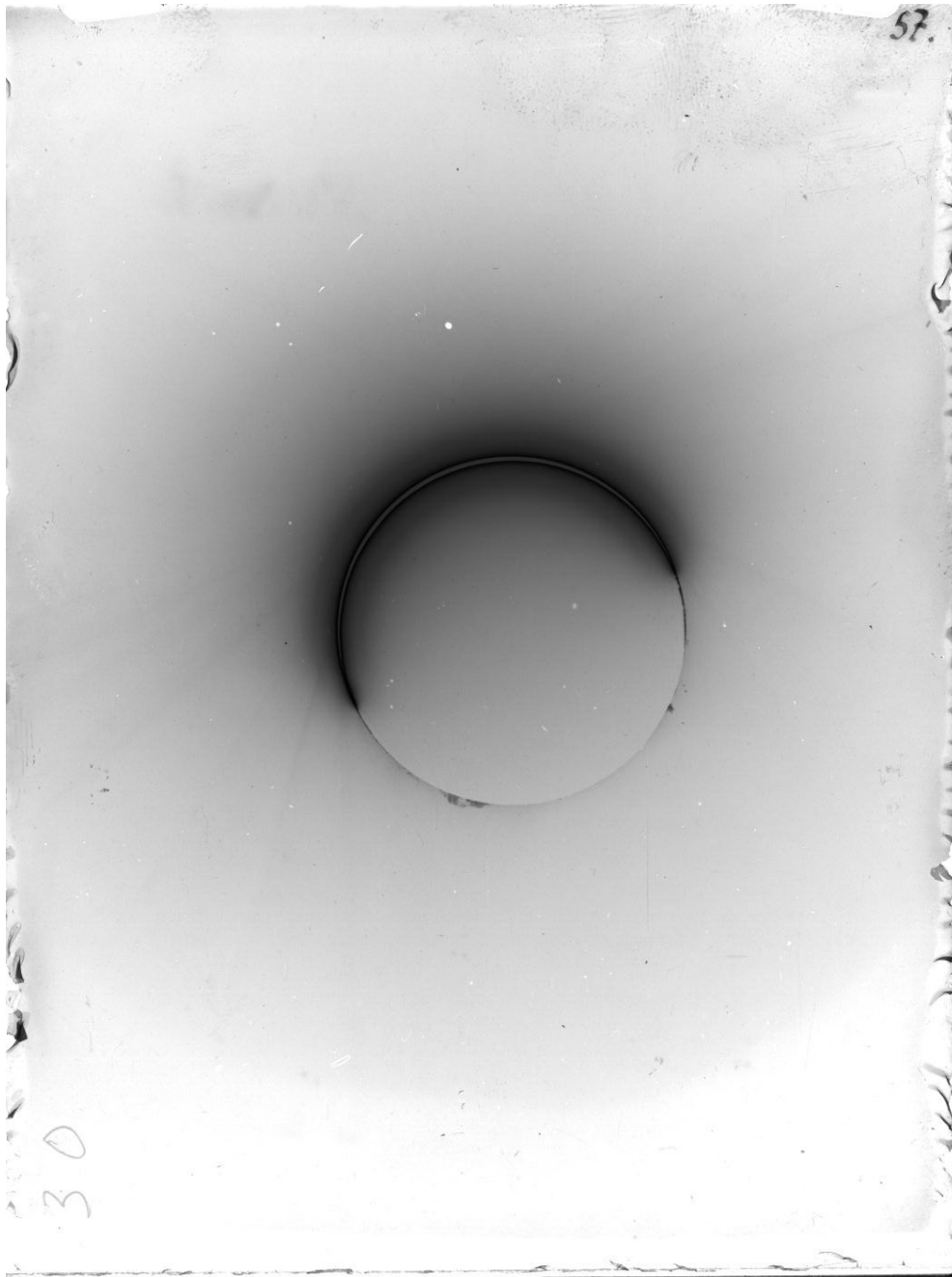


Figure 8: Solar eclipse in 1912 as photographed using Hamburg Observatory's Lippert Astrograph telescope. Credit: Digital Plate Archives of Hamburger Sternwarte

The SNO+ experiment: current status and future prospects.

Valentina Lozza¹ for the SNO+ Collaboration

¹Institut für Kern- und Teilchenphysik, TU Dresden, Zellescher Weg 19, 01069 Dresden, Germany

DOI: <http://dx.doi.org/10.3204/DESY-PROC-2016-05/5>

SNO+ is a multi-purpose neutrino experiment whose main physics goal is the search for the neutrinoless double-beta ($0\nu\beta\beta$) decay of ^{130}Te . With an initial loading of 0.5% (by weight) of natural tellurium SNO+ is expected to reach a sensitivity on the $0\nu\beta\beta$ lifetime of the order of 10^{26} years at 90% C.L. in a 5-year run. Along with the $0\nu\beta\beta$ decay search, SNO+ has the capability to measure the low energy solar neutrinos, like pep and CNO neutrinos. It has also an extraordinary opportunity to do the first measurement of the supernova ν_x energy spectrum.

1 Introduction

The SNO+ experiment is reusing the Sudbury Neutrino Observatory detector which is located at a depth of 2 km in the Vale's Creighton mine in Sudbury, Canada. The deep underground location, the large volume, and the high radio-purity of the materials used allows SNO+ to explore several neutrino physics topics.

The primary goal of SNO+ is the search for the Dirac or Majorana nature of the neutrinos via searching for the neutrinoless double-beta ($0\nu\beta\beta$) decay of ^{130}Te . The neutrinoless double-beta decay is an extremely rare nuclear process that can only happen if neutrinos are their own antiparticles, i.e. they have a Majorana mass component. With an initial loading of 0.5% of tellurium by weight, SNO+ aims to reach a sensitivity on the effective Majorana neutrino mass smaller than 100 meV, exploring the top of the inverted hierarchy region in five years.

The low energy threshold of the SNO+ experiment, the deep underground location and the high radiopurity allows the measurement of the low-energy solar neutrinos, like pep, ^8B , and CNO neutrinos. The measurement of the pep neutrino flux and of the spectral shape of the ^8B -neutrinos will shed light on oscillation models, while the measurement of the CNO neutrino flux can solve the solar metallicity problem.

Along with these goals SNO+ can measure antineutrinos from nuclear reactors and the Earth's crust and mantle, can watch for neutrinos and antineutrinos from core collapse supernovae, and has the potential to search for exotics physics, like invisible nucleon decay, and axion-like particles.

This article is structured as follows. In Section 2 the SNO+ detector is described together with the most recent upgrades, and the liquid scintillator and tellurium purification processes. In Section 3 the physics goals, the expected phases of the experiment and the run plan is presented. In Sections 4 to 6 the physics program of SNO+ is described: the neutrinoless

double-beta decay search (Section 4), the measurement of low energy solar neutrinos (Section 5), and the watch for supernova neutrinos and antineutrinos (Section 6). The conclusion will follow at the end.

2 The SNO+ Experiment

The SNO+ experiment is located at a depth of 5890 ± 94 m.w.e. in the SNOLAB underground laboratory [1]. The flat overburden provides a shield against the cosmic muons, reducing the muon flux to 63 muons per day passing through a 8.3m radius circular area. SNO+ will reuse the SNO detector infrastructure [2, 3] which consists of a spherical acrylic vessel of 12 m diameter and 5.5 cm thickness suspended in a cavity excavated in the rock via a system of high purity ropes. The vessel will be filled by about 780 tonnes of liquid scintillator and is viewed by 9300 8 inch PMTs placed on a geodesic stainless steel structure (PSUP) of 19 m diameter. Each PMT is equipped with a light concentrator for an overall coverage of 54%. The volume between the acrylic vessel and the PSUP and the one outside the PSUP is filled with high purity water to shield against the radioactivity coming from the rock and the PMTs. Due to the lower density of the liquid scintillator (LS) contained in the acrylic vessel compared to the one of the surrounding water a new system of high purity ropes has been installed on the top of the vessel and anchored to the cavity floor to offset the LS buoyancy [4].

2.1 Liquid scintillator

The SNO+ liquid scintillator consists of linear alkylbenzene (LAB) as a solvent and 2 g/L of 2,5-diphenyloxazole (PPO) as a fluor. The LAB+PPO mixture has been selected among others due to its chemical compatibility with the acrylic vessel, its high light yield of more than 10000 photons per MeV, its transparency and good optical properties (long attenuation and scattering lengths), its linear response in energy, and its long term stability. Additionally, the fast decay time allows to discriminate between alpha-like and beta-like signals.

Despite the high purity levels available directly from the manufacturer, a further purification of the liquid scintillator is necessary in order to achieve a U- and Th-chain radiopurity close to the one of Borexino and KamLAND, i.e. less than 10^{-17} g/g_{LAB} [5]. The scintillator purification plant of SNO+ is fully described in [6, 7]. Heavy metals and optical impurities are removed by a multi-stage distillation and high temperature flash vacuum distillation. Gases and residual water are then removed by a N₂/steam gas stripping process. Once the SNO+ detector is filled with LAB+PPO the mixture can be further purified in-situ by recirculating the scintillator (about four days for the entire volume) through a rotating-stage liquid-liquid extraction column and metal scavengers. The liquid scintillator purification plant has been fully installed at the SNOLAB depth and is currently undergoing commissioning.

2.2 Te-loading

To search for the $0\nu\beta\beta$ decay SNO+ will load tellurium into the liquid scintillator. The SNO+ collaboration has developed a new technique to load several tonnes of tellurium into LAB maintaining a high light emission level and good optical properties. In the initial phase SNO+ will load 3.9 tonnes of natural tellurium (a concentration of 0.5% by weight) by forming an organometallic compound of tellurium and butanediol which is soluble in LAB scintillator. A

secondary wavelength shifter (bis-MSB) is added to better match the PMT quantum efficiency. The currently predicted light yield in SNO+ for the 0.5% Te-loaded cocktail is 390 Nhits (detected photoelectron hits) per MeV of energy.

The purification technique for tellurium is described in [8]. It has been designed to remove both the U- and Th-chain impurities and the isotopes produced by cosmogenic neutron and proton activation of the material during handling and storage on the earth's surface. The purification plant for tellurium consists of two stages. Both the stages are expected to happen underground. A first double-pass acid recrystallization (Stage I) reduces the U/Th and cosmogenic-induced isotope level of a factor larger than 10^4 . In the second purification stage (Stage II) tellurium is dissolved in water at 80° C and left to cool to recrystallize without further rinsing. This stage will further reduce the impurity level of a factor larger than 100.

2.3 Detector Upgrades

In addition to the installation of the hold-down rope system several detector upgrades have been done in the latest years. The read-out boards and the data acquisition system of SNO have been upgraded with a higher bandwidth one to cope with the higher rate and lower energy events expected in SNO+. The trigger system has been improved for a more flexible calibration interface. The electronics and the trigger system have been tested in runs with the detector empty and partially filled with water. A new calibration hardware has been designed which consists of a set of radioactive sources (beta, gamma, alpha and neutron) and a set of optical sources. The optical calibration system consists of deployable sources and a fixed external system of optical fibers attached to the PSUP as described [9]. The SNO cover gas system, a sealed system of bags filled with high-purity nitrogen that shields the detector against the radon contained in the mine air, has been upgraded for a radon reduction of about 10^5 .

3 Physics Goals and Run Plan

The main goal of the SNO+ experiment is the search for the $0\nu\beta\beta$ decay of ^{130}Te . However, due to the deep underground location and the high purity of the materials used, SNO+ has the potential to explore other physics topics: the measurement of the low energy *pep* and CNO neutrino flux, the measurement of the spectral shape of the ^8B -neutrinos, the watch for supernova (SN) neutrinos and antineutrinos, and the measurement of antineutrinos produced in nuclear reactors and in the Earth's crust and mantle.

Currently, there are planned three main phases for the experiment. During the initial phase the detector will be filled with about 905 tonnes of ultra-pure water (1, *water phase*). This phase will start by the end of 2016 and last for a few months. In this phase the detector performance and the PMT response will be checked. At the same time SNO+ will search for exotic physics events, like the invisible nucleon decay, and will watch for SN-neutrinos.

The water phase will be followed by a *pure liquid scintillator phase* (2) where the detector is filled with about 780 tonnes of LAB+PPO. Also this phase will last few months. The physics topics covered are the measurement of the low energy solar neutrinos, the watch for SN neutrinos, and the measurement for reactor and geo- antineutrinos. This phase will be also used to measure the liquid scintillator background and verify the optics model.

Tellurium will be loaded into the detector starting from the end of 2017 with the beginning of the data taking expected for the summer of 2018. The *double-beta decay phase* (3) will last

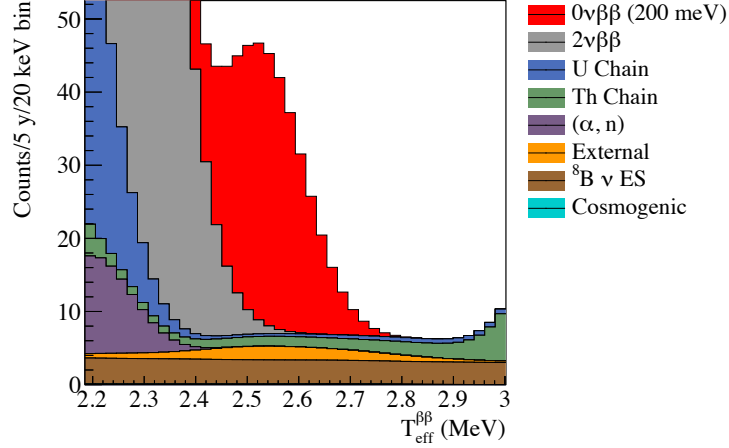


Figure 1: Energy spectrum plot (stacked) of all backgrounds and an hypothetical $0\nu\beta\beta$ signal corresponding to $m_{\beta\beta} = 200$ meV. The plot is shown for 5 years live-time, 0.5% Te-loading and a light yield of 390 Nhits/MeV. A fiducial volume of 20% has been applied. External backgrounds are further reduced by a factor of two, while $^{214}\text{BiPo}$ and $^{212}\text{BiPo}$ are reduced by $>99.99\%$ and 98% , respectively. $T_{\beta\beta}$ is the effective kinetic energy.

about 5 years. Simultaneously to the $0\nu\beta\beta$ search the detector will be live for a potential SN, and the geo- and reactor antineutrinos can be observed.

4 ^{130}Te neutrinoless double-beta decay search

The observation of the $0\nu\beta\beta$ decay would demonstrate lepton number violation, and shed light on the ordering of the neutrino masses, both intriguing open questions in the neutrino research area. The $0\nu\beta\beta$ decay is a nuclear process in which two neutrons are converted into two protons and two electrons without the emission of the neutrinos. It can be seen as two simultaneous β -decays in which the neutrinos from the two weak vertices mutually annihilate. The signature of the decay is a peak at the Q-value of the reaction in the summed energy spectrum of the two electrons. The measured observable is the reaction's rate, from which it is derived the half-life of the decay. The effective Majorana neutrino mass, $m_{\beta\beta}$, is then extracted from the half-life as described in [10].

In SNO+ the search for the $0\nu\beta\beta$ decay is done by loading large amounts of ^{130}Te into the detector volume. ^{130}Te has a large isotopic abundance of 34.08%, which allows to load several tonnes of the isotope without the need of enrichment. The Q-value of the decay (2527.518 ± 0.013 keV [11]) is above many of the U- and Th-chain decays' endpoints. The half-life of the associated $2\nu\beta\beta$ decay ($7.0 \pm 0.9(\text{stat}) \pm 1.1(\text{syst}) \times 10^{20}$ yr [12]), one of the main irreducible backgrounds in the $0\nu\beta\beta$ decay search, is among the longest of all the $0\nu\beta\beta$ decay candidates. Currently, loadings up to few percent (by weight) of natural tellurium in LAB have been successfully obtained with very good optical properties, high light yield and no inherent optical

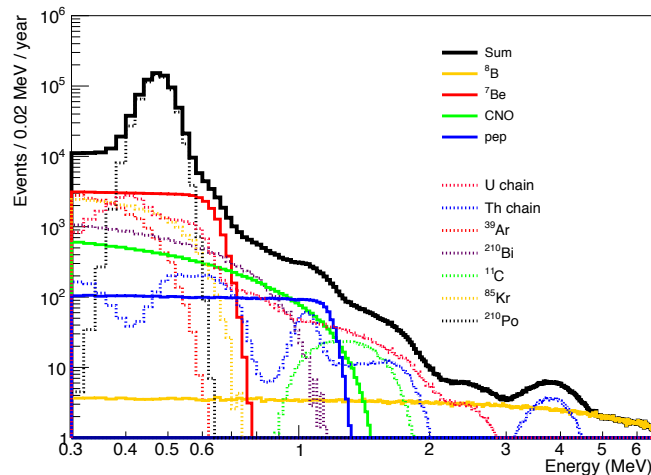


Figure 2: Expected solar neutrino fluxes and backgrounds as detected by the SNO+ experiment. The background levels are assumed to be similar to the one initially achieved by Borexino. A fiducial volume cut of 5.5 m and a light yield of 400 Nhits/MeV are assumed. The $^{214}\text{BiPo}$ events are rejected by 95% using delayed coincidences, while a 95% reduction is applied to the ^{210}Po and remaining ^{214}Po alpha signals. U and Th-chain backgrounds have a constrain of 7% and 25%, respectively.

absorption line in the visible wavelength range.

The expected energy spectrum for a 0.5% Te loading and a five-year live-time is shown in Figure 1. A fiducial volume (FV) cut of 3.5 m, corresponding to 20% of the total volume, has been applied. The region of interest (ROI) for the $0\nu\beta\beta$ decay search extends from -0.5σ to $+1.5\sigma$ around the Gaussian signal peak. The asymmetric ROI considerably reduces the background events from the $2\nu\beta\beta$ and the low energy U- and Th-chain decays, leaving as main background contribution the $^8\text{B}-\nu$ elastic scattering (irreducible flat background). $^{214}\text{BiPo}$ (U chain) and $^{212}\text{BiPo}$ (Th chain) events are rejected using a delayed coincidence tagging and, for the events happening in the same trigger window, pile-up cuts [1]. The $0\nu\beta\beta$ decay signal shown in Figure 1 corresponds to a $m_{\beta\beta} = 200\text{ meV}$, or to a $T_{1/2}^{0\nu\beta\beta} \sim 10^{25}\text{ yr}$ using IBM-2 nuclear matrix elements [13]. The expected sensitivity of SNO+ in 5 years of running is $T_{1/2}^{0\nu\beta\beta} > 1.96 \times 10^{26}\text{ yr}$ at 90% CL, corresponding to a limit on the effective Majorana neutrino mass of $38 - 92\text{ meV}$ ($G = 3.96 \times 10^{-14}\text{ yr}^{-1}$ [14] and $g_A = 1.269$), depending on the nuclear matrix elements used.

5 Low-energy Solar Neutrinos

The solar neutrino spectrum as detected by SNO+ is shown in Figure 2 together with the main background sources during the pure scintillator phase. With a liquid scintillator purity similar to the one achieved by Borexino in its Phase I [5], SNO+ can detect *pep* and CNO neutrinos with

a sensitivity of few percent. Additionally, a spectral shape measurement of the ${}^8\text{B}$ neutrinos can be performed also during the $0\nu\beta\beta$ phase for energies above the ${}^{130}\text{Te}$ endpoint.

5.1 Pep neutrinos

The *pep* reaction in the Sun produces monoenergetic neutrinos (1.44 MeV) which have very well predicted flux (1.2% uncertainty) constrained by the Sun luminosity. A measurement of these neutrinos has the potential to probe the transition region between the vacuum oscillation ($E \leq 1$ MeV) and the matter-enhanced oscillation ($E \geq 1$ MeV) energy regions of the ν_e survival probability. The shape of the survival probability in the transition region is sensitive to alternate models of neutrino-matter interactions, such as flavor changing neutral currents or mass-varying neutrinos. A minimum precision of 10% is necessary to discriminate among different models. To improve the sensitivity to non standard neutrino interactions, the spectral shape of ${}^8\text{B}$ - ν s can be used. Due to their production closer into the core of the Sun, the effect of new physics is enhanced for these neutrinos.

With a background level similar to the one achieved in Borexino Phase I, MonteCarlo simulations suggest that, with one year of data and a 50% fiducial volume cut, the expected uncertainty on the *pep* neutrinos is 8.9% (13% in six months), while the expected uncertainty on the ${}^8\text{B}$ neutrinos is about 7% (10% in 6 months).

5.2 CNO Neutrinos

Recent improvements in the solar atmospheric modelling suggest a photosphere's metallicity (abundance of elements heavier than helium) about 30% lower than what was predicted by the older but quite successful model. This broke the excellent agreement between the solar model calculations and helioseismology, opening the question about the homogeneous distribution of the elements in the Sun. The prediction for the CNO neutrino flux depends linearly on the core metallicity and thus can shed light on the solar metallicity problem. Additionally, the CNO- ν flux can be further constrained by a precision measurement of the ${}^8\text{B}$ - ν flux as it depends on the same environmental factors.

The major background for the CNO neutrino flux measurement are the ${}^{210}\text{Bi}$ decays (Q-value = 1.16 MeV). The shape of this decay is very similar to the CNO- ν one making the discrimination difficult. The separation can be achieved by an ex-situ constraint on the ${}^{210}\text{Bi}$ decay rate or using observable different from energy. In one year of data the expected uncertainty on the CNO+ ${}^{210}\text{Bi}$ linked data is 4.4% (6.5% in six months). The CNO flux alone has a predicted uncertainty of 15%.

6 Supernova Neutrinos and Antineutrinos

The high radiopurity of SNO+ and its deep underground location makes it one of the most promising experiments for the detection of neutrinos from core collapse supernovae (CCSNe). CCSNe are expected to emit more than 99% of their energy via neutrinos of all flavours and type. A measurement of these fluxes is expected to shed light on the explosion mechanism. Current models estimate that about half of the neutrinos are emitted in the first second of the CCSN's burst [15].

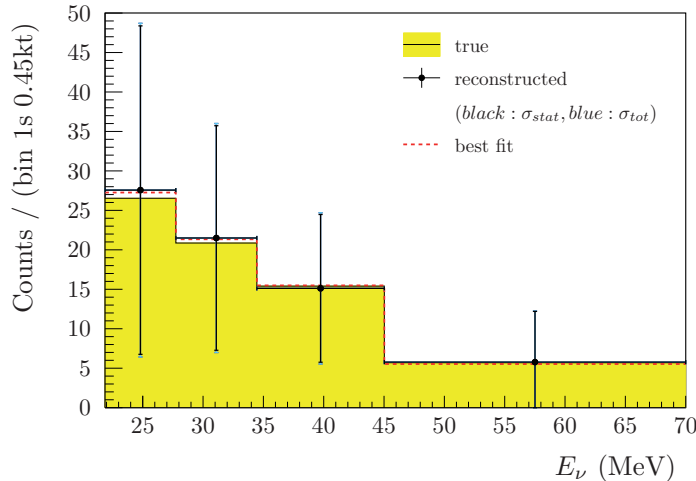


Figure 3: Supernova (SN) neutrino energy distribution for the ν -p ES interaction in the SNO+ experiment. A FV cut of 5.5 m and a detector threshold of 0.2 MeV have been applied. Shown are the true, reconstructed and best fit energy distribution of the sum of ν_e , $\bar{\nu}_e$, and ν_x emitted in the first second of the burst for a 10 kpc away SN with a total 3×10^{53} erg energy ejected in the form of neutrinos. The uncertainties shown are statistical (black) and total (blue). The systematic uncertainty which includes the ν -p ES cross section, the number of target protons, the proton quenching parameter, the detector's energy resolution, and the spectral ν_e and $\bar{\nu}_e$ parameters, is too small to be resolved. The best fit spectrum shows excellent agreement.

SNO+ has the potential to measure both the averaged energy as well as the total electromagnetic energy of the neutrinos emitted in the CCSN. The possible interaction channels during the pure liquid scintillator phase are summarized in [1]. For a 10 kpc away SN, with 3×10^{53} erg of binding energy released in form of neutrinos (equally partitioned among all six flavours and types), SNO+ expects to detect about 195 events via inverse beta decay (IBD) reactions, and about 119 events via elastic scattering (ES) on protons (for an energy threshold above 0.2 MeV) with a 5.5 m FV cut. The reconstructed energy spectrum of ν_e , $\bar{\nu}_e$, and ν_x (sum of ν_μ , $\bar{\nu}_\mu$, ν_τ , and $\bar{\nu}_\tau$) neutrinos emitted in the first second of the CCSN and detected by ν -p ES reaction is shown in Figure 3, together with the true neutrino spectrum. The reconstructed energy spectrum is obtained from the unfolded proton energy, taking into account the non-linear quenching of the proton energy and the finite detector resolution [1].

7 Conclusion and Outlook

SNO+ is a large-scale liquid scintillator experiment whose primary goal is the search for the neutrinoless double-beta decay of ^{130}Te . During the initial Te-phase about 3.9 tonnes of natural tellurium are loaded into the liquid scintillator by which SNO+ is expected to reach a sensitivity on the effective Majorana neutrino mass on the top of the inverted hierarchy region.

Additionally, due to the low energy threshold, the deep underground location and the high purity of the materials used SNO+ is also able to measure low energy solar neutrinos, like *pep* and CNO neutrinos. Furthermore, SNO+ can provide the first measurement of the spectral shape of the ν_x neutrinos ejected from a CCSN.

Several upgrades have been made to the detector in order to reuse the old SNO vessel and electronics. We expect to start the water phase data taking soon, with the tellurium loading foreseen for the end of the 2017.

Acknowledgments

This work is supported by the German Research Foundation (DFG).

References

- [1] S. Andringa, *et al.*, The SNO+ Collaboration, *Advances in High Energy Physics* **vol. 2016** 6194250 (2016).
- [2] J. Boger *et al.*, SNO Collaboration, *Nuclear Instruments and Methods in Physics Research A* **vol. 449** pp. 172–207 (2000).
- [3] N. Jelley, A. B. McDonald, and R.G. H. Robertson, *Annual Review of Nuclear and Particle Science* **vol. 59** pp. 431–465 (2009).
- [4] A. Bialek *et al.*, *Nuclear Instruments and Methods in Physics Research A* **vol. 827** pp. 152 – 160 (2016).
- [5] G. Alimonti *et al.*, Borexino Collaboration, *Nuclear Instruments and Methods in Physics Research A* **vol. 609** pp. 58–78 (2009).
- [6] R. Ford, M. Chen, O. Chkvorets, D. Hallman, and E. Vázquez-Jáuregui, *AIP Conference Proceedings* **vol. 1338** pp. 183–194 (2011).
- [7] R. Ford for the SNO+ Collaboration, *AIP Conference Proceedings* **vol. 1672** 080003 (2015).
- [8] S. Hans, *et al.*, *Nuclear Instruments and Methods in Physics Research A* **vol. 795** pp. 132–139 (2015).
- [9] R. Alves *et al.*, *Journal of Instrumentation* **vol. 10** P03002 (2015).
- [10] K. Zuber, *Contemporary Physics* **vol. 45** pp. 491–502 (2004).
- [11] M. Redshaw, B. J. Mount, E. G. Myers, and F. T. Avignone III, *Physical Review Letters* **vol. 102** 212502 (2009).
- [12] R. Arnold *et al.*, NEMO–3 Collaboration, *Physical Review Letters* **vol. 107** 062504 (2011).
- [13] J. Barea, J. Kotila, and F. Iachello, *Physical Review C* **vol. 87** 014315 (2013).
- [14] J. Kotila and F. Iachello, *Physical Review C* **vol. 85** 034316 (2012).
- [15] G. Pagliaroli, F. Vissani, M. L. Costantini, and A. Ianni, *Astroparticle Physics* **vol. 31** pp. 163–176 (2009).

Measurement of solar neutrino fluxes with Borexino

S. Marcocci²⁴, M. Agostini^{24,22}, K. Altenmüller²², S. Appel²², G. Bellini¹³, J. Benziger¹⁷, D. Bick⁴, G. Bonfini¹², D. Bravo²⁰, B. Caccianiga¹³, F. Calaprice¹⁶, A. Caminata³, M. Carlini¹², P. Cavalcante¹², A. Chepurinov²³, D. D'Angelo¹³, S. Davini²⁴, A. Derbin¹⁵, L. Di Noto³, I. Drachnev²⁴, A. Etenko¹⁰, K. Fomenko², A. Formozov¹³, D. Franco¹, F. Gabriele¹², C. Galbiati¹⁶, C. Ghiano³, M. Giammarchi¹³, M. Goeger-Neff²², A. Goretti¹⁶, M. Gromov²³, C. Hagner⁴, E. Hungerford²⁵, Aldo Ianni¹², Andrea Ianni¹⁶, K. Jedrzejczak⁶, D. Jeschke²², M. Kaiser⁴, V. Kobychiev⁷, D. Korablev², G. Korga¹², D. Kryn¹, M. Laubenstein¹², B. Lehnert²⁶, E. Litvinovich^{10,11}, F. Lombardi¹², P. Lombardi¹³, L. Ludhova¹³, G. Lukyanchenko^{10,11}, I. Machulin^{10,11}, S. Manecki²⁰, W. Maneschg⁵, E. Meroni¹³, M. Meyer⁴, L. Miramonti¹³, M. Misiaszek^{6,12}, M. Montuschi²¹, P. Mosteiro¹⁶, V. Muratova¹⁵, B. Neumair²², L. Oberauer²², M. Obolensky¹, F. Ortica¹⁴, M. Pallavicini³, L. Papp²², L. Perasso³, A. Pocar¹⁹, G. Ranucci¹³, A. Razeto¹², A. Re¹³, A. Romani¹⁴, R. Roncin^{12,1}, N. Rossi¹², S. Schönert²², D. Semenov¹⁵, H. Simgen⁵, M. Skorokhvatov^{10,11}, O. Smirnov², A. Sotnikov², S. Sukhotin¹⁰, Y. Suvorov^{27,10}, R. Tartaglia¹², G. Testera³, J. Thurn²⁶, M. Toropova¹⁰, E. Unzhakov¹⁵, A. Vishneva², R.B. Vogelaar²⁰, F. von Feilitzsch²², H. Wang²⁷, S. Weinz²⁸, J. Winter²⁸, M. Wojcik⁶, M. Wurm²⁸, Z. Yokley²⁰, O. Zaimidoroga², S. Zavatarelli³, K. Zuber²⁶, and G. Zuzel⁶

¹AstroParticule et Cosmologie, Université Paris Diderot, CNRS/IN2P3, CEA/IRFU, Observatoire de Paris, Sorbonne Paris Cité, 75205 Paris Cedex 13, France

²Joint Institute for Nuclear Research, 141980 Dubna, Russia

³Dipartimento di Fisica, Università degli Studi e INFN, Genova 16146, Italy

⁴Institut für Experimentalphysik, Universität Hamburg, 22761 Hamburg, Germany

⁵Max-Planck-Institut für Kernphysik, 69117 Heidelberg, Germany

⁶M. Smoluchowski Institute of Physics, Jagiellonian University, 30059 Krakow, Poland

⁷Kiev Institute for Nuclear Research, 06380 Kiev, Ukraine

⁸Institute for Theoretical and Experimental Physics, 117218 Moscow, Russia

⁹Kepler Center for Astro and Particle Physics, Universität Tübingen, 72076 Tübingen, Germany.

¹⁰NRC Kurchatov Institute, 123182 Moscow, Russia

¹¹National Research Nuclear University MEPhI (Moscow Engineering Physics Institute), 115409 Moscow, Russia.

¹²INFN Laboratori Nazionali del Gran Sasso, 67010 Assergi (AQ), Italy

¹³Dipartimento di Fisica, Università degli Studi e INFN, 20133 Milano, Italy

¹⁴Dipartimento di Chimica, Università e INFN, 06123 Perugia, Italy

¹⁵St. Petersburg Nuclear Physics Institute NRC Kurchatov Institute, 188350 Gatchina, Russia

¹⁶Physics Department, Princeton University, Princeton, NJ 08544, USA

¹⁷Chemical Engineering Department, Princeton University, Princeton, NJ 08544, USA

¹⁸Physics Department, Queen's University, Kingston ON K7L 3N6, Canada

¹⁹Amherst Center for Fundamental Interactions and Physics Department, University of Mas-

sachusetts, Amherst, MA 01003, USA

²⁰Physics Department, Virginia Polytechnic Institute and State University, Blacksburg, VA 24061, USA

²¹Dipartimento di Fisica e Scienze della Terra Università degli Studi di Ferrara e INFN, Via Saragat 1-44122, Ferrara, Ital

²²Physik-Department and Excellence Cluster Universe, Technische Universität München, 85748 Garching, Germany.

²³Lomonosov Moscow State University Skobeltsyn Institute of Nuclear Physics, 119234 Moscow, Russia.

²⁴Gran Sasso Science Institute (INFN), 67100 L'Aquila, Italy.

²⁵Department of Physics, University of Houston, Houston, TX 77204, USA.

²⁶Department of Physics, Technische Universität Dresden, 01062 Dresden, Germany.

²⁷Physics and Astronomy Department, University of California Los Angeles (UCLA), Los Angeles, California 90095, USA.

²⁸Institute of Physics and Excellence Cluster PRISMA, Johannes Gutenberg-Universität Mainz, 55099 Mainz, Germany.

DOI: <http://dx.doi.org/10.3204/DESY-PROC-2016-05/30>

Solar neutrinos have been of extraordinary importance for the discovery of neutrino oscillations and allow to study directly the Sun's innermost core. The Borexino experiment, located in the Gran Sasso National Laboratory, is an ultra-pure liquid scintillator detector conceived for the real time spectroscopy of low energy solar neutrinos. We review Borexino's results and we discuss its upcoming future, since the precision era of solar neutrino measurements has just started.

1 Solar neutrinos

The Standard Solar Model (SSM) is a theoretical framework which aims to describe the Sun, and particularly to study the energy production mechanisms, thus predicting the solar neutrino fluxes coming out of them [1]. The SSM has been continuously refined during the years, including results about cross section measurements of relevant nuclear reactions at low energy [2] and Helioseismology measurements [3, 4].

The Sun produces energy via different nuclear reactions. The so called pp chain, which results in the fusion of 4 protons into ${}^4\text{He}$ (see the left part of Fig. 1), is the set of nuclear transitions which gives the most important contribution to the total energy production. The CNO cycle (see the right part of Fig. 1) involves a subdominant set of reactions in the Sun, accounting for $\sim 1\%$ of the Sun's energy release. However, the CNO cycle plays a key role in astrophysics, since it is the dominant source of energy in stars more massive than the Sun and in advanced evolutionary stages of Sun-like stars. A CNO neutrino measurement would constrain the chemical composition of the Sun, leading to improved models for star formation and supernova explosions. A direct measurement of the CNO neutrino component could also solve the long-standing solar metallicity problem [5], for which, basically, two different solutions are possible, namely the *High Metallicity* and *Low Metallicity*.

The theoretical solar neutrino spectra resulting both from the reactions of the pp chain and the CNO cycle are shown on the left panel of Fig. 2.

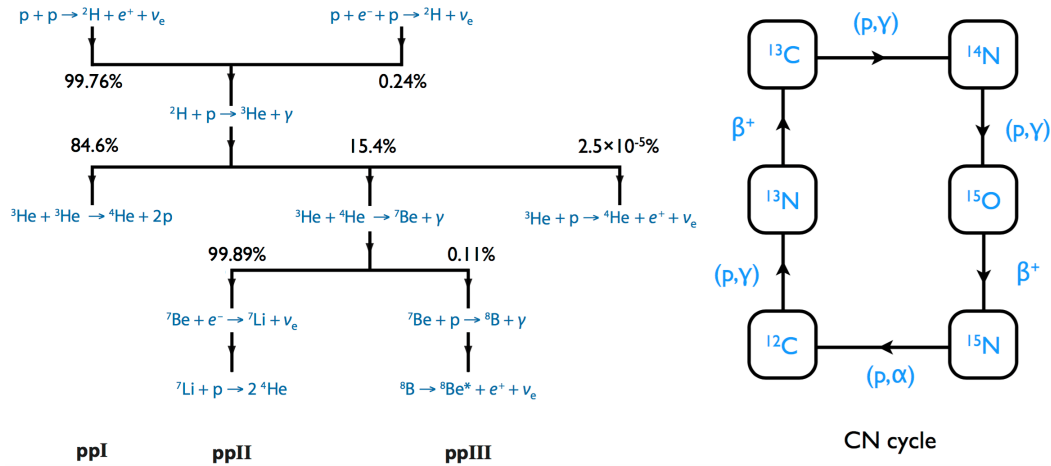


Figure 1: **Left:** Schematic drawing of the pp reactions chain, [6]. **Right:** Sketch of the CNO cycle.

2 The Borexino experiment

The study of low energy solar neutrinos with a ultra-pure liquid scintillator technique is relevant both for testing the predictions of the Standard Solar Model and for investigating the MSW-LMA neutrino oscillation scenario in an energy range that is not accessible to water Cherenkov detectors [7, 8]. In fact, up to a few years ago, spectroscopic measurements were performed by water Cherenkov detectors above ~ 5 MeV and concerned only ${}^8\text{B}$ neutrinos for less than the 1% of the total flux. The bulk of neutrinos at lower energies were detected only with radiochemical experiments, unable to resolve the individual components. The original main goal of Borexino [9, 10] was the precise measurement of the rate induced by the monochromatic electron neutrinos (862 keV) produced by the electron capture decay of ${}^7\text{Be}$ in the Sun. However, the very high radio purity of the scintillator made it possible for Borexino to largely exceed the expected performance and broaden the original physics program.

Borexino is a liquid scintillator calorimeter [11] designed for the real-time observation of low energy solar neutrinos and anti-neutrinos. Neutrinos are detected through their elastic scattering on electrons and by means of the consequent emission of scintillation light, while anti-neutrinos are detected through inverse beta decay on protons. A sketch of the experiment is shown in Fig. 2. It is located at the Gran Sasso National Laboratories (LNGS) in central Italy, at a depth of 3800 m w.e.. The inner part of the Borexino detector is an unsegmented stainless steel sphere (SSS) that is both the container of the scintillator and the mechanical support of the photomultipliers. Within this sphere, the active mass consists of 278 tons of pseudocumene (PC), doped with 1.5g/l of PPO. The scintillator is contained in a thin ($125 \mu\text{m}$) nylon Inner Vessel (IV), 8.5 m in diameter. The IV is surrounded by two concentric PC buffers doped with a light quencher. The scintillation light is collected by nominally 2212 photomultipliers

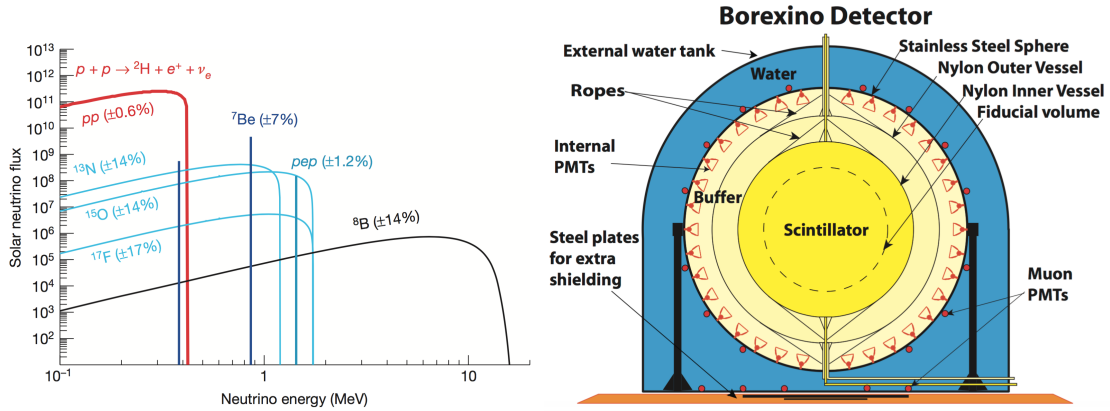


Figure 2: **Left Panel:** Solar neutrino spectral components. **Right Panel:** Sketch of the Borexino detector.

(PMTs) that are uniformly attached to the inner surface of the SSS. All but 384 PMTs are equipped with light concentrators that are designed to reject photons not coming from the active scintillator volume, thus reducing the background due to radioactive decays originating in the buffer liquid or gammas from the PMTs. The 384 PMTs without concentrators are used to study this background, and to help identify muons that cross the buffer, but not the IV.

The SSS is supported by 20 steel legs and enclosed within a large tank (WT) that is filled with ultra-pure water. The WT has a cylindrical base with a diameter of 18 m and a hemispherical top with a maximum height of 16.9 m. The WT is a powerful shielding against external backgrounds (γ rays and neutrons from the rock) and is also used as a Cherenkov muon counter and muon tracker. The muon flux, although reduced by a factor of 10^6 by the 3800 m w.e. depth of the Gran Sasso Laboratory, is of the order of $1 \text{ m}^{-2} \text{ h}^{-1}$, corresponding to about 4000 muons per day crossing the detector. This flux is well above the Borexino requirements and a strong additional reduction factor (about 10^4) is necessary. Therefore the WT is equipped with 208 photomultipliers that collect the Cherenkov light emitted by muons in the water.

The Borexino scintillator has a light yield of $\sim 10^4$ photons/MeV, resulting in ~ 500 detected photoelectrons/MeV. The fast time response of the scintillating mixture allows to reconstruct the events position by means of a time-of-flight technique with a good precision. The signature of ${}^7\text{Be}$ neutrinos is a Compton-like shoulder at 665 keV in the electron recoil spectrum. The energy resolution (1σ) at the ${}^7\text{Be}$ energy is as low as 44 keV (roughly $5\% / \sqrt{\text{MeV}}$).

3 Results from Borexino

${}^7\text{Be}$ neutrinos The measurement of the flux of ${}^7\text{Be}$ neutrinos was the primary goal of Borexino. The first observation was published in the summer of 2007, after only 3 months of data taking. The signal of the ${}^7\text{Be}$ solar neutrinos is extracted from the data through a fit of the energy spectrum of the events collected within the fiducial volume. There is not special signature other than the shape of the spectrum itself (the Compton like shoulder with endpoint at 665 keV) that allows to distinguish the signal from background. The main background is due to the radioactive decay of the isotopes ${}^{85}\text{Kr}$, ${}^{210}\text{Po}$, ${}^{210}\text{Bi}$, and ${}^{11}\text{C}$ contaminating the scintillator,

but their contributions can be disentangled very efficiently through the spectral fit, as shown in Fig. 3.

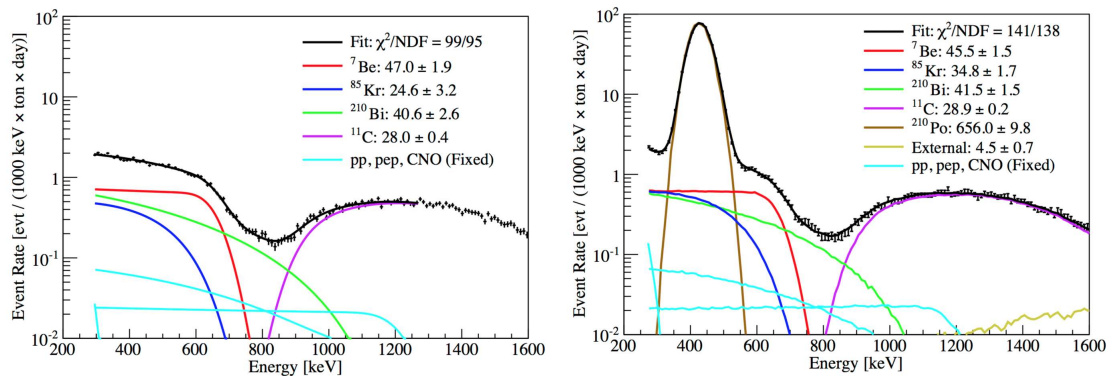


Figure 3: Two example of fitted spectra for the ${}^7\text{Be}$ solar neutrino measurement, [12]. On the left, an analytic fit over the 290-1270 keV energy region to a spectrum obtained with statistical subtraction of the α background is shown. The plot on the right presents a Monte Carlo based fit over the energy region 270-1600 keV to a spectrum where the α component has not been removed. The fit results in the legends have units [counts/(day·100 ton)].

The rate of the neutrino-electron elastic scattering interactions from 862 keV ${}^7\text{Be}$ solar neutrinos in Borexino resulted of $46.0 \pm 1.5(\text{stat}) \pm 1.5(\text{syst})$ counts/(day·100 ton), [12]. This corresponds to a ν_e -equivalent ${}^7\text{Be}$ solar neutrino flux of $(3.10 \pm 0.15) \times 10^9 \text{ cm}^{-2}\text{s}^{-1}$ and, under the assumption of ν_e transition to other active neutrino flavors, yields an electron neutrino survival probability of 0.51 ± 0.07 at 862 keV. The no flavor change hypothesis is ruled out at 5.0σ . Borexino also investigated the eventual day-night asymmetry in the ${}^7\text{Be}$ solar neutrino interaction rate. The measured asymmetry is $0.001 \pm 0.012(\text{stat}) \pm 0.007(\text{syst})$ [13], in agreement with the prediction of MSW-LMA solution for neutrino oscillations. This result disfavors MSW oscillations with mixing parameters in the LOW region at more than 8.5σ . This region is, for the first time, strongly disfavored without the use of reactor anti-neutrino data and therefore the assumption of CPT symmetry.

pep and CNO neutrinos Thanks to the development of novel data analysis techniques for the rejection of the cosmogenic ${}^{11}\text{C}$ and of external gammas (the main backgrounds in the 1-1.5 MeV region), a first evidence of pep solar neutrinos could be obtained. Particularly, a “three-fold coincidence” vetoing method was developed [14]. It consists in eliminating the parts of the fiducial volume through which the muon tracks passed, possibly creating the ${}^{11}\text{C}$ isotope. For a further reduction of the background of positrons produced by the ${}^{11}\text{C}$ decays, a pulse shape discrimination variable for $\beta/\beta+$ events has been developed (see *e.g.* the left side of Fig. 4). It exploits the different time distribution of the scintillation photons, due to the possible ortho-positronium formation [15]. The fit is then performed with a multivariate approach, fitting simultaneously the energy spectrum, the pulse shape discrimination variable for $\beta/\beta+$ and the radial distribution of the events, in order to decouple the uniformly distributed neutrino-like events from the external gammas. All the details can be found in Ref. [16].

The interaction rate of pep neutrinos in Borexino is $3.1 \pm 0.6(\text{stat}) \pm 0.3(\text{syst})$ counts/(day·100 ton) [16]. The absence of the solar neutrino signal is disfavored at 99.97% C.L., while the ab-

sence of the pep signal is disfavored at 98% C.L. . The strongest constraint on the CNO solar neutrino interaction rate (<7.9 counts/(day·100 ton), at 95% C.L.[16]), could be obtained through the likelihood ratio test shown in the right part of Fig. 4.

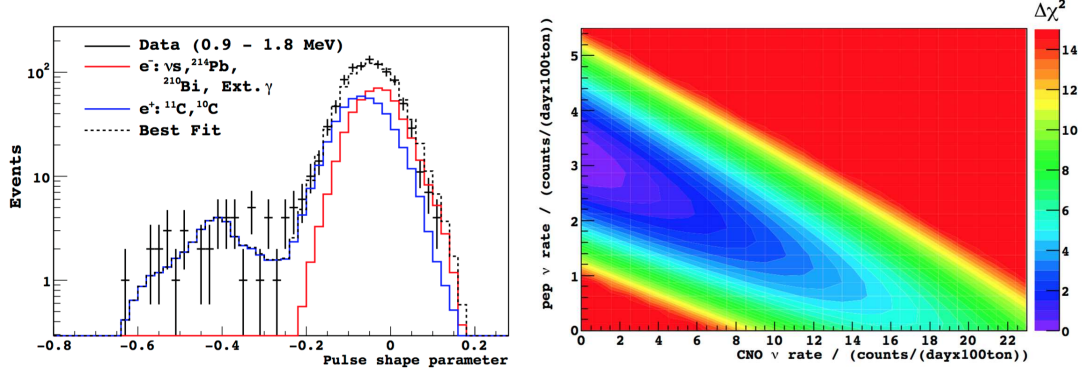


Figure 4: **Left Panel:** Experimental distribution (black) of the pulse shape parameter for $\beta/\beta+$ discrimination. The best-fit distribution (black dashed) and the corresponding β (red) and $\beta+$ (blue) contributions are also shown. **Right Panel:** $\Delta\chi^2$ profile obtained from likelihood ratio tests between fit results where the pep and CNO neutrino interaction rates are fixed to particular values (all other species are left free) and the best-fit result.

pp neutrinos The pp reaction in the core of the Sun is the keystone process for the energy production and is the source of the largest component of the neutrino flux. Its measurement is a major experimental milestone in solar neutrino physics, and paves the way to a deeper understanding of the Sun dynamics. This measurement was made possible by the very low radioactive background, particularly in ^{85}Kr , achieved after an extensive purification campaign performed in 2010-2011 and thanks to the extremely good performance of the detector as a whole. Most of the remaining, unavoidable, background is due to ^{14}C β -decays, whose endpoint is 156 keV, very close to the pp region of interest. To estimate its rate independently from the main analysis, a sample of data in which the event causing the trigger is followed by a second event within the same trigger window (16 μs long, while physical events last 100-500 ns) has been analyzed. These second events are not subject to the trigger threshold, so they register down to much lower energies. By fitting this spectrum against the known ^{14}C spectral shape, the ^{14}C rate in Borexino results of 40 ± 1 Bq per 100 tons.

Because of its high rate, ^{14}C naturally generates a considerable amount of pile-up: two physical events can occur so close to each other in time that the detector fails to resolve them. With the above measurement of the ^{14}C rate, the expected rate of ^{14}C - ^{14}C pile-up is 100 per day per 100 tons, comparable to the expected pp neutrino interaction rate. The pile-up component can be determined using an independent, data-driven method: real triggered events with no cuts are artificially overlapped with random data obtained from the ends of real trigger windows, uncorrelated with the triggering event. The synthetic events are then reconstructed using the same software used for real events, and selected with the same criteria. Using this method, it is possible to obtain the true rate and spectral shape of pile-up in the detector.

The solar pp neutrino interaction rate measured by Borexino is $144 \pm 13(\text{stat.}) \pm 10(\text{syst.})$ counts/(day·100 ton) [17]. The spectral fit result is summarized in Fig. 5. The absence of pp

MEASUREMENT OF SOLAR NEUTRINO FLUXES WITH BOREXINO

solar neutrinos is excluded with a statistical significance of 10σ . Once statistical and systematic errors and the latest values of the neutrino oscillation parameters are taken into account, the measured solar pp neutrino flux is $(6.6 \pm 0.7) 10^{10} \text{ cm}^{-2}\text{s}^{-1}$, in accordance with the Standard Solar Model.

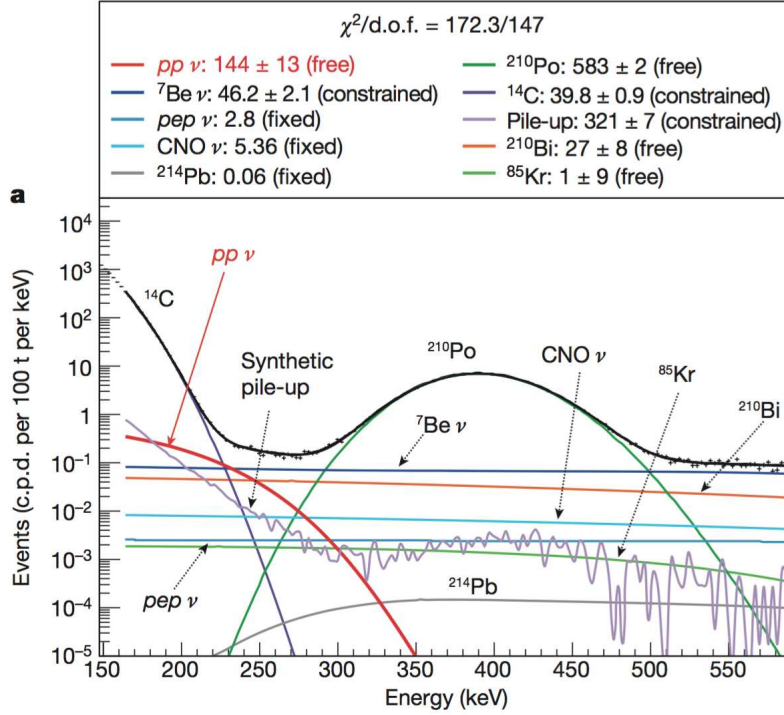


Figure 5: The best fit of Borexino’s spectrum in the pp energy window is shown. The best-fit pp neutrino component is shown in red, the ^{14}C background in dark purple and the synthetic pile-up in light purple. The large green peak is ^{210}Po α -decays. The values of the parameters (in counts per day per 100 t) are in the inset above the figure.

^8B neutrinos Borexino could measure for the first time ^8B solar neutrinos with an energy threshold of only 3 MeV. The rate of ^8B solar neutrino-induced electron scattering events above this energy in Borexino is $0.217 \pm 0.038(\text{stat}) \pm 0.008(\text{syst})$ counts/(day·100 ton [18], which corresponds to a flux of $(2.4 \pm 0.4) \times 10^6 \text{ cm}^{-2}\text{s}^{-1}$, in good agreement with the measurements from SNO and SuperKamiokaNDE.

4 Other Borexino measurements

Borexino is a “big” ultra-pure calorimeter and, apart from solar neutrinos, could investigate many other rare processes. Other results include the study of solar and other unknown anti-neutrino fluxes [19], a 5.9σ observation of geo-neutrinos with a 98% C.L. evidence of a signal from the mantle [20, 21], a measurement of neutrino velocity [22], searches for solar axions [23],

experimental limits on heavy neutrinos [24], and a test of the electric charge conservation and electron decay [25].

5 Outlook

The high impact of Borexino on neutrino physics is very well summarized by Fig. 6, where the survival probability of solar neutrinos is plotted as a function of the neutrino energy. For all the solar neutrino components that Borexino measured, the trend is in good agreement with the MSW-LMA prediction.

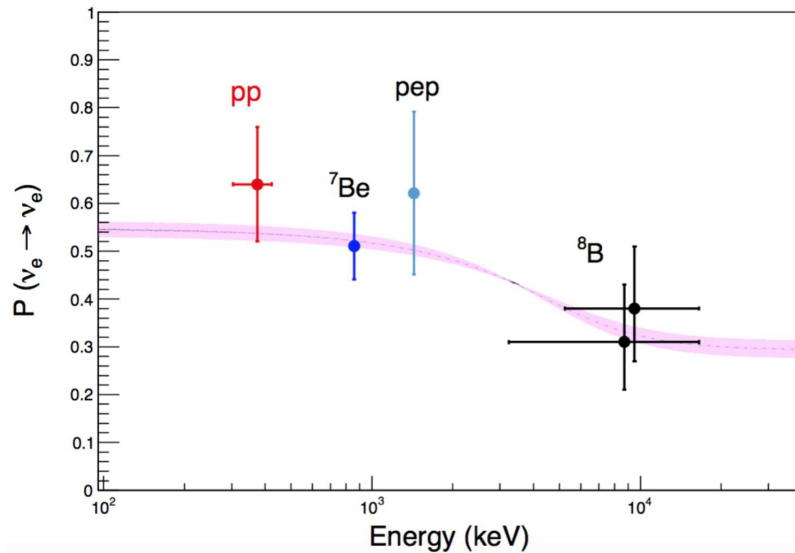


Figure 6: Survival probability of electron-neutrinos produced by the different nuclear reactions in the Sun. All the experimental numbers are from Borexino’s measurements. The violet band corresponds to the $\pm 1\sigma$ prediction of the MSW-LMA solution.

Apart from the result on the pp solar neutrinos flux, which has been obtained after the purification campaign, all the other solar neutrino components were measured with data sets coming from the so called Borexino Phase-I [26]. The Phase-II, which started right after the purification campaign at the end of Phase-I, is now close to its end, and this will hopefully lead to a general improvement of all the measurements of the solar neutrino fluxes. Particularly, the efforts of the Collaboration are pushing to achieve the best possible result (either an eventual measurement or an improvement of the limit) regarding the CNO flux determination. This would be of extreme importance, since the CNO flux has not been observed yet, and could solve the Solar Metallicity puzzle [5].

The Borexino detector will also be used to search for sterile neutrinos by means of and artificial anti-neutrino source in the framework of the SOX project [27].

6 Acknowledgements

The Borexino program is made possible by funding from the INFN (Italy); the NSF (USA); the BMBF, DFG and MPG (Germany); the JINR, RFBR, RSC and NRC Kurchatov Institute (Russia); and the NCN: Grant No. UMO-2013/10/E/ST2/00180 (Poland). We acknowledge the generous support of the Laboratori Nazionali del Gran Sasso (Italy) and that of the Gran Sasso Science Institute. The SOX project is funded by ERC with grant ERC-AdG-2012 N. 320873.

References

- [1] A. M. Serenelli, *Astrophys. Space Sci.* **328**, 13 (2010) doi:10.1007/s10509-009-0174-8.
- [2] F. Confortola *et al.* [LUNA Collaboration], *Phys. Rev. C* **75**, 065803 (2007) doi:10.1103/PhysRevC.75.065803.
- [3] W. J. Chaplin, A. M. Serenelli, S. Basu, Y. Elsworth, R. New and G. A. Verner, *Astrophys. J.* **670**, 872 (2007) doi:10.1086/522578.
- [4] S. Basu, W. J. Chaplin, Y. Elsworth, R. New, A. M. Serenelli and G. A. Verner, *Astrophys. J.* **655**, 660 (2007) doi:10.1086/509820.
- [5] C. Pena-Garay and A. Serenelli, arXiv:0811.2424 [astro-ph].
- [6] E. G. Adelberger *et al.*, *Rev. Mod. Phys.* **83**, 195 (2011) doi:10.1103/RevModPhys.83.195.
- [7] K. Abe *et al.* [Super-Kamiokande Collaboration], *Phys. Rev. D* **83**, 052010 (2011).
- [8] B. Aharmim *et al.* [SNO Collaboration], *Phys. Rev. C* **81**, 055504 (2010).
- [9] G. Alimonti *et al.* [Borexino Collaboration], *Astropart. Phys.* **16**, 205 (2002).
- [10] C. Arpesella *et al.* [Borexino Collaboration], *Astropart. Phys.* **18**, 1 (2002).
- [11] G. Alimonti *et al.* [Borexino Collaboration], *Nucl. Instrum. Meth. A* **600**, 568 (2009).
- [12] G. Bellini *et al.*, *Phys. Rev. Lett.* **107**, 141302 (2011).
- [13] G. Bellini *et al.* [Borexino Collaboration], *Phys. Lett. B* **707**, 22 (2012).
- [14] C. Galbiati, A. Pocar, D. Franco, A. Ianni, L. Cadonati and S. Schonert, *Phys. Rev. C* **71**, 055805 (2005) doi:10.1103/PhysRevC.71.055805
- [15] D. Franco, G. Consolati and D. Trezzi, *Phys. Rev. C* **83**, 015504 (2011) doi:10.1103/PhysRevC.83.015504
- [16] G. Bellini *et al.* [Borexino Collaboration], *Phys. Rev. Lett.* **108**, 051302 (2012).
- [17] G. Bellini *et al.* [Borexino Collaboration], *Nature* **512**, no. 7515, 383 (2014).
- [18] G. Bellini *et al.* [Borexino Collaboration], *Phys. Rev. D* **82**, 033006 (2010).
- [19] G. Bellini *et al.* [Borexino Collaboration], *Phys. Lett. B* **696**, 191 (2011).
- [20] M. Agostini *et al.* [Borexino Collaboration], *Phys. Rev. D* **92**, no. 3, 031101 (2015).
- [21] G. Bellini *et al.* [Borexino Collaboration], *Phys. Lett. B* **722**, 295 (2013).
- [22] P. Alvarez Sanchez *et al.* [Borexino Collaboration], *Phys. Lett. B* **716**, 401 (2012).
- [23] G. Bellini *et al.* [Borexino Collaboration], *Phys. Rev. D* **85**, 092003 (2012).
- [24] G. Bellini *et al.* [Borexino Collaboration], *Phys. Rev. D* **88**, no. 7, 072010 (2013).
- [25] M. Agostini *et al.* [Borexino Collaboration], *Phys. Rev. Lett.* **115**, 231802 (2015).
- [26] G. Bellini *et al.* [Borexino Collaboration], *Phys. Rev. D* **89**, no. 11, 112007 (2014).
- [27] G. Bellini *et al.* [Borexino Collaboration], *JHEP* **1308**, 038 (2013).

Monte Carlo simulations in neutrino physics: the example of the SOX experiment

A. Caminata¹, M. Agostini², K. Altenmüller², S. Appel², G. Bellini³, J. Benziger⁴, N. Berton⁵, D. Bick⁶, G. Bonfini⁷, D. Bravo⁸, B. Caccianiga³, F. Calaprice⁹, M. Carlini⁷, P. Cavalcante⁷, A. Chepurinov¹⁰, K. Choi¹¹, M. Cribier⁵, D. D'Angelo³, S. Davini¹², A. Derbin¹³, L. Di Noto¹, I. Drachnev¹², M. Durer⁵, A. Etenko¹⁴, S. Farinon¹, V. Fischer⁵, K. Fomenko¹⁵, A. Formozov^{3,15}, D. Franco¹⁶, F. Gabriele⁷, J. Gaffiot⁵, C. Galbiati⁹, C. Ghiano¹, M. Giammarchi³, M. Goeger-Neff², A. Goretti⁹, M. Gromov¹⁰, C. Hagner⁶, Th. Houdy⁵, E. Hungerford¹⁷, Aldo Ianni⁷, Andrea Ianni⁹, N. Jonquères¹⁸, K. Jedrzejczak¹⁹, D. Jeschke², M. Kaiser⁶, V. Kobychew²⁰, D. Korablev¹⁵, G. Korga⁷, V. Kornoukhov²¹, D. Kryn¹⁶, T. Lachenmaier²², T. Lasserre⁵, M. Laubenstein⁷, B. Lehnert²³, J. Link⁸, E. Litvinovich^{14,24}, F. Lombardi⁷, P. Lombardi³, L. Ludhova³, G. Lukyanchenko^{14,24}, I. Machulin^{14,24}, S. Manecki⁸, W. Maneschg²⁸, S. Marcocci¹², J. Maricic¹¹, G. Mention⁵, E. Meroni³, M. Meyer⁶, L. Miramonti³, M. Misiaszek^{7,19}, M. Montuschi²⁵, P. Mosteiro⁹, V. Muratova¹³, R. Musenich¹, B. Neumair², L. Oberauer², M. Obolensky¹⁶, F. Ortica²⁶, M. Pallavicini¹, L. Papp², L. Perasso¹, A. Pocar²⁷, G. Ranucci³, A. Razeto⁷, A. Re³, A. Romani²⁶, R. Roncin^{7,16}, N. Rossi⁷, S. Schönert², L. Scola⁵, D. Semenov¹³, H. Simgen²⁸, M. Skorokhvatov^{14,24}, O. Smirnov¹⁵, A. Sotnikov¹⁵, S. Sukhotin¹³, Y. Suvorov^{14,29}, R. Tartaglia⁷, G. Testera¹, J. Thurn²³, M. Toropova¹⁴, C. Veyssiére⁵, M. Vivier⁵, E. Unzhakov¹³, R.B. Vogelaar⁸, F. von Feilitzsch², H. Wang²⁹, S. Weinz³⁰, J. Winter³⁰, M. Wojcik¹⁹, M. Wurm³⁰, Z. Yokley⁸, O. Zaimidoroga¹⁵, S. Zavatarelli¹, K. Zuber²³, G. Zuzel¹⁹

¹Dipartimento di Fisica, Università degli Studi e INFN, Genova 16146, Italy

²Physik-Department and Excellence Cluster Universe, Technische Universität München, 85748 Garching, Germany

³Dipartimento di Fisica, Università degli Studi e INFN, 20133 Milano, Italy

⁴Chemical Engineering Department, Princeton University, Princeton, NJ 08544, USA

⁵Commissariat à l'Énergie Atomique et aux Énergies Alternatives, Centre de Saclay, IRFU, 91191 Gif-sur-Yvette, France

⁶Institut für Experimentalphysik, Universität Hamburg, 22761 Hamburg, Germany

⁷INFN Laboratori Nazionali del Gran Sasso, 67010 Assergi (AQ), Italy

⁸Physics Department, Virginia Polytechnic Institute and State University, Blacksburg, VA 24061, USA

⁹Physics Department, Princeton University, Princeton, NJ 08544, USA

¹⁰Lomonosov Moscow State University Skobeltsyn Institute of Nuclear Physics, 119234 Moscow, Russia

¹¹Department of Physics and Astronomy, University of Hawai'i, Honolulu, HI 96822, USA

¹²Gran Sasso Science Institute (INFN), 67100 L'Aquila, Italy

¹³St. Petersburg Nuclear Physics Institute NRC Kurchatov Institute, 188350 Gatchina, Russia

¹⁴NRC Kurchatov Institute, 123182 Moscow, Russia

¹⁵Joint Institute for Nuclear Research, 141980 Dubna, Russia

¹⁶AstroParticule et Cosmologie, Universit Paris Diderot, CNRS/IN2P3, CEA/IRFU, Observatoire de Paris, Sorbonne Paris Cit, 75205 Paris Cedex 13, France

¹⁷Department of Physics, University of Houston, Houston, TX 77204, USA

¹⁸Commissariat à l'Énergie Atomique et aux Énergies Alternatives, Centre de Saclay, DEN/DM2S/SEMT/BCCR, 91191 Gif-sur-Yvette, France

¹⁹M. Smoluchowski Institute of Physics, Jagiellonian University, 30059 Krakow, Poland

²⁰Kiev Institute for Nuclear Research, 06380 Kiev, Ukraine

²¹Institute for Theoretical and Experimental Physics, 117218 Moscow, Russia

²²Kepler Center for Astro and Particle Physics, Universität Tübingen, 72076 Tübingen, Germany

²³Department of Physics, Technische Universität Dresden, 01062 Dresden, Germany

²⁴National Research Nuclear University MEPhI (Moscow Engineering Physics Institute), 115409 Moscow, Russia

²⁵Dipartimento di Fisica e Scienze della Terra Università degli Studi di Ferrara e INFN, Via Saragat 1-44122, Ferrara, Italy

²⁶Dipartimento di Chimica, Università e INFN, 06123 Perugia, Italy

²⁷Amherst Center for Fundamental Interactions and Physics Department, University of Massachusetts, Amherst, MA 01003, USA

²⁸Max-Planck-Institut für Kernphysik, 69117 Heidelberg, Germany

²⁹Physics and Astronomy Department, University of California Los Angeles (UCLA), Los Angeles, California 90095, USA

³⁰Institute of Physics and Excellence Cluster PRISMA, Johannes Gutenberg-Universität Mainz, 55099 Mainz, Germany

DOI: <http://dx.doi.org/10.3204/DESY-PROC-2016-05/21>

The SOX project aims to test the existence of light sterile neutrinos. A solid signal would mean the discovery of the first particles beyond the Standard Electroweak Model and would have profound implications in our understanding of the Universe and of fundamental particle physics. In case of a negative result, it is able to close a long standing debate about the reality of the neutrino anomalies. The SOX experiment will use a ^{144}Ce - ^{144}Pr antineutrino generator placed at short distance from the Borexino liquid scintillator detector. Particular emphasis is devoted in describing how a simulation of a neutrino detector is implemented and how it can be used to obtain useful information for the future data analysis.

1 Introduction

Although most of the collected neutrino experimental data in neutrino flux rates and their oscillations fit well into the three-flavour oscillation model, several short-baseline neutrino experiments have reported anomalies which significantly deviates from the three active neutrino pictures ([1, 2, 3, 4]).

All these anomalies can be related to the presence of a fourth type of neutrino with Δm_{14}^2 of about 1 eV^2 . This new particle, not predicted from the standard model, is called sterile since it is not coupled with the Z^0 boson. The SOX project will exploit the unprecedented performances of the Borexino detector to investigate the existence of unexpected oscillations in the low L/E region and therefore investigate the existence of sterile neutrinos in the Δm_{14}^2

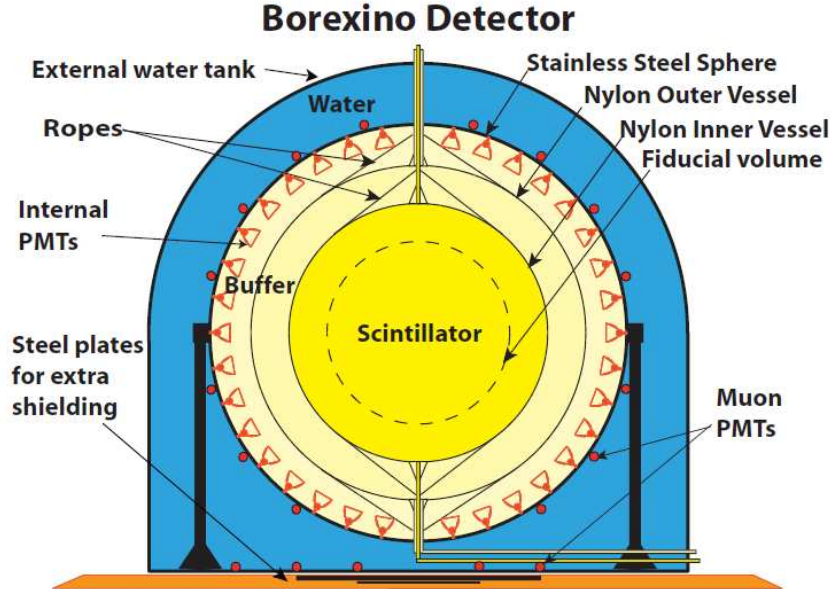


Figure 1: Schematic drawing of the Borexino detector.

region of $\sim 1 eV^2$ [5]. The first part of the project consists in deploying a 150 kCi $^{144}Ce-^{144}Pr$ $\bar{\nu}_e$ source in a dedicated pit located 8.5 m below the detector's center.

2 Antineutrino detection in Borexino

2.1 The Borexino detector

Borexino is an underground liquid scintillator detector located at Laboratori Nazionali del Gran Sasso in Italy [6]. It has an active mass of 278 tons of pseudocumene (PC, 1,2,4-trimethylbenzene), doped with 1.5 g/liter of PPO (2,5-diphenyloxazole, a fluorescent dye). The scintillator is contained in a thin nylon vessel (125 μm in thickness) and it is surrounded by two concentric PC buffers doped with 2 g/liter of DMP (dimethylphthalate), a component that quenches the PC scintillation light. The two PC buffers are separated by a second thin nylon membrane to prevent radon diffusion toward the scintillator. The scintillator and buffers are contained in a stainless steel sphere (SSS) with diameter of 13.7 m. The scintillation light is detected by 2212 8 inch PMTs uniformly distributed in the inner surface of the SSS. The detector energy and vertex reconstruction performances are respectively 5% at 1 MeV and 15 cm. Antineutrinos are detected in Borexino by means of inverse beta decay (IBD, 1.8 MeV threshold) on protons. IBD events are clearly tagged using the space-time coincidence between the prompt e^+ signal and the delayed neutron capture ($\tau = 254 \mu s$ [7]) event. Therefore, accidental background is almost negligible. A 18.0-m diameter - 16.9-m high domed water tank

(WT) containing 2100 tons of ultrapure water surrounds the SSS providing additional shielding against external background. Moreover, additional 208 8-inch PMTs instrument the WT and detect the Cherenkov light radiated by muons in the water shield, serving as muon veto. Right beneath the Borexino detector, there is a cubical pit (side 105 cm) accessible through a small squared tunnel (side 95 cm) that was built at the time of construction with the purpose of housing possible neutrino sources. The existence of this tunnel is one of the reasons why the ^{144}Ce source can be deployed with no changes to the Borexino layout. The center of the pit is at 8.5 m from the detector center, requiring a relatively high source activity for the source.

2.2 The antineutrino source

The antineutrino source must accomplish to several requirements. To get a reasonable number of interaction inside the active volume, an activity of about 100 kCi is required. Moreover, since antineutrinos are detected via inverse beta decay (IBD), an energy spectrum that extends above the IBD threshold is necessary. Furthermore, the half-life must be reasonably long to produce and transport the source nearby the detector. The ^{144}Ce source β -decays to ^{144}Pr ($t_{1/2} = 296$ days) which rapidly ($t_{1/2} = 17$ min) β -decays to ^{144}Nd emitting a spectrum of $\bar{\nu}_e$ part of which falls above the IBD threshold (the endpoint of the ^{144}Pr decay is about 3 MeV). The $^{144}\text{Ce} - ^{144}\text{Pr}$ source has been identified as a suitable $\bar{\nu}_e$ emitter having a long enough half-life to allow the source production and the transportation to LNGS.

The production of the source can be realized by isolating and extracting ^{144}Ce from spent nuclear fuel (SNF). The source is produced as few kilograms of CeO_2 containing a few tens of grams of ^{144}Ce . The source emits also gamma rays that have to be shielded both for biological protection purposes and to avoid source-induced background. Consequently a cylindrical tungsten alloy shielding (density greater than 18 g/cm^3) surrounds the source (which is contained in a stainless steel capsule). The shielding, 60 cm in height and diameter, has been designed driven by the 2.185 MeV gamma ray emitted with 0.7% intensity. Such dimensions ensure a 19-cm thick shielding and a 10^{12} gamma-ray attenuation factor along any directions.

3 Data analysis

Borexino can study short distance neutrino oscillations in two ways. The first way is the standard disappearance technique (rate technique): if oscillations into sterile neutrino occur, the total count rate in the detector is lower than the expected rate without oscillations. Knowing the source activity (section 3.1) and measuring the interaction rate, it is possible to investigate the existence of the sterile neutrino state. The second way is based on an oscillometry measurement within the detector volume (shape technique).

If the values of m_{14}^2 are of the order of 1eV^2 and the antineutrino energy is of the order of 1 MeV, the typical oscillation length is about a few meters, being smaller than the detector typical dimension and greater than the spatial resolution. Consequently, the resulting oscillations waves can be directly seen in Borexino and a direct measurement of m_{14}^2 and θ_{14} can be performed (figure 2). Figure 3 shows the best fit values for the current allowed phase space. Consequently, from the plot it is clear that the SOX experiment will investigate almost all the region of the neutrino anomaly.

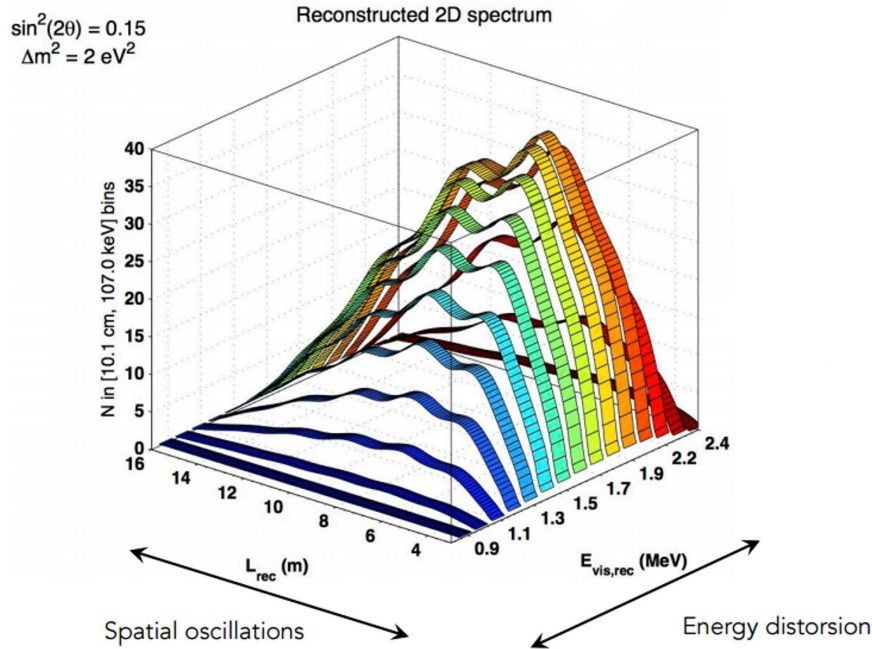


Figure 2: Oscillometry: waves in the reconstructed 2D spectrum for $m_{14}^2 = 2eV^2$ and $\sin^2(2\theta_{14}) = 0.15$.

3.1 Calorimetric measurement

In case of rate analysis, it is fundamental to have a precise measurement (uncertainties below 1%) of the source activity. In order to infer the source activity, the heat released by the source is measured by two calorimeters (INFN-TUM and CEA). Both the calorimeters have been conceived to measure the source activity with high precision by knowing the power released by the radiation in the tungsten shield and absorbed by a water flow. In the INFN-TUM calorimeter, the water flows inside a copper heat exchanger in contact with the tungsten shield [8], while in the CEA calorimeter, the source with the tungsten is directly immersed in the water contained in the calorimeter apparatus. In both systems, neglecting the heat losses (that are measured by a calibration apparatus), the power is measured from the difference between the water temperature entering and exiting from the calorimeter and from the water mass flow.

4 Monte Carlo simulation code and the physics modelling the detector response

In order to properly take into account efficiencies and signal properties, for both the rate and shape analyses, a deep understanding of the detector behavior is necessary. Consequently, a full Monte Carlo simulation code has been developed.

Particles depositing energy in the scintillator produce light (both scintillation and Cherenkov

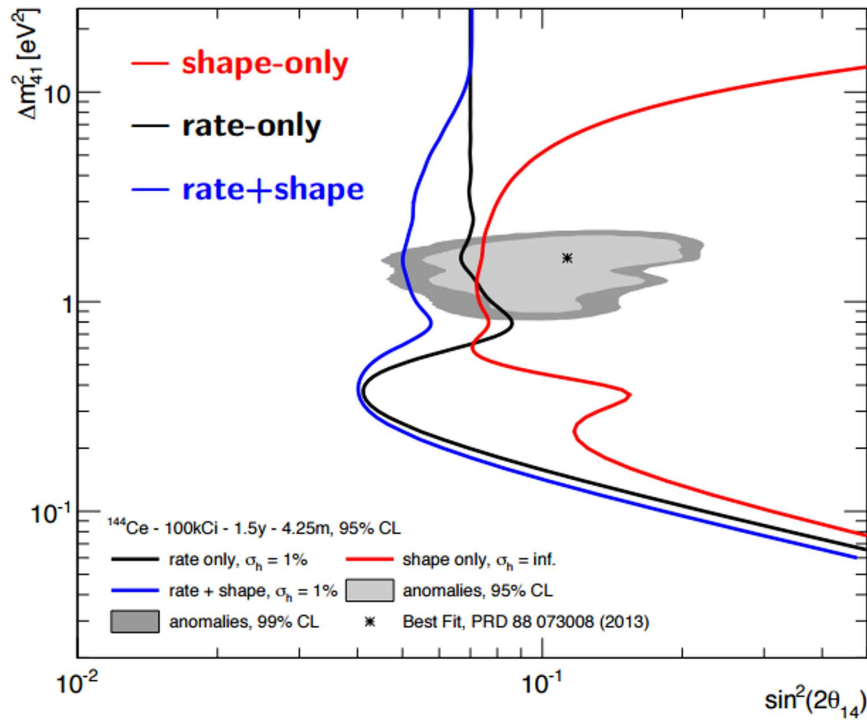


Figure 3: Neutrino anomaly region and foreseen sensitivity for SOX.

effect) which propagates inside the detector and it is detected by the 2212 PMTs. For each event, it is important to relate measurable quantities (the number of photons measured and the charge collected by each PMT, the time of arrival of each photon) with physical properties of the event (energy, position, particle identification). Consequently, a precise knowledge of the detector response for different particle types and energies is important for properly connecting measurable and physical quantities. The method of evaluation of the detector response function is based on a Monte Carlo simulation. This code is able to predict the shapes of the signal and the background both for SOX and solar neutrino analysis. The simulation takes into account all the processes that can influence the energy deposits inside the detector. The scintillation and Cherenkov light emission, the light propagation and detection processes are fully simulated. Moreover the read-out electronics is simulated as well. The Monte Carlo simulation output is a raw data file with the same format of the real data raw file, allowing an identical data processing. The simulation of the whole detector, from the energy deposit up to the detection of light is simulated using the standard GEANT4 [9] package. The simulation of the readout electronics is performed with a custom c++ code. In view of the Borexino phase II solar neutrino analysis and the SOX measurement, the Monte Carlo code has been extended. Particular attention has been devoted in developing generators for sterile neutrino signal as well as in improving the reliability of the light collection and the detector's response for events far away from the center. The code has been widely used for solar neutrino analysis and has been tested and validated deploying calibration sources inside the active volume and comparing the simulation

result with the acquired data (an example is reported in figure 4).

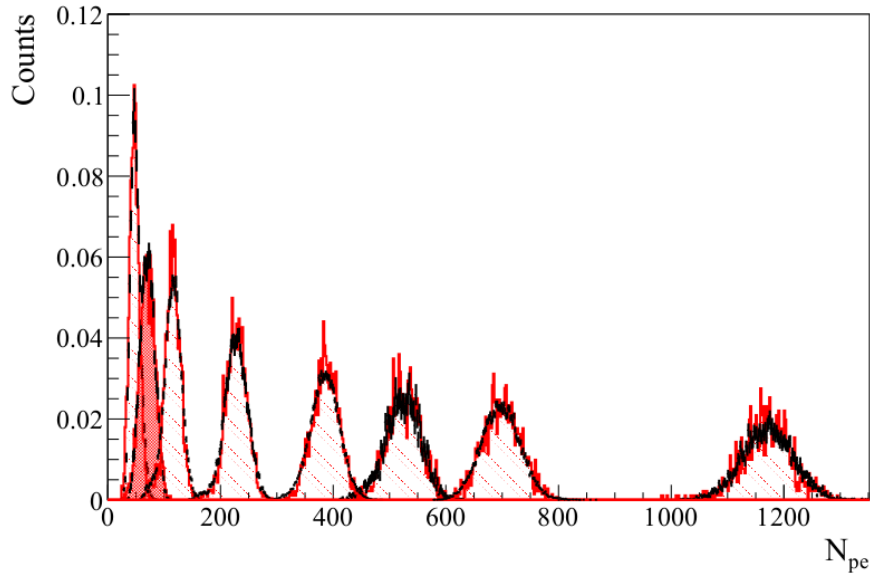


Figure 4: Comparison between data and Monte Carlo: several radioactive gamma sources have been deployed in the scintillator. In black the collected charge for real events, in red for simulated events. The agreement is better than 1%.

5 Conclusions

The Borexino detector is an ideal tool to search for sterile neutrinos. It is possible to test the existence of sterile neutrinos using an anti-neutrino source with almost negligible background. A deep knowledge of the detector response is fundamental for a proper interpretation of the acquired data. Consequently a Borexino Monte Carlo simulation code has been developed. In the last years the code has been refined and extended to take into account the SOX needs. Calibration campaigns with radioactive sources have been performed over the years. A new calibration is foreseen for the end of this year allowing a final tuning of the code before the start of the data-taking expected for the first part of 2017.

References

- [1] Aguilar A *et al.* 2001 *Phys. Rev. D* **64** 112007
- [2] Aguilar A *et al.* 2013 *Phys. Rev. Lett.* **110** 161801
- [3] Mention G *et al.* 2011 *Phys. Rev. D* **83** 073006
- [4] Giunti C and Laveder M 2011 *Phys. Rev. C* **83** 065504
- [5] Bellini G *et al.* 2013 *JHEP* **38** 1308
- [6] Bellini G *et al.* 2014 *Phys. Rev. D* **89** 112007
- [7] Agostini M *et al.* 2015 *Phys. Rev. D* **92** 031101

- [8] Farninon S *et al.* 2016 *INFN technical note INFN-16-08/GE*
- [9] Geant4 Collaboration, Physics Reference Manual

Solar neutrino detection in a large volume double-phase liquid argon experiment

Davide Franco

APC, Université Paris Diderot, CNRS/IN2P3, CEA/Irfu, Observatoire de Paris, Sorbonne Paris Cité, Paris 75205, France

DOI: <http://dx.doi.org/10.3204/DESY-PROC-2016-05/14>

Two-phase liquid argon time projection chambers (LAr TPCs) are prime candidates for the ambitious program to explore the nature of dark matter. The large target, high scintillation light yield and good spatial resolution in all three cartesian directions concurrently allows also a high precision measurement of solar neutrino fluxes via elastic scattering. We studied the cosmogenic and radiogenic backgrounds affecting solar neutrino detection in a 100 tonne fiducial LAr TPC operating at LNGS depth. Such a detector has the potential to measure the CNO neutrino rate with 5σ sensitivity, and to significantly improve the precision on the measured ${}^7\text{Be}$ and *pep* neutrino fluxes.

1 Introduction

The study of solar neutrinos has given a fundamental contribution to both astroparticle and elementary particle physics, offering an ideal test of solar models and, at the same time, relevant indications on the fundamental interactions among particles. Radiochemical (Homesake [1], GALLEX/GNO [2, 3], SAGE [4]) and real-time experiments (Kamiokande [5], SuperKamiokande [6], SNO [7] and Borexino [8]) have already measured the solar neutrino components from the ${}^7\text{Be}$, ${}^8\text{B}$, *pep*, and *pp* reactions, all belonging to the dominant mechanism for the energy production in the Sun: the proton-proton chain. At the same time, no neutrino from the ${}^{13}\text{N}$, ${}^{15}\text{O}$, and ${}^{17}\text{F}$ reactions, from the CNO cycle, has been yet observed. The CNO cycle has a key role in astrophysics, since it is the dominant source of energy in stars more massive than the Sun and in advanced evolutionary stages of solar-like stars. In addition, constraining the chemical composition of the Sun will improve astrophysical models like for star formation and Super Nova explosion.

CNO neutrinos may also solve the long-standing and well-known solar metallicity problem. The abundance of the heavy elements, Z (aka metals) in the Sun is a critical parameter in the SSM, since it affects the radiative opacity, and the boundary definition of the convective zone. In particular, abundances of oxygen, carbon, and nitrogen have a direct impact on the energy production of the Sun via the CNO cycle. The SSM predicts different neutrino fluxes if assuming either high- Z [9] or low- Z [10] chemical compositions in the Sun. The largest discrepancy in the prediction of solar neutrino fluxes resides in the CNO component: a measurement of the CNO neutrino flux at 10-20% accuracy has the potential to solve the metallicity problem.

The most stringent experimental limit on the CNO neutrino rate is from Borexino [8] using elastic neutrino-electron scattering. They obtained an upper limit for the interaction rate of

Neutrino Source	Low Metallicity (LZ)		High Metallicity (HZ)	
	All	[0.6-1.3] MeV	All	[0.6-1.3] MeV
pp	107.9 ± 2.0	0	107.0 ± 2.0	0
pep	2.28 ± 0.05	1.10 ± 0.02	2.23 ± 0.05	1.07 ± 0.02
${}^7\text{Be}$	36.10 ± 2.60	2.85 ± 0.21	39.58 ± 2.85	3.13 ± 0.23
CNO	3.06 ± 0.30	0.64 ± 0.06	4.28 ± 0.44	0.90 ± 0.09
${}^8\text{B}$	0.30 ± 0.04	0.035 ± 0.005	0.36 ± 0.06	0.042 ± 0.007
Total		4.63 ± 0.22		5.14 ± 0.25

Table 1: Expected solar neutrino rates in cpd/100 tonne of LAr active mass, comparing the low-metallicity [11] and high-metallicity [12] predictions using the Standard Solar Model and neutrino oscillation parameters from the MSW-LMA [13] region with $\Delta m^2 = 7.54 \times 10^{-5} \text{ eV}^2$ and $\sin^2(\theta_{12}) = 0.307$.

7.9 counts per day per 100 tonnes (cpd/100 tonne) at the 95% C.L., which corresponds to a flux limit of $<7.9 \times 10^6 \text{ cm}^{-2} \text{ s}^{-1}$ [8]. Despite the contamination from ${}^{210}\text{Bi}$ in the active mass of Borexino is exceptionally low (~ 20 cpd/100 tonne), its spectral shape is very similar to the expected CNO signal, precluding a positive observation of CNO neutrinos.

Liquid argon (LAr) may represent the ideal target for measuring the CNO neutrino component from the Sun. LAr, in fact, is a powerful scintillator, 4-5 times brighter than organic liquid scintillators and, as a liquefied noble element, does not react and does not bond with chemical species. In addition, the use of a two-phase time projection chamber (TPC) technique can further abate the background. In a two-phase TPC, a thin gas layer above the LAr target volume converts the ionization electrons, once extracted and accelerated by an electric field, in a secondary light signal by gas proportional scintillation. LAr TPC can determine the position of energy deposit events in the liquid to within a few mm in the drift direction, and ~ 1 cm or better in the two transverse directions, removing backgrounds from surfaces with a sharp definition of a fiducial volume. Moreover, the identification of multiple-Compton scatter events and other events having multiple energy deposition sites.

The overall solar neutrino-electron scattering rate expected in LAr is ~ 150 cpd/100 tonne, as shown in table 1. However, the spectral range below 0.6 MeV is inaccessible due to the intrinsic contamination of ${}^{39}\text{Ar}$, a β -decay ($Q = 0.565 \text{ MeV}$) produced by cosmic ray spallation of ${}^{\text{nat}}\text{Ar}$. Argon extracted from underground gas wells (UAr) has been shown by the Darkside collaboration to contain only $\sim 0.7 \text{ mBq/kg}$ of ${}^{39}\text{Ar}$ [14]. But even this level would prevent extraction of solar neutrino signals in the low energy region, which is dominated by pp neutrinos. However, ${}^7\text{Be}$ neutrino interactions, whose Compton-like edge is expected at $\sim 0.66 \text{ MeV}$, would be accessible thanks to the excellent energy resolution achievable in LAr.

Assuming a light yield of 6,000 photoelectrons / MeV, as measured by MicroCLEAN [15], the number of expected CNO neutrinos, interacting via elastic scattering in 400 tonne \times year exposure of LAr and above 0.6 MeV, is between ~ 900 and 1,300 events, depending on the metallicity model, as shown in figure 1. The main limitation to their detection is the background from *in situ* produced cosmogenic isotopes, radon emanated from the detector inner walls and distributed throughout the purification/recirculation loop, and from the external background. In the following sections, we will review the impact of each contaminant on the solar neutrino detection with a 100 ton fiducial mass two-phase LAr TPC .

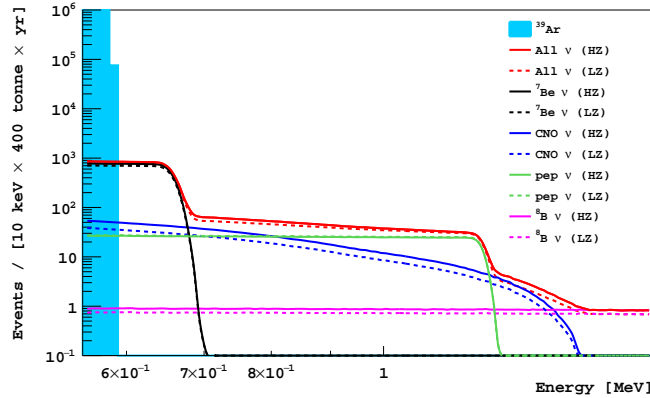


Figure 1: Simulated solar neutrino spectra in a 400 tonne-yr LAr TPC exposure, assuming $\sigma = 1.3\%$ energy resolution at 1 MeV, corresponding to a PE yield of 6 PE/keV. The blue shaded area represents the tail of the ^{39}Ar contamination, intrinsic to underground LAr.

2 The background

The detector is assumed to be located at the Gran Sasso Laboratory, shielded by 1,400 m of rock. Despite the deep underground location, the residual muon flux may still produce measurable amounts of radioactive isotopes by muon-induced spallation on argon. These can produce dangerous, delayed electron-recoil background in the solar neutrino energy window. The cosmogenic radionuclide production was simulated with FLUKA assuming a cylindrical TPC of 3.3 m radius and 3 m height. The TPC sidewall is a 3 cm thick teflon layer, and the top and bottom ends are covered with 2 mm thick silicon layers, representing silicon photomultiplier arrays. The 2 cm thick gaseous argon region sits just below the upper silicon layer. The TPC is contained in a 3 mm thick cylindrical stainless steel cryostat with 3.5 m radius and 3.2 m height. Gaseous argon is also present in the cryostat, outside the TPC region and above the LAr level. The cryostat is housed in a Borexino-like veto detector consisting of a 6 m radius stainless steel sphere filled with liquid scintillator placed within a larger cylindrical tank (17 m height, 16 m diameter) filled with water. Cosmic muons were generated 3 m above the cylindrical water tank, crossing 0.7 m rock layer, in order to fully develop the hadronic showers.

The simulation resulted in the production of more than 80 isotopes by muon spallation on argon, each of them handled by a GEANT4-based simulation, which generated decays and tracked the products in the full detector geometry. This allowed to estimate the efficiency of the multiple scattering cut. The predicted single scatter background induced by cosmogenic isotopes is evaluated in 0.733 cpd/100 tonne a factor ~ 7 lower than the overall neutrino signal in the energy region of interest between 0.7 and 1.3 MeV. The dominant contribution comes from ^{32}P , ^{38}Cl , and ^{32}P , with a decay rate of 0.332, 0.147, and 0.106 cpd/100 tonne respectively [16].

The external background contribution is due to radioactive contaminants in the detector materials. The largest contributions are expected to have origin in the photosensors and in the cryostat. Gamma-rays are the only events able to reach the active mass and to produce

a signal that can mimic a neutrino event. The strategy to abate this class of background is primarily based on the multiple scattering cut and on the fiducialization of the active volume. We estimated that the attenuation lengths for γ 's induced by ^{40}K , ^{214}Bi , and ^{208}Tl originating in the photosensors are of the order of ~ 4 cm. As a consequence, a 30 cm cut from the TPC walls in combination with the multiple scattering cut, would reduce such contamination by a factor $\sim 10^6$.

In the present work we assume 2 mm thick silicon photomultipliers (SiPM) as photosensors, on the top and bottom of the TPC, corresponding to ~ 300 kg of silicon. A recent measurement by I. Ostrovskiy *et al.* [17] quoted an overall contamination in SiPM from ^{40}K , and the ^{238}U and ^{232}Th smaller than 0.1 mBq/kg. In the here-proposed detector, this activity corresponds to an upper limit of 30 mBq. After the selection cuts, the external background contribution from the SiPM's of $\sim 2.6 \times 10^{-3}$ cpd/100 tonne, negligible with respect to the solar neutrino rate.

The dominant contribution for the external background is expected coming from the cryostat, whose mass is of the order of the tonne-scale. Stainless steel cryostats are contaminated in ^{60}Co at the level of tens of mBq/kg. The correspondent activity in the LAr target was estimated to be of the same order of the solar neutrino interaction rate in the energy window of interest, assuming a fiducial volume of 30 cm from the TPC walls. The ^{60}Co issue could be solved by either applying stronger fiducial volume cuts or by making the cryostat of titanium, which is almost free of ^{60}Co [18]. Further, an external active veto as in DarkSide-50 [19] would further reduce the ^{60}Co background by vetoing events with ^{60}Co gammas detected in coincidence by the TPC and the veto. In the sensitivity study described in this work, we then assume negligible the background from external sources.

Contamination of the target argon mass by ^{222}Rn represents the most critical background for the solar neutrino measurements. ^{222}Rn can be emanated into the active argon from the TPC materials in contact with the LAr target and/or distributed throughout the LAr fill by the recirculation loop. The main goal of this work is to evaluate the maximum contamination of ^{222}Rn not preventing the CNO neutrino measurement. In particular, only the ^{214}Pb and ^{214}Bi isotopes of the ^{222}Rn decay segment can provide a signal that could mimic the neutrino one. In fact, α 's can be efficiently discriminated by the use of the LAr scintillation pulse shape discrimination, which has a rejection power at the 10^7 – 10^8 level [20]. β -decays with simultaneous emission of γ -rays produce multi-site energy deposits, that can be identified and rejected by means of the multiple scattering cut. The simulations indicate that only 6.9% (5.9%) of ^{214}Pb (^{214}Bi) decays will produce a single site deposit in the solar neutrino energy region. However, despite most of the ^{222}Rn induced events can be rejected, the residual contamination represents a serious background: we estimated that $45 \mu\text{Bq}/(100 \text{ tonne})$ of ^{222}Rn contamination would introduce a background rate equivalent to the expected solar neutrino signal. The overall spectrum, including all the contaminations, is shown in figure 2.

3 Sensitivity study

The measurement of the rate of each solar neutrino component relies on the identification of the individual spectral shapes. To study the sensitivity of a large LAr TPC we exploited a toy Monte Carlo approach. The data sample was produced by generating the neutrino signal and the background components discussed in the previous section, assuming a $400 \text{ tonne} \times \text{yr}$ statistics. The data sample was generated for each metallicity model and for a given radon

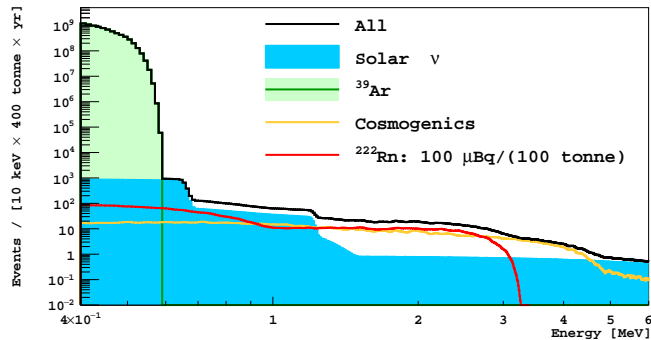


Figure 2: Components of the electron recoil energy spectrum, simulated for a 4 year exposure of 100 tonnes of LAr (see legend), assuming a radon contamination in LAr of $100 \mu\text{Bq}/(100 \text{ tonne})$.

contamination, and then fitted with an analytical model. The procedure was repeated 10,000 times for each set of parameters. An example of fit is shown in figure 3

The cosmogenic spectrum was observed to be rather flat after the multiple scattering cut, with the exception of the contribution from ^{32}P , as shown in figure 3. Cosmogenics have been then modeled with a linear energy function plus the beta shape from ^{32}P . The systematics associated to this model choice was deeply investigated and, as shown in reference [16], can be assumed negligible.

The CNO spectral shape is similar to that of the low energy radon component. At radon contamination levels above $200 \mu\text{Bq}/(100 \text{ tonne})$, the fit shows a systematic deviation from the central value of the simulated CNO component (SSM-LZ) by a few percent, implying that to guarantee a correct CNO measurement, the radon activity must be reduced below this level. No systematic deviations were observed for ^7Be and pep , whose spectral shapes have clear characteristic features.

4 Conclusions

The final results are summarized in figure 4. Assuming to be able to contain the radon contamination below $200 \mu\text{Bq}/(100 \text{ tonne})$, a LAr TPC with an exposure of $400 \text{ tonne} \times \text{years}$ exposure, has the power to observe ($>5 \sigma$) CNO neutrinos and to measure ^7Be and pep neutrinos with a statistical accuracy of $\sim 2\%$ and $\sim 10\%$, respectively. At the same time, the associated systematics connected to the definition of the fiducial volume and to the determination of the energy scale were evaluated to be less than 1%, thanks to the exceptional resolution in the position reconstruction and to the light yield, more than 10 times larger than in an organic liquid scintillator (more details can be found here: [16]).

In conclusion, a large volume LAr TPC, designed for direct dark matter WIMP search, has also the potential to experimentally observe the CNO neutrinos from the Sun, and, more in general, to provide a rich set of physics results for solar neutrinos.

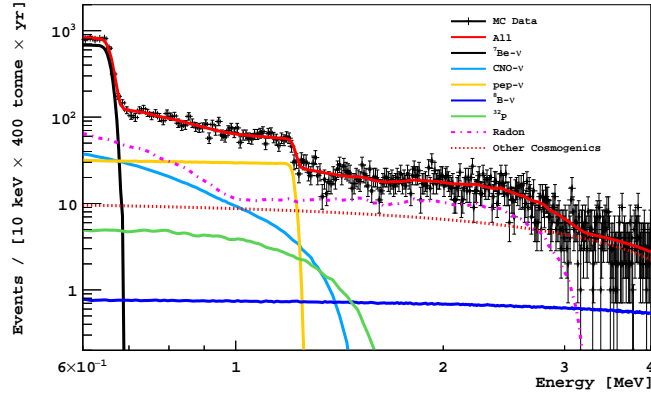


Figure 3: Example of simulated spectra and fit, assuming radon contaminations of $100 \mu\text{Bq}/(100 \text{ tonne})$, assuming the low-metallicity SSM. The cosmogenic component is modeled with a first degree polynomial, with the exception of an explicit spectrum for ^{32}P .

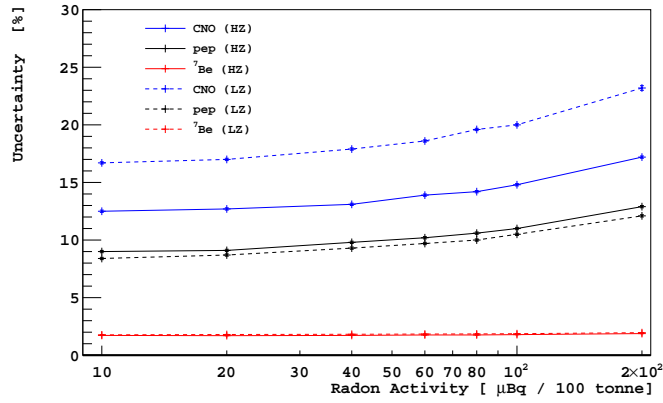


Figure 4: Statistical uncertainties on the solar neutrino components, as a function of the radon activity.

5 Acknowledgments

We acknowledge the financial support from the UnivEarthS Labex program of Sorbonne Paris Cité (ANR-10-LABX-0023 and ANR-11-IDEX-0005-02).

References

- [1] R. Davis, D. S. Harmer, K. C. Hoffman, Phys. Rev. Lett. **20** (1968) 1205.
- [2] W. Hampel et al. (GALLEX Collaboration), Phys. Lett. **B420** (1998) 114.
- [3] M. Altmann et al. (GNO Collaboration), Phys. Lett. B. **490**, 16 (2000).
- [4] J.N. Abdurashitov et al. (SAGE collaboration), Phys. Rev. C **80**, 015807 (2009).
- [5] Y. Fukuda et al. (Kamiokande Collaboration), Phys. Rev. Lett. **77** (1996) 1683
- [6] Y. Fukuda et al. (Super-Kamiokande Collaboration), Phys. Rev. Lett. **81**, 1562 (1998).
- [7] B. Aharmim et al. (SNO Collaboration), Phys. Rev. C **72**, 055502 (2005).
- [8] G. Bellini et al. (Borexino Collaboration), Phys. Rev. D **89** 112007 (2014).
- [9] N. Grevesse and J. Sauval, Space Science Reviews **85** (1998) 161.
- [10] M. Asplund et al., Ann. Rev. Astr. & Astrophys. **47** (2009) 481.
- [11] M. Asplund *et al.*, Ann. Rev. Astron. Astroph. **47** (2009) 481.
- [12] N. Grevesse, A. J. Sauval, Spece Sci. Rev. **85** (1998) 161.
- [13] S. P. Mikheyev and A. Yu. Smirnov, Sov. J. Nucl. Phys. **42** (1985) 913; L. Wolfenstein, Phys. Rev. D **17** (1978) 2369.
- [14] P. Agnes *et al.* (DarkSide Collaboration) Phys. Rev. D **93** (2016) 081101.
- [15] W. H. Lippincott *et al.*, Phys. Rev. C **81** (2010) 045803.
- [16] D. Franco *et al.*, arXiv:1510.04196 (2015).
- [17] I. Ostrovskiy *et al.*, IEEE T. Nucl. Sci. **62** (2015) 1825.
- [18] D. S. Akerib *et al.* (LZ Collaboration) arXiv:1509.02910 (2015).
- [19] P. Agnes *et al.* (DarkSide Collaboration) JINST **11** 03 (2016) 03016.
- [20] P. Agnes *et al.* (DarkSide Collaboration) Phys. Lett. B **743** (2015) 456.

Neutrino Astrophysics with JUNO

Sebastian Lorenz¹ for the JUNO collaboration

¹Johannes Gutenberg-Universität Mainz – Institut für Physik
Staudingerweg 7, 55128 Mainz, Germany

DOI: <http://dx.doi.org/10.3204/DESY-PROC-2016-05/20>

The Jiangmen Underground Neutrino Observatory will aim for the determination of the neutrino mass hierarchy with a medium baseline reactor $\bar{\nu}_e$ oscillation experiment. With its 20 kt liquid scintillator detector, it will also be sensitive to astrophysical low-energy neutrinos. In case of a typical galactic core-collapse supernova, ~ 5000 neutrino interactions will be detected via the inverse beta decay alone. Moreover, a 3σ evidence for the diffuse supernova neutrino background seems within reach after ten years of measurement. The performance of the experiment's solar neutrino program will decisively depend on the achieved radiopurity and cosmogenic background rejection efficiency.

As underlined by the ongoing measurements of solar neutrinos by BOREXINO [1], the search for the *diffuse supernova neutrino background* (DSNB) with SUPER-KAMIOKANDE [2] or the general waiting for the next core-collapse *supernova* (SN) after SN1987A [3] that provides a neutrino signal, neutrino astrophysics is a vivid, interdisciplinary field in neutrino physics. Measurements of astrophysical low-energy neutrinos by finished and still running experiments already provided valuable information on the light neutral leptons and their extraterrestrial sources. However, the answering of currently outstanding questions concerning SN neutrinos, the DSNB or ν_e 's from the Sun requires neutrino observatories of the next generation. The *Jiangmen Underground Neutrino Observatory* (JUNO) [4, 5], although under construction for a different primary purpose, prepares to aid with their answering.

A brief overview of the main goal of JUNO and the design of its 20 kt liquid scintillator detector is subject of Section 1. The use of the detector to collect a high-statistics neutrino sample with energy, time and partial flavor information in case of a galactic core-collapse SN is topic of Section 2. Besides the opportunity to learn more about the properties of neutrinos, such a sample of SN- ν events will be a critical test for models of stellar collapses. The estimated performance of JUNO to detect the predicted flux of low-energy neutrinos from past core-collapse SNe, the DSNB, is covered in Section 3. Finally, Section 4 outlines a possible solar neutrino program of JUNO.

1 The JUNO project

The JUNO project is an international undertaking centered on the construction of a 20 kt liquid scintillator neutrino detector in the south of China. Its primary goal is the determination of the neutrino *mass hierarchy* (MH). This means to answer the question whether the third neutrino mass eigenvalue m_3 is larger (Δm_{31}^2 and $\Delta m_{32}^2 > 0$; $\Delta m_{ij}^2 = m_i^2 - m_j^2$) or smaller (Δm_{31}^2 and

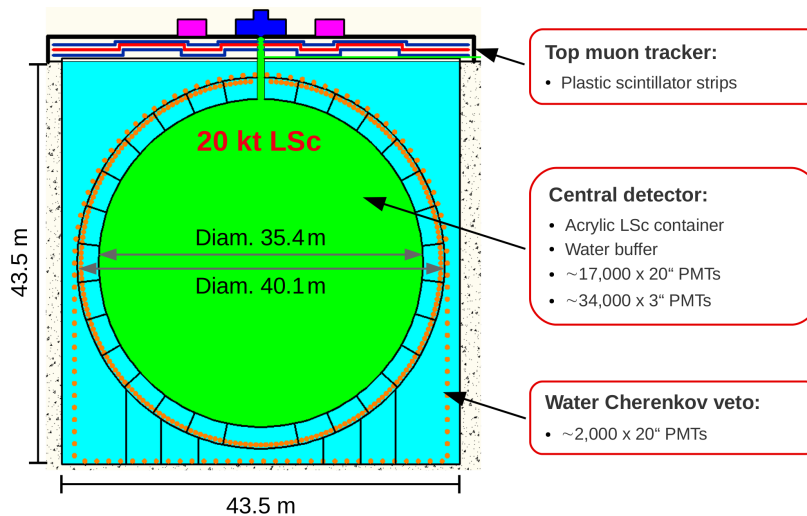


Figure 1: Design of the 20 kt liquid scintillator detector of JUNO. For details see [4, 5].

($\Delta m_{32}^2 < 0$) than the other two mass eigenvalues m_1 and m_2 , which are known to be separated by $\Delta m_{21}^2 > 0$. To do so, a precise measurement of the hierarchy-dependent oscillatory fine structure in the energy-dependent survival probability of reactor $\bar{\nu}_e$'s will be performed. Two nuclear reactor complexes with about 53 km distance to the detector will provide the $\bar{\nu}_e$ flux of interest. The measurement procedure requires an energy resolution of 3% at 1 MeV in order to discriminate the different hierarchy signatures (for details see [4]).

As usual for hydrocarbon-based detectors, the primary detection channel for the $\bar{\nu}_e$'s is the *inverse beta decay* (IBD) on free protons: $\bar{\nu}_e + p \rightarrow e^+ + n$. The signature from the coincidence of the prompt positron annihilation (on the order of nanoseconds) and the delayed neutron capture (after about $200 \mu\text{s}$) allows for an efficient background rejection. With about 100k IBD events, the expected median MH sensitivity of JUNO alone is around 3σ . This corresponds to six years of running with ten reactor cores and a total thermal reactor power of 36 GW.¹ Taking into account external information with 1.5-1% precision on the modulus of the atmospheric mass splitting $\Delta m_{\mu\mu}^2$ (a linear combination of Δm_{21}^2 , Δm_{31}^2 and Δm_{32}^2), the median sensitivity reaches 3.7-4.4 σ [4]. Additionally, the high-statistics reactor $\bar{\nu}_e$ measurement will reduce the uncertainty on the underlying (effective) flavor oscillation parameters $\sin^2 \theta_{12}$, Δm_{21}^2 and $|\Delta m_{ee}^2|$ to sub-percent level [4].

The site for the new neutrino observatory is located close to *Kaiping*, about 150 km west of *Hong Kong* and about 120 km south-west from *Guangzhou*. With JUNO being a funded project – and aiming for a start of data taking by 2020 – the first construction works for the underground laboratory started at the beginning of 2015. It will have a rock overburden of about 700 m (~ 1800 m w.e.), leaving an atmospheric muon event rate on the order of 3 s^{-1} in the detector.

Both the unprecedented liquid scintillator mass of 20 kt and the design requirements to reach the energy resolution goal will make JUNO advance the liquid scintillator technology beyond the

¹The total thermal reactor power at the start of data taking by 2020 will be 26.6 GW.

current state of the art. In the existing detector design, which is illustrated in Figure 1, the core component of the detector is the LAB-based liquid scintillator as designated neutrino target. It is contained in an acrylic sphere of 35.4 m inner diameter. Surrounded by ultra-pure water, the sphere is held in place by a stainless-steel latticed shell with 40.1 m inner diameter. The shell also holds the inward-facing photosensors. About 17,000 *photomultiplier tubes* (PMTs) with 20" diameter constitute the base system for the calorimetric energy measurement. Placed between the large PMTs, around 34,000 additional PMTs with 3" diameter provide a second calorimetry system and better timing for event position reconstruction. To reach the required energy resolution in terms of photon–electron statistics, the design goal for the *photoelectron* (pe) yield is about 1200 pe/MeV after non-uniformity corrections. This implies certain requirements for the PMT photocathode coverage ($\geq 75\%$), the maximum PMT quantum efficiency ($\geq 35\%$) and the liquid scintillator properties (attenuation length ≥ 20 m at 430 nm wavelength). Moreover, the energy resolution is also connected to a precise calibration of the energy scale, which must be ensured in the presence of dark noise from the PMTs and the electronics as well as finite vertex and PMT charge resolutions.

The described detector construct is submerged and anchored in a cylindrical water pool of 43.5 m height and diameter. Equipped with about 2,000 PMTs of 20" diameter, the ultra-pure water in the pool acts as Cherenkov-based atmospheric muon veto and as shielding against external radiation. A tracker composed of plastic scintillator strips for downward-going muons partially covers the pool on the top.

2 Neutrinos from a core-collapse supernova burst

The death of a massive star in a core-collapse SN is among the most violent phenomena in the visible universe. Most of the energy released in a SN burst, about 3×10^{53} erg, is carried away by myriads of neutrinos and antineutrinos of all flavors. They are produced at the origin of the final explosion, making the weakly interacting particles valuable messengers for information directly from the star's collapsing interior. The information they provide is complementary to the one from the optical SN signal and can be gathered even if the SN's visual appearance is obscured by galactic dust.

A flavor, time and energy resolved neutrino burst signal from a core-collapse SN would allow to test our current understanding of the dynamics inside a dying star (e.g., see [6]). In particular, theoretical expectations regarding different stages of the cosmic event, like the ν_e *burst*, the *accretion phase* and the *cooling phase*, or effects from (collective) neutrino flavor oscillations could be probed. Both gravitational wave data and an abruptly ending SN- ν signal could even indicate the formation of a black hole. As a consequence, the broad insights into core-collapse physics offered by SN- ν 's sets the collection of a high-statistics sample of these promising witnesses among the top priorities of neutrino astrophysics. Once operational, JUNO will stand by for the next of only 1-3 expected low-energy neutrino bursts per century from a galactic core-collapse SN.

Real-time detection of SN- ν 's with the liquid scintillator detector of JUNO will benefit from the very good energy resolution, the large target mass and partial flavor information. As listed in Table 10 of [4] for different SN- ν mean energies and a galactic core-collapse SN at a typical distance of 10 kpc,² between 4300 and 5700 SN- $\bar{\nu}_e$ events are expected in the IBD channel alone during the about 10 s lasting SN signal. However, the hydrocarbon-based target material offers

²Numbers are without flavor conversion effects.

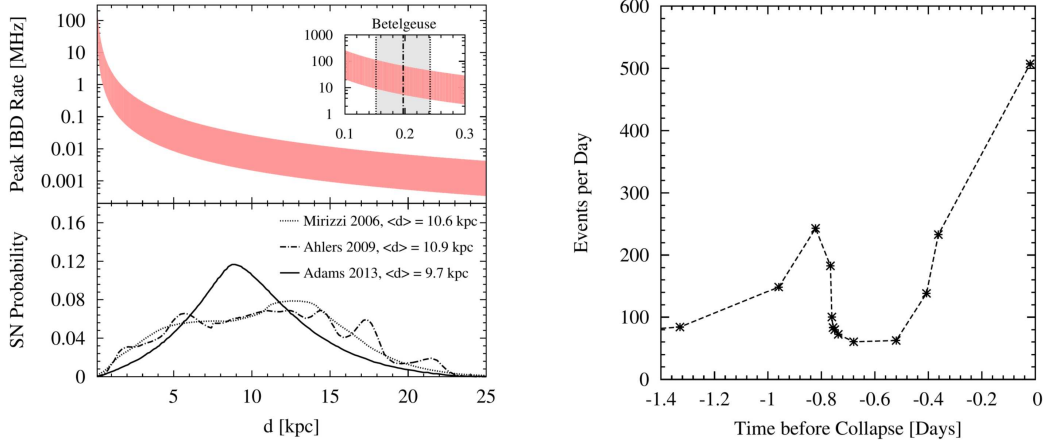


Figure 2: Left: Core-collapse SN probability (lower panel) based on different models and peak IBD event rate (upper panel) as a function of the distance to the SN. The inlay in the upper panel shows the expected peak IBD event rate specifically for *Betelgeuse* at 0.197 ± 0.045 kpc [8]. Right: Expected neutrino event rate in JUNO from the silicon burning stage of a massive $20 M_{\odot}$ star at 0.2 kpc distance as a function of the time before the SN explosion. The drop in the event rate after the silicon burned out gives information on the progenitor mass. Figures from [4].

additional opportunities for time-resolved detections of neutrino interactions: *Charged current* (CC) reactions on carbon nuclei, $\bar{\nu}_e + {}^{12}\text{C} \rightarrow e^+ + {}^{12}\text{B}$ and $\nu_e + {}^{12}\text{C} \rightarrow e^- + {}^{12}\text{N}$, probe the $\bar{\nu}_e$ flux, but additionally give access to the ν_e component. One *neutral current* (NC) interaction on carbon, $\nu(\bar{\nu}) + {}^{12}\text{C} \rightarrow \nu(\bar{\nu}) + {}^{12}\text{C}^*$, and elastic scattering on electrons are sensitive to the total neutrino flux. Even more NC events are expected to occur via elastic neutrino scattering on free protons [7]. These interactions are detectable in liquid scintillator, but require that the heavily quenched visible energy from the proton recoil is above the low-energy limit at about 200 keV, which is imposed by background from intrinsic ${}^{14}\text{C}$ decays. With 600 to 2000 expected events above this threshold, the elastic neutrino–proton scattering channel would have the second highest statistics.

JUNO will be sensitive mostly to galactic SNe. The large number of events in JUNO at such occasions provides detailed neutrino “light curve” spectra and allows to test core-collapse SN models. Due to the high event rate during the 10 s SN- ν signal, background is no serious concern. For SNe at larger distances R , the number of neutrino events decreases as $1/R^2$. As an example, only about 200 events are expected from the 50 kpc distant *Large Magellanic Cloud* where SN 1987A [3] exploded and produced the first and last measured SN- ν signal. The objective not to miss the next galactic core-collapse SN also means that the JUNO detector must not be “blinded” by neutrinos in case of a nearby incident. A particular close SN candidate is the around 0.197 kpc distant red supergiant *Betelgeuse* [8] with about 18 solar masses. If it becomes a SN, the expected peak IBD rate in JUNO reaches about 10^8 s^{-1} (see upper panel of Figure 2 left) for some tens of milliseconds roughly during the first 200 ms of the SN signal. This sets additional constrains for the design of the data acquisition.

Due to the capabilities of JUNO, the detector will surely become part of the *Supernova Early Warning System* (SNEWS) [9]. For close progenitors, e.g., *Betelgeuse*, the ultimate pre-

warning system is the detection of neutrinos from the short silicon-burning stage briefly before the explosion, as illustrated in Figure 2 right. Besides the use of such pre-SN neutrinos to verify stellar models, the sudden drop of the event rate when the silicon in the star burned out contains information on the progenitor mass.

Neutrinos from SNe can be used to locate the cosmic incident even if the visual appearance is obscured. One method relies on the study of the displacement between the IBD vertices from the prompt positron signal and the delayed neutron capture, which is statistically related to the original neutrino direction [10]. Assuming 5000 IBD events in JUNO, it is expected that the sky coordinates of the galactic core-collapse SN can be measured with about 9° uncertainty, perhaps even better.

3 Neutrinos from the diffuse supernova neutrino background

The DSNB is the flux of neutrinos from past core-collapse SNe in the visible universe. Its measurement would provide valuable information on the star formation rate, the average core-collapse neutrino spectrum and the rate of failed SNe. So far, only upper limits on the flux could be set by SUPER-KAMIOKANDE [2].

The DSNB sensitivity forecast for JUNO adopted the practice for the physics study of the *Low Energy Neutrino Astronomy* (LENA) project [11]. It relies on a parametric representation of the isotropic DSNB flux, where important ingredients are the SN rate as a function of red shift and the neutrino flux spectrum (for details see [4]). The latter was taken to be a Maxwell-Boltzmann distribution, which introduced the average neutrino energy as parameter with considered values between 12 and 21 MeV. Taking flavor conversion effects into account, it is assumed that the total energy release in neutrinos per core-collapse SN is distributed evenly between neutrinos and antineutrinos of all flavors. Therefore, the IBD channel is used to measure the $\bar{\nu}_e$ component of the DSNB flux with the liquid scintillator detector of JUNO.

About 0.9 to 1.7 DSNB events per year are expected for JUNO in the analysis energy window from 11 to 30 MeV after all cuts, depending on the average $\bar{\nu}_e$ energy. Below the lower limit of the visible energy window, the strong, irreducible background from reactor $\bar{\nu}_e$ dominates. At energies above the upper limit, CC interactions of atmospheric $\bar{\nu}_e$ are the dominant background. Moreover, the NC interactions of atmospheric neutrinos above 8 MeV can fake an IBD signal: If a neutron knocked-out from carbon scatters on protons, a prompt signal signature is created. The neutron capture subsequently makes the delayed signal. However, *pulse shape discrimination* (PSD) for the light³ signal of the prompt event and the search for a disexcitation of a left-behind ^{11}C nucleus can help to reduce this challenging background inside the energy range of interest. In fact, the PSD performance is decisive for the sensitivity to the DSNB. As for LENA, a NC background rejection efficiency of 98.9% at the cost of 50% of the signal is assumed. Due to the PSD and the energy cuts, backgrounds from cosmogenic isotopes and fast neutrons can be neglected. Table 13 in [4] lists expected DSNB detection significances after ten years of measurement with JUNO for different assumptions about the average neutrino energy and systematic background uncertainties. For favored DSNB parameters, a 3σ evidence for the DSNB signal seems within reach. As shown in Figure 3, a significant improvement of the

³The observed scintillation pulse shape of the liquid scintillator is different for traversing positrons and protons.

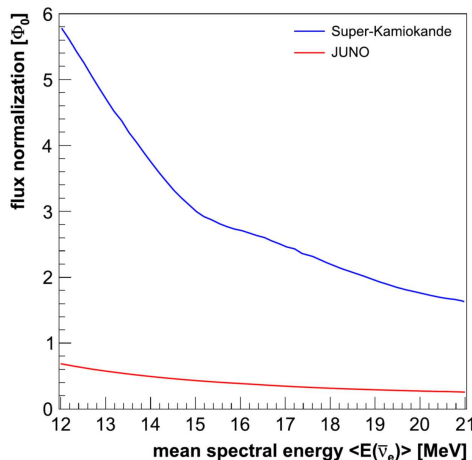


Figure 3: Predicted DSNB exclusion contour (90% C.L.; lower red line) if JUNO finds no DSNB signal above background after ten years of measurement. The upper limit for the DSNB flux normalization Φ_0 (for details see [4]) is given as a function of the mean energy of the SN- $\bar{\nu}_e$ spectrum $\langle E_{\bar{\nu}_e} \rangle$. For comparison, the upper limits from the SUPER-KAMIOKANDE results (upper blue line) presented in [2] are also shown. Figure from [4].

current upper limits on the DSNB flux from SUPER-KAMIOKANDE [2] can be made if there is no positive detection after ten years.⁴

4 Neutrinos from the Sun

Measurements of ν_e from the Sun, e.g., with SNO or BOREXINO [1], gave valuable insights into the energy release processes in our home star. Moreover, they enabled the study of neutrino flavor changes in surroundings with varying matter density, allowing first tests of predictions from the MSW effect (e.g., see Figure 5 in [13]). Yet there are still open issues: The solar metallicity, i.e., the composition of the Sun in terms of elements heavier than helium, is not conclusively determined. None of current solar models with different metallicities and opacities is in full agreement with neutrino measurements and observations from helioseismology. Moreover, looking at solar ν_e oscillations, the shape of the survival probability $P_{ee}(E_\nu)$ in the transition from the matter-dominated region at higher energies to the vacuum-dominated region at lower energies is not yet fixed. Especially the transition region around 3 MeV is sensitive to effects that can make P_{ee} deviate from the MSW *large mixing angle* (LMA) prediction.

Solar- ν measurements with the liquid scintillator detector of JUNO will be performed via elastic neutrino–electron-scattering as primary detection channel. They will benefit from the very good energy resolution of the detector and the large target mass. Table 1 lists the expected solar neutrino signal rates. However, for solar neutrino observations, the experiment needs

⁴The GADZOOKS! upgrade [12] of the water Cherenkov detector SUPER-KAMIOKANDE plans to dissolve the neutron absorber gadolinium in the 22.5 kt fiducial target mass. It is expected to increase the efficiency to tag the final state IBD neutron to $\sim 80\%$, allowing to detect 3 to 5 DSNB $\bar{\nu}_e$ events per year. For JUNO, this makes GADZOOKS! a direct competitor in the quest for the first measurement of the DSNB.

Neutrino flux	Signal rate (counts / day / kton)
pp ν	1378
${}^7\text{Be}$ - ν	517
pep ν	28
${}^8\text{B}$ - ν	4.5
${}^{13}\text{N}$ / ${}^{15}\text{O}$ / ${}^{17}\text{F}$ - ν	7.5 / 5.4 / 0.1

Table 1: Expected solar neutrino signal rates at JUNO. Data cited from [4].

to deal with radiopurity requirements that are more strict than for the MH measurement. Two scenarios for low-energy solar neutrino detection, named *baseline* and *ideal*, are currently assumed. They are summarized in Table 14 of [4]: The *baseline* case corresponds approximately to the KAMLAND solar phase purity level, yields a signal-to-background ratio of about 1:3 and makes the solar ${}^7\text{Be}$ neutrino branch accessible. In the *ideal* case, which assumes the BOREXINO phase-I purity level before 2010, the expected signal-to-background ratio is about 2:1, probably giving a solar ${}^7\text{Be}$ neutrino signal rate about three times larger than the total of all backgrounds.⁵

Besides the achievement of high radiopurity, an efficient rejection of cosmogenic background from ${}^{11}\text{C}$ and ${}^{10}\text{C}$ decays is another important task. With the experiment's overburden of ~ 700 m, about 1860 and 35 counts per day and kton are expected, respectively.

The focus of JUNO concerning solar neutrinos would be measurements of the ${}^7\text{Be}$ - ν and ${}^8\text{B}$ - ν fluxes. Together, the outcomes can help to break solar model ambiguities that cannot be resolved alone with results for neutrino fluxes from the CNO cycle in the Sun (see Figure 42 and Figure 43 in [4]). Moreover, a high-statistics measurement of the low-energy part of the ${}^8\text{B}$ - ν spectrum around 3 MeV will probe the P_{ee} transition region, allowing the search for deviations from the MSW-LMA prediction.

Conclusions

JUNO aims to determine the neutrino MH by precisely measuring the oscillatory fine structure in the survival probability of $\bar{\nu}_e$'s from nuclear reactors at a baseline length of 53 km. Once data taking begins around 2020, the neutrino observatory will feature a 20 kt liquid scintillator detector of unprecedented size and with a very good energy resolution. In case of a galactic core-collapse SN at the benchmark distance of 10 kpc, about 5000 IBD events with energy, time and partial flavor information will allow to test SN models. Concerning the DSNB, a 3σ evidence seems within reach after 10 years of measurement. If no positive DSNB signal is found, the current upper DSNB flux limits will be significantly improved. A solar neutrino program of JUNO will decisively depend on the achieved radiopurity and cosmogenic background rejection efficiency. The focus will likely be on ${}^7\text{Be}$ - ν and ${}^8\text{B}$ - ν measurements, which can help to shed light on the solar metallicity / opacity problem and on the transition region of the solar ν_e survival probability.

⁵JUNO will profit from BOREXINO expertise in terms of radiopurity.

References

- [1] G. Bellini et al. Final results of Borexino Phase-I on low energy solar neutrino spectroscopy. *Phys. Rev.*, D89(11):112007, 2014.
- [2] K. Bays et al. Supernova Relic Neutrino Search at Super-Kamiokande. *Phys. Rev.*, D85:052007, 2012.
- [3] W. David Arnett, John N. Bahcall, Robert P. Kirshner, and Stanford E. Woosley. Supernova 1987A. *Ann.Rev.Astron.Astrophys.*, 27(1):629–700, 1989.
- [4] Fengpeng An et al. Neutrino Physics with JUNO. *J. Phys.*, G43(3):030401, 2016.
- [5] Zelimir Djurcic et al. JUNO Conceptual Design Report. arXiv: 1508.07166. 2015.
- [6] Alessandro Mirizzi, Irene Tamborra, Hans-Thomas Janka, Ninetta Saviano, Kate Scholberg, Robert Bollig, Lorenz Hudepohl, and Sovan Chakraborty. Supernova Neutrinos: Production, Oscillations and Detection. *Riv. Nuovo Cim.*, 39(1-2):1, 2016.
- [7] John F. Beacom, Will M. Farr, and Petr Vogel. Detection of supernova neutrinos by neutrino proton elastic scattering. *Phys. Rev.*, D66:033001, 2002.
- [8] Graham M. Harper, Alexander Brown, and Edward F. Guinan. A New VLA-Hipparcos Distance to Betelgeuse and its Implications. *Astron. J.*, 135(4):1430, 2008.
- [9] Pietro Antonioli, Richard Tresch Fienberg, Fabrice Fleuret, Yoshiyuki Fukuda, Walter Fulgione, et al. SNEWS: The Supernova Early Warning System. *New J.Phys.*, 6:114, 2004.
- [10] M. Apollonio et al. Determination of neutrino incoming direction in the CHOOZ experiment and supernova explosion location by scintillator detectors. *Phys. Rev.*, D61:012001, 2000.
- [11] Michael Wurm et al. The next-generation liquid-scintillator neutrino observatory LENA. *Astropart. Phys.*, 35:685–732, 2012.
- [12] P. Fernandez. Status of GADZOOKS!: Neutron Tagging in Super-Kamiokande. *Nucl. Part. Phys. Proc.*, 273-275:353–360, 2016.
- [13] G. Bellini et al. First evidence of pep solar neutrinos by direct detection in Borexino. *Phys. Rev. Lett.*, 108:051302, 2012.

Latest results from LUNA experiment

Francesca Cavanna¹, for the LUNA collaboration

¹INFN, Sezione di Genova, Via Dodecaneso 33, 16146 Genoa, Italy

DOI: <http://dx.doi.org/10.3204/DESY-PROC-2016-05/10>

Nuclear processes are responsible for energy generation that makes stars shine, and for the synthesis of the elements in stars and also play a decisive role in explaining the chemical composition of the interstellar medium. Thermonuclear fusion reactions convert protons into heavier elements from He to Fe. Deep underground in the Gran Sasso Laboratory the key reactions of the proton-proton chain, the carbon-nitrogen-oxygen cycle and the neon-sodium cycle have been studied down to the energies of astrophysical interest. The latest results are reviewed, together with future developments of underground nuclear astrophysics.

1 Nuclear astrophysics at Gran Sasso

At the Laboratory for Underground Nuclear Astrophysics (LUNA), in the Gran Sasso National Laboratory, several cross sections have been measured in the past down to the energies of astrophysical interest [1, 2].

At low energy, the cross section of a charged particle induced reaction steeply drops with decreasing energy due to the Coulomb barrier. Generally, it has a very low value at the Gamow Peak, the energy region where most reactions occur; this prevents a direct measurement in a laboratory on the Earth's surface, where the signal to background ratio is too small because of cosmic ray interactions with detectors. The Gran Sasso underground facility is shielded against cosmic rays by a rock cover (1400 m thick) equivalent to 3800 m water, suppressing the muon and neutron flux by six and three orders of magnitude, respectively.

The measurement of the cross section for thermonuclear reactions require an experimental apparatus composed of an accelerator, a target, and a detection system.

The LUNA 400 kV accelerator delivers a proton beam of 500 μA or an alpha beam of 300 μA in the energy range of $E_{p-\alpha} = 50\text{-}400$ keV. The ions can be sent into one of two different, beam lines, thereby allowing the parallel installation of solid and gas target setups.

For nuclear reactions in which charged particles are emitted, silicon detectors are usually adopted to make an in-beam measurement.

For nuclear reactions in which only γ -rays are emitted, the choice of the most suitable detector depends on the physical information desired. The 4π bismuth germanate (BGO) summing crystal used at LUNA can reach an efficiency as high as 70% for a 7-MeV γ ray, thus allowing the measurement of extremely low reaction yields. However, the BGO's energy resolution is very poor and does not allow measurements of cascades and branching ratios to different levels because most of the γ -ray transitions are summed in a single peak. With a germanium detector, the efficiency decreases to the level of a few per mil, but the energy resolution is much

better, allowing complex γ -ray cascades to be disentangled. Moreover, angular distribution measurements can be made by placing the detector at different angles with respect to the ion beam.

2 Reactions studied at LUNA in the last years:

2.1 $^{17}\text{O}(p,\alpha)^{14}\text{N}$

This reaction plays an important role in the synthesis and abundance of key isotopes often used to test nucleosynthesis models of classical novae, Asymptotic Giant Branch (AGB) and post-AGB stars [3, 4, 5]. At energies of astrophysical interest its reaction rate is dominated [6] by a narrow and isolated resonance at $E_p=70$ keV. This resonance has been studied several times in the past, using both direct and indirect methods, as summarised in ref. [7]. However, the picture painted in the literature is still not completely satisfying. The uncertainty in the resonance strength is not negligible ($\approx 20\%$). Furthermore, published strength values obtained with direct measurements have all been retracted or reanalysed [7].

An experimental campaign aimed at measuring the $E_p=70$ keV resonance in $^{17}\text{O}(p,\alpha)^{14}\text{N}$ has been recently completed at the underground LUNA accelerator. The low background in the underground environment has been exploited in order to carry out a direct investigation of this weak ($\omega\gamma \approx \text{neV}$) resonance employing the thick-target yield technique. Protons have been accelerated on a solid Ta_2O_5 target and alpha particles detected at backward angles using an array of silicon detectors (Fig.1). The setup has been commissioned using the well-known $E_p=193$ keV resonance in $^{17}\text{O}(p,\alpha)^{14}\text{N}$ [8].

A clear peak has been observed at $E_p=71.5$ keV. The alpha peak from the $E_p=70$ keV resonance appears where expected and has a signal significance higher than 5 sigma. Results of the analysis indicate a resonance strength that is significantly higher than reported in previous investigations. Because of the importance of this resonance [6], LUNA results is expected to have significant astrophysical consequences in a number of scenarios.

2.2 $^{22}\text{Ne}(p,\gamma)^{23}\text{Na}$

The $^{22}\text{Ne}(p,\gamma)^{23}\text{Na}$ reaction is involved in the hydrogen burning neon-sodium (NeNa) cycle which is active in Red Giant Branch stars (Gamow peak 30-100 keV), Asymptotic Giant Branch Stars (AGB), classical novae (Gamow peak 100-600 keV) [9] as well as in type Ia supernovae [10] and contributes to the nucleosynthesis of neon and sodium isotopes.

The $^{22}\text{Ne}(p,\gamma)^{23}\text{Na}$ is the NeNa cycle reaction with the most uncertain cross section. In the energy range relevant for astrophysics, the $^{22}\text{Ne}(p,\gamma)^{23}\text{Na}$ reaction rate was poorly known because of the contribution of a large number of resonances, many of which were never observed directly [11, 12], before the experiment performed at LUNA in 2015. The lowest-lying resonance with a directly measured strength was the one at $E_R^{lab} = 436$ keV [13]; for the resonances below that energy, only upper limits were reported in the literature [14, 15, 16]. The mere existence of several ^{23}Na energy levels, e.g. the ones corresponding to the $E_p = 215, 104,$ and 70 keV resonances, is even doubted [17].

An experimental campaign structured in two phases has been started in 2013 to measure directly the resonance strength of several resonances below 400 keV. The data taking for the first phase, with High Purity Germanium Detectors (HPGe), has been concluded and the results

have been published in 2015 [18]. The data taking for the second phase, with BGO detectors, has been recently accomplished, the data analysis is still on going.

Phase I: HPGe detectors

The setup consisted of two HPGe detectors, one at 90° with respect to the beam direction, and the other one at 55° effective angle. The use of two high resolution detectors with well defined solid angles allowed a measurement not only of the total resonance strength, but also of the different branching ratios of the resonance decay. The two detectors were surrounded by a 4 cm thick copper shielding and a 25 cm thick lead shielding in order to suppress the environmental background [19].

The gamma detection efficiency has been determined in the energy range of interest for the measurement (i.e. $440 \text{ keV} < E_\gamma < 9.5 \text{ MeV}$) with radioactive sources at the lower energies (^7Be , ^{137}Cs , ^{60}Co and ^{88}Y) and with the $^{14}\text{N}(p,\gamma)^{15}\text{O}$ nuclear reaction at the higher energies.

Enriched neon-22 gas has been used for the measurements; for each resonance the yield profile as a function of the proton beam energy has been studied in 1-2 keV steps.

The resonances at $E_R^{lab} = 156.2$, 189.5 and 259.7 keV have been detected for the first time. In Fig. 2 the spectrum of the $E_R^{lab} = 156.2$ keV resonance is shown together with the identified ^{23}Na transitions. Also the background lines are shown. Detailed branching schemes have been developed for the new resonances, and in two cases, even a coincidence analysis of the two HPGe detectors has been possible. The thermonuclear reaction rate obtained with these new LUNA results [18] is shown in Fig. 3 compared with previous rates reported in literature.

Phase II BGO detector

In phase II of the experiment, a high-luminosity 4π bismuth germanate summing crystal (BGO) was used in order to address several low-energy resonances and the direct capture component, as well. The typical γ -ray detection efficiency of 70% of this detector [20] enable either a positive confirmation or a severe upper limit for the low-energy resonances that make up much of the discrepancy between the Sallaska and NACRE reaction rates (fig. 3).

The efficiency of the new setup was measured by means of four radioactive sources (^7Be , ^{137}Cs , ^{60}Co and ^{88}Y) and the well known $E_p=278$ keV resonance of the $^{14}\text{N}(p,\gamma)^{15}\text{O}$ reaction.

During the whole 2015 the data taking of this phase has been completed. The non resonant contribution to the S-factor has been measured in an energy range from 200 keV up to 360 keV and the two purported resonances at 70 and 105 keV, for which only upper limits exist from the HPGe phase, have been studied in detail.

2.3 Future project: LUNA-MV

In the last years LUNA obtained important achievements in experimental Nuclear Astrophysics, mainly studying hydrogen burning reactions. In order to make a step forward and be able to measure reactions belonging to the helium burning that are important at higher temperatures in stars that ultimately means larger interaction energies, a higher voltage accelerator is necessary. With this aim, a new project just started, the LUNA-MV, which foresees the installation of a 3.5 MV machine in hall B of Gran Sasso Laboratories. The LUNA MV accelerator will provide intense beams of H^+ , $^4\text{He}^+$, $^{12}\text{C}^+$ e $^{12}\text{C}^{++}$ in the energy range: 200 keV - 3.5 MeV. The accelerator will be built and tested by November 2017. Delivery at LNGS is scheduled for

January 2018. Finally, by July 2018 the accelerator will be installed and tested in hall B. The first five years of experimental program foresee the measurement of $^{14}\text{N}(p,\gamma)^{15}\text{O}$, $^{13}\text{C}(\alpha,n)^{16}\text{O}$, $^{22}\text{Ne}(\alpha,n)^{25}\text{Mg}$ and $^{12}\text{C}+^{12}\text{C}$. Important achievements are expected soon.

2.4 Tables and figures



Figure 1: Picture of the target chamber used for the $^{17}\text{O}(p,\alpha)^{14}\text{N}$ cross section measurement. All silicon detectors are mounted. Protective foils are mounted on the inner dome in front of each detector.

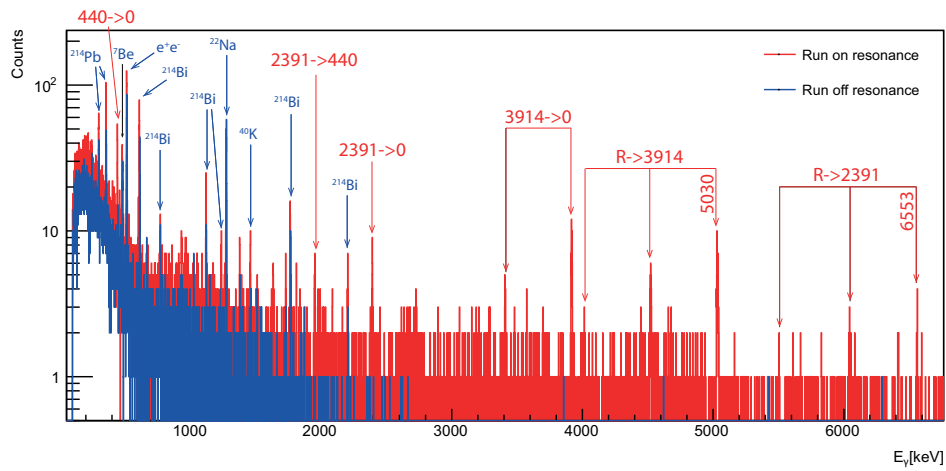


Figure 2: (Color online) In red spectrum measured at $E_p = 162$ keV, on top of the resonance at 156.2 keV. The off-resonance spectrum (in blue) is superimposed.

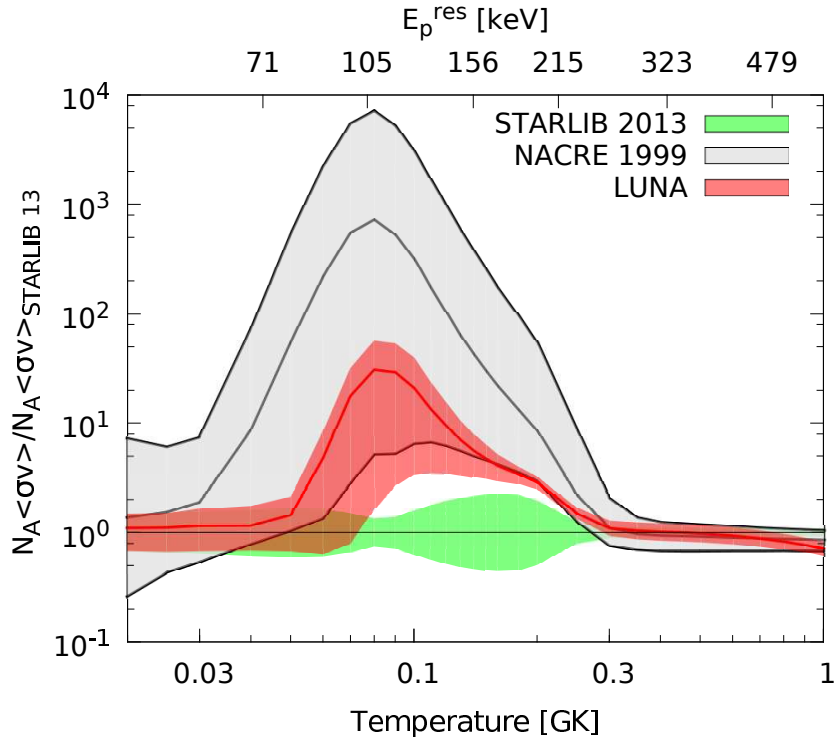


Figure 3: Thermonuclear reaction rate of LUNA [18], NACRE Collaboration [11] and STARLIB group [21], normalized to STARLIB group.

References

- [1] H. Costantini, A. Formicola, G. Imbriani, M. Junker, C. Rolfs, and F. Strieder. LUNA: a laboratory for underground nuclear astrophysics. *Rep. Prog. Phys.*, 72(8):086301–+, August 2009.
- [2] Carlo Brogгинi, Daniel Bemmerer, Alessandra Guglielmetti, and Roberto Menegazzo. LUNA: Nuclear Astrophysics Deep Underground. *Annu. Rev. Nucl. Part. Sci.*, 60:53–73, 2010.
- [3] M. Lugaro, A. I. Karakas, L. R. Nittler, C. M. O. Alexander, P. Hoppe, C. Iliadis, and J. C. Lattanzio. On the asymptotic giant branch star origin of peculiar spinel grain OC2. *Astron. Astrophys.*, 461:657–664, January 2007.
- [4] S. Palmerini, M. L. Sergi, M. La Cognata, L. Lamia, R. G. Pizzone, and C. Spitaleri. The RGB and AGB Star Nucleosynthesis in Light of the Recent $^{17}\text{O}(p, \alpha)^{14}\text{N}$ and $^{18}\text{O}(p, \alpha)^{15}\text{N}$ Reaction-rate Determinations. *Astrophys. J.*, 764:128, February 2013.
- [5] K. M. Nollett, M. Busso, and G. J. Wasserburg. Cool Bottom Processes on the Thermally Pulsing Asymptotic Giant Branch and the Isotopic Composition of Circumstellar Dust Grains. *Astrophys. J.*, 582:1036–1058, January 2003.
- [6] M. Q. Buckner, C. Iliadis, K. J. Kelly, L. N. Downen, A. E. Champagne, J. M. Cesaratto, C. Howard, and R. Longland. High-intensity-beam study of $^{17}\text{O}(p, \gamma)^{18}\text{F}$ and thermonuclear reaction rates for $^{17}\text{O}+p$. *Phys. Rev. C*, 91(1):015812, January 2015.
- [7] M. L. Sergi, C. Spitaleri, M. La Cognata, L. Lamia, R. G. Pizzone, G. G. Rapisarda, X. D. Tang, B. Bucher, M. Couder, P. Davies, R. deBoer, X. Fang, L. Lamm, C. Ma, M. Notani, S. O’Brien, D. Roberson, W. Tan,

- M. Wiescher, B. Irgaziev, A. Mukhamedzhanov, J. Mrazek, and V. Kroha. Improvement of the high-accuracy $^{17}\text{O}(p, \alpha)^{14}\text{N}$ reaction-rate measurement via the Trojan Horse method for application to ^{17}O nucleosynthesis. *Phys. Rev. C*, 91(6):065803, June 2015.
- [8] C. G. Bruno, D. A. Scott, A. Formicola, M. Aliotta, T. Davinson, M. Anders, A. Best, D. Bemmerer, C. Brogini, A. Cacioli, F. Cavanna, P. Corvisiero, R. Depalo, A. Di Leva, Z. Elekes, Z. Fülöp, G. Gervino, C. J. Griffin, A. Guglielmetti, C. Gustavino, G. Gyürky, G. Imbriani, M. Junker, R. Menegazzo, E. Napolitani, P. Prati, E. Somorjai, O. Straniero, F. Strieder, T. Szücs, and D. Trezzi. Resonance strengths in the $^{17,18}\text{O}(p, \alpha)^{14,15}\text{N}$ reactions and background suppression underground. Commissioning of a new setup for charged-particle detection at LUNA. *European Physical Journal A*, 51:94, August 2015.
- [9] Christian Iliadis, Art Champagne, Jordi José, Sumner Starrfield, and Paul Tupper. The effects of thermonuclear reaction-rate variations on nova nucleosynthesis: A sensitivity study. *Astrophys. J. Suppl. Ser.*, 142:105–137, 2002.
- [10] D. A. Chamulak, E. F. Brown, F. X. Timmes, and K. Dupczak. The Reduction of the Electron Abundance during the Pre-explosion Simmering in White Dwarf Supernovae. *Astrophys. J.*, 677:160–168, April 2008.
- [11] Carmen Angulo, M. Arnould, M. Rayet, P. Descouvemont, D. Baye, C. Leclercq-Willain, A. Coc, S. Barhoumi, P. Aguer, C. Rolfs, R. Kunz, J. W. Hammer, A. Mayer, T. Paradellis, S. Kossionides, C. Chronidou, K. Spyrou, S. degl’Innocenti, G. Fiorentini, B. Ricci, S. Zavatarelli, C. Providencia, H. Wolters, J. Soares, C. Grama, J. Rahighi, A. Shotter, and M. Laméhi Racht. A compilation of charged-particle induced thermonuclear reaction rates. *Nucl. Phys. A*, 656:3–187, 1999.
- [12] C. Iliadis, R. Longland, A. E. Champagne, and A. Coc. Charged-particle thermonuclear reaction rates: III. Nuclear physics input. *Nucl. Phys. A*, 841:251–322, 2010.
- [13] R. Depalo, F. Cavanna, F. Ferraro, A. Slemmer, T. Al-Abdullah, S. Akhmadaliev, M. Anders, D. Bemmerer, Z. Elekes, G. Mattei, S. Reinicke, K. Schmidt, C. Scian, and L. Wagner. Strengths of the resonances at 436, 479, 639, 661, and 1279 keV in the $^{22}\text{Ne}(p, \gamma)^{23}\text{Na}$ reaction. *Phys. Rev. C*, 92(4):045807, October 2015.
- [14] J. Görres, C. Rolfs, P. Schmalbrock, H. P. Trautvetter, and J. Keinonen. Search for low-energy resonances in $^{21}\text{Ne}(p, \gamma)^{22}\text{Na}$ and $^{22}\text{Ne}(p, \gamma)^{23}\text{Na}$. *Nucl. Phys. A*, 385:57–75, 1982.
- [15] J. Görres, H. W. Becker, L. Buchmann, C. Rolfs, P. Schmalbrock, H. P. Trautvetter, A. Vlieks, J. W. Hammer, and T. R. Donoghue. Proton-induced direct capture on ^{21}Ne and ^{22}Ne . *Nucl. Phys. A*, 408:372–396, October 1983.
- [16] S. E. Hale, A. E. Champagne, C. Iliadis, V. Y. Hansper, D. C. Powell, and J. C. Blackmon. Investigation of the $^{22}\text{Ne}(p, \gamma)^{23}\text{Na}$ reaction via $(^3\text{He}, d)$ spectroscopy. *Phys. Rev. C*, 65:015801, 2001.
- [17] R. B. Firestone. Nuclear Data Sheets for $A = 23$. *Nucl. Data Sheets*, 108:1–78, 2007.
- [18] F. Cavanna, R. Depalo, M. Aliotta, M. Anders, D. Bemmerer, A. Best, A. Boeltzig, C. Brogini, C. G. Bruno, A. Cacioli, P. Corvisiero, T. Davinson, A. di Leva, Z. Elekes, F. Ferraro, A. Formicola, Z. Fülöp, G. Gervino, A. Guglielmetti, C. Gustavino, G. Gyürky, G. Imbriani, M. Junker, R. Menegazzo, V. Mossa, F. R. Pantaleo, P. Prati, D. A. Scott, E. Somorjai, O. Straniero, F. Strieder, T. Szücs, M. P. Takács, D. Trezzi, and LUNA Collaboration. Three New Low-Energy Resonances in the $^{22}\text{Ne}(p, \gamma)^{23}\text{Na}$ Reaction. *Physical Review Letters*, 115(25):252501, December 2015.
- [19] F. Cavanna et al. A new study of the $^{22}\text{Ne}(p, \gamma)^{23}\text{Na}$ reaction deep underground: Feasibility, setup, and first observation of the 186 keV resonance. *Eur. Phys. J. A*, 50:179, 2014.
- [20] C. Casella, H. Costantini, A. Lemut, B. Limata, D. Bemmerer, R. Bonetti, C. Brogini, L. Campajola, P. Cocconi, P. Corvisiero, J. Cruz, A. D’Onofrio, A. Formicola, Z. Fülöp, G. Gervino, L. Gialanella, A. Guglielmetti, C. Gustavino, G. Gyürky, A. Loiano, G. Imbriani, A. P. Jesus, M. Junker, P. Musico, A. Ordine, F. Parodi, M. Parolin, J. V. Pinto, P. Prati, J. P. Ribeiro, V. Roca, D. Rogalla, C. Rolfs, M. Romano, C. Rossi-Alvarez, A. Rottura, F. Schuemann, E. Somorjai, F. Strieder, F. Terrasi, H. P. Trautvetter, A. Vomiero, and S. Zavatarelli. A new setup for the underground study of capture reactions. *Nucl. Inst. Meth. A*, 489:160–169, August 2002.
- [21] A. L. Sallaska, C. Iliadis, A. E. Champagne, S. Goriely, S. Starrfield, and F. X. Timmes. STARLIB: A Next-generation Reaction-rate Library for Nuclear Astrophysics. *Astrophys. J. Suppl. Ser.*, 207:18, July 2013.

Connecting neutrino Astrophysics to Multi-TeV to PeV gamma-ray astronomy with TAIGA

M. Tluczykont⁶, N. Budnev², I. Astapov⁹, P. Bezyazeekov², A. Bogdanov⁹, V. Boreyko¹⁰, M. Brückner⁸, A. Chiavassa⁴, O. Chvalaev², O. Gress², T. Gress², O. Grishin², A. Dyachok², S. Epimakhov⁶, O. Fedorov², A. Gafarov², N. Gorbunov¹⁰, V. Grebenyuk¹⁰, A. Grinuk¹⁰, D. Horns⁶, A. Ivanova², A. Kalinin¹⁰, N. Karpov¹, N. Kalmykov¹, Y. Kazarina², N. Kirichkov², S. Kiryuhin², R. Kokoulin⁹, K. Komponiest⁹, A. Konstantinov¹, E. Korosteleva¹, V. Kozhin¹, M. Kunnas⁶, L. Kuzmichev^{1,2}, V. Lenok², B. Lubsandorzhev³, N. Lubsandorzhev¹, R. Mirgazov², R. Mirzoyan^{5,2}, R. Monkhoev², R. Nachtigall⁶, E. Osipova¹, A. Pakhorukov², M. Panasyuk¹, L. Pankov², A. Petrukhin⁹, V. Platonov², V. Poleschuk², E. Popova¹, A. Porelli⁸, E. Postnikov¹, V. Prosin¹, V. Ptuskin⁷, G. Rubtsov³, A. Pushnin², V. Samoliga², P. Satunin⁷, Yu. Semenyev², A. Silaev¹, A. Silaev (junior)¹, A. Skurikhin¹, V. Slucka¹⁰, C. Spiering⁸, L. Sveshnikova¹, V. Tabolenko², B. Tarashansky², A. Tkachenko¹⁰, L. Tkachev¹⁰, D. Voronin², R. Wischnewski⁸, A. Zagorodnikov², V. Zurbanov², I. Yashin⁹

¹ Skobeltsyn Institute of Nuclear Physics MSU, Moscow, Russia

² Institute of Applied Physics, ISU, Irkutsk, Russia

³ Institute for Nuclear Research of RAN, Moscow, Russia

⁴ Dipartimento di Fisica Generale Universiteta di Torino and INFN, Torino, Italy

⁵ Max-Planck-Institute for Physics, Munich, Germany

⁶ Institut für Experimentalphysik, Universität Hamburg, Germany

⁷ IZMIRAN, Moscow Region, Russia

⁸ DESY, Zeuthen, Germany

⁹ NRNU MEPhI, Moscow, Russia

¹⁰ JINR, Dubna, Russia

DOI: <http://dx.doi.org/10.3204/DESY-PROC-2016-05/27>

Recent evidence for neutrinos in the PeV energy range from IceCube provides additional motivation for the search for the most energetic Galactic accelerators. Gamma-ray astronomy is a sound strategy to reach this goal, providing the energy range beyond 10 TeV can be covered at a sufficient sensitivity level. The energy spectra of most known gamma-ray emitters only reach up to few 10s of TeV. The HEGRA IACT installation reported evidence for gamma-ray energies from the Crab Nebula as high as 80 TeV. Uncovering their spectral shape up to few 100s of TeV could answer the question whether some of these objects are cosmic ray Pevatrons, i.e. Galactic PeV accelerators. Extending observations beyond this energy range requires very large effective detector areas, as planned by the TAIGA collaboration.

1 Introduction

Ground based gamma-ray astronomy has rapidly evolved in the past decade, significantly affecting our knowledge of the non-thermal universe. Imaging atmospheric Cherenkov telescopes (IACT) led to a break-through with the first significant detection of gamma-rays in the TeV energy range from the direction of the Crab Nebula [1]. Further innovations such as fast high-resolution PMT cameras (CAT) and the stereoscopic detection technique (HEGRA) led to currently existing instruments (H.E.S.S., MAGIC, and VERITAS). Today, more than 150 sources of very high energy (VHE, $E > 100$ GeV) gamma-rays are known [2].

Above 100 GeV, the stereoscopic imaging technique is the method of choice. Existing and planned instruments, such as the Cherenkov Telescope Array CTA [3], are relying on the IACT technique. Their optimal operation regime is typically located in the TeV energy range. The total energy coverage spans from few 10s of TeV to 100 TeV. Beyond these energies, at multi-TeV to PeV energies, the gamma-ray universe is so far only poorly explored. Due to the powerlaw shape of source spectra, the observable flux drops quickly with increasing energy. Much larger sensitive areas than the ones from existing instruments are required for detection here.

While imaging air Cherenkov telescopes have proven to be the instruments of choice in the GeV to TeV energy range, large detector areas are more easily accessed with the (non-imaging) shower-front timing technique which also naturally provides large viewing angles. The poor gamma-hadron separation power of shower front timing arrays can be compensated by a combination with small imaging air Cherenkov telescopes. Such a new hybrid detector concept is currently being implemented by the TAIGA collaboration in the Tunka-valley in Siberia.

In the next section, the astrophysical motivation for multi-TeV to PeV astronomy is addressed. Subsequently, the strategy pursued by the TAIGA collaboration to access this energy range is described.

2 Astrophysics with ultra-high energy gamma-rays and neutrinos

Observations in the multi-TeV energy range have a potential for discovery of new sources, and are particularly important to measure the spectral shape of known gamma-ray sources in the cutoff regime, where the objects reach their maximum acceleration energy. The accelerators of cosmic rays up to the knee region of the cosmic ray spectrum, the Pevatrons, are especially in the focus of observations in the multi-TeV to PeV range. The paradigm of charged Galactic cosmic ray production is the scenario of acceleration in shock fronts at the boundaries of expanding shells of supernova remnants (SNR). Nuclear scattering of the accelerated nuclei off the ambient medium produce neutral and charged pions which subsequently decay into gamma-rays and neutrinos at energies of about a factor 10 less than the primary cosmic ray particles (due to the typical inelasticity of the hadronic interaction). A Pevatron accelerating charged cosmic ray particles up to cutoff energies of 3 PeV would produce hard gamma-ray and neutrino spectra up to cutoff energies of roughly 300 TeV.

While neutrinos from an astrophysical source are an unambiguous smoking-gun signature for hadronic processes, this is not necessarily the case for gamma-rays. From few 10s of GeV up to about 10 TeV, the origin of a gamma-ray signal is difficult to identify. Gamma-rays can also be produced in leptonic scenarios, in which electrons scatter off low energy seed photons, boosting

the photons up to TeV energies (Inverse Compton scattering). Above few 10s of TeV, the inverse Compton effect becomes less efficient because of Klein-Nishina suppression, resulting in soft spectra. As opposed to that, nucleonic gamma-ray production increases efficiency because of increasing inelastic cross-sections, resulting in harder spectra. Therefore, the observation of hard gamma-ray spectra in this energy regime would resolve the leptonic/hadronic ambiguity and represent a smoking-gun signature of cosmic ray acceleration. The difference in leptonic and hadronic spectra is illustrated qualitatively in Figure 1. Observations of the Galactic center by H.E.S.S. [4], and recent evidence for astrophysical neutrinos from IceCube [5, 6] are further motivation for a search for multi-TeV to PeV gamma-rays.

As reported in [6], the IceCube neutrinos were detected in the energy range from 100 TeV to about 1 PeV. The data are reported to be in favour of an astrophysical interpretation. Among the 37 neutrino events detected by IceCube, 5 were speculated to be associated with extreme Blazars by other authors [7]. Based on this tentative association, [8] have presented model calculations for gamma-ray fluxes expected in a hadronic emission scenario and using the neutrino events as flux constraints. The predicted fluxes (see Figure 1) are reaching their maximum between 1 and 10 PeV, a region so far not accessed by gamma-ray experiments.

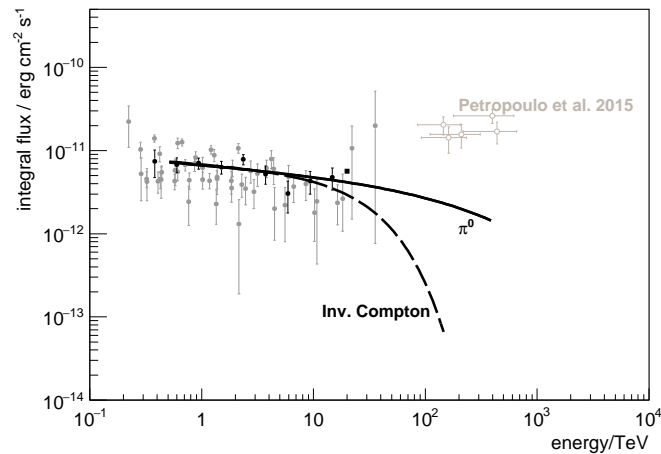


Figure 1: Extrapolations to the multi-TeV regime: π^0 -decay spectrum (solid curve, powerlaw with exponential cut-off, no attenuation), inverse Compton spectrum (dashed curve, double exponential cutoff). Curves are scaled to data from the H.E.S.S. Galactic plane survey [9] (grey circles) and the Milagro source MGRO J1908+06 (black square: Milagro [10], black circles: H.E.S.S. [9]). Open circles: hypothetical gamma-ray fluxes from Blazars possibly associated with ν events [8].

While gamma-rays and neutrinos must both be produced in the same astrophysical environments, their detection requires slightly different approaches on considerably different scales. Gamma-rays from GeV to PeV energies can be detected on the ground via extended air shower (EAS) detectors, which measure either the particles (scintillators, water Cherenkov detectors) produced in electromagnetic interactions in the EAS, or their secondary Cherenkov light emission (IACTs, timing arrays). Neutrinos can be detected in large volume detectors via their neutral current or charged current interaction with the ambient medium. While for both particle types the detection methods mostly rely on the measurement of Cherenkov light emission from secondary particles resulting from the interaction in the atmosphere or the detector medium, the scale of the required instrumentation is much larger for neutrino detection due to the low cross section of the weak interaction.

The much higher cross section of the electromagnetic interaction makes the detection of gamma-rays possible on smaller scales. On the other hand and for the same reason, gamma-ray fluxes can be strongly attenuated in astrophysical environments and during their propagation to Earth. Gamma-rays can interact with photons from low energy photon fields and produce

electron-positron pairs, therewith reducing the observable flux at Earth as compared to the source intrinsic flux. The attenuation effect depends on the gamma-ray energy, the energy of the low energy photon, and the distance travelled. The absorption of TeV gamma-rays from Active Galactic Nuclei (AGN) has been extensively studied by Fermi-LAT and the current generation of IACT experiments, providing limits on the density of the extragalactic background light (EBL) in the wavelength range from $0.1 \mu\text{m}$ to $5 \mu\text{m}$. Spectroscopy of nearby AGN in the energy range from 5 TeV to 50 TeV would access the wavelength band from $5 \mu\text{m}$ to $50 \mu\text{m}$. It was shown by [11] that gamma-rays in this energy range from nearby AGN might undergo less absorption by pair production than expected. Possible explanations for this effect could be mixing of photons with light pseudoscalars or effects of breaking of Lorentz-invariance [12], which would lead to a reduction in the effective cross-section for electron positron pair production due to a modification of the kinematics of the interaction (see e.g. [13]).

In the ultra-high energy regime, the absorption effect is strong enough to be relevant also for Galactic sources. [14] have shown that the dominant photon fields are the interstellar radiation field (ISRF), and the cosmic microwave background (CMB). The strength of absorption by pair production on the ISRF reaches a maximum at about 100 TeV, and can vary from few percent for nearby sources up to 50% for faraway sources (i.e. located inside the Galactic disk at a distance of 20 kpc beyond the Galactic center). The absorption caused by the CMB is maximal at about 3 PeV, where more than 90% of the gamma-ray flux from a faraway Galactic source is absorbed. Beyond 3 PeV, the Galaxy becomes transparent to gamma-rays again. A measurement of gamma-ray spectra modified by the absorption effect can provide an estimate of the ISRF density. Since the CMB density is very well known, such a measurement up to PeV energies could provide a new method to measure the distance of Galactic sources from their spectral shape in the gamma-ray energy range.

3 Accessing the ultra-high energy gamma-ray regime

3.1 Detection techniques

The questions described above can be addressed by accessing the ultra-high energy gamma-ray regime, i.e. energies beyond 10 TeV and up to the PeV regime. While it is in principle possible to reach energies beyond 100 TeV with IACTs, the existing and planned instruments are limited by their instrumented area, the large number of required channels per km^2 , and their dynamical range. Even CTA will only be able to do spectroscopy beyond 100 TeV by investing a significant fraction of its available observation time. Considering a flux of only few photons per km^2 per hour even from the strongest gamma-ray sources, a very large instrumented area is obviously the key to making spectroscopic studies at these energies.

Ground-based non-imaging EAS detectors measure the arrival-time distribution and density of particles or photons on the ground. A high reconstruction quality (and thus sensitivity) can be achieved using the density and arrival-time distribution of particles or photons on the ground. While Milagro, HAWC [15], and LHAASO [16] mainly use charged particle detectors to access the multi-TeV regime, the timing of the air shower front is best measured using the Cherenkov photons emitted by the secondary air shower particles. Air Cherenkov timing-arrays can provide an angular resolution of the order of 0.1° and relative energy resolution of better than 15% (see, e.g. [17]), as compared to 1° and 100% for particle shower front sampling techniques. However, the rejection of the predominant hadronic background is difficult using

the timing-array technique alone. This is better achieved by IACTs, using the image shape for hadron rejection.

3.2 HiSCORE

One concept to access the multi-TeV energy range with a very large area wide angle instrument is the HiSCORE experiment [18]. HiSCORE consists of an array of timing stations, measuring the air Cherenkov photon front emitted by the secondary particles in the EAS. A HiSCORE detector station consists of four 8 inch photomultipliers (PMTs), each equipped with a 40 cm Winston cone light concentrator, built from flexible segments of reflective foil sheets. The light collection area per station is 0.5 m^2 and the solid angle covered is 0.6 sr . A picture of a HiSCORE station is shown on the left side of Figure 2. The analog signals from the anodes and the next to last dynode are digitized in the GHz regime using a custom developed readout board based on the DRS 4 chip. Before readout, an analog summator board is dividing the analog signals, and summing the anodes. The analog sum is used for triggering. The stations can be manually tilted along the N-S axis in order to access different parts of the sky. A relative time synchronization at sub-ns level is required over the full scale of the array. Two independent time-calibration methods were successfully employed, reaching the required accuracy [19].

A first implementation of the HiSCORE concept was realized by the Tunka-HiSCORE group. Today, the HiSCORE detector is operated as part of the TAIGA collaboration and consists of 28 HiSCORE timing stations distributed over an area of 0.25 km^2 in the Tunka valley in Siberia. The layout of the 28 station array is shown in Figure 2. An extension to a 0.6 km^2 array and a combination with an IACT is planned between 2016 and 2017. This combination is described in the next section. First results from the HiSCORE timing array were presented recently and

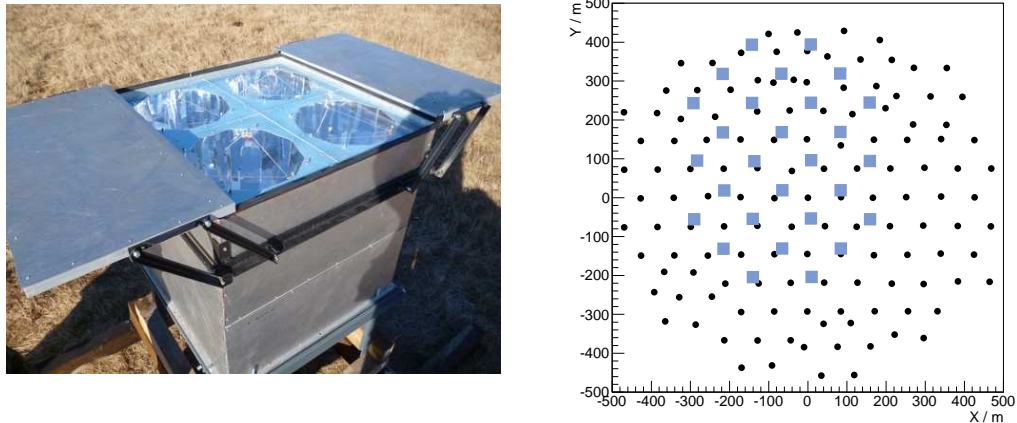


Figure 2: *Left:* Picture of a HiSCORE timing station. *Right:* Layout of the 28 HiSCORE stations (Filled squares). The optical stations of Tunka-133 are shown as filled circles.

will be the subject of proceedings publications [20].

3.3 TAIGA: combining imaging and timing

TAIGA [21, 22] stands for Tunka Advanced Instrument for cosmic ray and Gamma ray Astronomy. The TAIGA experiment is planning to combine the HiSCORE timing array with 10 small sized imaging air Cherenkov telescopes. A first IACT is currently under construction on the Tunka site.

A TAIGA IACT consists of a Davies-Cotton mirror dish with 34 mirror facets of a diameter of 60 cm each. The mirror dish diameter will be 4.3 m. A PMT camera is mounted at a focal distance of 4.75 m. The camera consists of 547 PMTs with a 0.36° field of view (foV) per pixel, resulting in a total field of view of 9.72° in diameter. The PMTs will be arranged with a 30 mm center-to-center distance in 11 hexagonal rings around the central pixel. The expected energy threshold for monoscopic events is 500 GeV. Near the threshold and up to few 10s of TeV, the IACTs will operate in stand alone mode, using the classical imaging technique, performing monitoring observations of transient sources. Above few 10s of TeV and in the overlapping part of the IACT foV with the larger foV of the HiSCORE timing array, the IACTs will operate together with the timing array in a new promising hybrid operation mode. The timing stations will trigger independently from the individual IACTs, and data will be merged using synchronized (sub-ns) event time-stamps.

The basic idea for a combination of the imaging and timing techniques is to use the timing array as estimator of the air shower core position and direction of the primary particle and to provide these parameters to the IACT for improvement of the monoscopic image analysis. Since a large instrumented area is the key aspect for reaching the multi-TeV range, the telescopes will be placed at a distance of roughly 600 m from each other. In this configuration all telescopes will operate in monoscopic mode for zenith angles up to 60° . Since the direction of the air shower is not unambiguously known to a monoscopic IACT, the timing array will provide this information, therewith allowing to reject a large fraction of isotropic hadronic background events. Furthermore, the knowledge of the core impact position from the timing array will allow to introduce the hybrid scaled width parameter, similarly to the classical stereoscopic mean scaled width parameter used in standard imaging analyses based on the Hillas parameters. This concept was previously described in [23, 24] and was also presented at this conference [25]. Using the hybrid scaled width and further gamma-hadron separation parameters based on the IACT image analysis as well as the timing array, we expect to reach a gamma-hadron separation quality factor of the order of 3-5. The hybrid imaging-timing point-source sensitivity of a 0.6 km^2 TAIGA detector is estimated to reach a sensitivity of $5 \cdot 10^{-13} \text{ erg cm}^{-2} \text{ s}^{-1}$ at 100 TeV after 200 h of observation time. The integral sensitivities to point sources for this, and a 5 km^2 detector stage (after 1000 h) are shown in Figure 3 and compared to the sensitivities from other experiments. Already the upcoming 0.6 km^2 array will significantly extend the spectra of known sources into the multi-TeV regime.

4 Summary

While the field of gamma-ray astronomy has made tremendous progress over the past decades, the observation window in the multi-TeV to PeV regime needs yet to be covered by sensitive instruments. This energy range is the key to different astrophysical questions, foremost the question of the origin of cosmic rays and the localization of the highest energy Galactic accelerators. Recent observations from H.E.S.S. and the IceCube neutrino events are further motivating this search.

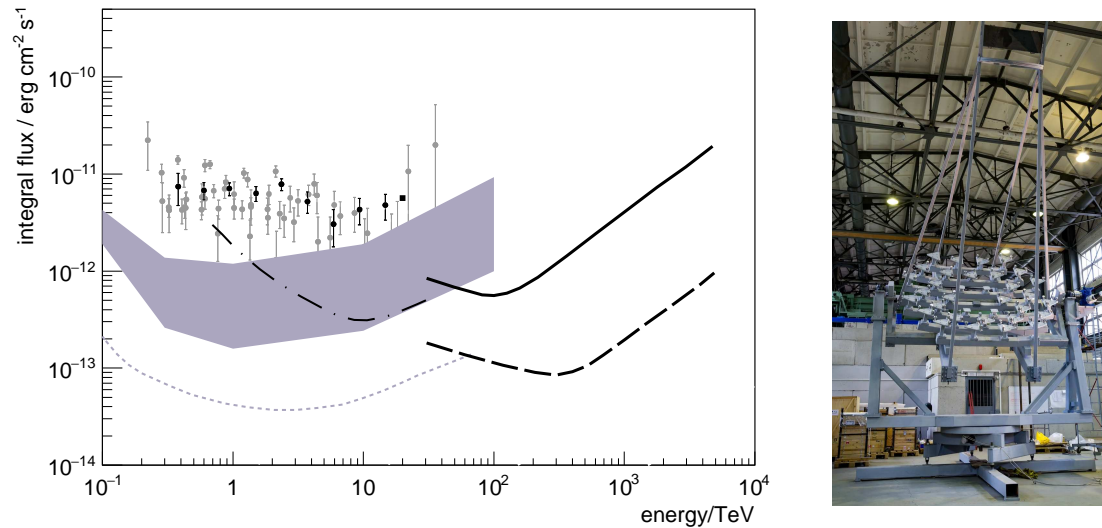


Figure 3: *Left*: Integral flux survey sensitivities of TAIGA, combining timing array stations with IACTs, for a 0.6 km^2 array after 200 h of observation time (solid red line, requiring 5σ and at least 10 gamma-rays) and a 5 km^2 array after 1000 h of observation time (dashed red line). For comparison, further sensitivities are shown: CTA survey (grey area [26]), HAWC ([15] dash-dotted line), CTA pointed observations (large exposure on specific sources, dashed grey). Data points as in Fig. 1. *Right*: Photograph of the first TAIGA IACT, shortly before transportation to the Tunka valley.

The TAIGA collaboration is aiming at this goal, using a novel hybrid approach, combining the air Cherenkov timing technique with the imaging technique. The upcoming 0.6 km^2 stage of TAIGA will for the first time allow to probe the ultra high energy gamma-ray regime at a sensitivity level comparable to the sensitivity of existing instruments at lower energies.

5 Acknowledgments

We acknowledge the support of the Russian Federation Ministry of Education and Science (agreements N 14.B25.31.0010, zadanie No 3.889.2014/K), the Russian Foundation for Basic research (13-02-00214, 13-02-12095, 15-02-10005, 15-02-05769), the Helmholtz association (grant HRJRG-303), and the Deutsche Forschungsgemeinschaft (grant TL 51-3).

References

- [1] T. C. Weekes, M. F. Cawley, D. J. Fegan, et al. Observation of TeV gamma rays from the Crab nebula using the atmospheric Cerenkov imaging technique. *ApJ*, 342:379–395, 1989.
- [2] S. Wakely and D. Horan. The TeV catalogue, TeVCat, <http://tevcat.uchicago.edu/>.
- [3] B. S. Acharya, M. Actis, T. Aghajani, G. Agnetta, J. Aguilar, et al. Introducing the CTA concept. *Astr.Part.Phys.*, 43:3–18, 2013.

- [4] HESS Collaboration, A. Abramowski, F. Aharonian, F. A. Benkhali, A. G. Akhperjanian, E. O. Angüner, M. Backes, A. Balzer, Y. Becherini, J. B. Tjus, and et al. Acceleration of petaelectronvolt protons in the Galactic Centre. *Nature*, 531:476–479, 2016.
- [5] M. G. Aartsen, R. Abbasi, Y. Abdou, M. Ackermann, et al. First Observation of PeV-Energy Neutrinos with IceCube. *Physical Review Letters*, 111(2):021103, July 2013.
- [6] M. G. Aartsen et al. Observation of High-Energy Astrophysical Neutrinos in Three Years of IceCube Data. *Phys. Rev. Lett.*, 113:101101, 2014.
- [7] P. Padovani, E. Resconi, P. Giommi, B. Arsioli, and Y. L. Chang. Extreme blazars as counterparts of IceCube astrophysical neutrinos. *MNRAS*, 457:3582–3592, 2016.
- [8] M. Petropoulou, S. Dimitrakoudis, P. Padovani, A. Mastichiadis, and E. Resconi. Photohadronic origin of γ -ray BL Lac emission: implications for IceCube neutrinos. *MNRAS*, 448:2412–2429, 2015.
- [9] F. Aharonian, A. G. Akhperjanian, G. Anton, U. Barres de Almeida, Bazer-Bachi, et al. Detection of very high energy radiation from HESS J1908+063 confirms the Milagro unidentified source MGRO J1908+06. *A&A*, 499:723–728, 2009.
- [10] A. A. Abdo, B. Allen, D. Berley, S. Casanova, C. Chen, et al. TeV Gamma-Ray Sources from a Survey of the Galactic Plane with Milagro. *ApJ*, 664:L91–L94, 2007.
- [11] M. Meyer, D. Horns, and M. Raue. Indications for a low opacity universe from Fermi-LAT data. In F. A. Aharonian, W. Hofmann, and F. M. Rieger, editors, *American Institute of Physics Conference Series*, volume 1505 of *American Institute of Physics Conference Series*, pages 598–601, 2012.
- [12] D. Colladay and V. A. Kostelecký. Lorentz-violating extension of the standard model. *Phys. Rev. D*, 58(11):116002, 1998.
- [13] G. Rubtsov, P. Satunin, and S. Sibiryakov. Prospective constraints on Lorentz violation from ultrahigh-energy photon detection. *Phys. Rev. D*, 89(12):123011, 2014.
- [14] I. V. Moskalenko, T. A. Porter, and A. W. Strong. Attenuation of Very High Energy Gamma Rays by the Milky Way Interstellar Radiation Field. *ApJL*, 640:L155–L158, 2006.
- [15] G. Sinnis. HAWC: A Next Generation VHE All-Sky Telescope. In F. A. Aharonian, H. J. Völk, and D. Horns, editors, *Heidelberg Gamma-Ray Symposium*, volume 745 of *AIP*, page 234, 2005.
- [16] Shuwang Cui, Ye Liu, Yujuan Liu, and Xinhua Ma. Simulation on gamma ray astronomy research with LHAASO-KM2A. *Astr.Part.Phys.*, 54:86 – 92, 2014.
- [17] D. Hampf, M. Tluczykont, and D. Horns. Event reconstruction techniques for the wide-angle air cherenkov detector HiSCORE. *NIMA*, 712:137, 2013.
- [18] M. Tluczykont, D. Hampf, D. Horns, D. Spitschan, L. Kuzmichev, V. Prosin, C. Spiering, and R. Wischniewski. The HiSCORE concept for gamma-ray and cosmic-ray astrophysics beyond 10 TeV. *Astroparticle Physics*, 56:42–53, 2014.
- [19] O. Gress, I. Astapov, N. Budnev, et al. The wide-aperture gamma-ray telescope taiga-hiscore in the tunka valley: design, composition and commissioning., 2016. To appear in proc. of VCI2016 - The 14th Vienna Conference on Instrumentation.
- [20] 2016. M. Tluczykont et al. and L. Kuzmichev et al. for the TAIGA collaboration, 16th RICAP, Frascati, Italy, <https://agenda.infn.it/>.
- [21] R. Mirzoyan. TAIGA detector for cosmic and gamma rays for TeV - EeV energy range. In *40th COSPAR Scientific Assembly*, volume 40 of *COSPAR Meeting*, 2014.
- [22] N. Budnev et al. The TAIGA experiment: from cosmic ray to gamma-ray astronomy in the Tunka valley, 2016.
- [23] M Tluczykont, I Astapov, N Barbashina, et al. Towards gamma-ray astronomy with timing arrays. *Journal of Physics: Conference Series*, 632(1):012042, 2015.
- [24] M Kunnas, I Astapov, N Barbashina, et al. Simulation of the hybrid tunka area instrument for cosmic rays and gamma-ray astronomy (taiga). *Journal of Physics: Conference Series*, 632(1):012040, 2015.
- [25] M. Kunnas et al., 2016. These proceedings.
- [26] G. Dubus et al. Surveys with the Cherenkov Telescope Array. *Astr.Part.Phys.*, 43:317, 2013.

Simulation of imaging air shower Cherenkov telescopes as part of the TAIGA Project

M.Kunna⁶, I. Astapov⁹, P. Bezyazeev², A. Bogdanov⁹, V. Boreyko¹⁰, M. Brückner¹¹, N. Budnev², A. Chiavassa⁴, O. Chvalaev², O. Gress², T. Gress², O. Grishin², A. Dyachok², S. Epimakhov⁶, O. Fedorov², A. Gafarov², N. Gorbunov¹⁰, V. Grebenyuk¹⁰, A. Grinuk¹⁰, D. Horns⁶, A. Ivanova², A. Kalinin¹⁰, N. Karpov¹, N. Kalmykov¹, Y. Kazarina², N. Kirichkov², S. Kiryuhin², R. Kokoulin⁹, K. Komponiest⁹, A. Konstantinov¹, E. Korosteleva¹, V. Kozhin¹, L. Kuzmichev^{1,2}, V. Lenok², B. Lubsandorzhev³, N. Lubsandorzhev¹, R. Mirgazov², R. Mirzoyan^{5,2}, R. Monkhoev², R. Nachtigall⁶, E. Osipova¹, A. Pakhorukov², M. Panasyuk¹, L. Pankov², A. Petrukhin⁹, V. Platonov², V. Poleschuk², E. Popova¹, A. Porell⁸, E. Postnikov¹, V. Prosin¹, V. Ptuskin⁷, G. Rubtsov³, A. Pushnin², V. Samoliga², P. Satunin⁷, Yu. Semenev², A. Silaev¹, A. Silaev (junior)¹, A. Skurikhin¹, V. Slucka¹⁰, C. Spiering⁸, L. Sveshnikova¹, V. Tabolenko², B. Tarashansky², A. Tkachenko¹⁰, L. Tkachev¹⁰, M. Tluczykont⁶, D. Voronin², R. Wischniewski⁸, A. Zagorodnikov², V. Zurbanov², I. Yashin⁹

¹ Skobeltsyn Institute of Nuclear Physics MSU, Moscow, Russia

² Institute of Applied Physics, ISU, Irkutsk, Russia

³ Institute for Nuclear Research of RAN, Moscow, Russia

⁴ Dipartimento di Fisica Generale Universiteta di Torino and INFN, Torino, Italy

⁵ Max-Planck-Institute for Physics, Munich, Germany

⁶ Institut für Experimentalphysik, University of Hamburg, Germany

⁶ Institut für Experimentalphysik, Universität Hamburg, Luruper Chaussee 149, 22761 Hamburg, Germany

⁷ IZMIRAN, Moscow Region, Russia

⁸ DESY, Zeuthen, Germany

⁹ NRNU MEPhI, Moscow, Russia

¹⁰ JINR, Dubna, Russia

DOI: <http://dx.doi.org/10.3204/DESY-PROC-2016-05/33>

The Tunka Advanced International Gamma-ray and Cosmic ray Astrophysics (TAIGA) project aims at observation of cosmic rays beyond 100 TeV and gamma rays above 1 TeV via observation of the extensive air showers (EAS) caused in the atmosphere. Two common detection techniques are timing arrays and imaging air shower cherenkov telescopes (IACT). Timing arrays yield good directional and energy reconstruction, but provide only mediocre gamma-hadron-separation at their energy threshold. IACTs are good at separation, but since a stereoscopic view of a shower is needed for high reconstruction accuracy, it is difficult to achieve the large effective areas needed for ultra high energy observations.

In this work we present the simulations performed to explore and optimize our IACT design and the first steps towards hybrid reconstruction.

1 Motivation

The highest energies in the gamma ray spectrum are a very interesting domain of cosmic accelerators. Many kinds of sources have already been studied up to a range of tens of TeV, but latest results from experiments like IceCube hint at the existence of sources accelerating particles up to the PeV range, so-called Pevatrons. While the charged particles from such sources are lost in the interstellar magnetic fields, they produce pions in the ambient medium which subsequently decay into gamma-rays. These gammas carry less energy than the original particle had ($O(10)$ less), so a gamma ray source at >100 TeV would be a Pevatron. For further details on Pevatrons, see [1] (these proceedings).

The flux of gammas with such a high energy is low, making it necessary to instrument large areas on the Earth's surface to reach sufficiently large effective areas needed for sensitivity. This paper presents a method to address this challenge.

2 A combination of known approaches

Two common and well-understood methods of observing the high energy gamma ray sky are timing arrays and imaging air cherenkov telescopes (IACTs).

Timing arrays sample the Cherenkov light front of EAS. Core position and direction of incidence are calculated from the arrival time distribution of the air shower front. The comparatively low number of readout channels per km^2 is an advantage for instrumenting the very large areas needed for proper sensitivity.

IACT systems use two or more telescopes with (most often tessellated) mirrors and multi-channel cameras to take images of the EAS. Using a Hillas-type image shape analysis[2], a good distinction between EAS initiated by gammas and EAS caused by the proton background is possible. The downside of this method is that a stereoscopic view of a shower is needed to reconstruct impact core position and shower angle with sufficient accuracy. This sets an upper limit to the spacing of the telescopes (about 300 m) since at least two telescopes need to be inside the Cherenkov light pool to get more than one shower image. Consequently, covering large areas with IACTs requires a large number of detection and readout channels per instrumented km^2 .

The idea behind the TAIGA project is to combine both techniques to use both their strengths while compensating for their weaknesses. A timing array will determine arrival direction and impact point of the air shower, which is then used to interpret the IACT camera image to determine the nature of the EAS primary. Since the directional information is reconstructed by the timing array, the need for stereoscopy does not apply and the spacing between the telescopes can be doubled.

The TAIGA experiment will consist of the already deployed HiSCORE timing array and custom designed IACTs.

HiSCORE stations contain 4 photomultiplier tubes (PMTs, 8" diameter) each, looking directly into the night sky through winston cones. 28 stations have been deployed at Tunka Valley, Russia ($51^\circ 48' 35''$ N, $103^\circ 04' 02''$ E, 675 m a.s.l.) with a spacing between 100 m - 150 m covering about 0.25 km^2 and have been in operation since winter 2014. Further extension is envisaged up to 3 km^2 .

The custom designed IACTs will be Davies-Cotton telescopes with a 4.3 m tessellated mirror dish, a focal length of 4.74 m and a 540 PMT pixel camera with a field of view of 10° diameter. These telescopes will be placed at a 600 m spacing, a prototype is already in construction.

3 Simulations

To evaluate the detector design, a Monte Carlo (MC) simulation was done in three steps. First, the shower itself was simulated using CORSIKA-6990 [3](IACT option for generation of Cherenkov light, hadronic interaction models QGSJET [4] and Gheisha [5]). The shower data is then evaluated independently by the simulation routines for HiSCORE and for the IACTs.

Detection by HiSCORE is calculated with the `sim_score`[6] code, a custom simulation software based on the IACT package performing a full detector simulation including all response functions. From the simulation of gamma-ray induced EAS, the resolution for core position, incidence angle, and reconstructed energy is determined.

The IACT simulation is done with `sim_telarray`[7] and performs a full raytracing of the Cherenkov photons through the telescopes' optics. This takes the telescope design properties into account, e.g. mirror dish shape, mirror reflectivity and (mis-)alignment, camera size, shadowing by masts and camera, and camera PMT efficiency. Last simulation step is the addition of noise from NSB and the electronic parts.

After generation of camera images, `sim_telarray` carries out the image cleaning and the calculation of the Hillas parameters and, if more than one telescope triggered, stereoscopic reconstruction of direction, incidence angle, and energy, even though the stereoscopic evaluations are not necessary for our studies.

The simulations presented in these proceedings are the IACT's point spread function, which is a property of the telescope design, and first insights into the quality of the gamma hadron separation. Please note all results presented here are preliminary.

3.1 Point Spread Function (PSF)

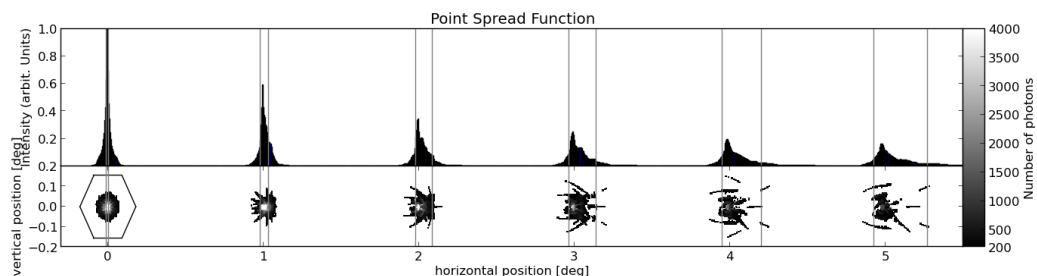


Figure 1: IACT PSF for angles of 0° - 5° from the optical axis in 1D projection and in greyscale. Vertical lines indicate each spot's projected 86% range. Perfectly aligned mirrors are assumed. The finger-like structures are an effect of the outermost mirror segments.

Simulation To evaluate the intended design of the IACTs, the `sim_telarray` ray tracing routine was used to simulate light from an infinitely far away point source. The image of the source in the camera plane is not perfect due the aberrations from the mirrors, and the resulting intensity distribution is called the PSF. To find the theoretical lower limit of the PSF, we assume perfect mirrors, no misalignments and no NSB.

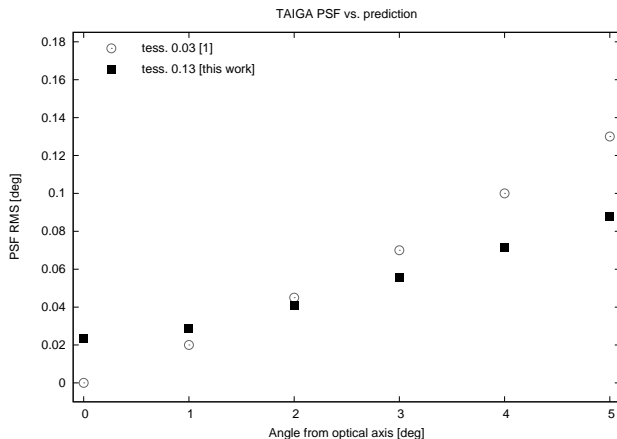


Figure 2: Comparison between analytical and simulated predictions for the PSF for $F/D = 1.1$. Circles: Analytical prediction [8] for a tessellation ratio of 0.03, boxes: Prediction by `sim_telarray` simulation ($\alpha = 0.13$). The difference in the steepness of the curve is caused by the difference in tessellation ratio.

The TAIGA IACTs are composed of 30 spherical mirror tiles (60 cm \varnothing) on a 4.75 m \varnothing Davies-Cotton dish. To compare our results to a semi-analytical model prediction, one must take note of the tessellation ratio, the ratio between the diameters of the individual mirror tile (d_{tile}) and the main dish (D_{dish}):

$$\alpha = \frac{d_{tile}}{D_{dish}} \quad (1)$$

The relative size of the individual mirror tiles is important since larger tiles contribute larger aberration effects due to their spherical nature. TAIGA's IACTs are designed with a tessellation ratio of 0.13.

Figure 1 shows the image of the point source at different off-axis angles in the camera layer. The PSF is significantly smaller than a single camera pixel even at an off-axis angle of 5° at the assumption of perfect mirror alignment. The star-like shape of the spot is an effect of the outermost mirror tiles.

The impact of the tessellation ratio on the PSF can be seen in Figure 2. The analytical prediction by Schliesser and Mirzoyan[8] assumes a tessellation ratio of 0.03, meaning much smaller mirror tiles as compared to the TAIGA telescopes ($\alpha = 0.13$). The overall shape is closer to the shape of the main dish, with less aberration effects from the rims of the individual tiles.

For small angles, the minimal PSF of the TAIGA IACTs is not as good as expected from the analytical predictions. With increasing angle however the TAIGA design shows a better PSF than predicted from the 0.03 model. This is an expected and desired effect since TAIGA IACTs are telescopes with a large field of view, so faithful imaging at large off-axis angles is more important than reaching zero at the very center. Even at 5° off-axis, the TAIGA PSF stays considerably smaller than the radius of the camera pixels (0.19°), leaving enough room for the deviations brought by a real setup.

Single mirror PSF measurement The MC results shown in Figure 1 represent the minimal PSF possible under the assumption of perfect mirrors. Real mirrors have inaccuracies which will add up and increase the overall PSF of the telescopes. To get an estimate on these inaccuracies, the PSFs of several mirror tiles have been measured individually by placing a point-like light

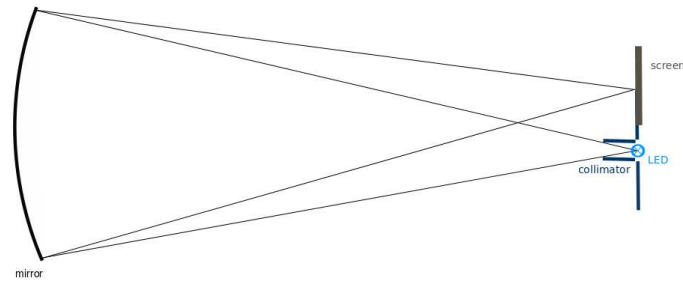


Figure 3: Schematic view of the single-mirror PSF measurement setup. To the left is the mirror, to the right the light source and screen close to the focal point.

source in the focal distance of the mirror and determining the angular size of the reflected spot (see Figure 3). For a perfect mirror, this spot should have the exact same dimensions as the source, with any spread being the contribution of deviations from a perfect spherical shape.

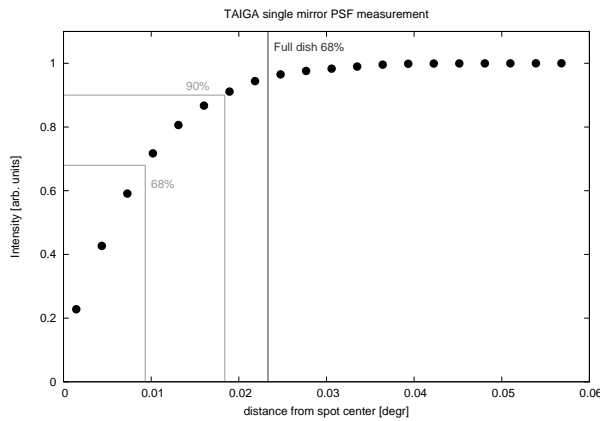


Figure 4: Example for the cumulative intensity distribution of a point source reflected by a single TAIGA mirror. Marked are the 68% (1σ) and 90% containment radius as well as the MC-determined radius of the minimal PSF of the whole dish. It can be seen that the single-mirror PSF is smaller than the full dish PSF by about a factor of 2.

Since a spherical mirror reflects a light source back onto itself when the source is put at the exact focal point, the measurements are done in a slight off-axis angle ($<2^\circ$). 28 TAIGA mirrors have been measured in this procedure with all mirrors showing a PSF significantly smaller than that of the full dish (for an example, see figure 4) while not varying much between each other. Therefore, the chosen mirrors are suitable for use in the TAIGA IACTs.

3.2 Gamma Hadron Separation

The TAIGA IACTs are meant to improve the gamma hadron separation of the TAIGA array, especially at its energy threshold at about 10-50 TeV[9]. To understand the range of improvement, we first evaluate how powerful the IACTs are on their own. Since shower energy, impact parameter and direction are derived from the timing array's measurements, we can focus our analysis of the IACT images on the primary.

The parameter with the greatest dependence on the nature of the shower primary is the image width, calculated via the second moment of the amplitude distribution after image clean-

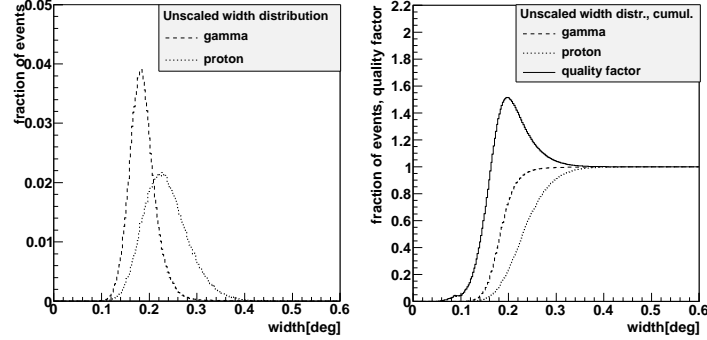


Figure 5: Raw image width distribution for zenith showers with $E_{EAS} = 10\text{-}50$ TeV . Dashed: Gammas, dotted: Protons, Solid: Quality factor. Left: Differential distribution. The proton distribution has a bigger mean and spread than the gamma distribution, but the two peaks still overlap much. Right: Cumulative distribution and Q for the width cut. If a cut is made on the raw data, the maximum Q does not reach 1.6.

ing. This second moment depends mainly on the overall camera PMT amplitude ('size'), impact parameter and the primary. The higher number of hadronic interactions in a hadron-induced shower lead to a broader transversal momentum distribution of the particles in the shower, which in turn increases the image width compared to gamma- or electron-induced showers as seen in figure 5. A cut on the image width can separate gamma from hadron events. The cut quality factor is defined by:

$$Q = \frac{\epsilon_\gamma}{\sqrt{\epsilon_p}} \quad (2)$$

with

$$\epsilon_i = \frac{n_i(w < w_{cut})}{n_i}, \quad \epsilon_i \in (\gamma, p) \quad (3)$$

Even though the two distributions have different shapes, they still overlap strongly due to variation in the impact parameter and image size. With a width cut on the raw data, only a quality factor of $Q=1.4$ is reached. In order to improve the quality factor, each image width is scaled to the expectancy value for the respective image size, impact parameter and zenith angle. An exclusive gamma-only MC event data set was used to generate a lookup-table which contains the width expectancy values.

In the final experiment, the selection of the correct lookup-table entry will be done with core distance and zenith angle determined by the HiSCORE timing array. To give a first estimate of the final separation quality, a Toy core simulation was performed (see Figure 6). To emulate reconstruction by HiSCORE, the core position which is known from the MC is randomised with the HiSCORE core position resolution, and the resulting value is used as the 'reconstructed' core position when selecting the lookup table entry. This cuts on computing time since actually simulating the showers in `sim_score` is not necessary.

The value after scaling is called the Hybrid Scaled Width (HSCW):

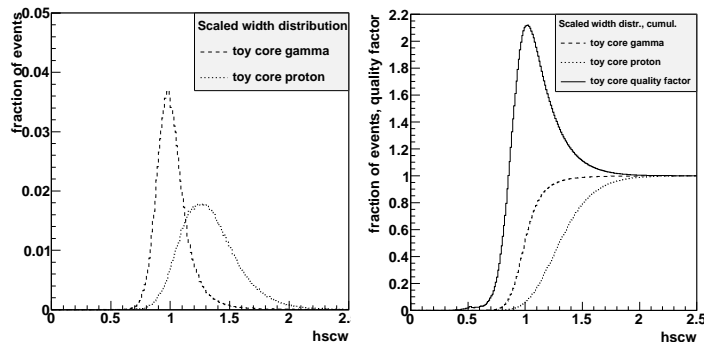


Figure 6: HSCW distribution for zenith showers with $E_{EAS} = 10\text{-}50$ TeV. Dashed: Gammas, dotted: Protons, Solid: Quality factor. Left: Differential distribution. Compared to the unscaled plot, the gamma and the proton distribution have moved apart significantly. Right: Cumulative distribution and Q for the width cut. If a cut is made on the HSCW, the maximum Q is about 2.1.

$$HSCW = \frac{w_{tel}}{w_{MC}^{\gamma}(d_{array}, size_{tel})} \quad (4)$$

Scaling the width makes the two distributions move apart, and now a cut on the HSCW yields us $Q \sim 1.9$, which is not only better than an unscaled cut, but also better than the HiSCORE-only separation at those. The timing array can achieve $Q \sim 1$ at the threshold and only starts to approach 2 at a hundred TeV.[10][9]

The blurring of the core position lowers the separation quality only little compared to the direct use of the MC core position (~ 1.9) even though HiSCORE's core resolution is strongly energy-dependent near the energy threshold.

4 Conclusion and Outlook

TAIGA's combination of IACTs with timing arrays is a valid method of obtaining the large areas needed to observe ultra high energy gamma rays. The design of the TAIGA telescopes will provide suitable shower images as tested both by MC simulation and measurement of prototype parts. Also, adding IACTs to a timing array will provide a possibility of rejecting the hadronic background with a quality factor of 2.1 near the energy threshold, where the timing array alone could not make a distinction.

The studies so far are not yet a full hybrid reconstruction. In the full reconstruction, the directional information stored in the IACT images will also be taken into account to improve the resolution of shower core position and incidence angle. Also the timing array signals do contain information on the nature of the primary in the signal rise time, so for higher energies the gamma hadron separation quality will be much better than 2.

Furthermore, the IACTs can be used to reduce the energy threshold. The timing array needs 4 stations with signal for a proper reconstruction, but a shower can also be reconstructed with the IACT image and one station only. The combination also makes it possible to indirectly increase the field of view of the telescopes. So far, shower images that are cut off by the edge

of the camera are rejected because they are incomplete, but the shower information from the timing array might allow to interpolate the shape of the full shower.

5 Acknowledgments

We acknowledge the support of the Russian Federation Ministry of Education and Science (agreements N 14.B25.31.0010, N2014/15, project 1366, zadanie N 3.889.2014/K), the Russian Foundation for Basic Research (grants 13-02-00214, 15-02-10005, 13-02-12095), The Helmholtz Association (grant HRJRG-303), and the Deutsche Forschungsgemeinschaft (grant TL 51-3).

References

- [1] M. Tluczykont et al, *Connecting neutrino Astrophysics to Multi-TeV to PeV gamma-ray astronomy with TAIGA these proceedings* (2016)
- [2] Hillas A M 1985 Cherenkov light images of EAS produced by primary gamma *Int. Cosm. R. Conf.* **3** 4458.
- [3] D. Heck et al, Report *FZKA 6019* (1998), available from http://www-ik.fzk.de/corsika/physics_description/corsika_phys.html
- [4] N. N. Kalmykov, S. S. Ostapchenko, and A. I. Pavlov *Nucl. Phys. B (Proc. Suppl.)* **52B** 17 (1997)
- [5] H. Fesefeldt, Report **PITHA-85/02** (1985)
- [6] M. Tluczykont et al, *The HiSCORE concept for gamma-ray and cosmic-ray astrophysics beyond 10 TeV Astropart. Phys.* **56** 42-53 (2014) [1403.5688].
- [7] K. Bernlöhner *Simulation of imaging atmospheric Cherenkov telescopes with CORSIKA and sim_telarray, Astropart. Phys.* 149-158 (2008)
- [8] A. Schliesser and R. Mirzoyan, *Wide-field prime-focus imaging atmospheric Cherenkov telescopes: A systematic study, Astrop. Phys.* **24** 382-390 (2005) [astro-ph/0507617]
- [9] M. Tluczykont et al, *Towards gamma-ray astronomy with timing arrays* in proceedings of *ECRS* (2014)
- [10] D. Hampf, M. Tluczykont and D. Horns, *Event reconstruction techniques for the wide-angle air Cherenkov detector HiSCORE Nucl. Inst. Meth. in Phys. Res. A* 137-146 (2012/13) [1302.3957]

Recent Results from the MAGIC Telescopes

Dorit Eisenacher Glawion¹, for the MAGIC Collaboration²

¹Universität Würzburg, Institut für Theoretische Physik und Astrophysik, Emil-Fischer-Straße 31, 97074 Würzburg, Germany

²<https://magic.mpp.mpg.de/>

DOI: <http://dx.doi.org/10.3204/DESY-PROC-2016-05/24>

MAGIC consists of two imaging air Cherenkov telescopes located at La Palma, Spain. Since 12 years, the telescopes are performing scientific observations of gamma rays with energies between 35 GeV and 50 TeV.

Scientific highlights from MAGIC concerning both galactic and extragalactic sources in the context of multi-messenger astronomy are presented. Among these, measurements of the TeV emission from Crab observations are shown. Also, the ultra-fast variability of IC 310, which challenges jet emission models in AGNs, is discussed. Furthermore, the detection of very-high-energy gamma-ray emission from two active galaxies, B0 218+357 and PKS 1441+25, located at redshift of ~ 0.94 is presented.

1 Introduction

Cosmic rays were discovered more than one hundred years ago by Victor Hess. Still, there is an increasing research field connected to their nature, their origin, and their propagation. Due to the deflection of the charged particles of the cosmic rays, e.g., by the magnetic fields of the interstellar and the intergalactic medium they reach the Earth mostly isotropic.

Interactions of cosmic rays among themselves and/or with photon fields result in the production of pions. These decay into neutral and charged muons, which themselves decay into gamma rays and neutrinos, respectively. This means that the detection of gamma rays and neutrinos from point sources can provide an unambiguous signature of the origin of the cosmic rays. While the detection of neutrinos is more challenging, a large and rising number of sources of gamma rays have already been discovered. While in the high-energy gamma-ray regime $20 \text{ MeV} \lesssim E \lesssim 100 \text{ GeV}$, satellite-based instruments such as the *Fermi*-LAT instrument are used, gamma-rays at higher energies ($100 \text{ GeV} \lesssim E \lesssim 100 \text{ TeV}$) are detected with ground-based telescopes based on the Imaging Air Cherenkov Technique.

The Major Atmospheric Gamma Imaging Cherenkov Telescope (MAGIC) is a system of two Imaging Air Cherenkov Telescopes (IACT) with a mirror dish diameter of 17 m each, separated by a distance of 85 m. It is located at the Observatorio del Roque de los Muchachos on the Canary island of La Palma, Spain, at an altitude of ~ 2200 m above sea level. The construction of the first telescope, MAGIC-I, was completed in 2003 and it performs scientific observations since 2004. In 2009, the second telescope, MAGIC-II, joined in. Since then, the two telescopes are working together as a stereoscopic system which allows an improved performance in terms of sensitivity and angular resolution, among other things. The energy range covered by MAGIC overlaps with the accessible range of *Fermi-LAT* at low energies, starting at 50 GeV (standard

trigger) and reaching up to 50 TeV. Some observations are also performed with a new digitalized trigger technique and allows for measurements even below 50 GeV [1].

The IACT technique is based on the production of air showers by highly energetic particles in the Earth's atmosphere. If a gamma-ray photon with more than 10 MeV of energy enters the atmosphere the production of an electron-positron pair dominates the absorption. Due to an interaction with molecules in the air, secondary gamma rays are produced by Bremsstrahlung. These secondaries again may produce e^+e^- pairs. The resulting electromagnetic cascade continues until the average energy reaches the value at which the losses due to ionization and Bremsstrahlung are equal. The secondary electrons in those showers, if energetic enough, i.e., when moving faster than the speed of light in the atmosphere, can activate the emission of Cherenkov photons in a cone with a small opening angle. Inside the Cherenkov light pool, mirror telescopes can be placed in order to measure the Cherenkov light. The spectrum of this light is mostly in the optical and ultra-violet range. The faint emission can be measured with photo-multipliers as also done with MAGIC. Due to a short duration of the Cherenkov pulses, a fast readout system needs to be connected with the telescope. Besides showers introduced by gamma rays, showers induced by hadrons (e.g., protons) exist. Those showers form the dominating background and hence are the limiting factor for ground-based gamma-ray astronomy. Typically, one gamma-ray event observed by an IACT telescope is hidden behind 1000 background events.

With this technique, MAGIC is able to achieve a sensitivity of 0.6% of the Crab Nebula flux for a 5σ detection in 50 h of observation in the best range at energies of $E \sim 400$ GeV. The angular and energy resolution, both dependent on the energy, is $0.1^\circ - 0.07^\circ$ and 15–20%, respectively. Details about the performance of MAGIC can be found in [2].

The scientific focus of MAGIC is set on the investigation of the gamma-ray emission from galactic objects of various types as well as on active galactic nuclei and gamma-ray bursts as extragalactic objects. Follow-up observations of gamma-ray bursts by MAGIC are reported in [3]. Furthermore, MAGIC concentrates on the indirect measurements of dark matter [4, 5, 6] as well as on setting constraints on the cosmic rays [7], the extragalactic background light [8], the Lorentz invariance violation [9], and the intergalactic magnetic field. In this paper, only results from galactic objects, active galactic nuclei, and follow-up observations of neutrino events are being reviewed.

2 Galactic science

MAGIC observes a variety of galactic objects which are mostly in connection with the end stages of stars, e.g., novae, supernova remnants, pulsars, and pulsar wind nebulae.

2.1 Crab Nebula and its pulsar

The Crab Nebula is the standard candle for the very-high-energy astrophysics at energies $E > 50$ GeV. Although it is known to be a TeV emitter for a long time this pulsar wind nebula is still of interest for current research. Recent MAGIC observations between October 2009 and April 2011 of 69 h revealed a spectrum ranging over the entire accessible energy range over three decades in energy [10]. Together with *Fermi*-LAT data, these yielded the most precise measurement of the inverse Compton peak of $53_{-3\text{stat}-13\text{syst}}^{+3\text{stat}+31\text{syst}}$ GeV that is dominated by systematic effects. Only a modified log-parabola function with an exponent of 2.5 instead of

2 fits the obtained spectrum. It was found that a constant magnetic field model does not reproduce the broadness of the inverse Compton peak. Most probably, this suggests that the assumption of homogeneity of the magnet field inside the nebula is wrong. Three state-of-the-art models were applied to the spectral energy distribution. A time-dependent 1D spectral model is able to match the data with a magnetic field of $80\mu\text{G}$. However, it fails to describe the data when including the morphology of the nebula at higher frequencies.

Inside the nebula one finds the pulsar. The first detection of its pulsed gamma-ray emission above 25 GeV by a ground-based instrument was already achieved in 2008 by MAGIC [11]. After the accumulation of 320 h of observations, a spectrum between 70 GeV and 1.5 TeV was measured [12]. The pulse profile shows two narrow peaks which are synchronized with the ones measured, e.g., by *Fermi*-LAT in the lower energy gamma-ray range. The spectra of pulse I and II were found to follow different simple power-law indices, 3.2 ± 0.4 and 2.9 ± 0.2 , respectively. The pulsed TeV emission can not be produced by synchrotron-curvature radiation. Instead, the inverse Compton process plays a dominating role at energies above 50 GeV. Furthermore, all current existing models fail to reproduce the observed narrowness of the peaks. The observation poses strong constraints on the Lorentz factors of the electrons. A parent population of electrons with $\gamma > 5 \times 10^6$ is needed. This suggests an inverse Compton scattering of low energy photons as the emission and that the gamma-ray production region is located near by the light cylinder.

2.2 The supernova remnant W51 C

In 2010 and 2011, MAGIC collected more than 50 h of data from the region of W51 [13]. This complex field hosts the supernova remnant W51 C which interacts with molecular clouds in the star forming region of W51 B. Observations at other frequencies suggest a possible association of a pulsar wind nebula with the remnant. Gamma rays were detected from W51 but it was not clear if this emission is originating from the pulsar wind nebula, the supernova remnant shell, and/or the molecular cloud. The spatial resolution of the measurements by MAGIC helped to pinpoint the location of the gamma-ray emission. The skymaps show an extension at high energies towards the pulsar. However, it was not possible to establish it as an independent source. The contribution from the pulsar wind nebula was estimated to be $\sim 17\%$ of the flux, but the shocked cloud region is dominant at all energies.

Furthermore, the measured spectrum follows the high-energy points measured with *Fermi*-LAT and ranges up to ~ 5 TeV with a simple-power law function. Modeling of the spectral energy distribution is consistent with a hadronic origin of the gamma-ray emission. It was found that an ongoing acceleration of ions in the interaction zone between the supernova remnant and the cloud can explain the observations.

2.3 Novae and dwarf novae

The *Fermi*-LAT telescope detected gamma-rays at GeV energies from a few novae in the last years. This emission can be interpreted in terms of the inverse Compton process of electrons which are accelerated in shocks of novae. In the same manner, protons might be accelerated to much higher energies under the same condition. This could produce a second gamma-ray emission component in the spectra possibly at TeV energies.

For this reason, MAGIC performed follow-up observations of novae and dwarf novae [14]. One example is the observation of the classical novae V339 Del in August and September 2013. These measurements were triggered by an outburst found in the optical and GeV band. MAGIC

did not detect a significant signal, but upper limits to the spectral energy distribution together with the data points from *Fermi*-LAT limit the ratio of the proton-to-electron luminosity to be $L_p \lesssim 0.15 L_e$ in theoretical models.

3 Extragalactic science

The extragalactic gamma-ray sky currently counts ~ 65 objects¹. The parent population consists of radio-loud active galactic nuclei with jets pointing towards the earth. Those objects are called blazars and they are typically characterized by their strong variability in all wavelengths and on all time scales. The so-called Doppler boosting effect plays an important role for the interpretation of the emission of these objects. However, a handful of radio galaxies for which the angle between the jet-axis and the line-of-sight is larger were discovered as well.

3.1 Black hole lightning from IC 310

IC 310 is an active galaxy located in the outskirts of the Perseus cluster of galaxies at a cosmological redshift of $z = 0.0189$. Originally, this object was classified as a head-tail radio galaxy, where the jets of the nucleus are being bend due to the movement of the galaxy through the cluster. However, studies of the multi-wavelength emission showed several properties similar to those of blazars as well as radio galaxies.

During an extensive multi-wavelength program in late 2012, MAGIC detected an exceptionally bright TeV flare from IC 310 on one night reaching an average flux level of up to one Crab above 1 TeV with a hard spectrum over two decades in energy [15]. The intra-night light curve showed a series of strong outbursts with flux-doubling time scales as fast as a few minutes. The fast variability constrains the size of the gamma-ray emission regime to be smaller than 20% of the gravitational radius of its central black hole. Furthermore, very long baseline interferometry measurements in the radio band revealed a limit for the viewing angle of the active galactic nucleus to be $10^\circ \lesssim \theta \lesssim 20^\circ$. Thus, no strong Doppler boosting can be assumed in the explanation of the gamma-ray production mechanism. This challenges the standard model for gamma-ray emission of active galaxies being produced due to the acceleration of particles at shocks in the jets. It was found that a magnetospheric model similar to those used to interpret the gamma-ray emission from pulsars is able to explain the phenomena. Instead of having a neutron star in the center of the magnetosphere, a rotating black hole exists. In this model, the gamma rays are being produced by electromagnetic cascades, acceleration inside vacuum gaps, emission via the inverse Compton, and curvature radiation processes.

3.2 Gravitationally lensed blazar S3 0218+35

S3 0218+35 is a blazar at a redshift of $z = 0.944$, the most distant and the only gravitationally lensed gamma-ray emitting object of the very-high-energy sky today. The lensing galaxy is a spiral galaxy and is located at the redshift of $z = 0.68$. In July 2014, *Fermi*-LAT observed an outburst from this objects which triggered follow-up observations with MAGIC. This flare happened during full moon time where MAGIC interrupts observations. However, previous studies from the *Fermi* team as well as of the radio emission showed that the gravitationally lensed signals splits into two components separated by 10-12 days. MAGIC observations were

¹<http://tevcat2.uchicago.edu/>

scheduled around the expected time of arrival of the trailing component. Thus, MAGIC detected the object with a significance of more than 5σ at ~ 12 d after the flare seen by *Fermi*-LAT [16].

3.3 Quasar PKS 1441+25

The second most distant active galaxy in the very-high-energy range is PKS 1441+25, a flat-spectrum radio quasar located at a redshift of $z = 0.939$. Similar to the detection of S3 0218+35, the observations of PKS 1441+25 were triggered by an outburst of the object measured with the *Fermi*-LAT telescope in April 2015. MAGIC observed the object during April and May 2015, resulting in the detection of a signal of 25.5σ in an energy range of 40–250 GeV and a variability time scale of 6.5 ± 1.9 d [17]. In addition, many telescopes in various frequency bands performed observations, resulting in an excellent coverage of the multi-wavelength spectral energy distribution for the object at different flux states. All observations together suggest a subdivision of the high state into two distinct flux states. The theoretical interpretation of the spectral energy distribution with an external Compton model yielded that the location of the gamma-ray emitting region during the period of high activity is located in the jet but outside the broad-line region, while the emitting region during the low activity is partially inside the broad-line region.

4 Follow-up of neutrino events

As said before, the detection of neutrino emission from astronomical objects would certainly contribute to the search of the origin of the cosmic rays. However, measuring a significant neutrino excess especially from a point-source is challenging due to the much smaller cross section for neutrino interaction. The IceCube Collaboration reported on the detection of 37 neutrino events between 30 TeV and 2 PeV, spread over both hemispheres and rejecting an atmospheric origin at a 5.7σ level [18]. However, most of these events have a large median positional uncertainty of 10° to 20° . Thus, IACT instruments with an angular resolution of the order of $\sim 0.1^\circ$ could provide follow-up gamma-ray observations for neutrino candidates and transient neutrino events.

For this reason, IACT instruments, e.g., MAGIC have been receiving on-line triggers from the IceCube Collaboration for a few years. A precedent case including the precursor of IceCube, AMANDA, is being reported in [19]. So far, no significant signal was found from such observations but they are still crucial as they allow for performing of real-time multi-messenger astronomy.

5 Summary

The last few years of scientific operation of the MAGIC telescopes were very successful, e.g., resulting in the detection of the most energetic pulsed emission from an astronomical object, the measurement of gamma rays from active galactic nuclei in our neighborhood or from the middle age of the universe, and ultra-fast variability giving new clues on particle acceleration.

The MAGIC team makes strong efforts in collaborating with many telescopes in all other frequency ranges as well as the Cherenkov gamma-ray instruments VERITAS, H.E.S.S., FACT, and HAWC. In addition, MAGIC performs follow-up observations of gravitational wave as well as neutrino events.

In the next years, MAGIC will continue to observe the very-high-energy gamma-ray sky bridging the gap until the future Cherenkov Telescope Array, CTA, will start its operation. The building of the first prototype of a 23 m diameter Large Size Telescope for CTA has already started in 2015 right next to the MAGIC site.

Acknowledgments

We would like to thank the Instituto de Astrofísica de Canarias for the excellent working conditions at the Observatorio del Roque de los Muchachos in La Palma. The financial support of the German BMBF and MPG, the Italian INFN and INAF, the Swiss National Fund SNF, the ERDF under the Spanish MINECO (FPA2012-39502), and the Japanese JSPS and MEXT is gratefully acknowledged. This work was also supported by the Centro de Excelencia Severo Ochoa SEV-2012-0234, CPAN CSD2007-00042, and MultiDark CSD2009-00064 projects of the Spanish Consolider-Ingenio 2010 programme, by grant 268740 of the Academy of Finland, by the Croatian Science Foundation (HrZZ) Project 09/176 and the University of Rijeka Project 13.12.1.3.02, by the DFG Collaborative Research Centers SFB823/C4 and SFB876/C3, and by the Polish MNiSzW grant 745/N-HESS-MAGIC/2010/0.

References

- [1] F. Dazzi *et al.*, PoS ICRC2015 984, (2015).
- [2] J. Aleksić *et al.*, APh **72** 76 (2016).
- [3] A. Carosi *et al.*, PoS ICRC2015 809, (2015).
- [4] J. Aleksić *et al.*, ApJ **710** 634 (2010).
- [5] J. Aleksić *et al.*, JCAP **02** 008 (2014).
- [6] M.L. Ahnen *et al.*, JCAP **02** 039 (2016).
- [7] M.L. Ahnen *et al.*, A&A **589A** 33 (2016).
- [8] M.L. Ahnen *et al.*, arXiv:astro-ph/1602.05239 (2016).
- [9] MAGIC Collaboration *et al.*, Phys. Lett. B **668** 253 (2008).
- [10] J. Aleksić *et al.*, JHEAp **5** 30 (2015).
- [11] E. Aliu *et al.*, Science **322** 1221 (2008).
- [12] S. Ansoldi *et al.*, A&A **585A** 133 (2016).
- [13] J. Aleksić *et al.*, A&A **541A** 13 (2012).
- [14] M.L. Ahnen *et al.*, A&A **582A** 67 (2015).
- [15] J. Aleksić *et al.*, Science **346** 1080 (2014).
- [16] J. Sitarek *et al.*, PoS ICRC2015 825, (2015).
- [17] M.L. Ahnen *et al.*, ApJ **815L** 23 (2015).
- [18] M.G. Aartsen *et al.*, Phys. Rev. Lett. **113** 101101 (2014).
- [19] M. Ackermann *et al.*, arXiv:astro-ph/0709.2640 (2007).

Neutrino Geoscience

Livia Ludhova

IKP-2 Forschungszentrum Jülich, 52428 Jülich, Germany
RWTH Aachen University, 52062 Aachen, Germany

DOI: <http://dx.doi.org/10.3204/DESY-PROC-2016-05/7>

Neutrino geoscience is a newly born interdisciplinary field having as its main aim determination of the Earth's radiogenic heat through measurement of geoneutrinos: antineutrinos released in decays of long-lived radioactive elements inside the Earth. In fact, such measurements are a unique direct way how to pin-down this key element for many geophysical and geochemical Earth's models. The large-volume liquid scintillator detectors, originally built to measure neutrinos or anti-neutrinos from other sources, are capable to detect geoneutrinos, as it was demonstrated by KamLAND (Japan) and Borexino (Italy) experiments. Several future projects as SNO+ or JUNO have geoneutrino measurements among their scientific goals. This work covers the status-of-art of this new field, summarising its potential in terms of geoscience, the status of existing experimental results, and future prospects.

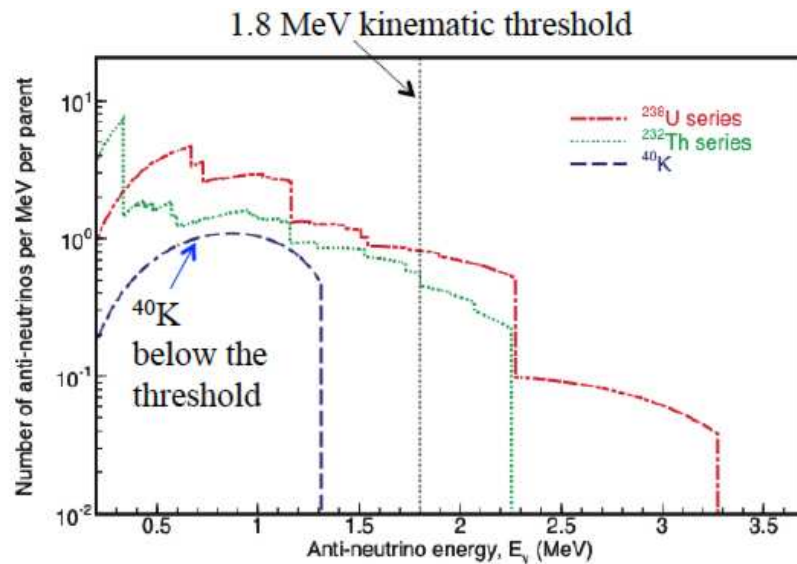


Figure 1: Energy spectrum of geoneutrinos. The dashed vertical line shows the energy threshold of the IBD interaction: currently the only detection method for geoneutrinos.

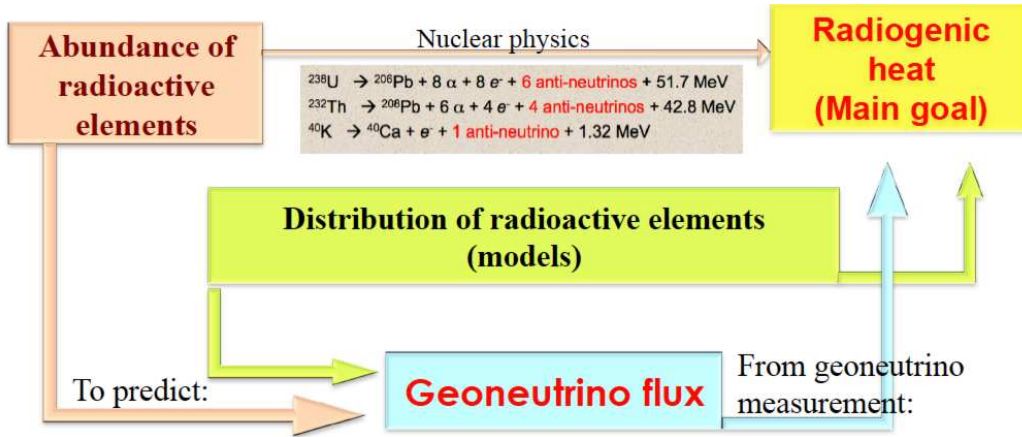
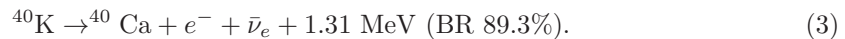
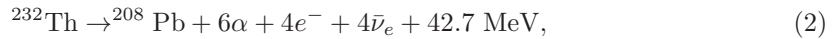
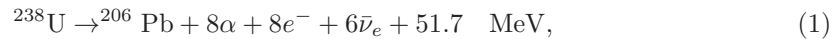


Figure 2: Schematic visualisation of the relations among the abundances and distributions of radioactive elements inside the Earth, the geoneutrino flux, and the radiogenic heat, the ultimate goal of geoneutrino measurements.

1 What are geoneutrinos and the main goal

Geoneutrinos are electron-flavour antineutrinos emitted in the β decays of long-lived radioactive elements, called also *the heat producing elements* (HPE). Geoneutrinos are emitted along the decay chains of ${}^{238}\text{U}$ and ${}^{232}\text{Th}$ and in the ${}^{40}\text{K}$ decay:



Geoneutrino spectrum is shown in Fig. 1. Geoneutrinos are detected by the so called Inverse Beta Decay (IBD) interaction:



Due to the 1.8 MeV kinematic threshold of this reaction, only the high-energy tail of ${}^{238}\text{U}$ and ${}^{232}\text{Th}$ geoneutrinos can be detected, while all ${}^{40}\text{K}$ geoneutrinos are below the threshold.

The main aim of geoneutrino studies is to determine the Earth's radiogenic heat, especially the unknown contribution from the mantle. The mantle composition is quite unknown with respect to the better-known crustal composition. Knowing the mass/abundances of HPE, the radiogenic heat is directly determined. The geoneutrino studies are, however, complicated through an unknown distribution of HPE, on which depends both the geoneutrino signal prediction as well as the final interpretation of the measured geoneutrino flux, see Fig. 2. Due to this, a close collaboration between neutrino physicists and geoscientists is strongly required in order to exploit the potential of geoneutrinos to its maximum.

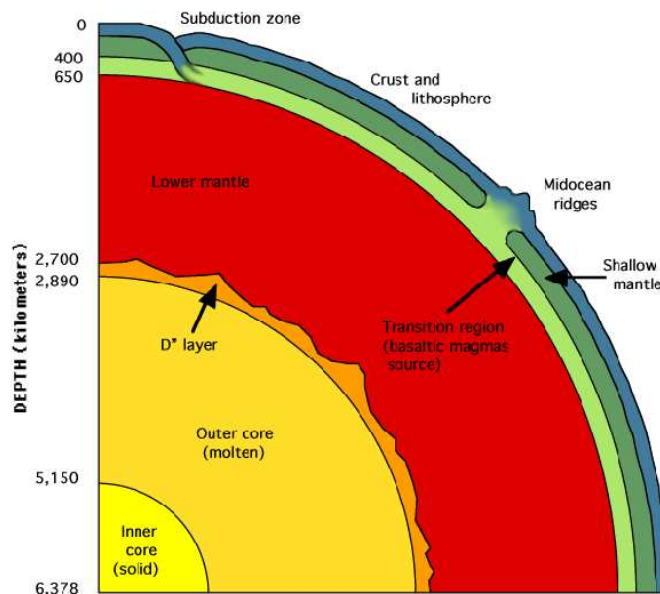


Figure 3: A schematic profile of the Earth structure (from <http://www.homepages.ucl.ac.uk/~ucfbdx/resint.htm>).

2 The Earth and GeoSciences

The Earth was created in the process of accretion from undifferentiated material, to which chondritic meteorites are believed to be the closest in composition and structure. The bodies with a sufficient mass undergo the process of differentiation, e. g., a transformation from an homogeneous object into a body with a layered structure. The metallic core (3500 km radius) was the first to separate from the silicate primordial mantle, which further differentiated into the current mantle (3000 km thickness) and the crust (5 to 75 km). The Fe-Ni metallic core with up to ~10% admixture of lighter elements, has a temperatures range from 4100 to 5800 K. Its central part, inner core with the radius ~1300 km is solid due to high pressure. The 2200 km thick outer core is liquid and has a key role in the geo-dynamo process generating the Earth's magnetic field. The D'' layer is a core-mantle boundary, a 200 km thick seismic discontinuity of unclear origin. The lower mantle (2000 km) with a temperature gradient from 600 to 3700 K is solid, but viscose on long time scales. It is involved in the convection driving the movement of tectonic plates with a speed of a few centimetres per year. A transition zone in the depth of 400 - 600 km is a seismic discontinuity due to mineral recrystallisation. The upper mantle contains viscose asthenosphere on which are floating the lithospheric tectonic plates. These comprise the uppermost, rigid part of the mantle and the crust of two types: oceanic and continental. The continental crust (30 km average thickness) has the most complex history being the most differentiated and heterogeneous, consisting of igneous, metamorphic, and sedimentary rocks. The oceanic crust (5 - 10 km) is created along the mid-oceanic ridges, where the basaltic magma differentiates from the partially melting mantle. A schematic profile of the Earth structure can be found in Fig. 3.

The HPE are so called refractory, lithophile elements: they bound to the lighter partially melted liquid, leaving behind the HPE-depleted solid and denser residuum. Due to this mechanism, the HPE are strongly concentrated in the most complex continental crust (at the level of few ppm in average) and present in sub-ppm concentrations in the oceanic crust. The HPE concentration in the mantle is suppressed by few orders of magnitude and largely unknown. Due to the chemical affinity to silicates, no HPE are expected to be present in the metallic core.

How do we get information about the deep Earth? Seismology studies the propagation of the S and P seismic waves, providing the velocity and density profiles of the Earth. Geochemistry studies the chemical composition of the Earth. The depth of accessible rock samples is limited to the upper mantle. The global composition of the Bulk Silicate Earth (BSE) is derived through geochemical modelling, considering the correlations in isotopic abundances in the solar photosphere and in meteorites, as well as composition of the present day rocks. These BSE models describe the composition of the Primitive Mantle, the Earth composition after the core separation and before the crust-mantle differentiation. The estimates of the composition of the present-day mantle can be derived as a difference between the mass abundances predicted by the BSE models in the Primitive Mantle and those observed in the present crust. In this way, the predictions of the U and Th mass abundances in the mantle are made. An overview of different BSE models can be found for example in Šrámek et al. [1].

The Earth's surface heat flux is estimated based on the measurements of temperature gradients along several thousands of drill holes around the globe. The most recent evaluation of these data leads to the prediction of 47 ± 2 TW predicted by Davies and Davies (2010) [2], consistent with the estimation of Jaupart et al. (2007) [3]. The relative contribution of the radiogenic heat from radioactive decays to this flux is not known and this is the key information which can be pinned down by the geo-neutrino measurements. The geochemical, cosmochemical, and geodynamical models predict the radiogenic heat of 20 ± 4 , 11 ± 2 , and 33 ± 3 TW, respectively [1]. The crustal radiogenic power was recently evaluated by Huang et al. [4] as $6.8^{+1.4}_{-1.1}$ TW. By subtracting this contribution from the total radiogenic heat predicted by different BSE models, the mantle radiogenic power can be as little as 3 TW and as much as 23 TW. To determine this mantle contribution is one of the main goals and potentials of Neutrino Geoscience.

3 Geoneutrino detection

Geoneutrinos are detected by the large-volume liquid scintillator detectors placed in underground laboratories, in order to shield them from the cosmic radiation. The target for the IBD detection interaction shown in Eq. 4 are hydrogen nuclei from the hydrocarbon molecules of organic liquid scintillator. In this process, a positron and a neutron are emitted as reaction products. The positron promptly comes to rest and annihilates emitting two 511 keV γ -rays, yielding a *prompt event*, with a visible energy E_{prompt} , directly correlated with the incident antineutrino energy $E_{\bar{\nu}_e}$:

$$E_{prompt} = E_{\bar{\nu}_e} - 0.784 \text{ MeV}. \quad (5)$$

The emitted neutron keeps initially the information about the $\bar{\nu}_e$ direction, but is typically captured on protons only after quite a long time ($\tau = 200 - 250 \mu\text{s}$, depending on scintillator), during which the directionality memory is lost in many scattering collisions. When the thermalised neutron is captured on proton, it gives a typical 2.22 MeV de-excitation γ -ray, which provides a coincident *delayed event*. The pairs of time and spatial coincidences between the

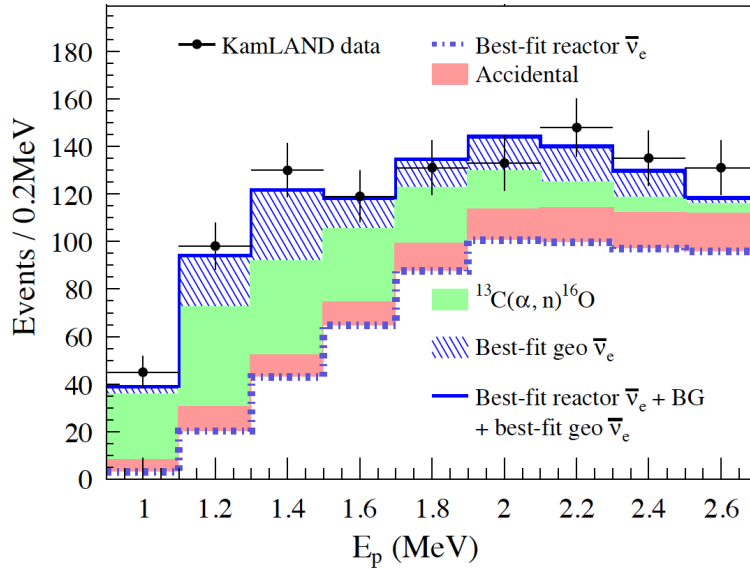


Figure 4: KamLAND prompt energy spectrum of $\bar{\nu}_e$ events in the geoneutrino energy region. Data together with the best-fit background and geo contributions are shown. Taken from [8].

prompt and the delayed signals offer a clean signature of $\bar{\nu}_e$ interactions, very different from the ν_e scattering process used in the neutrino detection.

For a ~ 3 MeV antineutrino, the oscillation length is of ~ 100 km, small with respect to the Earth's radius of ~ 6371 km: the effect of the neutrino oscillation to the total neutrino flux is well averaged. Considering also the local matter effects [5], the net effect of flavour oscillations during the geo-neutrino propagation through the Earth is the average electron flavour survival probability of ~ 0.55 with a very small spectral distortion, negligible for the precision of the current geo-neutrino experiments.

Typically, for the experimental sites built at the continental crust, about half of the total geoneutrino signal comes from the local crust in the area of few hundreds of kilometers around the detector [4]. In order to extract the mantle contribution from the measured geoneutrino signal, it is necessary to be able to subtract the crustal contribution. This means, that the local geology in the area of the experiment has to be known.

4 Latest geoneutrino measurements

Today, only two experiments succeeded to measure geoneutrinos: KamLAND [6, 7, 8] in Kamioka mine in Japan and Borexino [9, 10, 11] in Gran Sasso underground laboratory in Italy. KamLAND is a 1 kton liquid scintillator detector dedicated to the measurement of reactor antineutrinos, which provided one of the first proves of the existence of the phenomenon of neutrino oscillations and the most precise measurement of the Δm_{12}^2 mass splitting [12]. Borexino is 280 ton liquid scintillator detector, originally built to measure low-energy (below 1 MeV) solar neutrinos by means of elastic scattering off electrons. In contrast to IBD interac-

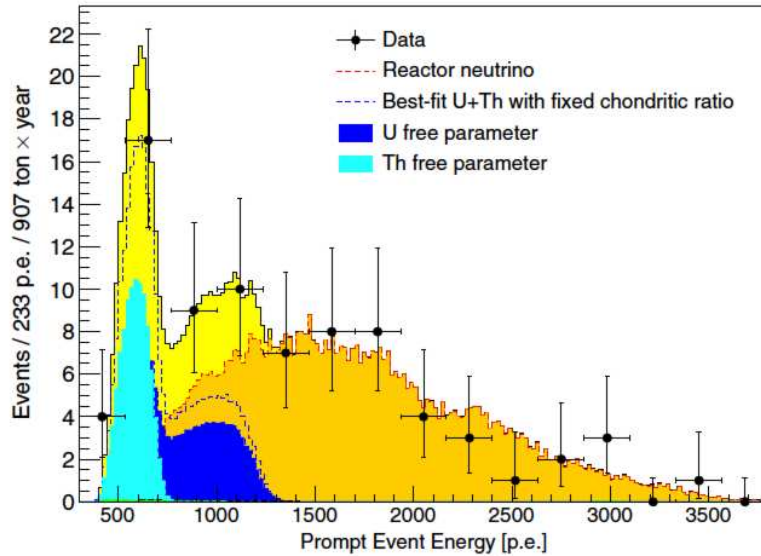


Figure 5: Prompt light yield spectrum in photoelectrons (p.e.) of 77 antineutrino candidates measured by Borexino and the best fit. 1 MeV corresponds to ~ 500 p.e. Taken from [11].

tions (delayed coincidences), the measurement of singles puts more stringent requirements on the detector radio-purity. Borexino detector reached extremely high levels of radio-purity and produced unique results in solar neutrino spectroscopy [13]. Borexino geoneutrino measurement is almost free of non-antineutrino background components, as random coincidences, (α , n) interactions and cosmogenic events. In addition, no nuclear power plants are in operation in Italy, further reducing the background for geoneutrino measurement.

The latest KamLAND result, 116_{-27}^{+28} geoneutrinos detected with 4.9×10^{32} target-proton \times year exposure, is from 2013 [8], including the period of low reactor antineutrino background after the April 2011 Fukushima disaster. The measured signal is in agreement with expectations, slightly disfavoring the geodynamical BSE models. The contribution of the local crust to the total geoneutrino signal was studied in [5, 14].

The new Borexino update from 2015 [11] is shown in Fig. 5. Within the exposure of $(5.5 \pm 0.3) \times 10^{31}$ target-proton \times year, $23.7_{-5.7}^{+6.5}(\text{stat})_{-0.6}^{+0.9}(\text{sys})$ geoneutrino events have been detected. The null observation of geoneutrinos has a probability of 3.6×10^{-9} (5.9σ). The contribution of the local crust to the total signal was studied in [15]. A geoneutrino signal from the mantle is confirmed at 98% confidence level. The radiogenic heat production for U and Th from the present best-fit result is restricted to the range 23 to 36 TW, taking into account the uncertainty on the distribution of HPE inside the Earth.

5 Future prospects

In the near future, a possible update is expected from KamLAND, including more data with low reactor antineutrino background. Borexino geoneutrino data-set will naturally end with the

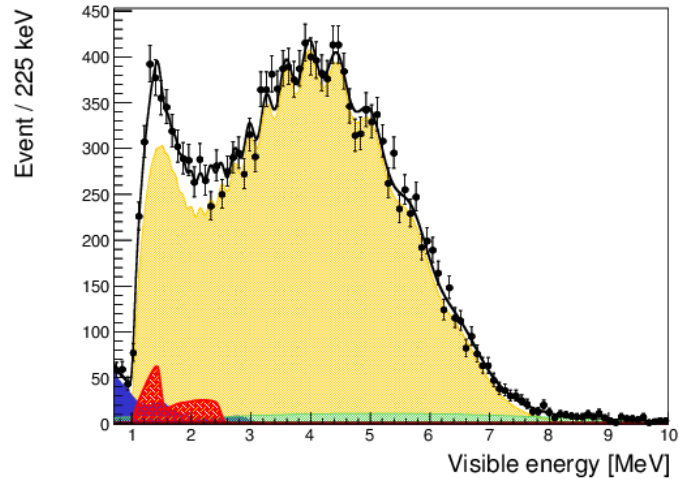


Figure 6: Example of a toy Monte Carlo for a possible 1-year geoneutrino measurement of JUNO. The different spectral components are shown as they result from the fit; black line shows the total sum for the best fit. The geoneutrino signal with Th/U fixed to chondritic ratio is shown in red. The following colour code applies to the backgrounds: orange (reactor antineutrinos), green (${}^9\text{Li} - {}^8\text{He}$), blue (accidental), small magenta (α, n). Taken from [17].

start of the SOX project at the end of 2017. Placing the strong ${}^{144}\text{Ce}$ - ${}^{144}\text{Pr}$ antineutrino source below the detector (in order to search for a hypothetical 1eV^2 sterile neutrino), will make it impossible to measure geoneutrinos with its low rate of about 1 event every 2-3 months.

From the future projects, the SNO+ experiment, 1 kton liquid scintillator detector in Sudbury mine in Canada, should start its data taking soon, having geoneutrinos among its goals. This is also the case of 50 kton liquid scintillator detector JUNO in Jiangmen, China, which will start its data taking in 2020, towards determination of the neutrino mass hierarchy by measurement of reactor antineutrinos with 53 km baseline. Inevitable disadvantage of the large reactor antineutrino background and a relatively shallow depth, are both balanced by the detector large size and an excellent energy resolution of 3% at 1 MeV. The expected number of geoneutrino events is about 400/year [16]. Figure 6 demonstrates a possible measurement after 1 full year of data taking with the expected level of backgrounds [17]. Within the first years, JUNO geoneutrino measurement can quickly exceed the precision of current geoneutrino results.

A real breakthrough in this field would come with the proposed Hanohano [18] project in Hawaii, a 10 kton movable detector placed underwater. Geological setting on the HPE-depleted oceanic crust is an ideal location: the mantle contribution to the total geoneutrino flux would be dominant and the principal goal of the geoneutrino measurements, determination of the mantle signal, could be reached without the complication of the subtraction of the signal from the local continental crust.

In conclusion it can be said, that the new field of Neutrino Geoscience has been born and an inter-disciplinary community of physicists and geoscientists is developing. The first geoneutrino

results confirm the feasibility of these measurements. The measured rates are in agreement with the expectations, confirming that at this level of precision we have a good understanding of our Earth. However, there is a potential to learn more about our planet from geoneutrinos: and we should take this chance and invest in the next generation of the experiments providing new more precise results.

For an interested reader, more comprehensive information about geoneutrinos can be found in dedicated review articles, as for example [19, 20, 21].

References

- [1] O. Šrámek *et al.*, *Earth and Plan. Sci. Lett.* **361** 356 (2013).
- [2] J.H. Davies and D.R. Davies, *Solid Earth* **1** 5 (2010).
- [3] C. Jaupart, S. Labrosse, and J.C. Mareschal, in: D.J. Stevenson (Ed.) *Treatise of Geophysics*, Elsevier, Amsterdam, pp. 1-53, 2007.
- [4] Y. Huang *et al.*, *Geochem. Geophys. Geosys.* **14** 2003 (2013).
- [5] S. Enomoto, E. Ohtani, K. Inoue, and A. Suzuki, *Earth Plan. Sci. Lett* **258** 147 (2007).
- [6] T. Araki *et al.* (KamLAND Collaboration), *Nature* **436** 499 (2005).
- [7] A. Gando *et al.* (KamLAND Collaboration), *Nature Geosc.* **4** 647 (2011).
- [8] A. Gando *et al.* (KamLAND Collaboration), *Phys. Rev. D* **88** 033001 (2013).
- [9] G. Bellini *et al.* (Borexino Collaboration), *Phys. Lett. B* **687** 299 (2010).
- [10] G. Bellini *et al.* (Borexino Collaboration), *Phys. Lett. B* **722** 295 (2013).
- [11] M. Agostini *et al.* (Borexino Collaboration), *Phys. Rev. D* **92** 031101 (R) (2015).
- [12] S. Abe *et al.* (KamLAND Collaboration), *Phys. Rev. Lett.* **100** 221803 (2008).
- [13] G. Bellini *et al.* (Borexino Collaboration), *Phys. Rev. D* **89** 112007 (2014).
- [14] G. Fiorentini *et al.*, *Phys. Rev. D* **72** 033017 (2005).
- [15] M. Coltorti *et al.*, *Geochim. Cosmochim. Acta* **75** 2271 (2011).
- [16] V. Strati *et al.*, *Progress in Earth and Planetary Science* **2** 5 (2015).
- [17] F. An *et al.* (JUNO Collaboration), *J. Phys. G: Nucl. Part. Phys.* **43** 030401 (2016).
- [18] J.G. Learned, S.T. Dye and S. Pakvasa, arXiv: 0810.4975 (2008).
- [19] G. Bellini *et al.*, *Prog. Part. Nucl. Phys.* **73** 1 (2013).
- [20] L. Ludhova and S. Zavaterli, *Adv. High En. Phys.* **2013** 425693 (2013).
- [21] S.T. Dye, *Earth Planet. Sci. Lett.* **297** 1 (2010).

SN 1987A - Exciting Physics

Bruno Leibundgut

ESO, Karl-Schwarzschild-Straße 2, 85748 Garching, Germany

DOI: <http://dx.doi.org/10.3204/DESY-PROC-2016-05/35>

Observing the evolution of a supernova over several decades is unique. SN 1987A is the only object where this has been possible in great detail and it has shown us some physics, which we never had expected. Even now – after 10000 days – does SN 1987A provide new surprises on its way to become a supernova remnant. We present here an overview of the current status of the observations of SN 1987A with a focus on the evolution of the emission from the circumstellar ring. SN 1987A can be detected at all electromagnetic wavelengths, which gives us a complete picture of the energy sources and some of the radiation transfer. There are several emission sites present in SN 1987A and we will present them in this overview.

1 The first two decades of SN 1987A

As the only celestial source other than the Sun from which so far neutrinos have been observed, SN 1987A has been an observational bonanza across the electromagnetic spectrum. It has provided insights in the many different astrophysical topics including stellar evolution, core collapse, nucleosynthesis, explosion physics and the interaction with surrounding material. The early phases of SN 1987A have been summarised in several reviews [1, 2, 3, 4]. The most important features are the evidence for the core collapse from the neutrino emission, the peculiar progenitor star as a blue supergiant (observed *before* the explosion), the evidence for mixing of elements within the explosion bringing some radioactive material to the surface very early on and the interaction with circumstellar material, which quickly was identified as being non-spherically distributed. In the following, the evidence for radioactive powering of the light curve and energy input from long-lived isotopes like ^{57}Co and ^{44}Ti could be found. Molecule formation could be observed directly through the emission of vibrational bands of CO and SiO and dust formation in the inner ejecta could be observed through an increased decline of the UV-optical-near-infrared (UVOIR) light curve and showed that the inner parts of the explosion had cooled down dramatically. The circumstellar environment of SN 1987A could be imaged and the surrounding torus identified. An outer ring system was also seen in narrow emission lines and light echoes from interstellar dust sheets in the Large Magellanic Cloud became obvious after some months. Over the years the supernova shock reaching the equatorial torus could be observed through the increased luminosity of individual knots in the ring.

A particular feature of SN 1987A was its observability from the ground. Its position in the Large Magellanic Cloud is close enough to the celestial south pole that it could be observed all year from many southern observatories. Hence the supernova light curve is without major gaps. If the SN would have been placed only a few degrees further north, we would have lost the maximum phase and also several of the other interesting details of the supernova. Its

proximity is, of course, the other characteristic which allows us to observe the supernova until today throughout the electromagnetic spectrum. This is one of the reason that we could learn so much from this single object.

The early light curve (see [4] for a figure which labels the various phases) displays all the characteristics of a core-collapse supernova and some more. The shock breakout can be inferred in the UV and the bluest bands as a decrease during the adiabatic expansion phase. The bolometric light curve then rose to a peak within several weeks and ended in a 'plateau' phase, which was extremely short due to the compact progenitor star. This is also the reason why SN 1987A did not reach a peak luminosity comparable to other core-collapse supernovae. After maximum the light curve settled into a steady decline, which followed the ^{56}Co decay time as all the energy generated in this radioactive decay was thermalised in the ejecta. After about 400 days the light curve started to decline faster because some optical light was blocked by dust and re-emitted in the mid-infrared ($> 20\mu\text{m}$) and was not observed from the ground. Only after about 1000 days did the light curve settle onto a slower decline again as the emission was powered by ^{57}Co with a longer lifetime. After some 2000 days the light curve decline was slowed even more due to the thermalisation of γ -rays from ^{44}Ti . After about 2500 days the emission from the ring was dominating over the ejecta by about a factor 10 in luminosity. This ratio has steadily increased over the years due to the supernova ejecta interacting with the stationary, dense equatorial torus. The supernova-ring interaction has been studied at many wavelengths and has led to a steady increase in flux in all wavebands. It certainly has been the dominating feature during the second decade of SN 1987A.

The second and third decade of SN 1987A are reviewed in [5]. Over the years five emission sites from SN 1987A could be distinguished. The inner ejecta (sometimes referred to as 'debris'), the stationary material in the circumstellar torus/ring, the shocked material in the torus, a reverse shock between the inner ejecta and the torus, and light echoes from scattered supernova light off interstellar dust sheets between SN 1987A and us. While the inner ejecta are powered by the radioactive decays of elements synthesised in the explosion, the ring glowed originally due recombination of stationary material ionised by the supernova shock breakout. The optical ring emission started to dominate over the ejecta about 5 years after the explosion as it was fading much more slowly than the ejecta. After 8 years a first 'hot spot' on the ring was detected [6, 7] and over the following years the ring brightness increased due to the outer supernova ejecta colliding with inward protrusions of ring material, which was observed as a series of bright knots (sometimes referred to as a 'pearl necklace'). The full ring evolution over the two decades from 1994 to 2014 is shown in [8]. The ring brightening could also be observed in the radio [9] and at X-ray energies [10] as the shocks from the fast-moving supernova ejecta and the nearly stationary ring material built up. The X-ray emission had started to increase already earlier as the shock was making its way through the dense material of an HII region created by the blue supergiant inside the ring [11].

2 The inner ejecta

Theoretical models of core-collapse supernova predict non-symmetric explosions. The reason are several hydrodynamic instabilities which are important for the neutrino-driven explosions (e.g. [12]). However, it has been so far impossible to observe the geometry of supernova ejecta directly. SN 1987A provided the possibility to obtain spatially resolved images of the inner ejecta with the VLT and HST. Integral-field observations in the near-infrared showed that the

extension of the inner ejecta as measured through the $1.64 \mu\text{m}$ line, which is probably a mixture of [Si I] and [Fe II], was at an unexpected angle [13]. If the ring indeed is equatorial to the progenitor star of SN 1987A, then in some models the explosion was expected to be along the stellar poles and hence should be elongated orthogonal to the ring. The VLT SINFONI observations showed that the ejecta lie mostly within the plane of the ring, i.e. inclined nearly 42 degrees [13]. Further studies confirmed this geometry, but also indicated a slight misalignment of the two lobes relative to the centre [14]. The appearance in the $\text{H}\alpha$ emission line at 10000 days after explosion is markedly different from the one in [Si I]. The $\text{H}\alpha$ image shows a shell-like structure with an emission hole near the centre, while the [Si I] image displays a filled, centrally located emission.

The inner ejecta had been fading for many years as the energy input from the radioactive decays was dwindling. However, [15] found that around 5500 days after explosion the ejecta started to increase in brightness at optical wavelengths again. This is a rather unexpected development as an extra energy source is needed. Radioactivity only provides diminishing energy with time and radiation effects, e.g. changes in the opacity, are not expected at such a late phase. It had to be external energy input and the X-ray radiation from the supernova shock with the circumstellar ring was identified as the culprit. The X-rays penetrate back into the inner ejecta and ionise the hydrogen creating the shell-like appearance. The silicon on the other hand is still powered by the radioactive decay of ^{44}Ti [15, 8].

Mid- and far-infrared measurements of SN 1987A were only enabled by the Spitzer and Herschel satellites around 9000 days after explosion. These are typically combined with millimetre wavelength observations from the ground. A large dust mass (up to half a solar mass) was inferred from these late observations [16], which needs to be compared to the dust measurement at 1150 days after the explosion ($3 \cdot 10^{-3} M_{\odot}$; [17]). Over the 22 years between these observations the refractory material must have formed the dust we observe today. Since ALMA became operational, it observed the dust continuum emission [18] and vibrational transitions of carbon monoxide (CO) and silicon oxide (SiO) [19]. The inner ejecta must be filled with cold ($<50 \text{ K}$) dust. Another molecule found in the inner ejecta is H_2 , which was observed after 6500 days [20]. It was predicted to be formed with CO and SiO, but was only recently detected in the near infrared. It is concentrated towards the core of the ejecta similar to the [Si I]/[Fe II] emission and most probably is heated by the radioactive decays.

The evolution of the inner ejecta is unclear. The X-rays will penetrate further into the ejecta and the radioactive input will decrease continuously, although with a long (^{44}Ti has a 60 year half-life) decay time. It will also expand in size and eventually will reach the circumstellar ring.

3 The equatorial ring

SN 1987A is surrounded by a circumstellar ring, whose origin remains unclear. It could be the remnant of a stellar merger shortly before explosion, but the details of such a scenario are not resolved (e.g. [5]). It is clear from the mottled appearance with many individual hot spots that the ring is not uniform. It rather seems that it is broken up into clumps and inward protrusions due to some dynamic instability during the formation process. We can distinguish shocked and unshocked gas in the ring. The emission from unshocked is coming from essentially stationary material moving with $\sim 10 \text{ km s}^{-1}$ and ionised through the soft X-rays from the shock. The shocked gas has been ionised and accelerated to about $>300 \text{ km s}^{-1}$ by the supernova forward

shock [21, 22, 23]. Some of the ionisation is so high that coronal lines, e.g. of [Fe XIV] are observed. High-resolution spectroscopy, even if the ring cannot be not spatially resolved, hence allows us to separate the different emission sites based on the observed velocities. In the near-infrared integral-field spectroscopy has yielded both spatial and spectral information. In this case the orientation of the ring could be determined by tracing the expanding ring on the sky [24]. This confirmed the previous geometry derived from HST imaging [25, 26]. The ring is inclined by 43 degrees with the northern part closer to us and a rotation out of the sky of 9 degrees with the eastern part slightly closer than the western ring. The systemic velocity of the ring is 286.5 km s^{-1} , which can be compared to the systemic velocity of the Large Magellanic Cloud of 278 km s^{-1} [27].

The first ring region reached by the supernova shock was to the north-east at around 4000 days after explosion. The ring then brightened through the north and the east wrapping around finally to the western part of the ring. This process took about 5 years [8]. The ring emission was maximum shortly after 8000 days (in B and R filters) and started to decline thereafter. This evolution is nicely traced by emission lines from the shocked gas, mostly $\text{H}\alpha$, [O III] 5007\AA , and coronal lines like [Fe XIV] 5303\AA . The narrower lines from the unshocked gas, $\text{H}\alpha$, [O III] and [N II] 6583\AA , declined already after 7000 days. The peak is reached later with increasing wavelength when observing into the infrared [28]. The fading of the ring is an indication that the shock has now overrun most of the ring material and is moving beyond the ring. Based on the fading of the individual emission lines the ring will become unobservable by around 2020 [8].

The optical peak brightness was reached at different times with the NE peaking around 6800 days and the SW only after 8500 days following roughly the time lag of the first appearance of the spots. The brightest parts now are in the west and the spots in this region have on average also reached a higher flux peak. Until today the ring emission is not been fully closed [14].

The ring is also observed in synchrotron emission at radio wavelengths. Here the shocks accelerate the electrons in the magnetic field. The shocks can be directly seen in X-rays, where the ring is resolved in Chandra observations [10]. Contrary to the optical the X-rays have not peaked yet, which is an indication that the shock is still running through lower density material, which does not radiate in the optical.

Recent HST observations have revealed new emission sites outside the equatorial ring [8]. The supernova forward shock has overrun the ring in several places and starts to interact with clouds outside the ring. Projection effects also have to be taken into account as the ring is inclined and we may see the shock outside the ring plane starting to interact with material above (or below) the ring plane. Since the shock has been decelerated in the ring, parts in other directions have now reached further out and eventually will start to interact with any material in its way. In particular, we should be able to distinguish whether there is a continuous connection between the inner and the outer rings and the shock should encounter such material. It will reveal the gas distribution in the wider surroundings of the supernovae.

4 The reverse shock

A reverse shock has built up between the forward shock moving through the equatorial ring and the inner ejecta. This is the outer ejecta catching up with the slowed down forward material encountering the dense equatorial ring and other material in the predicted HII region [11]. The reverse shock is characterised through high velocity ($>10000 \text{ km s}^{-1}$) hydrogen lines ($\text{Ly}\alpha$, $\text{H}\alpha$,

$H\beta$), which emerge from the ionised ejecta flowing into the shock region, where material has been decelerated behind the forward shock. SN 1987A has developed a strong reverse shock around 1997 [6, 29] and its flux has increased continuously until 2009 (more than 9000 days after explosion; [31, 32, 33]). A detailed description of the reverse shock in SN 1987A has been provided in [30] for the location and by [33] describing the temporal evolution of the spectral appearance. The direct imaging has provided evidence that the reverse shock emission has been observed outside the equatorial ring plane towards the outer rings [30], which is an indication that the SN shock has expanded into the hourglass shaped region connecting the outer rings with the equatorial ring. This is further supported by the large observed velocity, which indicates that there has to be flux outside the equatorial ring [8]. The outer ejecta appear to be heated by X-rays coming from the shocks and display a very high ratio of Lyman- α to Balmer- α emission, which leads to an increased Lyman- α flux. The flux evolution follows nearly exactly the soft X-ray increase, which is a clear indication that the heating of the reverse shock material is done through X-rays. An early prediction that the $H\alpha$ emission from the reverse shock will disappear by around 2014 due to the full ionisation of hydrogen before it reaches the shock region [31] has not been confirmed, but there appears to be a flattening of the flux coming from the reverse shock. This could mean that the reverse shock in the equatorial plane has reached the intrusions from the inner ring [33]. The emission outside the equatorial ring will increase in the coming years outlining the material distribution outside the equatorial plane and mapping the mass loss history of the progenitor star of SN 1987A. Future observations will map the evolution of the reverse shock in SN 1987A and hence the circumstellar matter distribution around the supernova explosion.

5 The compact object

The neutrino signal from SN 1987A indicated the core collapse to a neutron star. However, no signature of the neutron star or a possible black hole, if the neutron star due to fallback of material not expelled in the explosion became unstable and collapsed further, has so far been detected. A young neutron star is expected to rapidly lose energy as it spins down within a magnetic field. A resulting pulsar wind nebula, similar to the one observed in the Crab nebula should be expected, although the observed upper limits on the luminosity of a compact object in SN 1987A is already below the one observed in the Crab.

The distance of SN 1987A makes it difficult to isolate a central compact object in X-rays and at radio wavelengths from the ejecta, reverse shock and the ring interaction. The X-rays would be the most promising wavelength region for the detection of the plasma ionised by the pulsar wind. So far, no detection has been reported. Also, the synchrotron radiation could be detected at radio frequencies. No central point source has been seen to date (e.g. [34, 35]). Emission at optical wavelengths is difficult to detect as the dust, which formed in the inner ejecta (e.g. [18]) could block the line of sight towards the centre. An attempt to detect UV continuum emission between the many emission lines has been done some 10 years ago [36] setting the currently strongest limits of less than $1.3 L_{\odot}$. The lack of a detection of the compact source means that the magnetic field of the neutron star is fairly weak as a Crab-like plerion should have been detected already.

6 The future

SN 1987A continues its evolution towards a supernova remnant. The recent years have shown surprises, like the formation of massive dust in the ejecta, the additional heating of the hydrogen layers in the inner ejecta from the X-rays created in the shocks and the lack of emission from the central compact object, which must have formed in the collapse. Several predictions on how SN 1987A would evolve have been confirmed. Among them are the continued interaction with the equatorial ring, the emission coming from outside the ring and the strengthening of the reverse shock over the years. These also set the expectations on what the future will bring. Foremost the ring will be overrun by the shock in a few years and its emission will start to drop. The structure of the inner ejecta will be revealed further through the emission evolution due to the different heating mechanisms. The reverse shock will start to weaken when it approaches the ring in the equatorial plane, but will continue to map out the circumstellar structure outside that plane. It will be interesting to see whether more dust is forming in the inner ejecta and when the cold dust shell between the forward and reverse shocks will become detectable. The search for the central compact object will continue and it will hopefully become observable in the coming years.

There is still a lot in store for observers of SN 1987A. Eventually, this supernova will be joined by other objects detected through their neutrino emission. The prospects are excellent that we may be witnessing such an event in the not too distant future.

7 Acknowledgments

This research was supported by the DFG Cluster of Excellence 'Origin and Structure of the Universe' and a DFG Transregio network TRR33 'The Dark Universe'.

References

- [1] Arnett, W. D., Bahcall, J. N., Kirshner, R. P., & Woosley, S. E. 1989, *ARA&A*, 27, 629
- [2] McCray, R. 1993, *ARA&A*, 31, 175
- [3] McCray, R. 2003, *Supernovae and Gamma-Ray Bursters*, 598, 219
- [4] Fransson, C., Gilmozzi, R., Groeningsson, P., et al. 2007, *The Messenger*, 127, 44
- [5] McCray, R., Fransson, C. 2016, *ARA&A*, 54, 19
- [6] Sonneborn, G., Pun, C. S. J., Kimble, R. A., et al. 1998, *ApJL*, 492, 139
- [7] Lawrence, S. S., Sugerman, B. E., Bouchet, P., et al. 2000, *ApJL*, 537, 123
- [8] Fransson, C., Larsson, J., Migotto, K., et al. 2015, *ApJL*, 806, 19
- [9] Zanardo, G., Staveley-Smith, L., Ball, L., et al. 2010, *ApJ*, 710, 1515
- [10] Orlando, S., Miceli, M., Pumo, M. L., & Bocchino, F. 2015, *ApJ*, 810, 168
- [11] Chevalier, R. A., & Dwarkadas, V. V. 1995, *ApJL*, 452, 45
- [12] Janka, H.-T. 2012, *Annual Review of Nuclear and Particle Science*, 62, 407
- [13] Kjær, K., Leibundgut, B., Fransson, C., Jerkstrand, A., & Spyromilio, J. 2010, *A&A*, 517, A51
- [14] Larsson, J., Fransson, C., Kjær, K., et al. 2013, *ApJ*, 768, 89
- [15] Larsson, J., Fransson, C., Östlin, G., et al. 2011, *Nature*, 474, 484
- [16] Matsuura, M., Dwek, E., Barlow, M. J., et al. 2015, *ApJ*, 800, 50
- [17] Wesson, R., Barlow, M. J., Matsuura, M., & Ercolano, B. 2015, *MNRAS*, 446, 2089

SN 1987A - EXCITING PHYSICS

- [18] Indebetouw, R., Matsuura, M., Dwek, E., et al. 2014, ApJL, 782, 2
- [19] Kamenetzky, J., McCray, R., Indebetouw, R., et al. 2013, ApJL, 773, 34
- [20] Fransson, C., Larsson, J., Spyromilio, J., Leibundgut, B., McCray, R., Jerkstrand, A. 2016, ApJL, 821, 5
- [21] Gröningsson, P., Fransson, C., Lundqvist, P., et al. 2006, A&A, 456, 581
- [22] Gröningsson, P., Fransson, C., Lundqvist, P., et al. 2008a, A&A, 479, 761
- [23] Gröningsson, P., Fransson, C., Leibundgut, B., et al. 2008b, A&A, 492, 481
- [24] Kjær, K., Leibundgut, B., Fransson, C. 2007, A&A, 471, 617
- [25] Panagia, N., Gilmozzi, R., Macchetto, F., Adorf, H.-M., & Kirshner, R. P. 1991, ApJL, 380, 23
- [26] Sugerman, B. E. K., Crotts, A. P. S., Kunkel, W. E., Heathcote, S. R., & Lawrence, S. S. 2005, ApJS, 159, 60
- [27] Richter, O.-G., Tammann, A. G., Huchtmeier, W. K. 1987, A&A, 171, 33
- [28] Arendt, R. G., Dwek, E., Bouchet, P., et al. 2016, ApJ, 151 62
- [29] Michael, E., McCray, R., Pun, C. S. J., et al. 1998, ApJL, 509, 117
- [30] France, K., McCray, R., Fransson, C., et al. 2015, ApJL, 801, 16
- [31] Smith, N., Zhekov, S. A., Heng, K., et al. 2005, ApJL, 635, 41
- [32] Heng, K., McCray, R., Zhekov, S. A., et al. 2007, ApJ644, 959
- [33] Fransson, C., Larsson, J., Spyromilio, J., et al. 2013, ApJ, 768, 88
- [34] Ng., C.-Y., Zanardo, G., Potter, T. M., et al. 2013, ApJ, 777, 131
- [35] Zanardo, G., Staveley-Smith, L., Indebetouw, R., et al. 2014, ApJ, 796 82
- [36] Graves, G. J., Challis, P. M., Chevalier, R. A., et al. 2005, ApJ, 629, 944

Connecting Neutrino Physics and Astronomy

Poster Contributions



The SOX experiment: understanding the detector behavior using calibration sources

A. Caminata¹, M. Agostini², K. Altenmüller², S. Appel², G. Bellini³, J. Benziger⁴, N. Berton⁵, D. Bick⁶, G. Bonfini⁷, D. Bravo⁸, B. Caccianiga³, F. Calaprice⁹, M. Carlini⁷, P. Cavalcante⁷, A. Chepurinov¹⁰, K. Choi¹¹, M. Cribier⁵, D. D'Angelo³, S. Davini¹², A. Derbin¹³, L. Di Noto¹, I. Drachnev¹², M. Durer⁵, A. Etenko¹⁴, S. Farinon¹, V. Fischer⁵, K. Fomenko¹⁵, A. Formozov^{3,15}, D. Franco¹⁶, F. Gabriele⁷, J. Gaffiot⁵, C. Galbiati⁹, C. Ghiano¹, M. Giammarchi³, M. Goeger-Neff², A. Goretti⁹, M. Gromov¹⁰, C. Hagner⁶, Th. Houdy⁵, E. Hungerford¹⁷, Aldo Ianni⁷, Andrea Ianni⁹, N. Jonquères¹⁸, K. Jedrzejczak¹⁹, D. Jeschke², M. Kaiser⁶, V. Kobychew²⁰, D. Korablev¹⁵, G. Korga⁷, V. Kornoukhov²¹, D. Kryn¹⁶, T. Lachenmaier²², T. Lasserre⁵, M. Laubenstein⁷, B. Lehnert²³, J. Link⁸, E. Litvinovich^{14,24}, F. Lombardi⁷, P. Lombardi³, L. Ludhova³, G. Lukyanchenko^{14,24}, I. Machulin^{14,24}, S. Manecki⁸, W. Maneschg²⁸, S. Marcocci¹², J. Maricic¹¹, G. Mention⁵, E. Meroni³, M. Meyer⁶, L. Miramonti³, M. Misiaszek^{7,19}, M. Montuschi²⁵, P. Mosteiro⁹, V. Muratova¹³, R. Musenich¹, B. Neumair², L. Oberauer², M. Obolensky¹⁶, F. Ortica²⁶, M. Pallavicini¹, L. Papp², L. Perasso¹, A. Pocar²⁷, G. Ranucci³, A. Razeto⁷, A. Re³, A. Romani²⁶, R. Roncin^{7,16}, N. Rossi⁷, S. Schönert², L. Scola⁵, D. Semenov¹³, H. Simgen²⁸, M. Skorokhvatov^{14,24}, O. Smirnov¹⁵, A. Sotnikov¹⁵, S. Sukhotin¹³, Y. Suvorov^{14,29}, R. Tartaglia⁷, G. Testera¹, J. Thurn²³, M. Toropova¹⁴, C. Veyssiére⁵, M. Vivier⁵, E. Unzhakov¹³, R.B. Vogelaar⁸, F. von Feilitzsch², H. Wang²⁹, S. Weinz³⁰, J. Winter³⁰, M. Wojcik¹⁹, M. Wurm³⁰, Z. Yokley⁸, O. Zaimidoroga¹⁵, S. Zavatarelli¹, K. Zuber²³, G. Zuzel¹⁹

¹Dipartimento di Fisica, Università degli Studi e INFN, Genova 16146, Italy

²Physik-Department and Excellence Cluster Universe, Technische Universität München, 85748 Garching, Germany

³Dipartimento di Fisica, Università degli Studi e INFN, 20133 Milano, Italy

⁴Chemical Engineering Department, Princeton University, Princeton, NJ 08544, USA

⁵Commissariat à l'Énergie Atomique et aux Énergies Alternatives, Centre de Saclay, IRFU, 91191 Gif-sur-Yvette, France

⁶Institut für Experimentalphysik, Universität Hamburg, 22761 Hamburg, Germany

⁷INFN Laboratori Nazionali del Gran Sasso, 67010 Assergi (AQ), Italy

⁸Physics Department, Virginia Polytechnic Institute and State University, Blacksburg, VA 24061, USA

⁹Physics Department, Princeton University, Princeton, NJ 08544, USA

¹⁰Lomonosov Moscow State University Skobeltsyn Institute of Nuclear Physics, 119234 Moscow, Russia

¹¹Department of Physics and Astronomy, University of Hawai'i, Honolulu, HI 96822, USA

¹²Gran Sasso Science Institute (INFN), 67100 L'Aquila, Italy

¹³St. Petersburg Nuclear Physics Institute NRC Kurchatov Institute, 188350 Gatchina, Russia

¹⁴NRC Kurchatov Institute, 123182 Moscow, Russia

¹⁵Joint Institute for Nuclear Research, 141980 Dubna, Russia

¹⁶AstroParticule et Cosmologie, Universit Paris Diderot, CNRS/IN2P3, CEA/IRFU, Observatoire de Paris, Sorbonne Paris Cit, 75205 Paris Cedex 13, France

¹⁷Department of Physics, University of Houston, Houston, TX 77204, USA

¹⁸Commissariat à l'Énergie Atomique et aux Énergies Alternatives, Centre de Saclay, DEN/DM2S/SEMT/BCCR, 91191 Gif-sur-Yvette, France

¹⁹M. Smoluchowski Institute of Physics, Jagiellonian University, 30059 Krakow, Poland

²⁰Kiev Institute for Nuclear Research, 06380 Kiev, Ukraine

²¹Institute for Theoretical and Experimental Physics, 117218 Moscow, Russia

²²Kepler Center for Astro and Particle Physics, Universität Tübingen, 72076 Tübingen, Germany

²³Department of Physics, Technische Universität Dresden, 01062 Dresden, Germany

²⁴National Research Nuclear University MEPhI (Moscow Engineering Physics Institute), 115409 Moscow, Russia

²⁵Dipartimento di Fisica e Scienze della Terra Università degli Studi di Ferrara e INFN, Via Saragat 1-44122, Ferrara, Italy

²⁶Dipartimento di Chimica, Università e INFN, 06123 Perugia, Italy

²⁷Amherst Center for Fundamental Interactions and Physics Department, University of Massachusetts, Amherst, MA 01003, USA

²⁸Max-Planck-Institut für Kernphysik, 69117 Heidelberg, Germany

²⁹Physics and Astronomy Department, University of California Los Angeles (UCLA), Los Angeles, California 90095, USA

³⁰Institute of Physics and Excellence Cluster PRISMA, Johannes Gutenberg-Universität Mainz, 55099 Mainz, Germany

DOI: <http://dx.doi.org/10.3204/DESY-PROC-2016-05/22>

The SOX experiment investigates the existence of light sterile neutrinos. A solid signal would mean the discovery of the first particles beyond the Standard Electroweak Model and would have profound implications in our understanding of the Universe and of fundamental particle physics. In case of a negative result, it is able to close a long standing debate about the reality of the neutrino anomalies. The SOX experiment will use a $^{144}\text{Ce} - ^{144}\text{Pr}$ antineutrino generator placed 8.5 m below the Borexino liquid scintillator detector. In view of the SOX experiment, a precise knowledge of the energy response and the spatial reconstruction of the antineutrino events is very important. Consequently, a calibration campaign of the Borexino detector is foreseen before the beginning of the SOX data taking. This paper briefly reviews the techniques used for calibrate the Borexino detector.

1 Introduction

Although most of the collected neutrino experimental data are explainable within the three-flavor oscillation model, some short-baseline neutrino experiment have reported results that significantly deviates from the three active neutrino picture ([1, 2, 3, 4]), suggesting a possible short distance oscillation between the three known neutrino states and one hypothetical new state with a squared mass Δm_{14}^2 of about 1 eV^2 . Due to constraints on Z boson coupling asserted by LEP, this state would be sterile.

The SOX project aims to test the existence of light sterile neutrinos detecting the antineu-

trino flux coming from a 150 kCi $^{144}\text{Ce} - ^{144}\text{Pr}$ source placed at short distance from the Borexino liquid scintillator detector [5] (figure 1). Antineutrinos are detected inside Borexino via inverse beta decay, thus with a negligible background [6]. Borexino will investigate short distance neutrino oscillations in two ways. The first way is the standard disappearance technique (rate technique). Knowing the source activity and measuring the interaction rate, it is possible to investigate the existence of the sterile neutrino state. The second way is based on an oscillometry measurement within the detector volume (shape technique). Expected sensitivities are shown in figure 2.

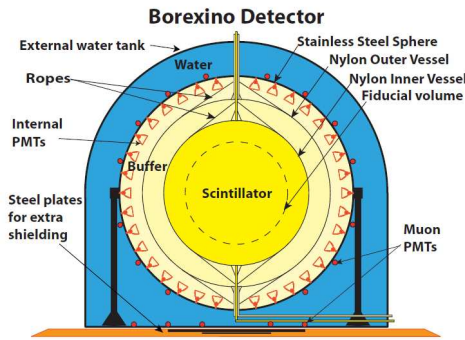


Figure 1: Schematic drawing of the Borexino detector.

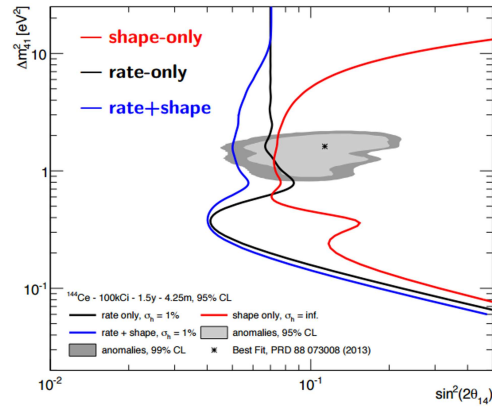


Figure 2: Neutrino anomaly region and foreseen sensitivity for SOX.

2 Motivation for a calibration campaign and Borexino source insertion system

A good knowledge of the Borexino detector response is a key requirement for the SOX analysis. Given the large dimensions of the detector, it is necessary to map the energy response and the position reconstruction accuracy in the whole active volume. Since the energy of the incoming antineutrino is reconstructed from the positron energy, the knowledge of the energy scale is mandatory. Consequently, a Monte Carlo simulation code have been developed and the detector response have been tested deploying radioactive sources in several positions (2008 and 2009 calibration campaigns [7]). These data are extremely useful in view of the SOX experiment. Since the SOX and geoneutrino signals have the same features, calibration data acquired for the geoneutrino analysis can be used also for SOX. Nevertheless, a new calibration campaign is foreseen before the arrival of the SOX antineutrino source. These calibration data are of extreme importance in understanding the detector behavior and to increase the reliability of the SOX Monte Carlo simulation code. Since in the SOX analysis the cut efficiencies and the sensitivity studies are performed analyzing the output of the simulations, having an accurate simulation code is crucial for a proper data analysis.

Sources are inserted in Borexino by means of a series of hollow interconnecting rods in a 4'' pipe connecting the top of the detector with the liquid scintillator (figure 1). One special rod has

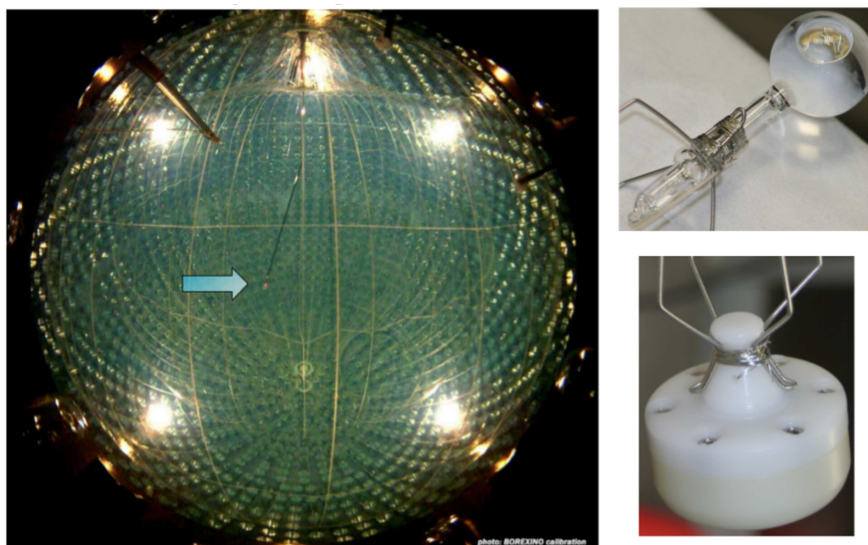


Figure 3: Left: picture shot by a CCD camera. The insertion system is visible and it is pointed by the blue arrow. Right: vials used for gamma (top) and neutron (bottom) sources.

an hinge that allows the arm to bend up to 90° and thus reaching most of the detector's active zone. Since it is important to know the position of the inserted source, a source location system have been developed. The system has to find the exact coordinate of the position in which the source is deployed. This information is crucial for estimating the position reconstruction accuracy. Consequently, seven CCD cameras look for the position of a red (wavelength about 630 nm) light diffuser attached close to the source (figure 3). The system is able to locate the source within 1 cm. The wavelength of this light has been chosen so as not to be harmful to the PMTs under HV.

3 Calibration campaign

3.1 Past calibration campaign

Gamma radioactive sources were dissolved in aqueous solution and contained in small quartz vials. α and β radioactive sources ($^{14}\text{C} - ^{222}\text{Rn}$) were contained in a quartz vial as well but scintillator was used as solvent. Table 1 shows all the sources used for calibration purpose.

A deep understanding of the detector response to the gamma sources is fundamental for the SOX analysis since the energy deposit of the prompt event is due to both positron interaction with matter and to positron-electron annihilation.

The $^{241}\text{Am} - ^9\text{Be}$ neutron source calibration was performed mainly for solar neutrino (^8B) and geoneutrino analyses. Nevertheless, they are of fundamental importance for SOX, since the delayed event is due to neutron capture. In the $^{241}\text{Am} - ^9\text{Be}$ neutron source, neutrons are produced in association with gammas, with a total energy releas of 4.44 MeV. Similarly to the SOX signal, the $^{241}\text{Am} - ^9\text{Be}$ source provides a prompt and a delayed event (figure 4). The prompt event is due to the gamma energy loss together with the signal of proton recoils

Source	Type	E [MeV]	Position	Motivations	Campaign
^{57}Co	γ	0.122	in IV volume	Energy scale	IV
^{139}Ce	γ	0.165	in IV volume	Energy scale	IV
^{203}Hg	γ	0.279	in IV volume	Energy scale	III
^{85}Sr	γ	0.514	z-axis + sphere R=3 m	Energy scale + FV	III,IV
^{54}Mn	γ	0.834	along z-axis	Energy scale	III
^{65}Zn	γ	1.115	along z-axis	Energy scale	III
^{60}Co	γ	1.173, 1.332	along z-axis	Energy scale	III
^{40}K	γ	1.460	along z-axis	Energy scale	III
$^{222}\text{Rn} + ^{14}\text{C}$	β, γ	0-3.20	in IV volume	FV+uniformity	I-IV
	α	5.5, 6.0, 7.4	in IV volume	FV+uniformity	
$^{241}\text{Am} + ^9\text{Be}$	n	0-9	sphere R=4 m	Energy scale + FV	II-IV
394 nm laser	light	-	center	PMT equalization	IV

Table 1: Radioactive sources used during the Borexino internal calibration campaigns. The radionuclides, energies and emitted particle types are shown in the first three columns. The fourth column indicates the positions where the sources were deployed within the scintillator. The main purposes for the individual source measurements are summarized in the fifth column. The last column indicates in which campaign the sources have been deployed: I (October 2008), II (January 2009), III (June 2009) and IV (Jul 2009). FV is the fiducial volume used in the solar analysis [8], the corresponding sources were used to evaluate the event position reconstruction performances.

due to interaction of neutron with the scintillator. Afterwards, neutrons thermalize in the hydrogen-rich organic scintillator and are captured either on protons or carbon nuclei, emitting characteristic 2.22 MeV and 4.95 MeV γ rays (figure 4). These γ rays produce a delayed signal according to the neutron capture time of about 254 μs .

3.2 Next calibration campaign

Next calibration campaign will take place next fall just before the SOX source arrival. During next calibration campaign both gamma and AmBe sources will be deployed inside Borexino. This calibration will be very useful both for phase 2 solar neutrino analysis (precision measurement of solar neutrino fluxes) and for SOX. Differently from old calibration campaigns, there will be an extensive calibration with AmBe source, especially nearby the inner vessel. The calibration points at large radii will be extremely important to study the neutron detection efficiency at the border of the active zones.

4 Conclusions

The SOX experiment aims to investigate the existence of sterile neutrinos placing a high activity $^{144}\text{Ce} - ^{144}\text{Pr}$ antineutrino source below the Borexino detector. Both a rate analysis and a shape analysis are foreseen. For both the analyses, a deep understanding of the detector response is necessary. In the past years, the detector have been calibrated deploying several sources in the active volume. A new calibration campaign is foreseen for the end of this year, just before the beginning of SOX data-taking.

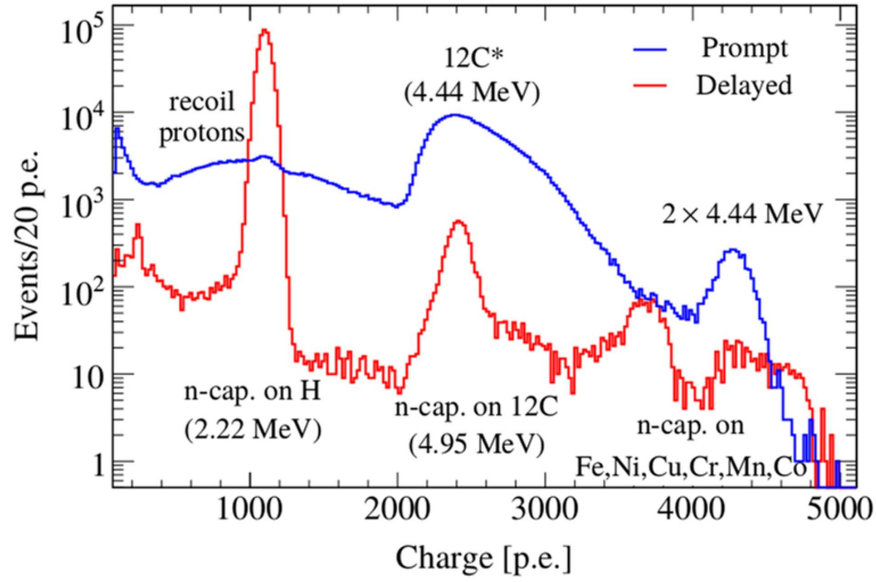


Figure 4: Energy spectrum of the $^{241}\text{Am}-^9\text{Be}$ source. The spectrum is subdivided in neutron-induced prompt signal (blue) and delayed signals (red).

References

- [1] Aguilar A *et al.* 2001 *Phys. Rev. D* **64** 112007
- [2] Aguilar A *et al.* 2013 *Phys. Rev. Lett.* **110** 161801
- [3] Mention G *et al.* 2011 *Phys. Rev. D* **83** 073006
- [4] Giunti C and Laveder M 2011 *Phys. Rev. C* **83** 065504
- [5] Bellini G *et al.* 2013 *JHEP* **38** 1308
- [6] Agostini M *et al.* 2015 *Phys. Rev. D* **92** 031101
- [7] Bellini G *et al.* 2012 *Journal of Instrumentation* **7** 10018
- [8] Bellini G *et al.* 2014 *Phys. Rev. D* **89** 112007

Neutron Shielding Simulations and Muon-induced Neutrons

Laura Vanhoefer¹, Iris Abt¹, Lucia Garbini¹, Raphael Kneißl¹, Heng-Ye Liao¹, Béla Majorovits¹, Matteo Palermo¹, Oliver Schulz¹

¹Max-Planck-Institut für Physik, Föhringer Ring 6, 80805 München, Germany

DOI: <http://dx.doi.org/10.3204/DESY-PROC-2016-05/41>

Cosmic-ray neutrons and muons can produce background in low-rate experiments due to the production of long-lived radioisotopes during transport above ground. This kind of background can be reduced by shielding the detector components during transport. Cosmic-ray neutron and muon (μ^+ and μ^-) shielding simulations with the GEANT4 based framework MaGe were done to estimate the shielding properties of water, plastic, soil, steel, concrete, copper, LNGS rock and lead. The shielding power of cosmic-ray neutrons and muon-induced neutrons as well as the total neutron fluxes at different shielding depths are presented. Also the neutron backscattering effect was investigated and was found to be significant.

1 Introduction

Cosmic-ray neutrons and muons which are produced in the Earth's atmosphere can produce background in low-rate experiments like $0\nu\beta\beta$ experiments. Any energy deposition near or above the Q-value of the $0\nu\beta\beta$ decay is background for such experiments. Radioisotopes which produce such energy depositions can be created by neutrons and muons via spallation, neutron capture, (n,p) reaction etc. Also inelastic scattering where the nucleus is put into an excited state can produce an energy deposition near or above the Q-value. Long-lived radioisotopes with half-lives of many years are still present during measurements in an underground laboratory. This kind of background can be reduced by restricting the overall exposure to cosmic-ray radiation and by shielding of the detector components during transport above ground.

To compare different possible shielding materials, cosmic-ray neutron and muon shielding simulations were done using the GEANT4 based framework MaGe [1] from the GERDA and Majorana collaboration to estimate the shielding properties of plastic, water, soil, concrete, LNGS rock [2], steel, copper and lead (see also [3]).

In the simulations, blocks from different shielding materials were exposed to neutrons, μ^+ and μ^- . The number of neutrons and muons which leave the block at the other side are counted. Since the particles scatter inside the material, particles can scatter back which leads to multiple counting of particles. The investigation of the backscattering effect of neutrons is described in section 2. In section 3, the results of the neutron simulations are discussed. The results of the muon simulations are presented in section 4. Using the cosmic-ray neutron and muon-induced neutron fluxes, the total neutron flux can be calculated for each material. These results are shown in section 5.

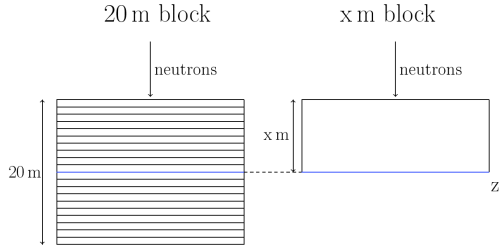


Figure 1: Illustration of the backscattering effect.

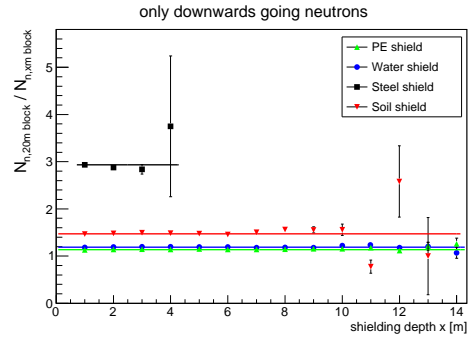


Figure 2: Ratio of neutrons counted inside a block and neutrons leaving blocks with different thicknesses.

Material	Plastic	Water	Soil	Steel
All neutrons	1.3552 ± 0.0006	1.4918 ± 0.0005	2.1718 ± 0.0005	5.340 ± 0.002
Downwards going neutrons	1.1370 ± 0.0005	1.1899 ± 0.0004	1.4723 ± 0.0004	2.9322 ± 0.0009
Upwards going neutrons	0.218 ± 0.001	0.3019 ± 0.0008	0.700 ± 0.001	2.408 ± 0.008

Table 1: Neutron flux inside a 20 m block at a certain shielding depth divided by the neutron flux behind a block with the corresponding thickness.

2 Backscattering effect

During particle transport in the simulation, the particle properties like momentum, energy and position are only stored if a boundary is crossed. Usually it is not monitored how often a particle crosses the same boundary. Therefore backscattering can lead to double or even multiple counting of neutrons. This can lead to wrong shielding indices. To estimate the fraction of backscattered neutrons, a 20 m block, which is divided into 20 sub-blocks, was simulated. The total neutron flux and the neutron flux pointing downwards are derived at different shielding depths inside the block. These numbers are then compared to the number of simulated neutrons leaving a block with the corresponding thickness. This is illustrated by Fig. 1. The ratio between the number of neutrons between the 20 m block and the block with the corresponding thickness is a measure of backscattering and is shown in Fig. 2. Without backscattering, the ratio would be one. The larger the ratio, the more neutrons scatter back. From Fig. 2 it can be seen that backscattering does not depend on the depth. Therefore the ratio can be obtained by averaging over all depths. The results are shown in Table 1. It can clearly be seen that backscattering is larger for denser materials with higher average mass number A like steel and that the backscattering effect is significant. Therefore one block for each shielding thickness has to be simulated. Further, the material blocks need to be placed in vacuum to avoid miscounting at the boundary of the block.

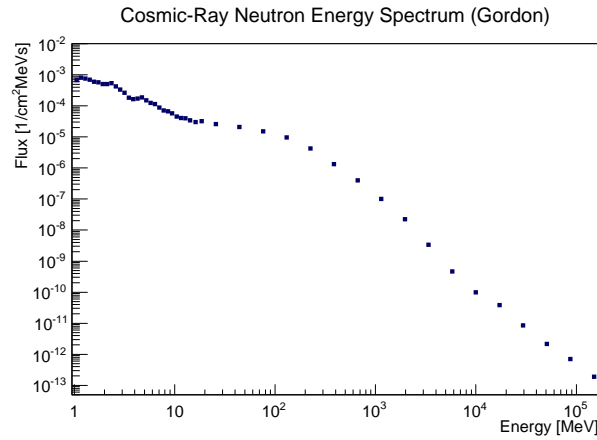


Figure 3: Used neutron energy spectrum. Datapoints are taken from [4].

3 Neutron simulations

For each shielding depth and material one block was simulated. Neutrons are injected following the energy spectrum shown in Fig. 3 measured by Gordon et al. [4]. Since the angular distribution of cosmic-ray neutrons is not well known, also the effect of using different angular distributions was investigated. For this purpose, a distribution where all neutrons are going only vertically downwards and an isotropic distribution were chosen, since the on average penetrated distance is the smallest for the first distribution and the largest for the second distribution. Also a distribution suggested by A. Nesterenok [5] for high-energetic cosmic-ray neutrons ($E \geq 10$ MeV) reaching the ground

$$J(\theta) = J_0 \exp[\alpha(1 - \cos \theta)] \quad \text{with } \alpha = -2.5 \quad (1)$$

was investigated. In Eq. 1, J_0 is the flux in the vertical direction and θ is the nadir angle. Figure 4 shows the energy spectra of cosmic-ray neutrons after penetrating steel blocks with different thicknesses. Only vertically downwards going neutrons were injected. A shielding thickness of 0 dm corresponds to the injected spectrum which is the Gordon spectrum shown in Fig 3. During penetration, neutrons lose energy by scattering off shielding material nuclei. Some neutrons are stopped, but also new neutrons and other particles are created. After a certain depth, the shower reaches equilibrium. When equilibrium is reached, the shape of the energy spectrum is not changing anymore and more particles are shielded than produced. In Fig. 4, it can be seen that the equilibrium for steel is reached after 6 dm of shielding. The depths at which equilibrium is reached is also listed in Table 2 for all simulated materials. After the equilibrium is reached, the decreasing neutron flux with increasing shielding depth can be described by a power law fit [6]:

$$y = 10^{sx+a} \quad (2)$$

with the shielding depth x , the neutron flux $y(x)$, the shielding index s and a fit constant a . Figure 5 shows the number of neutrons normalized to the number of arriving neutrons for different shielding depths and materials. The results of the power law fits are shown in Table 2.

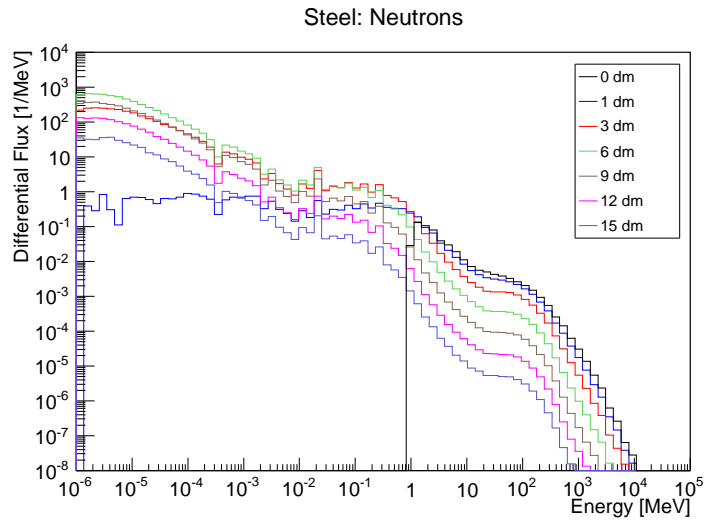


Figure 4: Simulated neutron energy spectrum at different depths for steel. Only downwards going neutrons were injected.

Material	EQ depth	Only downwards going neutrons	Nesterenok	Isotropic
Plastic	< 0.1	-0.354 ± 0.003	-0.366 ± 0.002	-0.388 ± 0.005
Water	< 0.1	-0.372 ± 0.003	-0.397 ± 0.007	-0.418 ± 0.005
Soil	< 0.1	-0.57 ± 0.01	-0.584 ± 0.007	-0.611 ± 0.009
Concrete	0.1 ± 0.05	-0.822 ± 0.006	-0.855 ± 0.004	-0.91 ± 0.02
LNGS rock	0.6 ± 0.05	-0.850 ± 0.003	-0.897 ± 0.005	-0.961 ± 0.009
Steel	0.6 ± 0.05	-2.01 ± 0.02	-2.12 ± 0.02	-2.22 ± 0.03
Copper	0.7 ± 0.05	-2.10 ± 0.02	-2.15 ± 0.01	-2.22 ± 0.02
Lead	1.6 ± 0.05	-1.368 ± 0.009	-1.39 ± 0.01	-1.42 ± 0.01

Table 2: Shielding index s [1/m] for different materials and angular distributions ($E \geq 0$ MeV). The depth at which equilibrium of the shower is reached (EQ depth [m]) is also shown.

More neutrons are shielded if the shielding index is smaller. This is the case for denser materials with higher mass number A . Comparing the shielding indices of different angular distributions for the same material, it can be seen that the shielding indices of the isotropic distribution are always the smallest and the shielding indices of the only vertically downwards going neutron distribution is always larger. This can be explained by the fact that the on average penetrated distance is larger for the isotropic distribution. It can also be seen that the difference of the indices is smaller compared to the difference between different materials. This means that the influence of the chosen material is much larger than the influence of the injection angular distribution.

NEUTRON SHIELDING SIMULATIONS AND MUON-INDUCED NEUTRONS

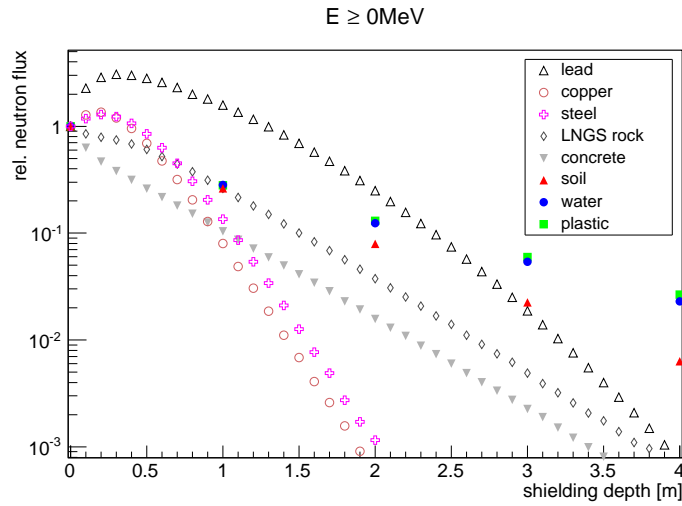


Figure 5: Simulated neutron flux at different shielding depths normalized to the incoming neutron flux for different materials. The angular distribution suggested by [5] (see Eq. 1) was used.

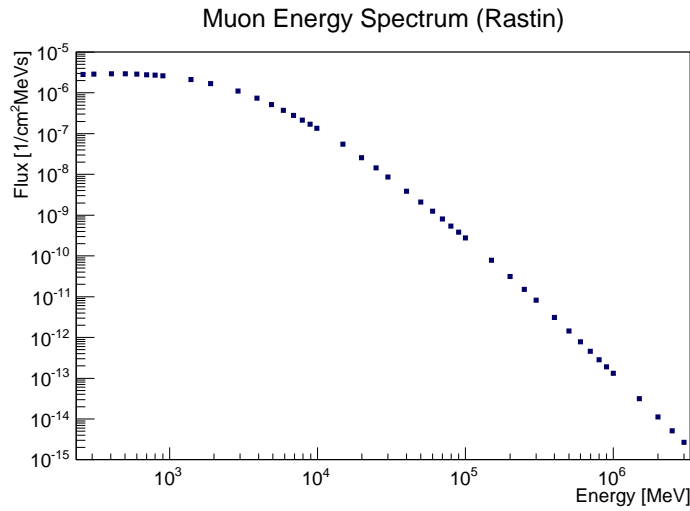


Figure 6: Used muon energy spectrum. Datapoints are taken from [7].

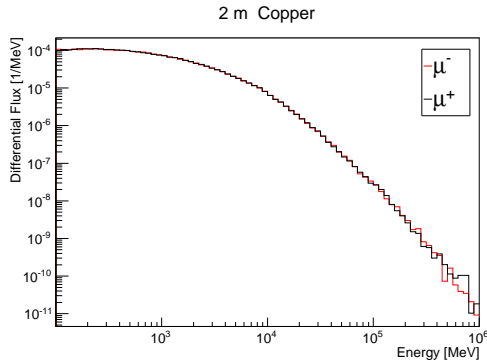


Figure 7: Comparison of the μ^- and μ^+ energy spectrum.

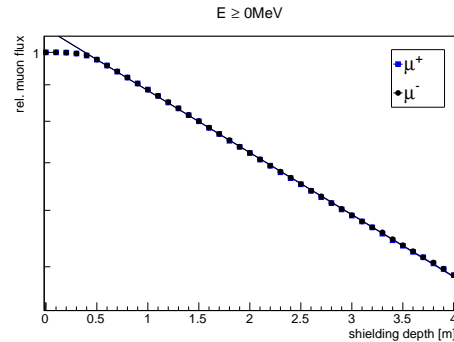


Figure 8: Muon flux at different shielding depths normalized to the incoming muons for LNGS rock.

4 Muon simulations

For the muon simulations the measured energy spectrum of Rastin [7], which is shown in Fig 6, was used as injection spectrum. Positive and negative charged muons were injected following a $\cos^2(\theta)$ angular distribution. Figure 7 compares the energy spectra of μ^+ and μ^- after the muons have penetrated 2 m of copper. It can clearly be seen that the energy spectra of μ^+ and μ^- are very similar. Also the number of muons at different shielding depths is the same which is shown by Fig. 8. This is expected since they undergo similar reactions. The only difference is that only μ^- can undergo muon capture. Low energetic μ^+ can only decay and can not be captured.

Muons induce neutrons during penetration. The number of neutrons normalized to the number of injected muons at different shielding depths is shown in Fig. 9. It can clearly be seen that the number of muon induced neutrons differs for μ^+ and μ^- . More neutrons are induced by μ^- . From looking at Fig. 8 it is evident that this can not be explained by different muon shielding properties, since they are the same for μ^+ and μ^- . The different amount of muon-induced neutrons can be explained by the fact that neutrons are produced during muon capture which only μ^- can undergo. During muon decay, no neutrons are produced.

From Fig. 9 it can also be seen that the difference between μ^+ and μ^- -induced neutrons becomes smaller at larger shielding depths, where the number of stopping muons is also smaller (see [8]). Figure 10 compares the energy spectra of μ^+ and μ^- -induced neutrons. The spectra differ since they are normalized with the number of induced neutrons which is smaller for μ^+ . The shape of both energy spectra is similar up to a few MeV. Above few tens of MeV the differential fluxes are the same for μ^+ and μ^- .

The power law fit of Eq. 2 was applied for depths at which the shower is in equilibrium. The results are shown in Table 3. As expected the shielding indices for neutrons are smaller than the shielding indices for muon-induced neutrons. Therefore the muon-induced neutron flux starts to dominate the total neutron flux at larger shielding depths. Denser material with higher mass number A shields cosmic-ray neutrons more efficiently, but also more neutrons are produced. Therefore the total neutron flux has to be considered.

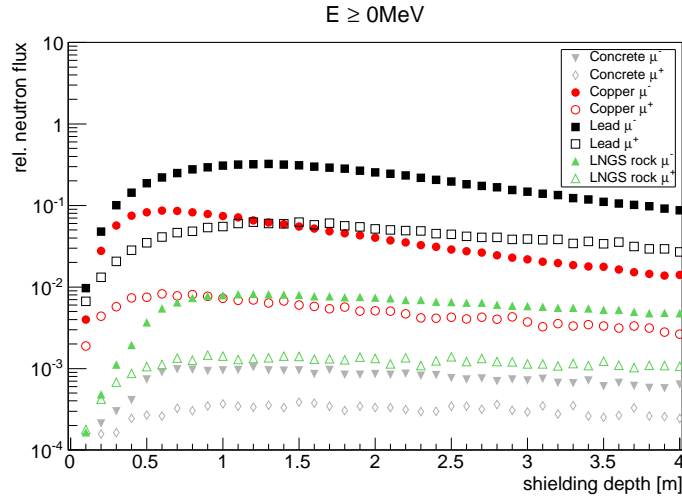


Figure 9: Muon-induced neutrons normalized to the incoming muons at different shielding depths for different materials.

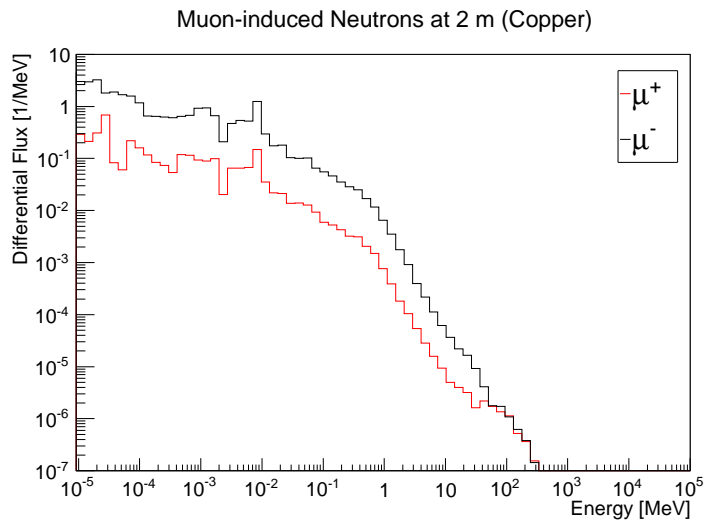


Figure 10: Comparison of the μ^- -induced and μ^+ -induced neutron energy spectrum.

Material	μ^+ [m^{-1}]	μ^- [m^{-1}]
Plastic	-0.0193 ± 0.0008	-0.0246 ± 0.0008
Water	-0.021 ± 0.001	-0.0271 ± 0.0007
Soil	-0.0264 ± 0.0009	-0.045 ± 0.001
Concrete	-0.041 ± 0.008	-0.079 ± 0.004
LNGS rock	-0.038 ± 0.006	-0.085 ± 0.003
Steel	-0.046 ± 0.004	-0.065 ± 0.002
Copper	-0.134 ± 0.005	-0.256 ± 0.003
Lead	-0.122 ± 0.006	-0.238 ± 0.002

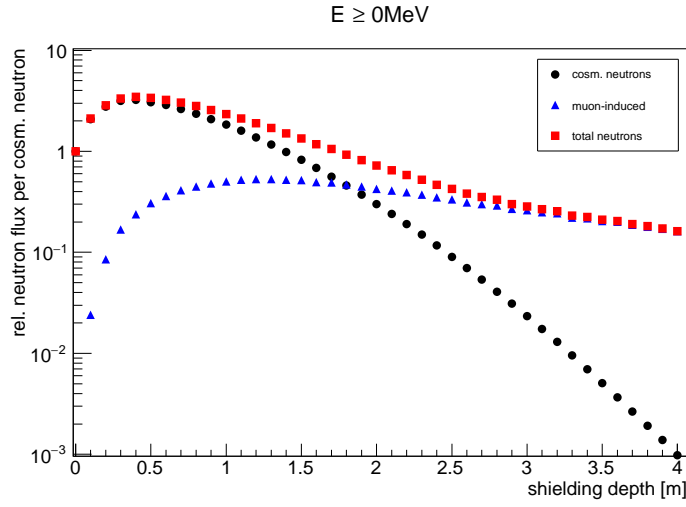
 Table 3: Shielding index s for muon-induced neutrons in [$1/\text{m}$] ($E \geq 0 \text{ MeV}$).


Figure 11: Neutron fluxes at different shielding depths for lead normalized to the incoming cosmic-ray neutrons. All cosmic-ray neutrons were injected vertically downwards going.

5 Total neutron flux

Using the results of the cosmic-ray neutron and muon simulations, the total neutron flux can be calculated. At sea-level, the ratio of neutrons to muons is 1:3 (see [9]). The muon charge ratio is $\mu^+/\mu^- \sim 1.25$ [10]. Therefore the neutron simulation results have to be weighted with a factor of 0.25, the μ^+ simulation results with a factor of 0.417 and the μ^- simulation results with a factor of 0.333 to get the total neutron flux.

Figure 11 shows the total neutron flux at different shielding depths of lead. Also the cosmic-ray and the total muon-induced neutron fluxes are shown. At smaller shielding depths, the total neutron flux is dominated by the cosmic-ray neutron flux. At larger depths, the flux is dominated by the muon-induced neutron flux.

In Fig. 12, the total neutron fluxes behind different materials is shown. Figure 13 shows the flux of neutrons with $E_n \geq 20 \text{ MeV}$. It can be seen that the total flux is lowest behind a concrete shielding. This is not the case for neutrons with an energy higher than 20 MeV. There are less

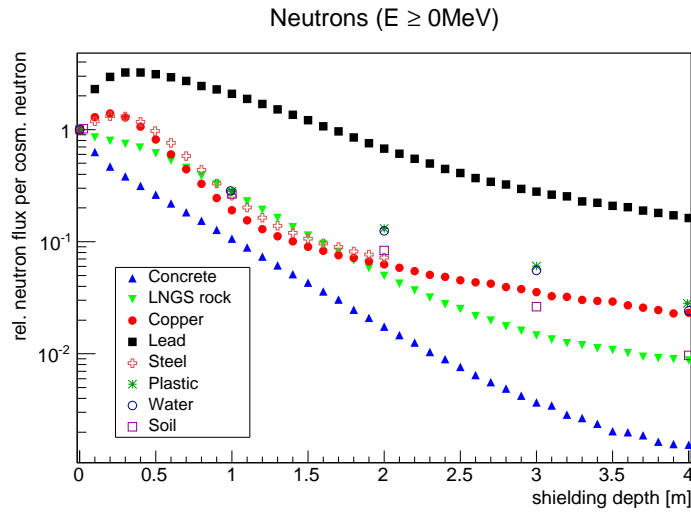


Figure 12: Total neutron flux at different shielding depths for different materials. The outgoing neutrons were normalized to the incoming cosmic-ray neutrons which were distributed by Eq. 1.

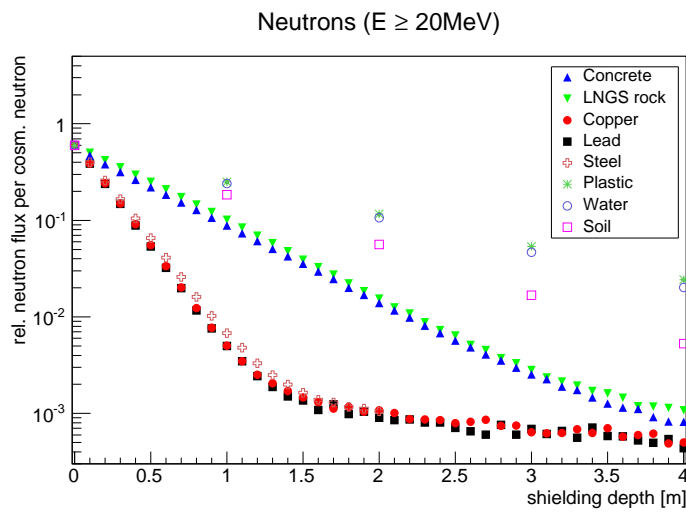


Figure 13: Total neutron flux at different shielding depths for different materials. The outgoing neutrons were normalized to the incoming cosmic-ray neutrons which were distributed by Eq. 1.

neutrons with $E_n \geq 20$ MeV after copper, lead or steel shielding. This shows that the best choice of shielding material depends on the energy of neutrons which one likes to shield.

6 Conclusion

Cosmic-ray neutron and muons (μ^+ and μ^-) were simulated with the GEANT4 based framework MaGe to get the shielding powers of cosmic-ray neutrons and muon-induced neutrons for different shielding materials. More neutrons are induced by μ^- than by μ^+ due to muon capture. This difference becomes smaller at larger shielding depths, since also the number of stopping muons becomes smaller.

Denser material shields more cosmic-ray neutrons, but also more neutrons are induced. Therefore the total neutron flux has to be calculated to compare different materials. The best choice of shielding material depends on the energy of neutrons which one wants to be shielded.

References

- [1] Melissa Boswell et al. MaGe-a Geant4-based Monte Carlo Application Framework for Low-background Germanium Experiments. *IEEE Trans. Nucl. Sci.*, 58:1212–1220, 2011.
- [2] H. Wulandari, J. Jochum, W. Rau, and F. von Feilitzsch. Neutron flux underground revisited. *Astropart. Phys.*, 22:313–322, 2004.
- [3] Laura Vanhoefer et al. Neutron Shielding Simulations and Muon-induced Neutrons. *PoS, NEUTEL2015:085*, 2015.
- [4] Gordon M. S. et al. Measurement of the Flux and Energy Spectrum of Cosmic-Ray Induced Neutrons on the Ground. *IEEE Trans. Nucl. Sci.*, 51:3427–3434, 2004.
- [5] Aleksandr Nesterenok. Numerical calculations of cosmic ray cascade in the Earth’s atmosphere: Results for nucleon spectra. *Nucl. Instrum. Meth.*, B295:99–106, 2013.
- [6] Aaron Michel. Investigation of cosmic ray shielding properties of different materials at shallow depths. diploma thesis, Technische Universität München, 2012.
- [7] B. C. Rastin. AN ACCURATE MEASUREMENT OF THE SEA LEVEL MUON SPECTRUM WITHIN THE RANGE 4-GEV/C TO 3000-GEV/C. *J. Phys.*, G10:1609–1628, 1984.
- [8] G. L. Cassiday, J. W. Keuffel, and J. A. Thompson. Calculation of the stopping-muon rate underground. *Phys. Rev.*, D7:2022–2031, 1973.
- [9] G. Heusser. Low-radioactivity background techniques. *Ann. Rev. Nucl. Part. Sci.*, 45:543–590, 1995.
- [10] W. R. Frazer, C. H. Poon, D. Silverman, and H. J. Yesian. Limiting fragmentation and the charge ratio of cosmic ray muons. *Phys. Rev.*, D5:1653–1657, 1972.

The Hamburg Observatory

After a small refreshment at the end of the second day, all participants were invited to make a trip to the Hamburg Observatory.



On the history of the Hamburg Observatory

Stefan K.G. Dahmke¹

¹Hamburger Sternwarte, Gojenbergsweg 112, D-20219 Hamburg, Germany

DOI: <http://dx.doi.org/10.3204/DESY-PROC-2016-05/42>

This contribution aims to provide an overview of the history of the Hamburg Observatory from its early days up to the present. It highlights some of the notable individuals as well as a select few projects that played major roles for astronomy and astrophysics in Hamburg.

1 Introduction

During the Magellan Workshop 2016 in Hamburg its participants were invited to visit the *Hamburger Sternwarte* (=Hamburg Observatory). This article is intended to give a brief summary of the century-long history of the observatory as well as some additional information on its current instruments. While this by far is not the most detailed possible analysis of the institute's history, it hopefully provides our international visitors with a quick overview, especially since most of the sources and literature so far are only available in German.

2 Establishment of the observatory

The history of the Hamburg Observatory does not begin in astronomical science but instead in the very down-to-Earth business of surveying. The Swiss expert Johann Casper Homer was conducting surveys of the Weser, Elbe and Eider rivers in northern Germany in the beginning of the 19th century. As he tried to find suitable optical instruments to help his work, he met with a certain Johann Georg Repsold, founder of a workshop for precision instruments and chief of the Hamburg fire brigade, who was capable of providing valuable assistance in constructing new surveying equipment. Repsold's interest in optical instruments grew rapidly and quickly led to an interest in astronomy. Thus he built his first own observatory in 1802, which he owned and operated privately for several years before French occupation under Napoleon put an end to it. [10]

Shortly after, in 1820, Repsold could convince the senate of Hamburg to grant permission to build a new and larger observatory at the Millerntor, not far from the city centre. Initially the observatory was again a private endeavour and was largely funded by being also working as a navigators' school. This is a very tight link between astronomy and seafaring, which would continue to play a significant role in the history of the observatory for more than a century. [10][11]

After Johann Georg Repsold, who had continued his work in the fire brigade of Hamburg, died in the line of duty on January 14th 1830, the senate decided to keep the observatory and officially opened it as a state institute in 1833. Christian Carl Ludwig Rümker became the first



Figure 1: The Millerntor observatory. [1]

director and using a Fraunhofer refractor telescope built by the Repsold workshops - which were now operated by Repsold's sons - he published a catalogue of stars, comets and asteroids which earned him a gold medal from the Royal Society of London in 1854. When Rümker retired in 1857 he, too, was succeeded by his son, who faced a major challenge in modernising the aging equipment of the observatory. [10]

In 1867 the observatory acquired a 26 cm refractor built on a modern equatorial mount from the Repsold company. This telescope still exists and remains functional. Despite this the observatory lost influence in Germany as Georg Rümker, contrary to trends of astronomy in Germany, had little interest in studying galaxies and instead kept the research focus on comets, asteroids and astrometry. [10][11]

3 Time ball

As already mentioned, there has always been a strong tie between astronomical observations and maritime navigation in Hamburg. This is due to two reasons, which also formed two of the major tasks for the observatory for a very long time: firstly, ships trying to fix their position by means of the stars need sufficiently precise stellar charts to know the coordinates of bright stars and consequently compare these to their own nightly observations. Secondly, to find their current longitude, ships had to know the exact time of a reference point (like Greenwich or their own homeport) indicated by a clock to be compared to the culmination of the sun or bright stars.

ON THE HISTORY OF THE HAMBURG OBSERVATORY

This method of determining one's position in longitude was introduced by the Yorkshire-born carpenter and tinkerer John Harrison who not only understood how knowing the time at a reference point was the key to solving the longitude problem, but also managed to build the first clocks that would provide this time aboard a ship with reasonable precision. Despite many astronomers' resistance - Sir Isaac Newton maintained up to his death in 1727 that it was utterly impossible to build an accurate shipboard clock - it became a standard method of navigation during the 19th century and again involved astronomers with the task of providing precise time to ports, where ship captains would correct their shipboard clocks. [3]

In 1876 a *time ball* was erected in Hamburg. Figure 2 shows a technical drawing of the structure. A roughly 2 m diameter leather ball was raised up in the tower and at precisely 12:00pm GMT, 12:43 local time, dropped back down to its original position, released by an electric mechanism which was actuated via telegraph from the observatory. As the time ball was located on top of a large storehouse, this visual signal could be made out from all over the harbour, enabling the navigators and captains to adjust their own clocks. Today a fully functional scale model built by Heinz-Otto Kult, who meticulously researched its history, is on display at the Hamburg Observatory. [7]

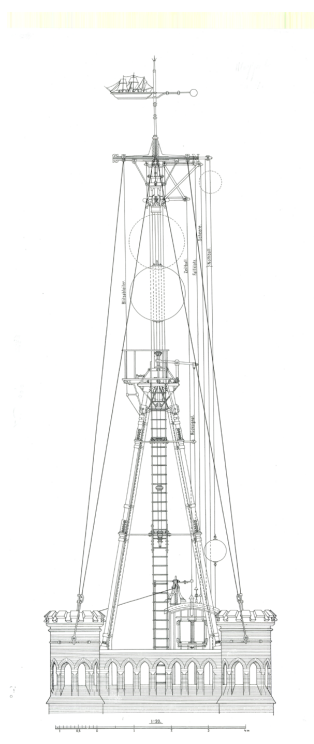


Figure 2: Schematic drawing of the time ball. The whole structure was located on top of a warehouse. [1]

The main instrument used for the determination of time was the Meridian Circle, a type of special telescope which does not traverse but strictly looks along the North-South-Meridian in variable altitude. The apparent movement of the stars as induced by the rotation of the Earth then makes stars pass through the field of view at different times. Noting these times and comparing them to stellar catalogues enables the observer to correct for errors in the observatory's own clocks, of which several were in operation in a well insulated room underneath the library. The advent of widespread telephone and radio networks rendered the time ball less and less important after the turn of the century and in 1934 it was finally demolished. Despite this the precise measurement of time remained a major task for the observatory up to the 1960s, when atomic clocks which allowed for even higher precision than astronomic observations were established. The Meridian Circle in Bergedorf remained in use until the 1970s when it was shipped to Australia to take part in observations in preparation for the Hipparcos space mission. [4][5][7]

4 Bergedorf

As has been noted before, the influence Hamburg Observatory had on the astronomical community declined during the second half of the 19th century. Besides the research focus shifting away from general trends in Germany and Europe at the time and the fact that the observatory was in need of modernising instruments and equipment, a major factor in this was the location. The Millerntor site was located near the harbour, which sometimes hampered observations due to vibrations and smoke from the increasing number of steam ships. Also from 1882 onward Hamburg introduced electric street lighting which further worsened the observation conditions. [10]

To combat these circumstances Georg Rümker and Richard Schorr, who in 1900 would become the next director, drew up plans to move the entire observatory away from the city. The navigation school had already split from the observatory in the 1860s for administrative reasons. The current site in Bergedorf was chosen for its relatively high elevation of 40 m, its distance from densely populated areas and the fact that the town of Bergedorf was already connected to Hamburg via railway. After 1900 construction of several separate buildings began and new instruments were ordered, making Hamburg one of Europe's largest observatories when the Bergedorf site was officially opened in 1912. Among these instruments were a new Meridian Circle, the *Great Refractor* measuring 60 cm in aperture and built by Respold, the 1 m reflector (*Meterspiegel*) built by Carl Zeiss and the *Lippert Astrograph*, a 34 cm refractor built by Carl Zeiss and donated by the local merchant Eduard Lippert. Also the 26 cm *Equatorial* refractor was moved from the old observatory. Each of these telescopes was housed in a separate building and could thus operate independently. This followed a new trend of keeping living quarters and offices away from the telescopes to reduce air turbulence related to heating. [6][10][11]



Figure 3: The dome housing the *Great Refractor* during construction. [1]

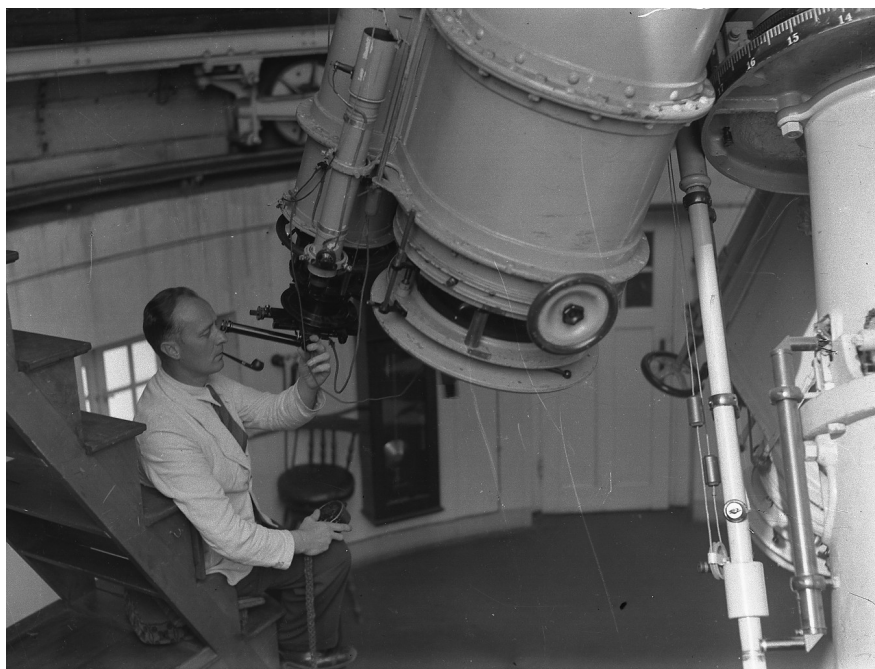


Figure 4: Arthur Arno Wachmann at the *Lippert Astrograph*. [1]

Now equipped with state-of-the-art equipment, Hamburg observatory gained new importance. In the 1920s multiple survey programmes began, among them the *Bergedorfer Spektraldurchmusterung* (=Bergedorf spectral survey) by Schwassmann und Wachmann (seen in figure 4), who used the Lippert Astrograph to obtain spectra of more than 160,000 stars. Also the *Astronomische Gesellschaft Katalog 2* (=Astronomical Society Catalogue 2), or AGK2 for short, a major astrometric catalogue, saw significant contributions from Bergedorf, even though it could not be published until 1951 due to the outbreak of the war. In 1920 also Walter Baade joined the observatory. He started out observing comets, planets and asteroids but then, towards the end of the 20s, became increasingly interested in the study of galaxies. [6][10]

In 1927 the probably most famous character arrived in Hamburg, when Bernhard Schmidt accepted an offer by Schorr to repair a horizontal telescope that Schmidt had originally built. This was a favour to Schmidt who had fallen on hard times and only received a small fee plus free lodging at the observatory at first. He anyway quickly made himself indispensable as a skilled optical engineer. [6][9][10]

During an expedition to the Philippines in 1929, in which both Baade and Schmidt participated, Bernhard Schmidt conceived his most famous invention: trying to tackle the problem of image aberrations of telescopes with short focal lengths he first used a semi-spherical mirror instead of the commonly found parabolic one. Then he counteracted the rising spherical aberration by introducing an additional optical element. The *Schmidt Corrector Plate* was an aspheric lens with convex and concave parts put in front of the mirror, at the center of the mirror's sphere shape. This lens was carefully shaped to counteract the aberration. The following year a complete telescope based on Schmidt's principle was built in Hamburg. The



Figure 5: Bernhard Schmidt in his workshop at Hamburg Observatory. [1]

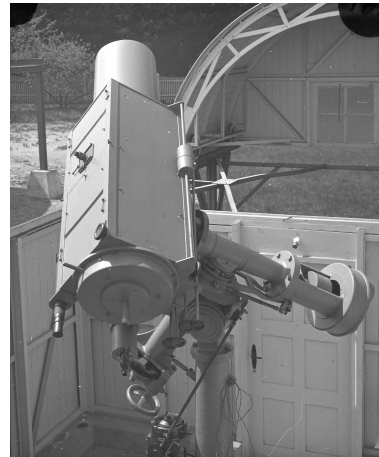


Figure 6: The original Schmidt telescope as seen in 1932. [1]

instrument, shown in figure 6, immediately was a resounding success. [2][9]

While Bernhard Schmidt himself died in 1935, telescopes of his design quickly became popular in astronomy. The Palomar Observatory near San Diego opened in 1936 with an 18 in Schmidt camera. The Mount Wilson Observatory near Los Angeles began construction of a 1.2 m Schmidt telescope. Walter Baade, who already had hoped to work at Mt Wilson prior to joining the Hamburg Observatory moved to the United States in 1937, while financial and organisational problems delayed Hamburg's *Great Schmidt Mirror* until the outbreak of the war. The instrument could only be built in 1954 and then was put to use on the new AGK3 project, for which Bergedorf mapped most of the northern Sky. The 1.2 m Schmidt Telescope was operated in Hamburg until 1969, when plans to move the telescope to Calar Alto Observatory in Spain came up to make use of the more favourable weather there. [2][10][11]

The fact that Walter Baade, who had left Hamburg in 1937, had been Richard Schorr's favourite candidate as a successor meant that somebody else had to be named as next director. There were several candidates and the decision was not very easy, as Schorr's preference was Otto Heckmann, who despite having joined the nazi party and successfully having used some of their structures to further his own work in Göttingen, had fallen out of favour with the politics due to his keen interest in cosmology and Einstein's theory of relativity, which he officially defended. Heckmann became director of the Hamburg Observatory in 1941 regardless. [10]

5 A word on ESO

Otto Heckmann as director of the Hamburg Observatory attended several international conferences in the early 1950s. These conferences concerned themselves with finding ways to strengthen astronomy and science in Europe in the economically difficult times. One promising idea was to concentrate efforts throughout Europe by starting a joint observatory, thus splitting the costs of building and operating it. [8][6]



Figure 7: Otto Heckmann (r) at the *Great Schmidt Mirror* 1.2m telescope. [1]

This idea, alongside the realisation that studying our own galaxy in detail would require a large and advanced observatory in the southern hemisphere, led to the Leiden Declaration in January 1954. This declaration states the intent of constructing a joint observatory including a 3m mirror telescope and a 1.2m Schmidt camera in South Africa. It was signed by leading astronomers from six countries (Heckmann and Unsöld from Germany, Burgeois from Belgium, Couder and Danjon from France, Redman from the UK, Oort, Oosterhoff and van Rhijn from the Netherlands, Lindblad, Lundmark and Malmquist from Sweden) and intended to gain more support from their respective governments. [8]

Scouting for a suitable location started in late 1955 and soon extended to South America, accounting for the troublesome political situation in South Africa. Finally, on October 5th 1962, the *European Southern Observatory* was founded. From the six countries involved in the Leiden Declaration five became founding members - the United Kingdom did not join. A month later Otto Heckmann was named as first director of ESO and offices for the newly founded organisation were prepared in the town of Bergedorf, not very far from Hamburg Observatory, where Heckmann remained director until 1968. By that time ESO required so much of his attention, that Alfred Behr relieved him as director of the observatory. By this time construction of the ESO site in La Silla, Chile was well advanced, two telescopes exceeding 1m in aperture diameter were already installed. Later in the same year the journal *Astronomy and Astrophysics*, which remains one of the most influential journals for the astrophysics community, was founded with the help of ESO. [8][6][10]

Since Heckmann no longer had to divide his time between ESO and Bergedorf, the vicinity of the headquarters to Hamburg Observatory wasn't as much of an issue anymore from 1968

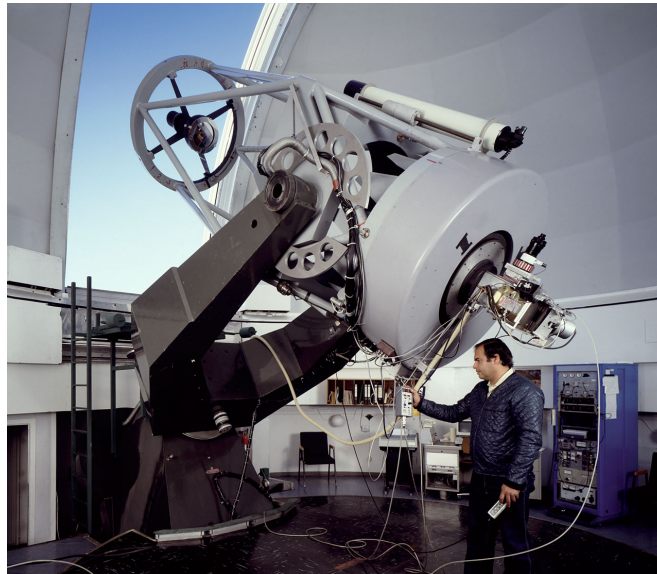


Figure 8: The 1-metre Telescope was the first instrument to operate at the La Silla site. Its *first light* was in the night of November 30th 1966. Image courtesy of ESO.

onwards. Also the old offices soon proved to be inadequate in size and plans for a new ESO site in Europe were drawn up. The planning of the new buildings lasted until the late 1970s, when finally construction began in Garching, near Munich, which not only allowed for much more extensive buildings, but was also easier to reach for the ever increasing number of astronomers from ever more European countries. When the Garching headquarters were finally inaugurated in 1981 Belgium, Denmark, France, Germany, The Netherlands and Sweden were already part of ESO; Italy and Switzerland joined shortly afterwards. [8]

While Otto Heckmann retired from the post of director general of ESO in 1970, his successor at the Hamburg Observatory kept close ties to the international organisation. Observations from Hamburg became less and less important, but Behr was involved in building instrumentation for ESO, including a polarimeter. That concludes the era of major contributions of the Hamburg Observatory to ESO, although of course scientists from Hamburg remain involved in projects up until today. [8][6]

6 Hamburg Observatory today

Hamburg Observatory has been a part of the University of Hamburg since 1968. This resulted in tremendous changes to the organisation of the observatory. Nowadays the majority of staff is made up by students of the university who specialised their studies of physics towards astronomy and astrophysics.

In 1969 Prof. Alfred Weigert joined the observatory and founded a workgroup concerned with stellar evolution and the modelling of the interior of stars. Both of these topics remain strong suits of the Hamburg Observatory up to the present, having expanded into two separate groups. Prof. Peter Hauschildt keeps expanding on the renowned stellar atmosphere simulation

code *PHOENIX* while Prof. Robi Banarjee continues work on stellar evolution.

Soon after, in 1972, Prof. Heinrich Wendker founded his workgroup on extragalactic astrophysics and made efforts to extend observations to both radio and X-ray wavelengths, the latter of which of course had to be conducted from space. The extragalactic work later developed into one of the major achievements of the 1980s, the *Hamburg Quasar Survey*, for which photographic plates taken with the *Great Schmidt Mirror* at Calar Alto as part of the *All Sky Objective Prism Survey* were scanned and analysed with the help of computers. Work on extragalactic astrophysics is still ongoing under direction of Prof. Marcus Brüggen and Prof. Annalisa Bonafede, including the observatory's involvement in the *LOW Frequency ARray*, LO-FAR, which consists of more than 48 stations across all of Europe.

Observations in wavelengths ranging from infrared to X-rays continue both in utilising Bergedorf's own telescopes and analysing data obtained at other observatories in the workgroup of Prof. Jürgen Schmitt, who specialised in stellar activity as well as characterisation of exoplanets through spectroscopy and photometry.

The work of Prof. Alfred Behr and others before him in designing new astronomical instruments is currently being carried on by Prof. Günter Wiedemann, who especially concentrates on spectroscopy and solar physics, as well as observations in optical and infrared wavelengths. For these projects a separate 70 cm telescope, designated *G1*, has recently been set up at Bergedorf.

The *Great Schmidt Mirror*, which was shipped to Spain, left Hamburg with an empty telescope dome. In 1975 the new *Oskar Lühning Teleskop* commenced observations. The 1.2 m mirror telescope remains the primary telescope for scientific observations in Hamburg today, in no small part thanks to a major effort of modernising the control system. The whole telescope is computer controlled, can be remotely operated and features modern CCD detectors since 2000.

Also in the mid-1970s the *Lippert Astrograph* underwent major changes and now features a 60 cm aperture mirror, effectively matching the *Great Refractor*. The telescope is manually controlled and can be used for both visual observations and camera exposures. While it's only used for scientific observations occasionally, it is used extensively for teaching purposes as well as for public outreach.

The historic *Great Refractor*, the *Meterspiegel* 1 m mirror telescope and the *Equatorial* all remain in varying degrees of restoration. The mirror telescope has widely been refurbished in recent years. A project to restore the *Great Refractor* is currently in planning, as the telescope itself is in fully operational condition, but the building around it and especially the dome mechanics are in bad repair prohibiting any use of the instrument. The *Equatorial* is still functional after almost 150 years, but has a seriously impaired field of view due to nearby trees. All three of these instruments are in no scientific use anymore and are mostly of historic and public interest today.

References

- [1] Photographic Archive of the Hamburg Observatory
- [2] Mark Christensen, *Schmidt - The Man and the Camera*, The Fox Valley Astronomical Society, 2000

- [3] Rupert T. Gould, *John Harrison and his Timekeepers*, Lecture recorded in The Mariner's Mirror Volume 21 Issue 2, 1935
- [4] Erik Høg, *Astrometry lost and regained - from a modest experiment in Copenhagen in 1925 to the Hipparcos and Gaia space missions*, Lecture held at Kroppedal Museum, 2010
- [5] Erik Høg, private communication
- [6] Jahresberichte Hamburger Sternwarte, Annual Reports of the Hamburg Observatory
- [7] Heinz-Otto Kult, private communication
- [8] Official ESO Timeline, <http://www.eso.org/public/about-eso/timeline/>
- [9] Richard Schorr, *Bernhard Schmidt* †, *Astronomische Nachrichten*, 1936
- [10] Jochen Schramm, *Sterne über Hamburg*, 2nd edition, Initiative zum Erhalt historischer Bauten, 2010
- [11] G. Wolfschmidt, A. Seemann, D. Köhl, *Hamburger Sternwarte - Geschichte und Erhaltung*, Förderverein der Hamburger Sternwarte e.V., 2001



Figure 1: Hamburg Observatory seen from the air in the late 1920s. Aerial photography was a rare event and it was decided to open all domes for the occasion. Credit: Photographic Archive of the Hamburg Observatory



Figure 2: The Great Refractor dome under construction in 1910. Credit: Photographic Archive of the Hamburg Observatory



Figure 3: Construction work on the mount for the Great Refractor telescope in March 1910.
Credit: Photographic Archive of the Hamburg Observatory



Figure 4: Walter Baade inside the dome of the 1912-built 1 m mirror telescope in Hamburg.
Credit: Photographic Archive of the Hamburg Observatory



Figure 5: The Beamtenwohnhaus (=Officials' Quarters) in which up to four astronomers and their families used to live. Despite ever improving connections to public transport and cars becoming widespread, employees lodged here up until the mid-1980s. Today the building is used as office space for the observatory. Credit: S. Dahmke



Figure 6: The Meridian Circle building today. The instrument built to determine the exact time used to be one of the most important ones for the Hamburg Observatory, yet today the building is empty. The telescope itself is currently stored in a museum in Munich. Credit: S. Dahmke



Figure 7: The dome of the Oskar Lühning Teleskop. The 1.2m telescope is Hamburg's primary science telescope housed in a dome originally conceived for the Great Schmidt Mirror. Credit: S. Dahmke

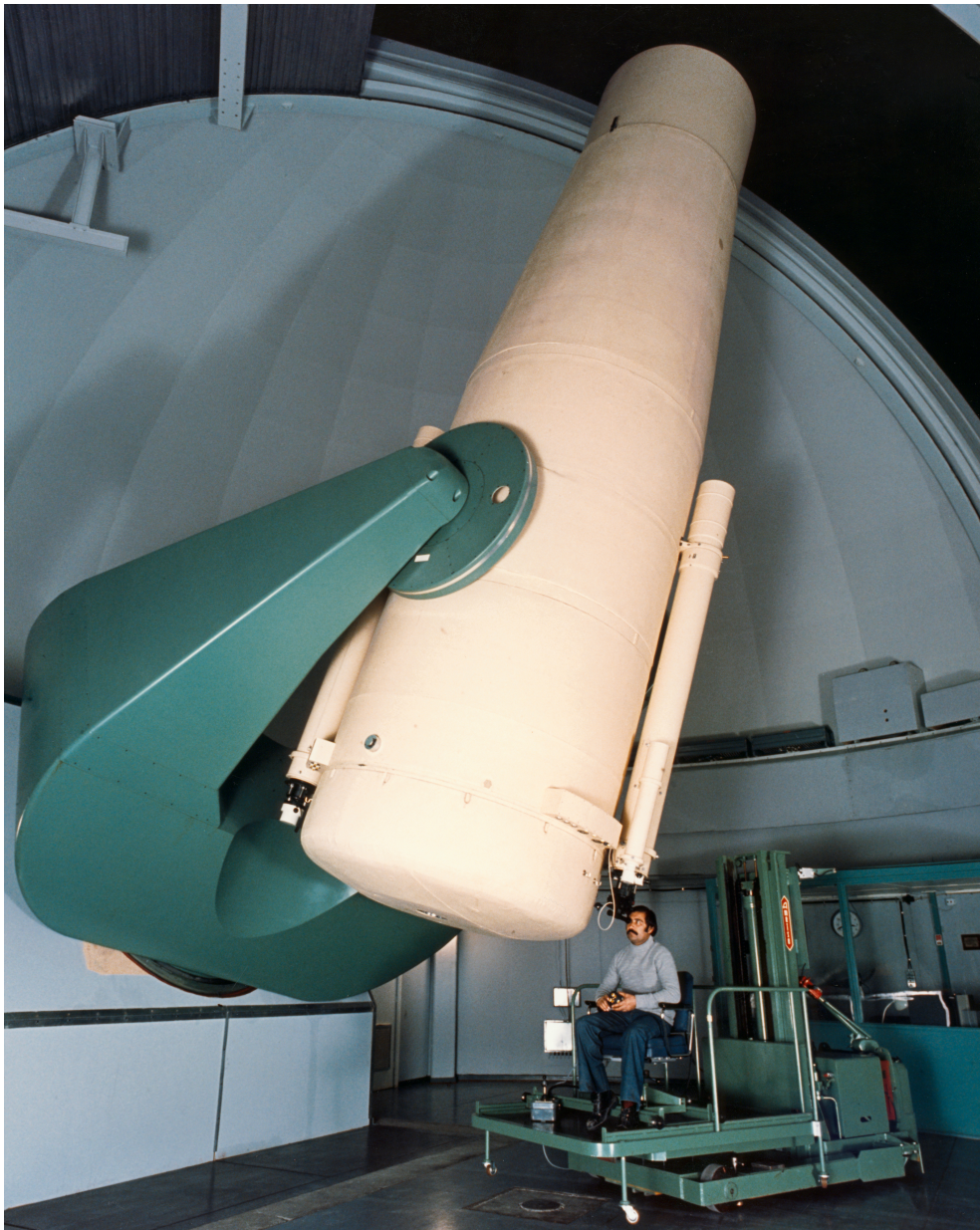


Figure 8: The ESO 1m Schmidt telescope which became operational in December 1971. Oscar Pizarro is adjusting the plateholder. Credit: ESO



Figure 9: Painting of Bernhard Schmidt, inventor of the Schmidt Mirror, by Erik Schmidt.



Figure 10: Painting of Richard Schorr, Director of Hamburg Observatory from 1900 to 1941.
Credit: Hamburg Observatory



Figure 11: Painting of Prof. Otto Heckmann, Director of Hamburg Observatory from 1941 to 1968, ESO Director General from 1962 to 1969. Credit: ESO



Figure 12: On June 8-10 1963, ESO officials were the guests of AURA on their property and on June 10 gathered on Cerro Morado, discussing ESO prospects in Chile. On June 8 1963, they undertook the trip on horseback to Tololo, where most of June 9 was spent for inspection of the AURA site. From there, both groups went on June 10 to the neighbouring mountain Morado on the AURA territory, south of Tololo; it was AURA's suggestion that this mountain, with its large surface and well tested, favourable observing conditions, might offer a suitable location for the ESO Observatory. On the photograph, from left to right: Ch. Fehrenbach, O. Heckmann, Sr Marchetti, J.H. Oort, N.U. Mayall, F.J. Edmondson and A.B. Muller. Credit: ESO/F.K.Edmondson

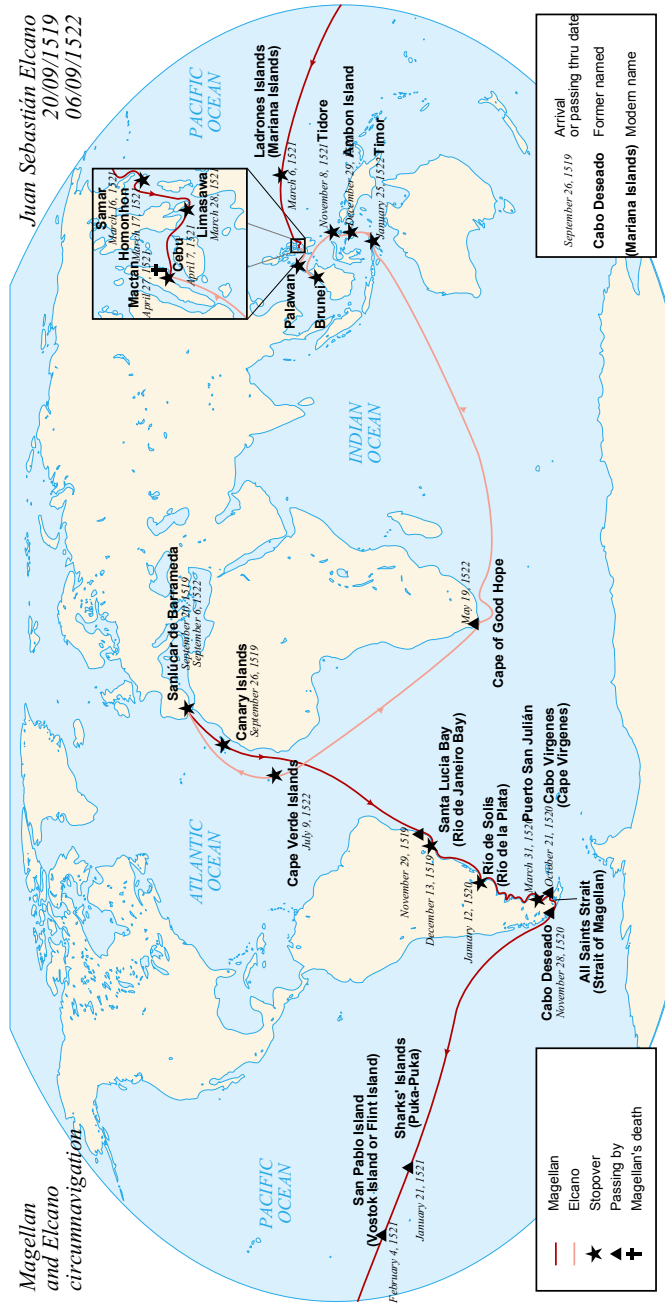


Figure 13: Map of the Magellan-Elcano voyage. Victoria, one of the original five ships, circumnavigated the globe and returned to Spain 16 months after Magellan's death. Credit: Atelier Graphique



Figure 14: An anonymous painting of Ferdinand Magellan, 16th or 17th century (The Mariner's Museum Collection, Newport News, VA).



Figure 15: Photographic image of the Large Magellanic Cloud, before (left) and after (right) the explosion of SN1987A. The supernova is visible on the right image just below the Tarantula nebula, in the upper part of the irregular galaxy. Credit: ESO



Figure 16: Large Magellanic Cloud and Small Magellanic Cloud. Credit: ESO/S. Brunier



Figure 17: Image obtained with the ESO Schmidt Telescope of the Tarantula Nebula in the Large Magellanic Cloud. Supernova 1987A is clearly visible as the very bright star in the middle right. At the time of this image, the supernova was visible with the unaided eye. Credit: ESO

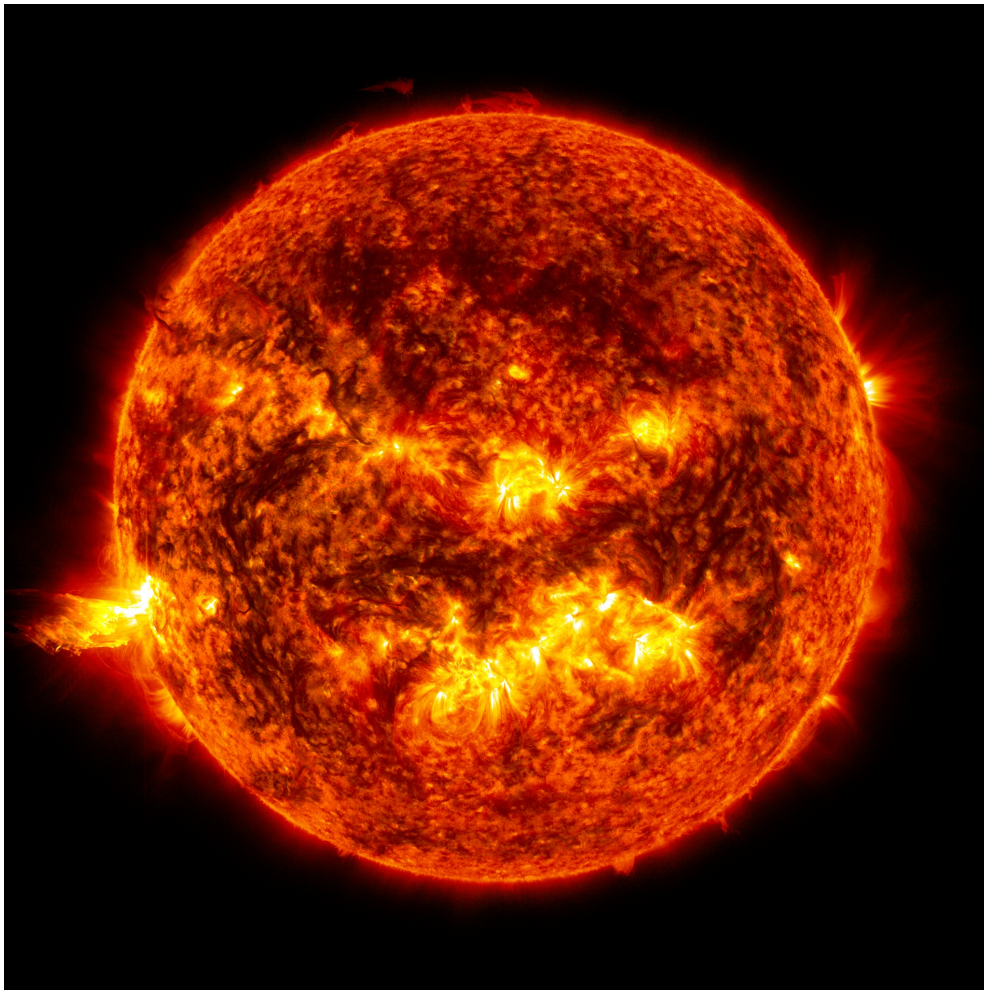


Figure 18: Solar flares. Credit: NASA



Figure 19: Exterior view of the Borexino detector located at Laboratori Nazionali del Gran Sasso. Credit: Borexino collaboration

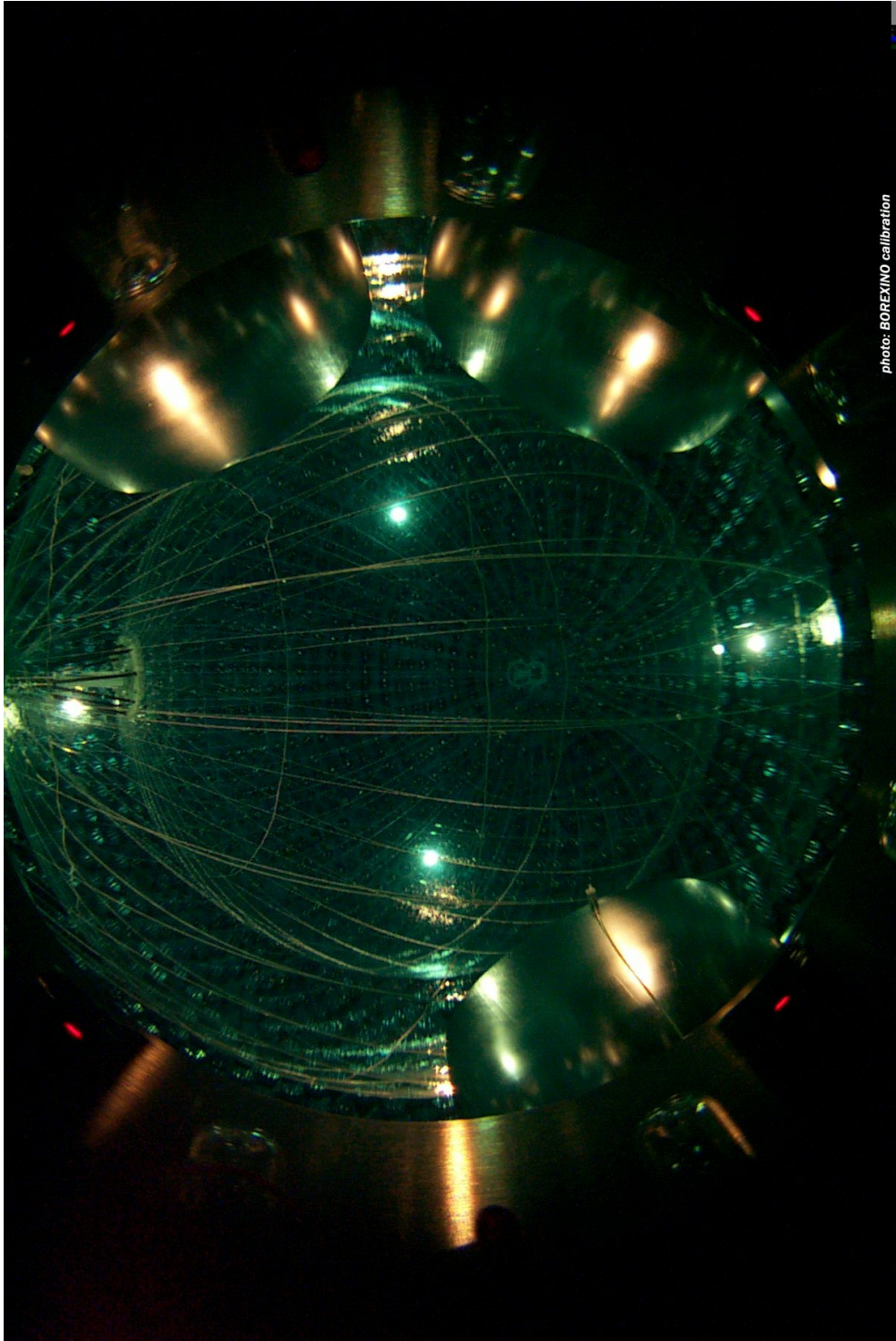


Figure 20: Interior view of the Borexino detector. Credit: Borexino collaboration



Figure 21: Hamburg in March of 2016. View over the Binnenalster. Credit: L. Vanhoefer

List of Authors

- Abt, I., 181
Agostini, M., 105, 175
Altenmüller, K., 105, 175
Appel, S., 105, 175
Astapov, I., 135, 143
- Barrios-Martí, J., 19
Bellini, G., 105, 175
Benziger, J., 105, 175
Berton, N., 105, 175
Bezyazeekov, P., 135, 143
Bick, D., 105, 175
Bogdanov, A., 135, 143
Bonfini, G., 105, 175
Boreyko, V., 135, 143
Brückner, M., 135, 143
Bravo, D., 105, 175
Budnev, N., 135, 143
- Caccianiga, B., 105, 175
Calaprice, F., 105, 175
Caminata, A., 105, 175
Carlini, M., 105, 175
Cavalcante, P., 105, 175
Cavanna, F., 129
Chepurnov, A., 105, 175
Chiavassa, A., 135, 143
Choi, K., 105, 175
Chvalaev, O., 135, 143
Clifton, G. A., 55
Cribier, M., 105, 175
- D'Angelo, D., 105, 175
Dahmke, S. K. G., 193
Davini, S., 35, 105, 175
Derbin, A., 105, 175
Di Noto, L., 105, 175
Drachnev, I., 105, 175
Durero, M., 105, 175
Dyachok, A., 135, 143
- Epimakhov, S., 135, 143
Etenko, A., 105, 175
- Farinon, S., 105, 175
Fedorov, O., 135, 143
Feilitzsch, F. von, 105, 175
Fischer, T., 11
Fischer, V., 105, 175
Fomenko, K., 105, 175
Formozov, A., 105, 175
Franco, D., 105, 113, 175
- Gabriele, F., 105, 175
Gafarov, A., 135, 143
Gaffiot, J., 105, 175
Galbiati, C., 105, 175
Garbini, L., 181
Ghiano, C., 105, 175
Giammarchi, M., 105, 175
Glawion, D., 151
Goeger-Neff, M., 105, 175
Gorbunov, N., 135, 143
Goretti, A., 105, 175
Grebennyuk, V., 135, 143
Gress, O., 135, 143
Gress, T., 135, 143
Grinuk, A., 135, 143
Grishin, O., 135, 143
Gromov, M., 105, 175
- Hagner, C., 105, 175
Horns, D., 135, 143
Houdy, Th., 105, 175
Hungerford, E., 105, 175
- Ianni, Aldo, 105, 175
Ianni, Andrea, 105, 175
Ivanova, A., 135, 143
- Jedrzejczak, K., 105, 175

Jeschke, D., 105, 175
Jonquères, N., 105, 175

Kaiser, M., 105, 175
Kalinin, A., 135, 143
Kalmykov, N., 135, 143
Karpov, N., 135, 143
Kazarina, Y., 135, 143
Kirichkov, N., 135, 143
Kiryuhin, S., 135, 143
Kobychev, V., 105, 175
Kokoulin, R., 135, 143
Komponiest, K., 135, 143
Konstantinov, A., 135, 143
Korablev, D., 105, 175
Korga, G., 105, 175
Kornoukhov, V., 105, 175
Korosteleva, E., 135, 143
Kozhin, V., 135, 143
Kryn, D., 105, 175
Kunnas, M., 135, 143
Kuzmichev, L., 135, 143

Lachenmaier, T., 105, 175
Lasserre, T., 105, 175
Laubenstein, M., 105, 175
Lehnert, B., 105, 175
Leibundgut, B., 165
Lenok, V., 135, 143
Liao, H.-Y., 181
Link, J., 105, 175
Litvinovich, E., 105, 175
Lohs, A., 11
Lombardi, F., 105, 175
Lombardi, P., 105, 175
Lorenz, S., 121
Lozza, V., 87
Lubsandorzhiev, B., 135, 143
Lubsandorzhiev, N., 135, 143
Ludhova, L., 105, 157, 175
Lukyanchenko, G., 105, 175

Machulin, I., 105, 175
Majorovits, B., 181
Maneck, S., 105, 175
Maneschg, W., 105, 175
Mancocci, S., 95, 105, 175
Maricic, J., 105, 175
Martinez-Pinedo, G., 11

Mauri, N., 47
Mention, G., 105, 175
Meroni, E., 105, 175
Meyer, M., 105, 175
Miloradovic, M., 41
Miramonti, L., 105, 175
Mirgazov, R., 135, 143
Mirzoyan, R., 135, 143
Misiaszek, M., 105, 175
Monkhoev, R., 135, 143
Montuschi, M., 105, 175
Mosteiro, P., 105, 175
Muratova, V., 105, 175
Musenich, R., 105, 175

Nachtigall, R., 135, 143
Neumair, B., 105, 175

Oberauer, L., 105, 175
Obolensky, M., 105, 175
Ortica, F., 105, 175
Osipova, E., 135, 143

Pakhorukov, A., 135, 143
Palermo, M., 181
Pallavicini, M., 105, 175
Panasyuk, M., 135, 143
Pankov, L., 135, 143
Paoletti, D., 71
Papp, L., 105, 175
Perasso, L., 105, 175
Petrukhin, A., 135, 143
Platonov, V., 135, 143
Pocar, A., 105, 175
Poleschuk, V., 135, 143
Popova, E., 135, 143
Porelli, A., 135, 143
Postnikov, E., 135, 143
Prosini, V., 135, 143
Ptuskin, V., 135, 143
Pushnin, A., 135, 143

Ranucci, G., 105, 175
Razeto, A., 105, 175
Re, A., 105, 175
Romani, A., 105, 175
Roncin, R., 105, 175
Rossi, N., 105, 175
Rubtsov, G., 135, 143

Samoliga, V., 135, 143
Satunin, P., 135, 143
Saviano, N., 3
Schönert, S., 105, 175
Schulz, O., 181
Scola, L., 105, 175
Semeney, Yu., 135, 143
Semenov, D., 105, 175
Serenelli, A., 27
Silaev (junior), A., 135, 143
Silaev, A., 135, 143
Simgen, H., 105, 175
Skorokhvatov, M., 105, 175
Skurikhin, A., 135, 143
Slucka, V., 135, 143
Smirnov, O., 105, 175
Sotnikov, A., 105, 175
Spiering, C., 135, 143
Sukhotin, S., 105, 175
Suvorov, R., 105, 175
Sveshnikova, L., 135, 143

Tabolenko, V., 135, 143
Tarashansky, B., 135, 143
Tartaglia, Y., 105, 175
Testera, G., 105, 175
Thurn, J., 105, 175
Tkachenko, A., 135, 143
Tkachev, L., 135, 143
Tluczykont, M., 135, 143
Toropova, M., 105, 175

Unzhakov, E., 105, 175

Vanhoefler, L., 181
Veyssiére, C., 105, 175
Vihonen, S., 65
Vinyoles, N., 27
Vivier, M., 105, 175
Vogelaar, R. B., 105, 175
Voronin, D., 135, 143

Wang, H., 105, 175
Weinz, S., 105, 175
Winter, J., 105, 175
Wischnewski, R., 135, 143
Wojcik, M., 105, 175
Wurm, M., 105, 175

Yashin, I., 135, 143
Yokley, Z., 105, 175

Zagorodnikov, A., 135, 143
Zaimidoroga, O., 105, 175
Zavatarelli, S., 105, 175
Zuber, K., 105, 175
Zurbanov, V., 135, 143
Zuzel, G., 105, 175

Participants

Ahlgren, Björn
Barrios Martí, Javier
Büttner, Benjamin
Caminata, Alessio
Cavanna, Francesca
Clifton, Alex
Dahmke, Stefan
Franco, Davide
Fuessling, Matthias
Glawion, Dorit
Heisel, Mark
Hekker, Saskia
Hollnagel, Annika
Izaguirre, Ignacio
James, Clancy
Kneissl, Raphael
Kowalski, Marek
Kunnas, Maike
Larsson, Josefin
Leibundgut, Bruno
Lohs, Andreas
Lorenz, Sebastian
Lozza, Valentina
Ludhova, Livia
Marcocci, Simone
Mauri, Nicoletta
Meyer, Mikko
Meyhöfer, David
Miloradovic, Michael
Müller, Cornelia
Opitz, Björn
Paoletti, Daniela
Ranitzsch, Philipp Chung-On
Rebber, Henning
Saviano, Ninetta
Serenelli, Aldo
Strotjohann, Nora Linn
Tamborra, Irene
Tluczykont, Martin
Vanhoefer, Annika
Vanhoefer, Laura
Vihonen, Sampsa
Voge, Markus
Vovk, Ievgen
Yanez Garza, Juan Pablo

*Steure, mutiger Segler! Es mag der Witz dich verhöhnen,
Und der Schiffer am Steuer senken die lässige Hand.
Immer, immer nach West! Dort muß die Küste sich zeigen,
Liegt sie doch deutlich und liegt schimmernd vor deinem Verstand.*

*Traue dem leitenden Gott und folge dem schweigenden Weltmeer,
Wär sie noch nicht, sie stieg jetzt aus den Fluten empor.
Mit dem Genius steht die Natur in ewigem Bunde,
Was der eine verspricht, leistet die andre gewiß.*

- Kolumbus (Friedrich Schiller)

*Steer, bold mariner, on! albeit wifings deride thee,
And the steersman drop idly his hand at the helm;
Ever, ever to westward! There must the coast be discovered,
If it but lie distinct, luminous lie in thy mind.*

*Trust to the God that leads thee, and follow the sea that is silent;
Did it not yet exist, now would it rise from the flood.
Nature with Genius stands united in league everlasting;
What is promised to one, surely the other performs.*

- Columbus (by Friedrich Schiller, translated by Henry Wadsworth Longfellow)